NASA

RESEARCH AND DEVELOPMENT PROGRAM FOR NONLINEAR
STRUCTURAL MODELING WITH ADVANCED
TIME-TEMPERATURE DEPENDENT
CONSTITUTIVE RELATIONSHIPS

FINAL REPORT

by

KEVIN P. WALKER

UNITED TECHNOLOGIES RESEARCH CENTER
400 MAIN STREET
EAST HARTFORD, CONNECTICUT 06108

Prepared for

NATIONAL AERONAUTICS AND SPACE ADMINISTRATION
NASA Lewis Research Center
Contract NAS3-22055

PWA-5700-50

1. Report No. NASA CR-165533	2. Government Accession No.	3. Recipient's Catalog No. *N82 16080*
4. Title and Subtitle Research and Development Program For Non-Linear Structural Modeling with Advanced Time-Temperature Dependent Constitutive Relationships		5. Report Date 25 November 1981
		6. Performing Organization Code
7. Author(s) Dr. Kevin P. Walker		8. Performing Organization Report No. PWA-5700-50
		10. Work Unit No.
9. Performing Organization Name and Address United Technologies Research Center 400 Main Street East Hartford, Conn. 06108		
		11. Contract or Grant No. NAS3-22055
		13. Type of Report and Period Covered Contractor Final Report
12. Sponsoring Agency Name and Address NASA/Lewis Research Center 21000 Brookpark Road Cleveland, Ohio 44135		
		14. Sponsoring Agency Code

16. Abstract

This report presents the results of a 20-month research and development program for nonlinear structural modeling with advanced time-temperature constitutive relationships. This program was conducted by Pratt & Whitney Aircraft and the United Technologies Research Center for the NASA-Lewis Research Center under Contract NAS3-22055. The program included: (1) the evaluation of a number of vicoplastic constitutive models in the published literature; (2) incorporation of three of the most appropriate constitutive models into the MARC nonlinear finite element program; (3) calibration of the three constitutive models against experimental data using Hastelloy-X material; and (4) application of the most appropriate constitutive model to a three dimensional finite element analysis of a cylindrical combustor liner louver test specimen to establish the capability of the viscoplastic model to predict component structural response.

17. Key Words (Suggested by Author(s)) Gas Turbine Engines, Creep, Plasticity, Visco-Plasticity, Constitutive Relationships, Thermovisco-Plasticity, Inelastic	18. Distribution Statement Unlimited, Unclassified	
19. Security Classif. (of this report) Unclassified	20. Security Classif. (of this page) Unclassified	21. No. of Pages 187	22. Price*

* For sale by the National Technical Information Service, Springfield, Virginia 22161

NASA-C-168 (Rev. 10-75)

Research and Development Program for Nonlinear
Structural Modeling with Advanced
Time-Temperature Dependent
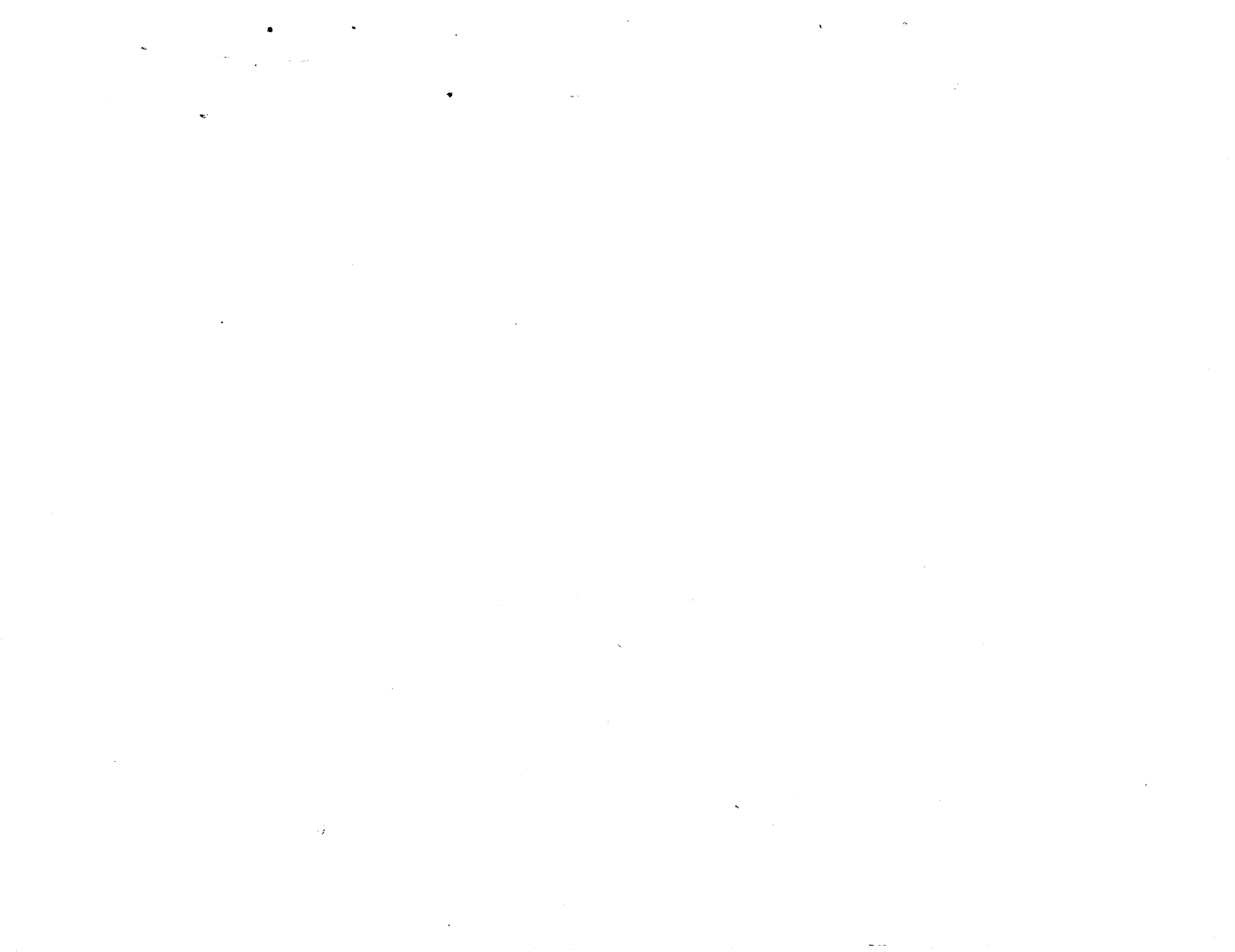Constitutive Relationships

TABLE OF CONTENTS

FOREWORD

The work described in this report was performed by the United Technologies Research Center and by Pratt and Whitney Aircraft Group, Commercial Products Division, for the NASA-Lewis Research Center under Contract NAS3-22055. The program manager and principal investigator was Dr. Kevin P. Walker. The NASA-Lewis technical project manager was Dr. Robert Kielb.

Research and Development Program for Nonlinear
Structural Modeling with Advanced
Time-Temperature Dependent
Constitutive Relationships

1.0 SUMMARY

   The results of a twenty (20) month technical program, entitled "Research and
Development Program for Nonlinear Structural Modeling with Advanced Time-Temperature
Constitutive Relationships", are presented. This program was conducted by Pratt
and Whitney Aircraft and the United Technologies Research Center for the NASA-Lewis
Research Center under Contract NAS3-22055. The program included: (1) the evalua-
tion of a number of viscoplastic constitutive models in the published literature;
(2) incorporation of three of the most appropriate constitutive models into the
MARC nonlinear finite element program; (3) calibration of the three constitutive
models against experimental data using Hastelloy-X material; and (4) application of
the most appropriate constitutive model to a three dimensional finite element analy-
sis of a cylindrical combustor liner louver test specimen to establish the capa-
bility of the viscoplastic model to predict component structural response.

   Based on a qualitative evaluation in Task I, three viscoplastic constitutive
theories of material behavior, namely: (1) Walker's functional theory; (2) Miller's
theory; and (3) Krieg, Swearengen and Rohde's theory, were chosen for further study
in Task IV. Evaluations of the three theories were based on a comparison of the
predicted and the experimentally observed constitutive response of Hastelloy-X
material developed in Task II. Each theory was incorporated into a subroutine
of the MARC nonlinear finite element program in Task III. (A listing of the
FORTRAN subroutine delivered to the NASA-Lewis Research Center is given at the end
of the report.) Based on the evaluations in Task IV, Walker's functional theory
was chosen to analyze the structural response of a combustor liner induction rig
test specimen under temperature and strain cycles comparable to those in actual
engine operation. The MARC subroutine incorporating the functional theory was
delivered to the NASA-Lewis Research Center and installed for use on the UNIVAC 1100
computer.

   The three viscoplastic constitutive theories were incorporated into the MARC
program by means of an initial stress technique. All of the material nonlinearity
in the constitutive equations is incorporated into an initial load vector and
treated as a pseudo body force in the finite element equilibrium equations.

   The structural analysis of the combustor liner specimen under complex thermo-
mechanical loading cycles has shown a deficiency in the currently proposed visco-
plastic constitutive theories. These theories use various internal state variables

which employ a hardening-recovery format to determine their growth. The growth of the internal state variables due to hardening takes place only in the presence of inelastic deformation, while the recovery of the internal state variables can take place in the absence of inelastic deformation. Because internal state variable growth due to hardening can only take place in the presence of inelastic deformation, no change in the state variables (other than recovery or annealing) can take place during the elastic unloading phases of a thermomechanical cycle. Experimental evidence suggests that the state variables can change with temperature variations during the elastic unloading phase of a thermomechanical cycle.

2.0 INTRODUCTION

2.1 Program Need

The overall operating cost of the modern gas turbine engine is greatly influenced by the durability of combustor and turbine structural components while operating at high temperatures. During each flight cycle, these components undergo large thermally induced stress and strain cycles which include significant amounts of creep and relaxation. Requirements for higher turbine inlet temperatures, uniformity of temperature profiles, increased turbine cooling, and reduced emission levels have increased heat and pressure loads on combustor liners, while limiting the amount of air available for cooling the liners. Creep/fatigue cracking and creep buckling distortion of combustor liners reduces turbine durability through higher temperatures, and through impact and erosion damage caused by liberated pieces of the liner and hard carbon particles.

2.2 Program Objectives

The current program addresses a critical issue in the development of advanced life prediction technologies – the need to develop advanced viscoplastic constitutive relationships and the evaluate their effectiveness in predicting the cyclic stress-strain history at critical fatigue locations in major hot section components.

In order to meet the objectives of the current program, the advanced constitutive models have been specifically calibrated against Hastelloy-X material which is used in the construction of combustor liners. But the constitutive models themselves, and the methods developed to evaluate the material constants required to support the models, are generally applicable to other materials. In addition, the modular form of the computer routines developed in the program should allow their incorporation, with necessary changes, into any nonlinear structural analysis finite element program.

2.3 Program Relevance

The current program provides an improved structural analysis capability and forms a sound base for future improvements in mission life analysis programs. With such screening tools available it will be possible to ensure that only promising new candidate schemes are put into hardware without waiting for one or two years of field operation to provide a feedback to the design scheme.

Improvements in hot section component durability will have a profound impact on the operating costs of high bypass ratio turbofan engines through reduced maintenance cost. Equally important is the need to achieve reduced emissions levels and fuel

3

consumption while maintaining the durability of hot section components. The achievement of advancements in hot section component durability technology will directly support the maintenance of U.S. leadership in the aircraft gas turbine engine industry.

2.4 Background

The overall operating cost of the modern gas turbine engine is significantly affected by the durability and efficiency of the major hot section components, the combustor and turbine. Primary responsibilities of the combustor are gas temperature level and pattern control, required for efficient turbine operation, and exhaust emission control at the various flight operating conditions. These goals are accomplished by the precise metering of air throughout the combustor structure. The high pressure and high combustion gas temperature characteristics of this environment require that the combustor liner be cooled for durability.

These requirements for control of exit gas temperature, emissions, and metal temperature generate an intense competition for utilization of combustor airflow. The more aggressive performance, efficiency, and emission goals set for future engines emphasize the need for development of durable combustor structures which can operate with reduced levels of cooling air. This requires detailed knowledge of the operating environment and the ability to accurately predict structural response for these loadings.

At high operating temperatures, the time dependence of the inelastic behavior of the structural material is a significant consideration in the design and analysis of combustor liners. Currently, most combustor liners are constructed of sheet metal louvers which rely on convective film cooling. Details of a louver geometry are shown in Fig. 1 where the individually formed pieces are seam welded together in the fabrication of the louver liner. Cooling of each individual louver is accomplished by compressor discharge air, introduced into the chamber created by the louver lip and knuckle region to generate an insulating film of cooling air on the downstream panel. Degradation of the cooling film, as it moves along the panel, results in increased metal temperature in the seam weld and louver lip regions. The thermal gradient between these regions and the knuckle of the next louver is a function of the engine operating condition. Figure 1 indicates the typical knuckle location (B) which is generally cooler than the typical louver lip location (A). The temperature difference between these two locations creates thermal stresses in the combustor liner. At the maximum power point, the thermally induced stress and strain state at the louver lip has significant amounts of plasticity which, when repeated over subsequent engine flight cycles, results in creep/fatigue failure of the liner. In large diameter annular combustor liners, fatigue cracks initiate in the louver lip region and grow axially toward the seam weld. Continued growth can result in distortion of the local cooling air stream, resulting in over-heating and burning of the liner and serious damage to the turbine components. Typical liner failures of this type are shown in Fig. 2. Analytical modeling and life prediction

of this kind of structural response has been hampered by lack of well-calibrated temperature data, high temperature cyclic material information, and precise engine failure data. With the advent of improved thermal and structural analysis capabilities and the development of test facilities to provide well-controlled component failure data, new structural modeling strategies and life prediction systems can be proposed and calibrated for the development of improved combustor liner structures. With such analytical screening tools available, it will be possible to ensure that only promising new candidate schemes are put into hardware without waiting for one or two years of field operation to provide feedback to the design scheme.

Life prediction of combustor liners requires a thorough knowledge of the thermal environment, accurate material characterization, general capability stress analysis techniques, calibrated failure data, and a life prediction model. The advent of general purpose finite element programs has provided a capability for detailed modeling of engine hot section components where the component structural response is dominated by significant amounts of nonlinear material behavior. However, the structural analysis of such components is usually carried out in nonlinear finite element programs, such as MARC (Ref. 1), which possess a degree of programming sophistication far in advance of their constitutive material modeling capability.

Most nonlinear finite element programs, in keeping with an accepted practice in the elevated-temperature design community, partition nonlinear elevated-temperature material behavior into rate-dependent "creep" and rate-independent "plasticity" components. Each component is assumed to obey a separate constitutive law in which the rate-dependent creep strain is assumed to be independent of the time-independent plastic strain and the plastic strain is assumed to be independent of the creep strain. No provision for interaction between creep and plastic behavior is present in the constitutive equations. These theories are therefore of questionable value at high temperatures where such interactions are known to occur.

In addition to the inability to model the interaction between creep and plasticity, most of the classical plasticity theories suffer from an inability to accurately model material behavior under cyclic load conditions. Under such loading conditions the classical theories are unable to predict the strain hardening/softening characteristics of the material. These limitations in constitutive modeling behavior have recently been discussed at a number of symposia (Refs. 2-6) and also in some depth by Krempl (Ref. 7).

Since the constitutive material model lies at the heart of all general purpose nonlinear finite element codes, including the MARC program, it is clear that the development and efficient implementation of new viscoplastic constitutive models into such programs is needed before the full potential of such codes can be fully utilized for advanced high temperature component structural analysis.

5

State-of-the-art finite element methodology and life prediction algorithms have been evaluated against failure data from a combustor liner induction rig test specimen under contract NAS3-21836 (Ref. 8), with the NASA-Lewis Research Center. The work described in the present report provides an enhanced ability to assess the degree of cyclic nonlinear structural behavior generally associated with thermo-mechanical fatigue damage. A flow chart indicating where better material modeling capability fits into an improved life prediction scheme is shown in Fig. 3.

2.5 Scope of Program

A twenty (20) month program was conducted to develop and evaluate a number of time-dependent constitutive theories suitable for the structural analysis of components which operate at elevated temperature. The work effort was organized into the following tasks.

Task 1 - Constitutive Model Selection

Ten viscoplastic constitutive models, available in the published literature, were examined to assess their potential capabilities and limitations in representing the thermomechanical response experienced by components (such as a combustor liner) which operate in a cyclic elevated temperature environment. Based on this examination, three (3) theories were selected for further evaluation and incorporation into the MARC nonlinear finite element program.

Task 2 - Materials Testing

Specimen tests were conducted using a representative combustor liner material, Hastelloy-X, to determine the required temperature dependent material constants and to evaluate each of the three selected constitutive theories. These tests utilized smooth, uniaxial bar specimens of Hastelloy-X together with a closed loop servo-hydraulic INSTRON testing machine. The following tests were performed on the uni-axial bar specimens:

(a) Fully reversed cyclic stress-strain tests for a range of strain rates and temperatures consistent with the operating conditions of a representative combustor;

(b) Creep tests at various stress levels and temperatures starting from various points on steady-state hysteresis loops executed at constant strain rate under fully reversed strain controlled conditions;

(c) Stress relaxation tests at various temperatures starting from zero initial strain values on steady state hysteresis loops executed at various strain rates under fully reversed strain controlled conditions.

Tests (a), (b), and (c) were used to determine the material constants for each of the constitutive theories at temperatures ranging from 427°C to 982°C (800°F to 1800°F).

A "faithful cycle" thermomechanical test having a prescribed strain-temperature history appropriate to that of a critical combustor liner fatigue location (location A at the louver lip in Fig. 1) provided an experimental thermomechanical hysteresis loop for evaluation of the constitutive theories under complex loading cycles involving large changes in temperature and strain rate.

Task 3 - Incorporation of Theories into Finite Element Program

Each of the three theories was incorporated into a FORTRAN user subroutine of the MARC nonlinear finite element program. An initial stress technique was used in which the incremental constitutive relationship used in evaluating the incremental initial load vector was determined by a subincrement method. An integral recursion relation was developed for Walker's functional theory which has proved to be stable and accurate, even for large incremental time/load steps. Miller's theory and the theory of Krieg, Swearengen and Rohde have been formulated as integral theories, but have not, as yet, been incorporated in integral form into the MARC program. These theories have been integrated over each subincrement by means of an explicit Euler forward difference method.

Task 4 - Comparison and Evaluation of Candidate Theories

The three candidate constitutive theories were evaluated by comparing the predicted uniaxial response of Hastelloy-X material with the experimental results generated in Task 2. Based on these evaluations the functional theory was selected to analyze the structural behavior of a simulated combustion chamber outerliner. The FORTRAN subroutines for both the differential and integral forms of the functional theory were then delivered to the NASA-Lewis Research Center and installed in the MARC program for use on the UNIVAC 1100 computer. Two demonstration problems were then executed to ensure correct functioning of the computer program at the NASA-Lewis Research Center.
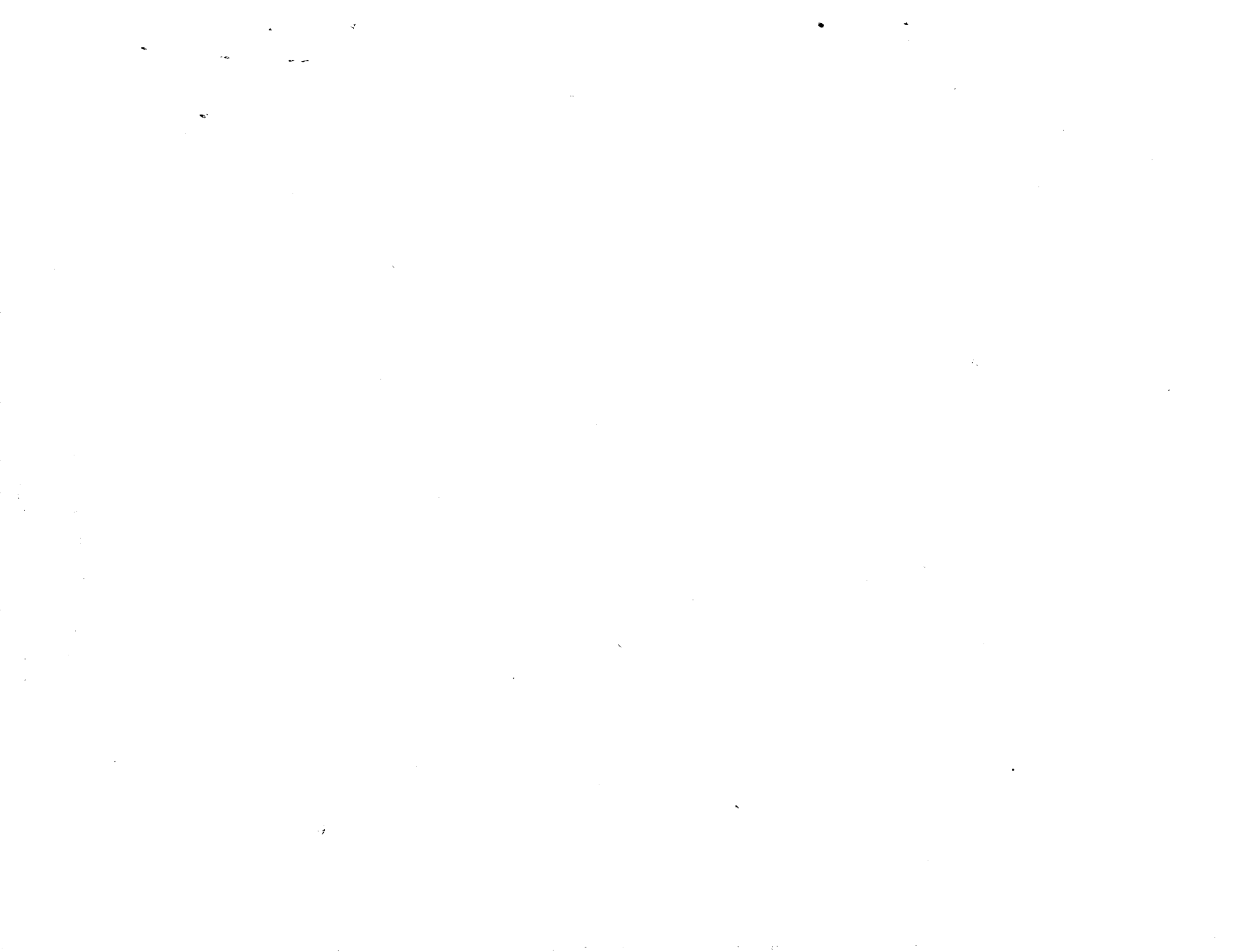
3.0   TASK I — TIME-DEPENDENT CYCLIC
PLASTICITY MODEL SELECTION

3.1   Constitutive Theory Review

Ten isotropic viscoplastic theories, listed in Appendices 1-12, were examined in order to assess their potential capabilities and limitations in representing the thermomechanical structural response experienced by a jet engine combustor liner. In order to obtain commonality in the theories, the equilibrium (rest or back) stress has been denoted by Ω_{ij}, the drag stress by K, and the inelastic strain by c_{ij}.

In the isotropic theories selected for further evaluation, it is assumed that the inelastic response of the material is incompressible with $c_{kk} = 0$. The formulation of the theories then implies that: (a) the response to a hydrostatic loading is linearly elastic, and (b) that the shear response of the material can be determined from its uniaxial response. The inelastic incompressibility assumption can easily be relaxed if future testing shows that the multiaxial response cannot be determined from uniaxial behavior. From the limited amount of available experimental data, it would appear (Ref. 9) that the incompressibility assumption for the inelastic response is not satisfied.

Some brief remarks on unified viscoplastic constitutive equations in general will now be given before proceeding to review each theory.

All of the theories listed in the Appendices, with the exception of Valanis' theory (Appendix 12) and the theory of Bodner, Partom and Stouffer (Appendix 7), allow the expression for the inelastic strain rate under monotonic loading conditions to be written in the form

$$\dot{c} = \dot{\epsilon} - \frac{\dot{\sigma}}{E} = f^{-1}\left(\frac{\sigma - \Omega}{K}\right),$$

(3.1)

where f^{-1} is a function of the argument $((\sigma-\Omega)/K)$ which differs amongst the theories and whose inverse is denoted by the function f, so that $ff^{-1} = 1$. Under rapid loading conditions the derivative terms in Eq. (3.1) become paramount and the response of the material approximates to $\dot{\sigma} \approx E\dot{\epsilon}$. The viscoplastic formulations therefore exhibit an elastic response under infinitely fast loading conditions. An inelastic response under infinitely fast loading conditions could be incorporated into the theories by replacing Eq. (3.1) with

$$\dot{\Xi} - \dot{\sigma} = f^{-1}\left(\frac{\sigma - \Omega}{K}\right),$$

(3.2)

in which $\sigma = \Xi$ is the instantaneous inelastic stress-strain response. A suitable growth law for Ξ would then be required.

Under monotonic loading conditions the tangent modulus of metals is much smaller than the elastic modulus, so that for large strain values $\dot{\sigma}/E << \dot{\epsilon}$, and the asymptotic stress-strain relation in Eq. (3.1) may be written as

$$\sigma \approx \pm \left[\Omega + Kf(\dot{\epsilon}) \right] \text{ as } \epsilon \to \pm \infty .$$

(3.3)

Cyclic hardening of the hysteresis loops can be accommodated by allowing the equilibrium stress Ω and the drag stress K to increase with an increase in the cumulative inelastic strain incurred by the material under cyclic loading conditions.

Two repositories exist for incorporating cyclic hardening into the viscoplastic theories. First, consider the case where the equilibrium stress Ω rapidly saturates to a limiting value at large strains, so that Ω has reached a constant value at the tip of the first cyclic hysteresis loop reversal. Cyclic hardening can be incorporated into the theories by assuming that the drag stress K increases with cumulative inelastic strain under cyclic loading conditions. If the material exhibits a positive strain rate sensitivity the cyclic stress amplitude increases with strain rate under strain-controlled conditions and the term $Kf(\dot{\epsilon})$ increases with increasing values of $\dot{\epsilon}$. At elevated temperatures and high strain rates the term $Kf(\dot{\epsilon})$ in Eq. (3.3) may be the dominant term at the tips of the hysteresis loops. Under such conditions the hysteresis peak stresses may be approximated by the expression $\sigma \approx \pm Kf(\dot{\epsilon})$. If the drag stress increases from an initial value of K_I to a final saturated value of K_F under sustained cycling, the fractional increase in stress amplitude, viz. $|\sigma_F - \sigma_I| / |\sigma_I|$ where $\sigma_F = K_F f(\dot{\epsilon})$ and $\sigma_I = K_I f(\dot{\epsilon})$, is independent of strain rate. The same relative amount of cyclic hardening is observed at all strain rates when the strain rate is large. Hardening of the drag stress K which is a scalar quantity, with cumulative deformation, introduces isotropic hardening into the viscoplastic formulation. At high strain rates the original stress amplitude $\pm\{\sigma_I = K_I f(\dot{\epsilon})\}$ increases equally in both the compressive and tensile directions to a final saturated value of $\pm\{\sigma_F = K_F f(\dot{\epsilon})\}$. An example of this type of isotropic hardening is shown in Fig. 4.

Another type of cyclic hardening can be incorporated into the viscoplastic theories by assuming that the drag stress rapidly saturates to a limiting value at large strains (or remains constant). Cyclic hardening is then assumed to occur due to increases in the value of the equilibrium stress tensor Ω_{ij} at the peaks of the hysteresis loops due to sustained cyclic loading. At the hysteresis loop peaks the term $Kf(\dot{\epsilon})$ is now constant for a given rate of straining and the stress amplitude increases due to increases in the magnitude of Ω. This type of kinematic hardening produces a response quite different to that produced with an isotropic hardening

mechanism. Since the hardening occurs in the equilibrium stress Ω, the relative amount of observed cyclic hardening will decrease with increasing strain rate. At sufficiently high strain rates where the term $Kf(\dot{\varepsilon})$ in Eq. (3.3) is paramount, virtually no cyclic hardening in the stress amplitude will be apparent. Kinematic hardening of the equilibrium stress produces the type of hardening observed in Fig. 5. In this figure, the peak stress amplitude increases with cycle number while the "yield stress" decreases with cycle number. This results in a plastic tangent modulus which increases with cycle number. An explanation of this effect can be obtained from an examination of Eq. (3.1). The production of an observable value of the inelastic strain rate, $\dot{c}$, depends on the magnitude of the stress difference $\sigma-\Omega$. As the magnitude of Ω increases at the hysteresis peaks due to cyclic hardening, the magnitude of stress σ required to produce "yielding", or an observable value of $\dot{c}$ in the reverse direction, decreases. In general, it is appropriate to incorporate both forms of cyclic hardening into the constitutive formulation. The hardening/softening mechanisms adopted by the unified viscoplastic theories are displayed in Table 1.

In addition to differences in the functional form adopted for the growth of the inelastic strain rate with the state variables Ω and K in Eq. (3.1), the viscoplastic theories also differ in the functional form assumed for the growth laws which determine the evolution of the state variables Ω and K. These state variables are assumed to evolve according to differential constitutive equations which exhibit a hardening/recovery format. At large strain values these state variables saturate to limiting functional forms which, in the theories of Walker, Chaboche and Lee & Zaverl, are independent of strain rate at high rates of strain. In the remaining state variable theories the limiting functional forms of Ω and K depend on the strain rate even at high rates of strain.

Saturation of the equilibrium stress and drag stress state variables is achieved when the antagonistic effects of hardening and recovery cancel each other in the state variable evolution equations. If these equations are written in the form

$$\dot{\Omega} = f_1 \dot{c} - f_2 \Omega |\dot{c}| - f_3 |\Omega| \qquad (3.4)$$

and

$$\dot{K} = f_4 |\dot{c}| - f_5 K |\dot{c}| - f_6 K , \qquad (3.5)$$

where f_1, f_2, ...f_6 are functions of Ω and K, and $\dot{c}$ is the inelastic strain rate, then the limiting saturation values are achieved when the growth rates of Ω and K become small. One may therefore set $\dot{\Omega} = 0$ and $\dot{K} = 0$ to obtain the limiting forms of Ω and K as

TABLE 1

MECHANISM FOR CYCLIC HARDENING/SOFTENING IN THE
UNIFIED VISCOPLASTIC THEORIES

Hardening/Softening due to both Ω and K [*]	Hardening/Softening due to K [**]	Hardening/Softening due to Ω [***]	No Hardening/ softening [****]
Walker Chaboche Lee & Zaverl	Miller	Cernocky and Krempl	Krieg, Swearengen & Rohde

[*] Hardening/softening of the Ω and K state variables implies a combination of cycle dependent kinematic hardening with an isotropic hardening component

[**] Hardening/softening of the K state variable implies a combination of ideal kinematic hardening with an isotropic hardening component

[***] Hardening/softening of the Ω state variable implies cycle dependent kinematic hardening with no isotropic component

[****] No hardening/softening of the state variables implies ideal kinematic hardening

$$\Omega = \frac{f_1 \dot{c}}{f_2 |\dot{c}| + f_3 |\Omega|/\Omega}$$

and   (3.6)

$$K = \frac{f_4 |\dot{c}|}{f_5 |\dot{c}| + f_6} \; .$$

These limiting forms depend on the strain rate at low rates of strain.

At high rates of strain $f_2 |\dot{c}| \gg f_3 |\Omega|/\Omega$ and $f_5 |\dot{c}| \gg f_6$. The state variables then achieve the rate independent forms

$$\Omega = \pm \left\{ f_1(\Omega,K)/f_2(\Omega,K) \right\}$$ (3.7)

and

$$K = \left\{ f_4(\Omega,K)/f_5(\Omega,K) \right\} \; .$$ (3.8)

The terms $f_2 \Omega |\dot{c}|$ and $f_5 K |\dot{c}|$ in Eqs. (3.4) and (3.5) which are responsible for these rate independent limits may be called dynamic recovery terms, since they are acti-vated only in the presence of an inelastic strain rate. The terms $f_3 |\Omega|$ and $f_6 K$ in Eqs. (3.4) and (3.5) represent the effects of static thermal recovery and are activated even in the absence of an inelastic strain rate. If the dynamic recovery terms are absent the limiting values of the state variables may be written in the rate dependent forms

$$\Omega = \dot{c} \left\{ f_1(\Omega,K)/f_3(\Omega,K) \right\}$$ (3.9)

and

$$K = |\dot{c}| \left\{ f_4(\Omega,K)/f_6(\Omega,K) \right\} \; .$$ (3.10)

The limiting state variable behavior of some of the viscoplastic formulations is listed in Table 2. It should be emphasized that although some formulations exhibit a rate independent state variable behavior at high strain rates, the viscoplastic theories still exhibit a rate dependent stress-strain response through the presence of the function $f(\dot{\varepsilon})$ in Eq. (3.3).

TABLE 2

LIMITING BEHAVIOR OF STATE VARIABLES AT LARGE STRAIN RATE

	Ω	K	z (see Appendix 7)	σ^* (see Appendix 11)
Walker	Rate Independent	Rate Independent		
Chaboche	Rate Independent	Rate Independent		
Miller	Rate Dependent	Rate Dependent		
Lee & Zaverl	Rate Independent	Rate Independent		
Bodner & Partom	Not used		Rate Independent If No recovery in z	
Krieg, Swearengen & Rohde	Rate Dependent	Rate Dependent		
Cernocky & Krempl	Rate Independent	Rate Independent		
Hart	Rate Dependent	Not Used		Rate Dependent

13

The behavior of the viscoplastic theories under creep and relaxation conditions is governed by the growth of the state variables. Figure 6 shows the steady state stress-strain hysteresis loop GJAHCFIG executed at a constant strain rate magnitude under fully reversed strain controlled conditions, while the equilibrium curve is shown as the "S" shaped hysteresis loop DEF. If, under steady state cycling, the stress is held constant at point A on the hysteresis loop the material will creep along the line ABC at constant stress. Initially, when the stress is held constant at point A, the equilibrium stress Ω is determined by the stress value at point D. As the material creeps along ABC the equilibrium stress grows along the curve DEF according to the growth laws for Ω in the Appendices. The difference between the actual stress and the equilibrium stress decreases to a constant value during creep. Since the creep rate depends on this difference, the creep rate also decreases (primary creep) and then remains constant (secondary creep). If the initial stress is large enough, so that the initial value of the equilibrium stress is at its saturation value, then the difference $\sigma - \Omega$ will remain constant in the creep test and secondary creep will occur without a primary transient. In the case where creep initiates at point J in Fig. 6, where the stress lies below the peak of the equilibrium stress-strain curve, no secondary creep takes place and creep terminates at point D on the equilibrium stress-strain curve.

If the stress is held constant at point C on the unloading branch of the hysteresis loop, the initial value of $\sigma - \Omega \approx CF$ is small, and very little creep is observed initially. At elevated temperature the equilibrium stress Ω will gradually decrease due to static thermal recovery (if included in the constitutive formulation), so that the creep rate gradually increases due to the increase in $\sigma - \Omega$. Eventually, the decrease in the equilibrium stress is halted when the hardening of Ω, governed by the f_1 term in Eq. (3.4), balances the recovery terms containing f_2 and f_3. Secondary creep then takes place at the point C. The creep behavior on the unloading branch of the hysteresis loop may be contrasted with the creep behavior, at the same stress level, on the loading branch of the hysteresis loop. Here, the initial value of $\sigma - \Omega$ is large, and a rapid primary transient in the creep curve is observed. This difference in creep response on the loading and unloading branches of the hysteresis loop is shown in Fig. 7.

The behavior of the constitutive theories in relaxation is analogous to the creep behavior. Under stress relaxation conditions at constant strain the relaxation rate depends on the difference $\sigma - \Omega$ so that if stress relaxation commences at point A in Fig. 6, the amount of relaxation is large. However, if stress relaxation commences at point C on the unloading branch, very little relaxation is initially observed. As with the creep behavior, the hesitation in the relaxation curve observed on the unloading branch of the hysteresis loop eventually gives way to more rapid relaxation as the term $\sigma - \Omega$ increases due to thermal recovery (if included) of the equilibrium stress.

When the initial point at which creep or relaxation commences on the unloading branch of the hysteresis loop is below the equilibrium curve, at point I in Fig. 6, the theories predict that the stress will initially relax upwards towards the equilibrium curve during a stress relaxation test in which the total strain is held constant, or will creep in the negative direction (contract) at the positive stress value at point I during a creep test. The negative creep and negative (upward) relaxation will terminate on the equlibrium curve if the static thermal recovery containing f_3 is absent in Eq. (3.4) governing the growth of Ω. However, if static thermal recovery is included, the equilibrium stress Ω will eventually drop below the actual stress σ at point I during a creep test and, with $\sigma-\Omega$ now being positive, the material will commence creeping in the positive direction. Similarly, the upward relaxation will cease when the equilibrium stress drops below the actual rising stress value and normal (downward) relaxation then ensues. Figure 8 shows that negative stress relaxation commences in compression at −21 MPa (−3 ksi) on the unloading hysteresis branch and progresses through zero to tensile values as the stress relaxes towards the equilibrium curve.

With the foregoing remarks in mind a review is now given of ten viscoplastic constitutive theories available in the published literature.

3.2 Walker's Functional Theory

This theory (Ref. 11) was developed in an integral form by modifying the constitutive relation for a three parameter viscoelastic solid. Both the integral and the differential forms of the theory are summarized in Appendices 1 and 2. Two state variables, Ω_{ij} and K, are introduced into the viscoelastic theory to account for the effects of viscoplasticity. The equilibrium (rest or back) stress Ω_{ij} introduces nonlinear kinematic hardening into the model to account for the Bauschinger effect, while the drag stress K introduces isotropic hardening into the model to account for cyclic hardening or softening of the material.

The growth law for the equilibrium stress contains both dynamic recovery and static thermal recovery terms. At high strain rates the thermal recovery term becomes insignificant in comparison with the dynamic recovery term and the equilibrium stress becomes independent of strain rate. In the growth law for the drag stress, static thermal recovery terms have been omitted, which permits the drag stress to be written in the integrated form shown in Eq. (3) of Appendix 1. This form has been found adequate in the modeling of Hastelloy-X behavior, but future applications may require the inclusion of static thermal recovery in the drag stress evolution law.

The theory is capable of modeling the cyclic hardening and softening of hysteresis loops without the use of a yield surface. Material constants required to model cyclic hardening/softening are obtained from cyclic hysteresis tests so

15

that cyclic hardening and softening can be accurately modeled. Both the
equilibrium stress Ω and the drag stress K contribute to the cyclic hardening
in the theoretical formulation.

Creep, relaxation and strain rate effects are modeled by a power law (Eq. (1)
of Appendix 2) for the inelastic strain rate. This expression has been found
adequate for the representation of strain rate effects encountered in a combustor
liner material under service conditions where strain rates may vary from 10^{-6} sec^{-1}
to 10^{-3} sec^{-1}. However, it appears that modifications are necessary if strain
rates greater than about 10^{-2} sec^{-1} are encountered. In particular, at higher
strain rates, the power law expression for the inelastic strain rate predicts values
of stress in a constant strain rate tensile test which are too large (cf. (Refs.
10 and 20)).

The integral expression for the equilibrium stress in Eq. (2) of Appendix 1
contains the material constant n_2 which appears outside the integral. On differen-
tiation with respect to time this integral expression reduces to the differential
form given in Eq. (2) of Appendix 2. The terms containing $\dot{\Theta}$ allow the equilibrium
stress to change during nonisothermal elastic excursions in which the inelastic
strain rate is zero. Reasons for the inclusion of the $\dot{\Theta}$ terms in the growth law
for the equilibrium stress are discussed in Section 6 of this report.

Calculations may be made with the theory to construct a theoretical yield
surface. For a given point in stress space one may construct a surface surrounding
this point such that in going from the given point to each point on the surface
the cumulative inelastic strain is the same for each point on the surface. If
this theoretical construct is called the yield surface, then the theory allows the
yield surface to translate in stress space by virtue of the presence of the equili-
brium stress (kinematic hardening) and to expand in stress space due to the presence
of the drag stress (isotropic hardening). No provision for a rotation of the yield
surface in stress space exists in the current theoretical formulation. All of the
material constants in this theory are functions of temperature and must be experi-
mentally determined at each temperature of interest.

3.3 Chaboche's Theory

This theory was developed by Chaboche (Refs. 12, 13), and is summarized in
Appendix 3. The theory is similar in form to the preceding functional theory
except that a yield surface concept is used. Inside the yield surface it is assumed
that no inelastic deformation can take place. The use of a yield surface permits
isotropic hardening to be modeled by an increase in the size of the yield surface
rather than by an increase in the drag stress state variable, K. Hence, in this
theory, K is assumed to be constant and the one-dimensional form of the inelastic
strain rate may be written in the form

$$\dot{c} = \dot{\epsilon} - \frac{\dot{\sigma}}{E} = \left\langle \frac{|\sigma - \Omega| - Y - k}{K} \right\rangle \frac{(\sigma - \Omega)}{|\sigma - \Omega|} , \qquad (3.11)$$

where the brackets < > are defined by the relation

$$\langle \alpha \rangle = \begin{cases} 0 & \text{if } \alpha \leq 0 \\ \alpha & \text{if } \alpha > 0 . \end{cases} \qquad (3.12)$$

Here, the isotropic state variable, Y, together with the yield surface concept, replaces the drag stress, K. Initially, the variable Y is assumed to be zero and inelastic deformation occurs only when $|\sigma - \Omega| > k$. As Y grows with inelastic deformation, the yield surface expands and inelastic deformation takes place only when $|\sigma - \Omega| > k + Y$. At high rates of uniaxial strain and large strain values (where $\dot{\sigma} \approx 0$), Eq. (3.11) takes the approximate form

$$\sigma \approx \Omega + Y + k + K \dot{\epsilon}^{1/n} \quad (\dot{\epsilon} \rightarrow +\infty) . \qquad (3.13)$$

At high strain rates Ω and Y become independent of strain rate, so that for very high strain rates

$$\sigma \approx K \dot{\epsilon}^{1/n} . \qquad (3.14)$$

This equation shows that at very high strain rates, no cyclic hardening is observed. Significant hardening will be observed only at lower strain rates when (Ω + Y + k) becomes comparable in magnitude with $K \dot{\epsilon}^{1/n}$.

The growth law for the equilibrium stress contains a $\dot{\Theta}$ term which allows the equilibrium stress to change with temperature during nonisothermal elastic excursions. Chaboche's theory, Walker's theory, and Cernocky & Krempl's theory, are the only viscoplastic formulations which permit such changes in the state variables to occur.

The yield surface can translate and expand in this formulation, but it cannot rotate. All of the material constants are functions of temperature and must be experimentally determined at each temperature of interest.

17

3.4 Miller's Theory

This theory (Ref. 14) is summarized in Appendices 4 and 5. Instead of a power law for the inelastic strain rate, the theory uses a hyperbolic sine function. In addition, only the material constants K_O and θ' are temperature dependent, K_O being the initial value of the drag stress K.

For monotonic one-dimensional loading, Miller's theory may be written in the form

$$\dot{c} = \dot{\epsilon} - \frac{\dot{\sigma}}{E} = B\theta' \left\{ \sinh\left(\frac{\sigma - \Omega}{K}\right)^{\frac{3}{2}} \right\}^n ,$$ (3.15)

$$\dot{\Omega} = H_1 \dot{c} - H_1 B\theta' \left\{ \sinh(A_1 \Omega) \right\}^n ,$$ (3.16)

$$\dot{K} = H_2 \dot{c}(C_2 + \Omega - A_2 K^3/A_1) - H_2 C_2 B\theta' \left\{ \sinh(A_2 K^3) \right\}^n .$$ (3.17)

The equilibrium stress is assumed to harden linearly with inelastic strain. Only static thermal recovery is included in the growth law for the equilibrium stress. In the absence of a dynamic recovery term, the equilibrium stress continues to increase with increasing strain rate; at high strain rates the growth law does not become independent of strain rate. In modeling the stress-strain behavior of materials, this theory exhibits the characteristic tri-linear curve in Fig. 9. The first portion of the tri-linear curve in Fig. 9 corresponds to an "elastic" loading phase in which the inelastic strain rate and rate of growth of the equilibrium stress is small. On entering the inelastic region the equilibrium stress grows linearly with inelastic strain which gives rise to the second portion of the tri-linear stress-strain curve. This may be seen by noting that in this region the growth law for Ω (with the neglect of the static thermal recovery term) may be written as $\Omega \approx H_1 c$, or since $\dot{\sigma} \ll E\dot{\epsilon}$, as $\Omega \approx H_1 \epsilon$. In this region, where the static thermal recovery term is small, the equilibrium stress increases linearly with strain. Since $\dot{\sigma} \ll E\dot{\epsilon}$, Eq. (3.15) governing the growth of inelastic strain, may be written for monotonic loading in the form

$$\sigma \approx \Omega + K \left\{ \sinh^{-1} \left(\frac{\dot{\epsilon}}{B\theta'}\right)^{1/n} \right\}^{2/3} .$$ (3.18)

Usually, the drag stress K grows slowly with deformation and the rate dependent term in Eq. (3.18) may be assumed to be constant (for $\dot{\epsilon}$ = constant). The stress then increases according to the relation $\sigma \approx H_1\epsilon$ + constant. Finally, the equilibrium stress reaches values sufficient to activate the static thermal recovery term in Eq. (3.16). This term increases very rapidly according to a hyperbolic

sine law and when it reaches a value equal in magnitude to that of the linear
hardening term, the equilibrium stress reaches a constant saturated value. This
gives rise to the third tri-linear portion of the stress-strain curve in Fig. 9.

The equilibrium stress saturates rapidly with deformation in this theory so
that no provision exists to model cyclic hardening or softening by means of cyclic
changes in the equilibrium stress. Cyclic changes in the stress-strain response
are modeled by cyclic changes in the drag stress. In the evolution equation for
the growth of the drag stress both dynamic recovery terms and static thermal
recovery terms are present. At fast strain rates only the dynamic terms (those
multiplied by $|\dot{c}|$) are significant. Now at large strain values the saturated value
of the equilibrium stress Ω may be determined from Eq. (3.15) by setting $\dot{\Omega} = 0$.
Hence, denoting the saturated value with the subscript s, the saturated equilibrium
stress may be written as

$$\Omega_s = \frac{1}{A_1} \sinh^{-1} \left(\frac{\dot{\epsilon}}{B\theta'} \right)^{1/n} , \qquad (3.19)$$

from which it is evident that the saturated equilibrium stress increases with strain
rate. From Eq. (3.17), only the first bracket is paramount at fast strain rates.
Within this bracket both Ω and K increase with strain rate. When the drag stress
reaches a saturation limit at a given constant strain rate, one may set $\dot{K} = 0$, and
by neglecting the constant C_2 in comparison with Ω and K, one obtains at satura-
tion

$$\Omega_s = \frac{A_2}{A_1} K_s^3 . \qquad (3.20)$$

This relation was derived under the assumption of rapid strain rate. But from the
construction of Eqs. (3.15)-(3.17), the relation may be shown to be valid at all
strain rates. For example, if Eq. (3.20) holds at all strain rates for the saturated
values of Ω and K, then setting Eq. (3.17) equal to zero at lower strain rates
where static thermal recovery is important produces the relation

$$|\dot{c}| = B\theta' \left\{ \sinh \left(A_2 K_s^3 \right) \right\}^n . \qquad (3.21)$$

Moreover, by setting Eq. (3.16) equal to zero, the saturated equilibrium stress is
governed by the relation

$$\dot{c} = B\theta' \left\{ \sinh \left(A_1 \Omega_s \right) \right\}^n . \qquad (3.22)$$

19

The relation between the saturated equilibrium and drag stresses given in Eq. (3.20) is now seen to hold at all strain rates by equating equations (3.21) and (3.22). One further relation between the equilibrium stress, drag stress and actual stress may be obtained by equating the saturated inelastic strain rates given in Eqs. (3.21) and (3.22) with that given in Eq. (3.15). One obtains

$$\left(\frac{\sigma_s - \Omega_s}{K_s}\right)^{\frac{3}{2}} = A_1 \Omega_s = \frac{A_2}{A_1} K_s^3 . \tag{3.23}$$

The assumption is now made that under steady-state creep conditions, the inelastic strain rate in Eq. (3.15) is governed by the Garofalo equation, viz.,

$$\dot{c} = B\theta' \left\{\sinh(A\sigma_s)\right\}^n . \tag{3.24}$$

Hence, under steady state conditions

$$\left(\frac{\sigma_s - \Omega_s}{K_s}\right)^{\frac{3}{2}} = A_1 \Omega_s = \frac{A_2}{A_1} K_s^3 = A\sigma_s . \tag{3.25}$$

The saturated equilibrium stress is linearly related to the saturated stress while the saturated back stress depends on the one-third power of the stress. This one-third power relation for the saturated drag stress, which is derived from the effect of warm working at various temperatures on the subsequent room-temperature yield strength of aluminum and 304 stainless steel, was assumed by Miller in setting up the framework of the viscoplastic theory.

Since cyclic hardening is incorporated into the isotropic drag stress state variable, hardening may be observed at all strain rates. At high strain rates the relative amount of cyclic hardening is the same for all strain rates as emphasized in Section 3.1.

The state variables Ω and K do not contain $\dot{\Theta}$ terms so that during nonisothermal "elastic" excursions the state variables "stick" at the values they had on entering the "elastic" region. If a theoretical yield surface is constructed with this theory, the yield surface can expand and translate in stress space, but no rotation of the surface is permitted.

The material constants n, H_1, H_2, A_1, A_2, C_2, Q^* and K of Appendix 4 are assumed to be independent of temperature. Those which depend on temperature are the elastic constants λ and μ; the initial value of the drag stress K_o, which depends on the initial temperature at time t = 0; and the constant θ' defined in Eqs. (7) and (8) of Appendix 4.

3.5 Lee & Zaverl's Theory

This theory (Ref. 15) employs a yield surface, which, in its general anisotropic form, can expand, translate and rotate. In this respect, it is the only theory considered in this report which allows the yield surface to rotate. However, in the more restricted isotropic form of the theory given in Appendix 6, no yield surface rotation due to deformation can occur.

Cyclic hardening has been incorporated into the yield stress state variable Y, the drag stress state variable K, and the equilibrium stress state variable Ω_{ij}. Since the inelastic strain rate in Eq. (1) of Appendix 6 depends on these state variables, it is appropriate to call them primary state variables. These state variables reach a saturation value at large strains by virtue of dynamic recovery terms alone, since no static thermal recovery terms are included in the theory. The dynamic recovery terms, which allow the primary state variables to reach their saturation values, contain the state variables σ_{ij}^S and Y^S. These additional state variables may be called secondary state variables since they govern the growth of the primary state variables. Because static thermal recovery terms are absent in the growth laws for the primary state variables, the saturated values of Y, K and Ω_{ij} are independent of strain rate. Moreover, the omission of $\dot{\Theta}$ terms in the state variable growth laws prohibits changes in the state variables during nonisothermal "elastic" excursions. The theory is more demanding on computer storage requirements than the preceding theories due to the presence of the secondary state variables.

3.6 Bodner, Partom and Stouffer's Theory

This formulation (Refs. 16-18), which is summarized in Appendix 7, differs from the other visoplastic theories by rejecting the concept of the equilibrium stress state variable Ω_{ij}. It is not, therefore, possible to describe negative creep effects at positive stress values, negative relaxation (see the experimental data in Fig. 8), or an aftereffect type of recovery in the material when the stress is removed.

The theory is capable of modeling kinematic and isotropic hardening, but accurate modeling of cyclic effects will probably require the constant q (which is equal to one for purely isotropic hardening and equal to zero for purely kinematic hardening) in Appendix 7 to be taken as a function of the plastic work.

Bodner and Stouffer have formulated a general anisotropic theory in Ref. (17), but only the isotropic form of this theory is shown in Appendix 7. Further comments concerning a generalization of the anisotropic model by Young may be found in Ref. (18).

The theory does not contain $\dot{\Theta}$ terms in the evolution equation for the state variable z. Consequently, this state variable cannot change during nonisothermal "elastic" excursions which precludes an accurate analysis of thermomechanical cycling.

If a theoretical yield surface is constructed from the model the surface can expand and translate in stress space but no rotation is permitted in an isotropic material.

3.7 Krieg, Swearengen and Rohde's Theory

This theory uses a power law to model the inelastic strain rate and was developed in a differential form (Ref. 19) by the authors. Both differential and integral forms of the theory are presented in Appendices 8 and 9.

An equilibrium stress and back stress are included in the formulation but no explicit provision exists to model cyclic hardening in either of the state variables. That is to say, the constants $A_1 - A_5$ appearing in the growth laws for the equilibrium and drag stresses do not explicitly depend on the cumulative inelastic deformation. Cyclic hardening could be modeled by assuming that the constants A_4 and A_5 are small in the growth law for the drag stress, so that the drag stress grows slowly with deformation.

The state variables saturate at large strain values when the static thermal recovery terms balance the linear strain hardening terms. No dynamic recovery terms are present in the formulation so that the saturated values of the state variables depend on the strain rate. Moreover, the linear hardening terms and the static thermal recovery terms in the state variable evolution equations produce stress-strain curves and hysteresis loops which exhibit the same tri-linear character as Miller's theory. The rapid final flattening of the stress-strain curve occurs when the static thermal recovery term grows rapidly with equilibrium stress according to the exponential law in Eq. (2) of Appendix 8. The sharpness of the final transition can be mitigated to some extent by assuming that the constant A_3 in Eq. (2) is very small. In this case the static thermal recovery term grows more slowly according to the fourth power of the equilibrium stress and this produces a smoother transition in the stress-strain curve and hysteresis loops.

The theory does not include $\dot{\Theta}$ terms in the state variable evolution equations, so that the state variables cannot change during nonisothermal "elastic" excursions. If a theoretical yield surface is constructed from the model the surface can expand and translate in stress space but no rotation of the surface can occur.

3.8 Cernocky and Krempl's Theory

This theory (Ref. 20) is written in an integral form in Appendix 10. In this particular form the theory is suitable for monotonic loading; for cyclic loading the "constants" E_t, α, β, K, δ and ζ are updated discontinuously according to a set of rules. Some of these updating rules are presented in Ref. (21) and the others are currently under development.

Both an equilibrium stress Ω_{ij} and a drag stress K are utilized in the theory. The updating of E_t, α and β in the equilibrium stress and the updating of the drag stress K with cyclic deformation allows for hardening in both state variables. Explicit relations are used for the equilibrium stress and the drag stress, so that only one differential (or integral) equation has to be solved (Eq. (1) in Appendix 10) rather than three. At large strains the state variables saturate to values which are independent of strain rate. Static thermal recovery terms have not yet been specified in the theoretical formulation.

Presumably, since the "constants" in the equilibrium stress, and in the drag stress itself, depend on the current temperature, the model permits the state variables to change under nonisothermal "elastic" excursions.

A theoretical construction of the yield surface from the model shows that the surface can both expand and translate in stress space, but cannot rotate.

3.9 Hart's Theory

Hart's theory (Ref. 22) is summarized in Appendix 11. Two state variables are employed, one being the equilibrium stress Ω_{ij}, and the other a scalar variable, σ^*, called the "hardness" by Hart. The "hardness", σ^*, may be called a secondary state variable since it serves only to modify the equilibrium stress state variable, Ω_{ij}, at large strain values (or after the imposition of cyclic loading) in the same manner as the secondary state variables in Lee & Zaverl's constitutive theory (Appendix 6).

The equilibrium stress grows linearly with inelastic strain in the initial loading phase and saturates when the static thermal recovery term containing the "hardness" state variable balances the linear work hardening term (the interpretation of the "hardness" term as being a static thermal recovery term is the author's). Since dynamic recovery terms are not included in the theoretical formulation, the saturated value of the equilibrium stress depends on the strain rate. The linear work hardening growth of the equilibrium stress together with the rapid growth of the static thermal recovery term at large strain values produces the tri-linear stress-strain response characteristic of Miller's theory and Krieg, Swearengen and Rohde's theory. A demonstration of this tri-linear behavior may be found in Fig. 6 of Delph's review paper (Ref. 23). Since the drag stress is assumed to be constant the theory can model only kinematic hardening. Due to the changes in the "hardness" state variable the saturated equilibrium stress can change with cumulative deformation during cycling in the manner depicted in Fig. 5. Here the peaks of the stress-strain hysteresis loop increase in amplitude, the "yield stress" decreases in value, and the tangent modulus increases as cycling continues. This behavior is just noticeable in Fig. 6 of Delph's paper (Ref. 23). It would have been even more apparent if Delph had increased the strain amplitude in his theoretical predictions. The fact that the drag stress is constant implies that isotropic hardening is absent in the theory. Hence, at high strain rates, where the saturated stress values in the peaks of hysteresis loops have the approximate

values, $\sigma \approx \pm K\dot{\varepsilon}^{1/n}$, the hardening is not apparent. The relative amount of hardening will increase at lower strain rates where the stress has the approximate form $\sigma \approx \pm (\Omega + K\dot{\varepsilon}^{1/n})$.

The theory does not include $\dot{\Theta}$ terms in the state variable evolution equations, so that the state variables cannot change during nonisothermal "elastic" excursions. If a theoretical yield surface is constructed from the model the surface cannot expand or rotate in stress-space since only kinematic hardening is permitted.

3.10 Valanis' Endochronic Theory

The endochronic theory (Ref. 24), summarized in Appendix 12, has been used mainly in a rate-independent form. Strain rate effects with creep-plasticity inter-action are still being developed by Wu and Chen (Ref. 25) and the rate-dependent aspect of the theory is still open. In the theory proposed by Wu and Chen (Ref. 25) different material functions are used in the formulation to describe the behavior of the material under constant strain rate, creep and relaxation conditions. A unification of the three material functions into one general function is required before the theory can be used under arbitrary loading conditions at high temperatures.

3.11 Laflen and Stouffer's Theory

This theory (Ref. 26) has no provision for cyclic hardening or static thermal recovery. It is therefore not suitable for describing the constitutive behavior of materials which exhibit significant cyclic hardening/softening. In its integral form the theory requires the evaluation of the entire integral of the strain history from the initiation of loading to the current time. For each new choice of the current time the entire integral must be recomputed (Ref. 28). This will exact severe economic and time penalties if it is used in a nonlinear finite element structural analysis code.

Three theories were selected for further evaluation based on the constitutive review in this section. These are: (a) Walker's functional theory; (b) Miller's theory; and (c) Krieg, Swearengen and Rohde's theory. However, the remaining theories are undergoing active development and it may be that in several years it will be possible to construct a hybrid theory which contains the best elements from each theory.
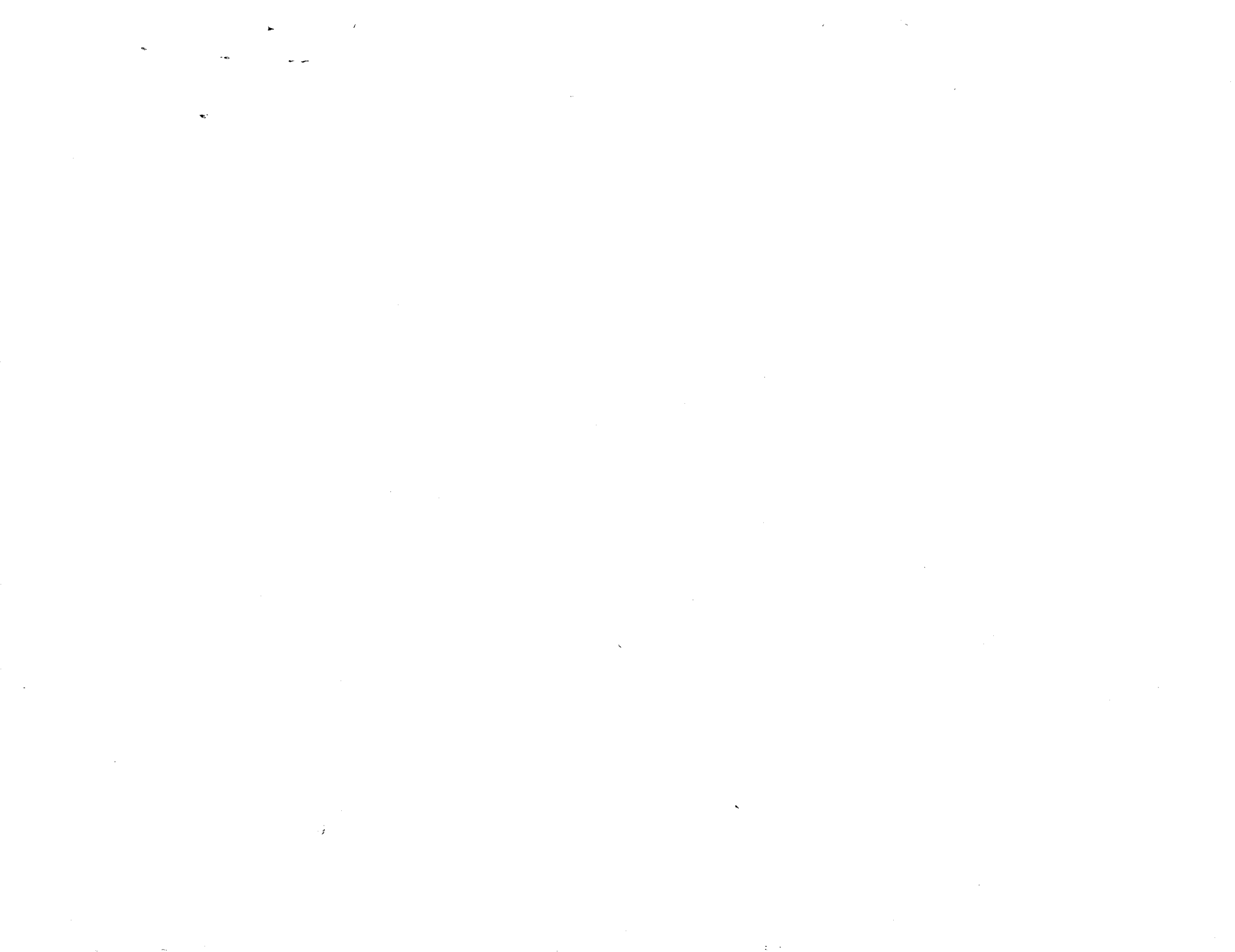
4.0 TASK II - CONSTITUTIVE TESTING

4.1 Choice of Material

Jet engine combustor liners are constructed from Hastelloy-X material. This material is a fine grained nickel base alloy which has relatively low strength but high ductility at elevated temperatures. The material constants required by the viscoplastic constitutive theories must be determined at various temperatures up to 2000°F (1093°C) in order to predict the structural response of combustor liners under engine operating conditions.

4.2 Choice of Testing Machine

The tests described in this section were conducted on uniaxial bar specimens using an INSTRON servo-hydraulic closed-loop testing machine capable of maintaining load or strain control with the inclusion of hold times. Specimens are maintained at a given temperature (to within 2°C (4°F)) in an oven heated by resistive elements which surround the specimen. Temperature control is maintained by a closed-loop system with thermocouples located at the ends of the cylindrical specimen. ASTM Class B-1 extensometry is used for the axial strain measurement. Load and total strain for this system can be controlled to within one percent. At $\pm$ 0.6 percent strain amplitude, a strain rate of 3.87 x 10^{-3} sec^{-1} corresponds to traversing the hysteresis loop about ten times per minute. Since the temperature of the specimen is controlled by thermocouples placed at its ends, it is possible that the dissipation of inelastic work into heat at these strain rates could raise the temperature at the center of the specimen above that registered by the thermocouples located at its ends. A computation in Appendix 13 shows that at 982°C (1800°F) the rise in temperature of the center of the specimen above the temperature at its ends is only 0.8°C (1.4°F), so that the effects of inelastic dissipation of work into heat can be neglected in the data reduction of the Hastelloy-X tests.

4.3 Uniaxial Hysteresis Tests

Uniaxial bar specimens of Hastelloy-X (see Fig. 10) were tested at temperatures of 427°C (800°F), 537°C (1000°F), 648°C (1200°F), 760°C (1400°F), 871°C (1600°F) and 982°C (1800°F).

This material is a fine grained nickel base alloy which has relatively low strength but high ductility at elevated temperatures. At each temperature the steady state hysteresis loops were determined under fully reversed strain controlled conditions. The input strain history consisted of a triangular wave function from a function generator with a strain amplitude of $\pm$ 0.6 percent at 760°C (1400°F), 871°C (1600°F), 982°C (1800°F) and a strain amplitude of $\pm$ 1.0 percent at 427°C (800°F), 537°C (1000°F) and 648°C (1200°F).

Hysteresis loops were obtained at strain rates of 1.25×10^{-6}, 1.11×10^{-5}, 3.70×10^{-5}, 3.66×10^{-4} and 3.87×10^{-3} sec^{-1} at each temperature. The material exhibits hysteresis loops which are asymmetric with respect to the strain axis at all temperatures, with the material being stronger in compression than in tension, and with the asymmetry increasing with temperature. However, the hysteresis loops are symmetric with respect to an axis which lies below the zero stress point. Experimental results for Hastelloy-X are shown in Figs. 11-16.

At 427°C (800°F) and 537°C (1000°F) an inverse strain rate sensitivity (Figs. 11 and 12) was observed in which the peak stresses of the hysteresis loops decreased with increasing strain rate. Apparently, the change from normal to inverse strain rate sensitivity takes place between 537°C (1000°F) and 648°C (1200°F). It is observed that as the temperature decreases from 982°C (1800°F) to 648°C (1200°F) the "yield stress" of the material increases, so that the hysteresis loops at 648°C (1200°F) show a greater stress amplitude, for a given strain amplitude, than the hysteresis loops at 760°C (1400°F), 871°C (1600°F) and 982°C (1800°F). However, the "yield stress" decreases when the temperature decreases from 537°C (1000°C) to 427°C (800°F), and the stress amplitude at 537°C (1000°F) is larger than the stress amplitude at 427°C (800°F) for the $\pm$ 1 percent strain amplitude hysteresis loops shown in Figs. 11 and 12.

In their present forms the constitutive theories under consideration cannot predict the inverse strain rate sensitivity observed in Hastelloy-X at 427°C (800°F) an 537°C (1000°F). However, since the strain rate sensitivity at these temperatures is relatively small, the material constants have been chosen to make the constitutive theories relatively rate insensitive at these temperatures.

Miller (Ref. 26) has included inverse rate sensitivity in a recent version of his theory by including another state variable to account for the effects of solute hardening. Effectively, this changes the drag stress of the material, so that at certain temperatures the drag stress decreases rapidly with increasing strain rates, and the material exhibits inverse rate sensitivity. In Section 3.1 a constitutive formulation was proposed in which the response to infinitely fast loading conditions is given by $\sigma = \Xi$, where Ξ is the instantaneous stress state variable whose growth law is prescribed. Inverse rate sensitivity may then be incorporated into the theory by assuming that the magnitude of Ξ is smaller than the magnitude of the equilibrium stress Ω under monotonic loading conditions at constant strain rate. Both Miller's method and the method here proposed require the abandonment of an infinitely fast elastic response in order to predict inverse rate sensitivity.

4.4 Creep and Relaxation Tests

Creep tests were performed at each temperature by starting at various points on a steady state hysteresis loop carried out under fully reversed strain controlled conditions at a strain rate of 3.66 x 10^{-4} sec^{-1} at $\pm$ 0.6 percent strain amplitude. At a given point on the hysteresis loop the load was held at a constant value and the resulting creep behavior was recorded on a strip chart. After each creep test the material was cycled at a strain rate of 3.66 x 10^{-4} sec^{-1} until the hysteresis loop stabilized before proceeding to the next creep test. Asymmetry in the creep response was noted at each temperature, with the material being stronger in compression than in tension, in conformity with the uniaxial hysteresis loop results. Figures 17 and 18 show the creep results at 871°C (1600°F) and 982°C (1800°F), in which the strain at the beginning of each creep test has been normalized to zero to facilitate comparison with the theoretical predictions.

In a steady state hysteresis loop executed at a constant strain rate, the equilibrium stress will saturate to a constant value at large strain amplitudes. This value can be determined from the preceding creep tests by locating the points on the unloading branches of the hysteresis loop at which the initial creep rate is zero. It should be emphasized that this point is difficult to define in an accurate manner due to the fact that the initial creep rate is small over a considerable portion of the unloading branches. A more accurate determination of this point can be made by observing the point at which the initial relaxation rate is zero. However, the function generator on the present experimental equipment would not allow a strain hold on the unloading portion of the hysteresis loop, so that the saturated equilibrium stress at a given strain rate and temperature was determined from the creep results. This saturated value of the equilibrium stress is used in the determination of the material constants.

Combustor liners are constructed from Hastelloy-X sheet material. In order to determine if the material constants developed from the Hastelloy-X bar specimens are appropriate for Hastelloy-X sheet material, creep tests were performed on Hastelloy-X sheet specimens at 871°C (1600°F) and 982°C (1800°F). The sheet specimen is shown in Fig. 19. It was initially intended to compare the monotonic uniaxial tensile response of bar and sheet specimens at these temperatures, but the small area of the sheet specimens precludes this comparison. During the initial heat-up of the sheet specimens from room temperature to 871°C (1600°F) and 982°C (1800°F), it was necessary to keep the sheet specimens under a small tensile load to make sure that buckling did not occur. At these elevated temperatures the sheet specimens creep under the small tensile load before the final temperature is attained. Hence, a comparison of the uniaxial tensile stress-strain response was abandoned. Instead, creep tests were repeated at 871°C (1600°F) and 982°C (1800°F) to test the variation of secondary creep rates from specimen to specimen.

The sheet specimens were loaded from zero to full load in three seconds under load control on a Data-Trak system and allowed to creep at constant load at 871°C (1600°F) and 982°C (1800°F). Creep tests on the Hastelloy-X bar specimens were initiated at constant load from various points on a steady state hysteresis loop. Since the initial conditions in the bar and sheet specimens are different it is not appropriate to compare the primary creep behavior. However, under conditions of steady state secondary creep the initial conditions are not of concern, and an examination of steady state secondary creep rates will provide a valid comparison between bar and sheet creep behavior at 871°C (1600°F) and 982°C (1800°F).

The test results are shown in Tables 3 and 4. In interpreting these results it should be kept in mind that due to the dependence of the creep rate on the 4th and 5th powers of the applied stress at 982°C (1800°F) and 871°C (1600°F), viz. $\dot{c} = A\sigma^n$ where n = 4 or 5, a small error in the stress (load) measurement can cause large errors in the creep rate. If the experiments were turned around and the saturated stress was measured due to a constant applied strain rate – in a monotonic tensile test for example – the agreement between theory and test would improve. Most of the secondary creep rates obtained with the sheet and bar specimens agree to within a factor of 1.5. Exceptions occur in the sheet specimen at σ = 74 MPa (10700 psi) at 982°C (1800°F) and at σ = 148 MPa (21500 psi) at 871°C (1600°F). The secondary creep rates in the sheet specimens were obtained from strip chart records. Variations in secondary creep rates by a factor of 1.5 can easily be obtained depending on which part of the chart the record is taken from. This figure provides an indication of the accuracy in reading from one record of one specimen.

From the creep tests at 871°C (1600°F) and 982°C (1800°F) one can say that the material constants determined from Hastelloy-X bar specimens are suitable for representing the constitutive behavior of Hastelloy-X sheet material. This is based on the experimental agreement in strain rates at a given stress level obtained in creep and hysteresis testing.

Relaxation behavior at 871°C (1600°F) and 982°C (1800°F) was determined by holding the strain at a zero value on the compressive portions of the steady state hysteresis loops carried out at 3.87×10^{-3}, 3.66×10^{-4}, and 3.70×10^{-5} sec^{-1} with a strain amplitude of $\pm$ 0.6 percent. Representative results obtained at 982°C (1800°F) are shown in Figs. 20 – 22.

4.5   Thermomechanical Test

Work performed under Contract NAS3-21836 with the NASA-Lewis Research Center on a simulated combustor liner rig has shown that after about one thousand (1000) operation cycles (Ref. 8) fatigue cracks initiate at the louver lip (point A in Fig. 1) and propagate axially towards the seam weld (point C in Fig. 1). In order

to predict the number of cycles to crack initiation the life prediction algorithms require a knowledge of the stress-strain hysteresis behavior at the fatigue critical location at point A. Since strain gages will not operate cyclically at 982°C (1800°F), the experimental stress-strain hysteresis behavior at point A cannot be measured. However, the stress field is one dimensional at point A, and consists of a uniaxial component in the circumferential, or hoop, direction. Moreover, because the combustor liner is a thermally driven structure, the total strain at the fatigue critical location is zero and the mechanical strain history at this point can be determined from the temperature history $\Theta(\xi)$ as $\varepsilon_M(t) = \int_0^t \alpha(\xi) [\partial\Theta(\xi)/\partial\xi] \, d\xi$. Thermocouples on the louver lip provide the experimental temperature history. Thus, both the mechanical strain history and the temperature history at the fatigue critical location, where the stress is uniaxial, are known. This temperature vs. mechanical strain history can then be applied cyclically to a uniaxial cylindrical tube specimen of Hastelloy-X to determine its stress vs. mechanical strain hysteresis behavior. Such a test is known as a "faithful cycle" test because it is meant to "faithfully" represent the "true" thermomechanical environment at a critical fatigue location in a combustor liner.

A thermomechanical test was performed on Hastelloy-X with a standard closed loop servohydraulic test machine using low frequency (10 kHz) induction heating and compressed air for temperature control on the specimen (Ref. 27). Specimen temperature measurement provided by a radiation pyrometer, in conjunction with independently computer controlled preprogrammed mechanical strain and temperature histories, allow virtually any complex cycle to be applied to the specimen. The system is capable of cycling at positive or negative mean strain, with either stress or strain control and hold times within each cycle. The tubular specimen used in the thermomechanical test is shown in Fig. 23. Axial strain is measured from the machined internal ridges utilizing a linear variable differential transformer and a quartz internal extensometer. Load and total strain for this system can be controlled to within 1 percent and temperature to within 2°C (4°F).

Figure 24 shows the experimental behavior of Hastelloy-X in a thermomechanical cycle. The temperature history consists of a sine wave with a forty one (41) second hold period at the maximum temperature of 975°C (1750°F) as shown in Fig. 25, the lowest temperature in the cycle being 504°C (940°F). The mechanical strain history is depicted in Fig. 26 and a corresponding cross-plot of the mechanical strain vs. temperature cycle is shown in Fig. 27. Axial mechanical strain in the specimen varied between -0.1 percent and -0.445 percent.

It should be noted that in the thermomechanical test the actual input temperature history consists of a sine wave with a hold period at the maximum temperature point of the cycle. In the actual liner rig experiment the temperature history, measured by thermocouples located at the fatigue critical location (see Fig. 68), is not a sine wave with a hold period. To account for this slight difference in temperature history the strain rate in the thermomechanical test is adjusted so that the cross-plot of mechanical strain vs. temperature is the same in the thermomechanical test and in the computations produced by a structural analysis of the combustor liner rig.

4.6 Combustor Liner Rig Test

A simulated combustor liner has been tested for fatigue life in a specially constructed experimental rig. This work was performed under Contract NAS3-21836 with the NASA-Lewis Research Center and is reported in Ref. 8. Cyclic engine level temperatures and thermal gradients are generated on simulated combustor liners by a 250 kW, 450 kHz induction heater used in conjunction with controlled cooling air temperature and flow rate. A schematic drawing of the rig depicting the principal components is shown in Fig. 28.

Cooling air is supplied to the lower plenum of the rig from a non-vitiated upstream air heater at temperatures up to 538°C (1000°F). The air in the lower plenum is then directed through flow straightener plates to the upper flow divider plate which permits ratioing of the shroud-side airflow to the hot-side airflow. Shroud-side air provides the total cooling air supplied to the specimen which is discharged to the hot-side flow annulus, and then, together with the metered hot-side flow, ejected to ambient temperature.

The specimen is inductively heated by power supplied from a 250 kW, 450 kHz induction heater. High frequency (450 kHz) was chosen to minimize depth of penetration of the induced current (heat) in the test specimen to best simulate the thermal surface loadings (radiative/conductive) experienced by combustor liners in engine operation.

The induction coil is supported on a framework of glass-bonded mica which is transparent to the induction field. A 48.3 cm (19 in.) diameter quartz cylinder (also transparent to the field) is positioned between the coil and the specimen to form the inner boundary of the hot-side flow annulus. The quartz cylinder is retained in position by a 45.4 kg (100 lb) quartz cover. A cylindrical test specimen of Hastelloy-X, which simulates a combustor outer liner and incorporates five (5) sheet metal louvers, was selected for fatigue testing (Ref. 8). Prior to testing, the cylindrical louvered test specimen, transition pieces and top shroud, are assembled as a unit. This provides a permanent instrumentation installation and facilitates frequent inspection during testing. The assembled louvered test specimen and cover are shown in Fig. 29a. Fine wire chrome-alumel thermocouples are used to determine temperature distributions during testing. Typical thermocouple locations are shown in Fig. 29b.

The test program consisted of a ninety (90) second thermal cycle in which the rig cooling air was maintained at a constant temperature and flow rate (of 504°C - 2.5 kg/sec (940°F - 5.5 lb/sec) while cycling power from the induction heater. A representative transient and steady state temperature distribution measured on the center (third) louver is shown in Fig. 26. The cycle consists of a twenty (20) second transient from an isothermal distribution of temperature at 504°C (940°F) to a maximum temperature distribution, a forty (40) second steady state portion, and a cool down back to the original isothermal condition.

During the testing, a maximum circumferential temperature difference of 44°C (80°F) was recorded at any time point in the cycle. For purposes of thermal and structural analyses, measurements were averaged to provide a circumferentially uniform temperature profile.

A comparison of a theoretical transient heat transfer analysis with the transient temperature distribution determined by the thermocouples may be found in Ref. 8. This thermal analysis was used to produce a thermal increment file for use in the structural analysis of the combustor liner rig specimen described in Section 6.7. Thermal histories measured by thermocouples on the specimen are shown in Fig. 30. Note that the thermal increment file used to "drive" the three dimensional combustor liner analysis corresponds to the actual temperature in the combustor liner rig and is not a sine wave approximation to the temperature history.

TABLE 3

Temperature 982°C (1800°F)

Stress (psi)	(MPa)	Secondary Creep Rate (sec^{-1}) for Sheet Material	Secondary Creep Rate (sec^{-1}) for Bar Material
28800	199	Spec #1 2.5×10^{-2}	–
14300	99	Spec #2 9.8×10^{-4}	9.0×10^{-4}
10700	74	Spec #3 3.9×10^{-4} Spec #4 1.1×10^{-4}	1.0×10^{-4}
7200	50	Spec #5 1.5×10^{-4} Spec #6 8.3×10^{-5}	9.0×10^{-5}

TABLE 4

Temperature 871°C (1600°F)

Stress (psi)	(MPa)	Secondary Creep Rate (sec^{-1}) for Sheet Material	Secondary Creep Rate (sec^{-1}) for Bar Material
21500	148	Spec #7 6.1×10^{-5} Spec #8 1.1×10^{-4}	1.3×10^{-4}
14200	98	Spec # 9 1.6×10^{-5} Spec #10 1.6×10^{-5}	1.4×10^{-5}
7150	49	Spec #11 2.2×10^{-6} Spec #12 2.4×10^{-6}	1.5×10^{-6}

5.0 TASK III – INCORPORATION OF CONSTITUTIVE THEORIES INTO NONLINEAR FINITE ELEMENT CODE

5.1 Description of The MARC Program

The viscoplastic theories of Walker, Miller and Krieg, Swearengen and Rohde have been incorporated into the MARC general purpose, nonlinear, finite element program (cf. Ref. 1). This program, in common with other general purpose finite element programs, has been developed expressly for nonlinear structural analysis. These programs involve sophisticated computational algorithms and advanced finite element formulations, yet rely on constitutive models whose applicability to the hot section component environment is questionable.

The constitutive theories commonly in use in such finite element programs artificially partition the total strain into rate-independent plastic and rate-dependent creep components. These computer programs are then used to approximate the time-dependent inelastic behavior of a structural component by alternately applying increments of creep and plasticity. This artificial partitioning of the total strain into components which are governed by separate constitutive relationships has no underlying physical basis and does not take account of the fact that creep and plasticity should interact within the constitutive equation.

A number of viscoplastic constitutive theories, in which creep and plasticity are united, have recently been proposed in the literature and were reviewed in Section 3.0. Scant experimental data exists to determine the material constants required by such theories. In addition, such theories comprise a system of "stiff" differential equations whose lack of stability has been a deterrent to their incorporation into large general purpose finite element programs.

In this contract the viscoplastic constitutive theories were incorporated into the MARC program by means of an initial stress technique. All of the material nonlinearity in the constitutive equations is incorporated into an initial load vector and treated as a pseudo body force in the finite element equilibrium equations. Because the viscoplastic constitutive theories form a "stiff" system of differential equations, it is necessary to form the incremental constitutive equation appropriate to the finite element load increment by means of a subincrement technique.

In the subincrement technique the finite element load increment is split into a number of equal subincrements and the viscoplastic constitutive theories are integrated over the small subincrements to form an accurate representation of the incremental constitutive equation over the finite element load increment. Integration over each subincrement was accomplished by means of an explicit Euler forward difference method. Provided the subincrements are sufficiently small (so that the stability level of the forward difference method is not exceeded), the technique has been found to work efficiently and accurately, even for large finite element load increments. However, the solution time required for a complete load increment

in a finite element program is linearly related to the number of subincrements used in formulating the initial load vector. There is, therefore, a considerable incentive to use as few subincrements as possible, consistent with the stability of the differential equations comprising the constitutive theory.

A method for reducing the number of subincrements has been developed for the functional theory. The constitutive relations for this theory are written in an integral form and recursion relations have been developed to integrate the equations over a subincrement in an efficient, accurate and stable manner. Recursion relations for the constitutive theory are implicit and a Newton-Raphson technique is required within each subincrement to accurately integrate the constitutive theory over the subincrement. The integral relations are sufficiently accurate and stable to permit the use of only one subincrement per finite element load increment. In this case the functional theory is integrated over an increment equal in size to the finite element load increment. Inaccuracies may arise from large finite element load increments due to the fact that the strain increment vector $\Delta\varepsilon_i$ and the temperature increment $\Delta\Theta$ are assumed to be constant over the finite element load increment. Hence the increments must be sufficiently small to enable the input history to be accurately modelled by piecewise constant values of $\Delta P_i/\Delta t$, $\Delta\varepsilon_i/\Delta t$ and $\Delta\Theta/\Delta t$, where ΔP_i is the applied incremental load vector. The fact that $\Delta\varepsilon_i/\Delta t$ is assumed to be constant over the increment implies that proportional loading occurs over the increment. Evidently the load increment must be small enough for this to be a valid approximation.

The principle of virtual work may be used to generate the MARC nonlinear equilibrium equations governing the incremental response of the structure to an increment of load. In evaluating the nonlinear structural response of a component, the program assumes that the load history is divided into a number of incrementally applied load steps. Each load step is sequentially analyzed as a linear matrix problem using an appropriate stiffness matrix and load vector. Although each load step uses linear matrix methods to solve the incremental equilibrium equations, the incremental equilibrium equations themselves are nonlinear since the load vector will depend on the displacement increment obtained in the solution of the incremental equilibrium equations.

The principle of virtual work may be written, for applied external point loads P_i, or displacements u_i, in the form

$$\Sigma \int_V \delta\epsilon_i^T \sigma_i \, dV = \delta u_i^T P_i \, , \tag{5.1}$$

where the integral extends over the volume, V, of each finite element and the summation sign extends to all the elements in the structure.

In Eq. (5.1) the virtual displacement vector δu_i is related to the virtual strain vector $\delta \epsilon_i$ through the relationship

$$\delta \epsilon_i = B_{ij} \delta u_j \text{ or } \delta \epsilon_i^T = \delta u_j^T B_{ij}^T, \tag{5.2}$$

where B_{ij} is the strain-displacement matrix and the superscript T denotes transposition. Since δu_i is an arbitrary virtual displacement vector, Eqs. (5.1) and (5.2) may be written in the form

$$\sum \int_V B_{ij}^T \sigma_j \, dV = P_i \cdot \tag{5.3}$$

This relation expresses the equilibrium of the structure when the applied load vector is P_i and the stress vector is σ_i. If an incremental load ΔP_i is applied to the structure and the stress vector changes to $\sigma_i + \Delta \sigma_i$, the relation expressing the equilibrium of the structure at the end of the incremental load application may be written as

$$\sum \int_V B_{ij}^T (\sigma_j + \Delta \sigma_j) \, dV = P_i + \Delta P_i \cdot \tag{5.4}$$

Hence, the relation expressing the equilibrium of the structure during the application of the incremental load vector ΔP_i is obtained from Eqs. (5.3) and (5.4) by subtraction in the form

$$\sum \int_V B_{ij}^T \Delta \sigma_j \, dV = \Delta P_i \cdot \tag{5.5}$$

The MARC code allows the user to implement very general constitutive relationships into the program by means of the user subroutine HYPELA. Within this subroutine the user must specify the values of the elasticity matrix D_{ij} and the inelastic stress increment vector $\Delta \zeta_i$ in the incremental vector constitutive relationship

$$\Delta \sigma_i = D_{ij} (\Delta \epsilon_j - \delta_j \alpha \Delta \Theta) - \Delta \zeta_i \cdot \tag{5.6}$$

The inelastic stress increment vector $\Delta \zeta_i$ is computed in HYPELA from the viscoplastic constitutive relationships summarized in the Appendices.

In Eq. (5.6) α denotes the coefficient of thermal expansion and δ_j is the vector Kronecker delta symbol,

$$\delta_j = \begin{cases} 1 & \text{if } 0 \leq j \leq 3 \\ 0 & \text{if } 3 < j \leq 6 \end{cases} \tag{5.7}$$

For the class of nonlinear visoplastic constitutive relationships under consideration in this contract, the incremental inelastic stress vector $\Delta\zeta_i$ depends in a highly nonlinear manner on the incremental strain vector $\Delta\varepsilon_i$. Since $\Delta\varepsilon_i = B_{ij}\Delta u_j$, the incremental inelastic stress vector $\Delta\zeta_i$ depends in a highly nonlinear manner on the nodal displacement vector increment Δu_j, so that $\Delta\zeta_i = \Delta\zeta_i(\Delta u_j)$.

Substitution of Eq. (5.6) into (5.5) produces the incremental equilibrium equations for MARC in the form,

$$\sum K_{ij}\,\Delta u_j = \Delta P_i + \Delta R_i + \sum \int_V B_{ij}^T\,\Delta\zeta_j\,dv + \sum \int_V B_{ij}^T\,\delta_j\,\alpha\,\Delta\Theta\,dv\;, \tag{5.8}$$

where K_{ij} is the elemental elastic stiffness matrix defined by the relation

$$K_{ij} = \int_V B_{ik}^T\,D_{k\ell}\,B_{\ell j}\,dv\;. \tag{5.9}$$

The vector ΔR_i is the residual load correction vector or out-of-equilibrium force vector from the preceding load increment,

$$\Delta R_i = P_i - \sum \int_V B_{ij}\,\sigma_j\,dv\;, \tag{5.10}$$

which is added to the current increment in order to restore the structure to equilibrium. The nonlinearity in the incremental equilibrium relationship, defined in Eq. (5.8), arises because the inelastic stress increment vector $\Delta\zeta_i$ depends nonlinearly on the displacement increment vector Δu_j. Values of D_{ij} and $\Delta\zeta_j$ appropriate to the current incremental load step are returned to the main program by subroutine HYPELA and the incremental equilibrium relations in Eq. (5.8) are solved by successive iterations.

The solution of the incremental equilibrium equations in (5.8) is accomplished within the MARC code by the following algorithm. At the start of the increment the user subroutine HYPELA is entered to determine the elasticity matrix D_{ij} and the incremental inelastic stress vector $\Delta\zeta_j$. On entry to the subroutine the input consists of the strain increment vector $\Delta\varepsilon_i$, the temperature increment $\Delta\Theta$, the time increment Δt over which the incremental external load vector ΔP_i is applied

to the structure, and the values of the stress, strain, temperature and viscoplastic state variables at the beginning of the increment. Since the incremental strain vector, $\Delta \varepsilon_i = B_{ij} \Delta u_j$, can only be accurately determined after the solution to the incremental equilibrium relationship in Eq. (5.8) has yielded the correct incremental solution vector Δu_j, the strain increment vector $\Delta \varepsilon_i$ initially used to generate the inelastic stress increment vector $\Delta \zeta_i$ must be estimated. The initial estimate for $\Delta \varepsilon_i$ is assumed to be the value obtained for $\Delta \varepsilon_i$ in the preceding increment. On exit from subroutine HYPELA the elasticity matrix D_{ij} and the estimated inelastic stress increment vector $\Delta \zeta_j$ are passed into the main program. After the values of D_{ij} and $\Delta \zeta_j$ are obtained for each integration point in the structure, the incremental equilibrium relationship in Eq. (5.8) is assembled and solved for the incremental node displacement vector Δu_j. The incremental strain vector, $\Delta \varepsilon_i = B_{ij} \Delta u_j$, is then computed and compared with the initial guess for $\Delta \varepsilon_i$ used to generate the inelastic incremental stress vector $\Delta \zeta_j$. If this incremental strain vector is equal, within a user specified tolerance, to the incremental strain vector used to compute $\Delta \zeta_j$ in the assembly phase, the solution is assumed to have converged. Otherwise the updated strain increment vector, obtained from the solution of the equilibrium relations in Eq. (5.8), is passed into subroutine HYPELA, a new vector, $\Delta \zeta_j$, is computed, and the equilibrium equations resolved to yield an improved value of Δu_i and $\Delta \varepsilon_i$. The process is repeated until the value of the vector $\Delta \varepsilon_i$ on the assembly phase is equal, within a user specified tolerance, to the value of the vector $\Delta \varepsilon_i$ on the solution phase. After convergence is achieved, the temperature, stress vector, strain vector and viscoplastic state variables are updated by adding the incremental values generated during the current increment to the values of these variables at the beginning of the increment. The program then passes on to the next load increment where the process is repeated. A flow chart of the iterative procedure required to implement the viscoplastic constitutive theories into the MARC program is shown in Fig. 31.

5.2 Implementation of Functional Theory in MARC

The recursive integration algorithm for the functional theory described in Appendices 14 and 15 has been introduced into the MARC code by means of the user subroutine HYPELA. This routine is called at each integration point in each element and supplies the elasticity matrix D_{ij} and the inelastic stress increment vector $\Delta \zeta_j$ to the main program.

The required header cards are:

```
SUBROUTINE HYPELA(D,G,E,DE,S,TEMP,DTEMP,NGENS,N,NN,KC,MAT,NDI,
1NSHEAR)
DIMENSION D(NGENS,NGENS),G(NGENS),E(NGENS),DE(NGENS),S(NGENS)
DIMENSION TEMP(1),DTEMP(1)


FORTRAN CODING IN APPENDIX 17


RETURN


END
```

where

D(NGENS,NGENS) is the elasticity matrix D_{ij} defined in this subroutine (output argument),

G(NGENS) is the inelastic stress increment vector $\Delta\zeta_j$ defined in this subroutine (output argument),

E(NGENS) is the mechanical strain $\varepsilon_i - \delta_i \int_0^t \alpha(\xi)[\partial\Theta(\xi)/\partial\xi]\,d\xi$ at the beginning of the increment (input argument),

DE(NGENS) is the increment of mechanical strain $\Delta\varepsilon_i - \delta_i\alpha\Delta\Theta$ (input argument),

S(NGENS) is the stress σ_i at the beginning of the increment (input argument),

TEMP(1) is the temperature Θ at the beginning of the increment (input argument),

TEMP(2) is the time t at the beginning of the increment (input argument),

TEMP(3) is the cumulative inelastic strain R at the beginning of the increment (input argument),

TEMP(4) through TEMP(9) are the values of the inelastic strains, c_1 through c_6, at the beginning of the increment (input argument),

TEMP(10) through TEMP(15) are the values of the equilibrium stresses Ω_1 through Ω_6 at the beginning of the increment (input argument),

TEMP(16) is the drag stress K at the beginning of the increment (input argument). On exit from the subroutine TEMP(16) contains the drag stress K at the end of the increment (output argument),

DTEMP(1) is the temperature increment $\Delta\Theta$ (input argument),

DTEMP(2) is the time increment Δt (input argument),

DTEMP(3) is the increment of cumulative inelastic strain ΔR (output argument),

38

DTEMP(4) through DTEMP(9)	are the incremental values of the inelastic strain Δc_1 through Δc_6 (output argument),
DTEMP(10) through DTEMP(15)	are the incremental values of the equilibrium stress $\Delta\Omega_1$ through $\Delta\Omega_6$ (output argument),
DTEMP(16)	is output as zero, since the drag stress K is updated in TEMP(16),
NGENS	is the size of the D_{ij} matrix (NGENS = 3 for plane stress problems, NGENS = 4 for plane strain and axisymmetric problems, NGENS = 6 for three dimensional problems) (input argument),
N	is the finite element number (input argument),
NN	is the integration point number (input argument),
KC	is the layer number in shell or beam problems (input argument),
MAT	is the material identifier (input argument),
NDI	is the number of direct stress components (NDI = 2 for plane stress problems, NDI = 3 for plane strain, axisymmetric and three dimensional problems) (input argument),
NSHEAR	is the number of shear components (NSHEAR = 1 for plane stress, plane strain and axisymmetric problems, NSHEAR = 3 for three dimensional problems) (input argument).

5.3 Notes on Subroutine HYPELA

The values of D_{ij} and $\Delta\zeta_i$ in the incremental constitutive relation,

$$\Delta\sigma_i = D_{ij}(\Delta\epsilon_j - \delta_j\,\alpha\,\Delta\Theta) - \Delta\zeta_i . \qquad (5.11)$$

are obtained by a subincrement method. Incremental values of the variables $\Delta\Theta$, Δt and $(\Delta\epsilon_i - \delta_i\alpha\Delta\Theta)$ for the current finite element load increment are split into N equal values, and the constitutive equations are integrated over the N subincrements to provide accurate values of D_{ij} and $\Delta\zeta_i$. Because the recursive scheme

is accurate and stable, even for large load increments, it is possible to use only one subincrement per MARC increment. Figure 32 shows the MARC finite element predictions for an axisymmetric problem is which a bar of Hastelloy-X material is strained at a uniform strain rate in tension. The rounded curve was obtained by loading to 0.64 percent strain in 64 load increments with one subincrement per MARC load increment. This corresponds to integrating the recursive algorithm directly over the same step size as the finite element step size. Each of the curves marked 8, 4, 2 and 1, respectively, was obtained by using only one subincrement per MARC load increment and loading to 0.64 percent strain in 8, 4, 2 and 1 finite element load increments, respectively. It is evident that the recursive scheme is stable and accurate even when loading to 0.64 percent strain directly in only one MARC increment.

The accuracy and stability of the integration algorithm will enable large increments to be used in a nonlinear finite element analysis with a concomitant reduction in computer run time. Although the recursive integration algorithm is implicit, requiring Newton-Raphson iterations within each subincrement, the number of iterations required is not large. In the numerical algorithm the initial guess for the inelastic strain increment in the first subincrement is taken as the deviatoric mechanical strain increment. If the material is in the elastic region this is not a good initial guess. However, if the response is elastic, then after two iterations it is found that the magnitude of the inelastic strain increment will generally be less than one percent of the mechanical strain increment and the iterations are stopped. If the material is in the inelastic region the initial guess for the inelastic strain increment is very well approximated by the deviatoric mechanical strain increment and one iteration is sufficient to produce an accurate result. In successive subincrements the initial guess for the inelastic strain increment is taken from the preceding subincrement. Although the computer time required to integrate the constitutive relations over one subincrement is longer than the time required to integrate the same equations by means of an Euler forward difference method (by about a factor of three or four in general), the recursive method is stable and accurate even when the constitutive equations are integrated over a large finite element increment with only one subincrement. Moreover, the forward difference method has a stability limit, which precludes the use of large subincrements. Backward difference and implicit integration methods could also be used to integrate the constitutive equations over a subincrement. Although these methods are stable they are not as accurate as the recursive integration algorithm.

MARC solves the incremental equilibrium Eq. (5.8) by successive iteration. To see how the equilibrium equation iterations are converging one can pick the integration point, NPRIN, in element number, NELPR, at which the maximum amount of nonlinearity is expected. As subroutine HYPELA is entered on the assembly phase the routine prints out the strain increment vector $\Delta\varepsilon_i$ and the stress increment vector $\Delta\sigma_i$ at integration point NPRIN in element number NELPR. After the equilibrium equations have been solved for the incremental displacement vector Δu_i, subroutine HYPELA is again entered with $\Delta\varepsilon_i = B_{ij}\Delta u_j$ and the incremental vectors are printed out on the assembly and solution phase of every successive iteration of

40

the equilibrium equations. In this way the convergence of the solution to the incremental equilibrium equations can be followed. If no printout of the incremental vectors is required, the variable IPR is set equal to zero in subroutine HYPELA.

For each subincrement the integral recursive algorithm requires Newton-Raphson iterations. A test is made within the subroutine to determine if the solution is in the elastic region. If it is in the elastic region and two Newton-Raphson iterations have been performed, the iterations are stopped and the subroutine goes on to the next subincrement. Another test is also made to see if the minimum number of iterations is met, or until the tolerance on the magnitude of the inelastic strain increment vector,

viz. $\left\{ |\Delta R_n - \Delta R_{n-1}| / \Delta R_{n-1} \right\} \leq 0.01$ where n is the iteration number,

is met. If the foregoing tolerance on the inelastic strain increment vector is not met but the maximum number of Newton-Raphson iterations, MAXIT, is exceeded, the subroutine exits from the iteration loop and proceeds to the next subincrement.

In order to use subroutine HYPELA, nine (9) constants must be defined in the subroutine, starting at card number forty-four (44). These constants are:

NTP = number of tabulated temperature points in the DATA statements,

MAXIT = maximum number of Newton-Raphson iterations allowed,

MINIT = minimum number of Newton-Raphson iterations allowed,

NELPR = element number for printout of incremental stress and strain vectors,

IPR = 1 if stress-strain increment output is required, 0 if stress-strain increment output is not required,

NPRIN = integration point number for printout of incremental stress and strain vectors,

NSPLIT = number of subincrements per MARC increment,

SFTEMP = stress free temperature; for isothermal calculations this is the isothermal temperature,

TDIF = temperature difference in the DATA statement in which the material constants are tabulated.

41

The material constants for the functional theory, viz.

λ, μ, $\overset{o}{\Omega}$, n, m, n_1, n_2, n_3, n_4, n_5, n_6, n_7, K_1, K_2 in Appendix 1,

depend on temperature. For Hastelloy-X these constants have been determined at six temperatures ranging from 427°C (800°F) to 982°C (1800°F) in 111°C (200°F) intervals. These material constants are entered into the MARC subroutine HYPELA in DATA statements. At a specified temperature, the material constants are found by a linear interpolation of the constants in the DATA statements. If the temperature lies outside of the tabulated values, a linear extrapolation, based on the last two entries in the DATA statement table, is performed. The material constant n is not entered directly into the DATA statements. Instead, values of its reciprocal, n^{-1}, are tabulated. At a given temperature n^{-1} is then found by linear interpolation in the table and n is determined as its reciprocal.

If the material constant n is determined by linear interpolation of its tabulated values, unreasonable results are obtained for the material response. Figure 33 shows the steady state hysteresis loops for Hastelloy-X at 704°C (1300°F) based on a linear interpolation of the tabulated material constant n at 648°C (1200°F) and 760°C (1400°F). This figure shows that the prediction of the 704°C (1300°F) response, based on the linear interpolation of n, lies outside of the range of the 640°C (1200°F) and 760°C (1400°F) responses. The constants at 648°C (1200°F) and 760°C (1400°F) were obtained from the experimental data and the theoretical predictions at these temperatures in Fig. 33 provide a reasonable correlation with the experimental data.

The tabulated material constants are obtained from the asymptotic response of the material at strain values large enough for the stress to obtain a saturated limit. In order to obtain a realistic response at a given temperature, the material constants should be obtained by a linear interpolation of the asymptotic response of the material. If σ_1 and σ_2 denote the theoretical asymptotic stress values corresponding to a strain rate $\dot{\varepsilon}$ at temperatures Θ_1 and Θ_2, where the strain value ε is large enough for the equilibrium stress to reach its maximum rate-independent value, Ω_{max}, then

$$\sigma_1 = \Omega_{max}(\Theta_1) + K(\Theta_1)\dot{\varepsilon}^{1/n(\Theta_1)} \tag{5.12}$$

and

$$\sigma_2 = \Omega_{max}(\Theta_2) + K(\Theta_2)\dot{\varepsilon}^{1/n(\Theta_2)}.$$

From these equations it is clear that in order to obtain a realistic asymptotic response for σ at a temperature Θ between Θ_1 and Θ_2, a linear interpolation of Ω_{max}, K and n^{-1} is appropriate. Numerical calculations show that a linear interpolation of n is inappropriate, and linear interpolation of n^{-1} is therefore performed in the HYPELA subroutine.

42

5.4 Input Data Required by MARC

A listing of the data cards required for the thermomechanical loading history described in Section 4.3 is given in Appendix 16. This problem consists of the thermomechanical loading of a bar of Hastelloy-X material in which the bar is subjected to the mechanical strain and temperature histories depicted in Figs. 25 - 27. Since only mechanical strain is being imposed on the bar, this condition can be simulated by setting the coefficient of thermal expansion α equal to zero and imposing a given total strain history at the ends of the bar. A four element axisymmetric problem is depicted in Fig. 34. Nodes one, two and three are given incremental displacements which follow the total strain history of Fig. 26, whilst each integration point of each element is given incremental temperature variations which follow the temperature history of Figure 25.

Two cards are required before the END card (Card 10 of Appendix 16). These are:

    HYPOELAS
    STATE VARS   16

A uniform temperature increment over the structure, together with an appropriate time increment, can be specified with the following cards;

    THERMAL LOADS
    1,
    5.0, 2.0
    BLANK CARD

In the above sequence of cards, the first state variable increment of 5.0 refers to the uniform temperature increment $\Delta\Theta = 5°F$ over the structure. The second state variable increment of 2.0 refers to a time increment of $\Delta t = 2$ seconds. The remainder of the card and the following BLANK card set the remaining fourteen (14) state variable increments to zero. Since the STATE VARS card (Card number 7 of Appendix 16) defines sixteen (16) state variables, MARC expects this number as input. However, only the first two state variables, $\Delta\Theta$ and Δt, are required as input by HYPELA, so that the remaining (14) state variable increments are set to zero. The remaining (14) state variable increments are defined within subroutine HYPELA.

If a nonuniform temperature over the structure is required (the usual case), the temperature increments and time increment must be set in user subroutine CREDE. This can be accomplished with the following header cards:

    SUBROUTINE CREDE(DTDL,M,NSTRES,NEQST,NSTATS)
    DIMENSION DTDL(NSTATS,NEQST,NSTRES)
    COMMON/FAR/DUM,L

    N = (where N = number of integration points in element number M)

```
      DO 2 II = 1, N

      DTDL(1,1,II)      =     temperature increment at integration point II

      DTDL(2,1,II)      =     time increment (can be made a function of load
                              increment number L)

   2  CONTINUE
      RETURN
      END
```

6.0 TASK IV – COMPARISON AND EVALUATION OF CONSTITUTIVE THEORIES

6.1 Determination of Material Constants

Material constants for each of the three candidate theories were determined from the experimental hysteresis data presented in Figs. 11-16 and from the saturated value of the equilibrium stress at a constant strain rate magnitude of 3.66×10^{-4} sec^{-1} at a temperature of 982°C (1800°F). Values of the constants for the functional theory, Miller's theory, and Krieg, Swearengen and Rohde's theory are presented in Tables 5 - 7.

The constant A_3 in Krieg, Swearengen and Rohde's theory has been assumed to have the value $A_3 = 10^{-12}$ for all temperatures. The thermal recovery term may then be approximated in the form

$$\text{recovery} = A_2 A_3 A^{\frac{2}{3}} \Omega_{ij} \Omega_{pq} \Omega_{pq} \sqrt{\frac{2}{3} \Omega_{rs} \Omega_{rs}} \, , \qquad (6.1)$$

so that in uniaxial loading the recovery term is proportional to the fourth power of the equilibrium stress. If A_3 were larger in value, the exponential term would grow very rapidly once the equilibrium stress reached a certain value, as shown in Fig. 9, and the resulting stress-strain curves would exhibit a tri-linear behavior. The small value of A_3 and the resulting dependence of the static thermal recovery term on Ω^4 mitigates the severity of this tri-linear behavior.

The constants $(n_1 + n_2)$ in the functional theory, H_1 in Miller's theory and A_1 in Krieg, Swearengen and Rohde's theory determine the rapidity of the approach of the equilibrium stress to its saturated value. For large values of these constants the equilibrium stress grows so rapidly that it virtually saturates in the "elastic" region and the stress-strain curve exhibits the "square" behavior depicted in Fig. 35. For intermediate values the equilibrium stress approaches its saturated value less rapidly and the stress-strain curve exhibits a rounded appearance. For very small values of these constants, the equilibrium stress grows very slowly. The asymptotic stress value, when $\Omega \approx 0$, is given by the functional theory and by Krieg, Swearengen and Rohde's theory as

$$\sigma \approx K \dot{\epsilon}^{1/n}, \qquad (6.2)$$

and by Miller's theory as

$$\sigma \approx K \left\{ \sinh^{-1} \left(\frac{\dot{\epsilon}}{B\theta'} \right)^{1/n} \right\}^{2/3} \qquad (6.3)$$

TABLE 5

Material Constants for Functional Theory

Material Constant	982°C 1800°F	871°C 1600°F	760°C 1400°F	648°C 1200°F	537°C 1000°F	427°C 800°F
λ	11.5E6	15.4E6	17.8E6	18.1E6	17.2E6	17.8E6
μ	4.9E6	6.9E6	8.4E6	9.0E6	9.0E6	9.8E6
K_1	59292	91505	251886	95631	75631	50931
K_2	0	0	0	0	0	0
n^{-1}	.233	.195	.244	.079	.059	.059
m	1.16	1.16	1.16	1.16	1.16	1.16
n_1	0	0	0	0	0	0
n_2	1.0E6	5.0E6	2.0E7	1.5E7	6.0E7	30.0E7
n_3	312	673	1179	781	1000	8000
n_4	0	0	0	0	0	0
n_5	0	0	0	0	0	0
n_6	2.73E-3	8.98E-4	0	0	0	0
n_7	0	0	0	0	0	0
$\overset{o}{\Omega}$	-1200	-1434	-2000	-2000	0	0

TABLE 6

Material Constants for Miller's Theory

K_o = 8000

n = 1.598

B = 1.0293E14

H_1 = 1.0E7

A_1 = 9.305E-4

H_2 = 100

C_2 = 50000

A_2 = 5.9425E-12

Q* = 104600

T_m = 1588°K

k = 1.9859

$\theta' = \exp\left\{-Q^*/kT\right\}$ for $T \geq .6T_m$

$\theta' = \exp\left\{\dfrac{-Q^*}{.6kT_m} \ln\left(1 + \dfrac{.6T_m}{T}\right)\right\}$ for $T < .6T_m$

where T is the temperature in degrees Kelvin. The Lame constants λ and μ are as given in Table 5.

TABLE 7

Material Constants for Krieg, Swearengen and Rohde's Theory

Material Constant	982°C 1800°F	871°C 1600°F	760°C 1400°F	648°C 1200°F	537°C 1000°F	427°C 800°F
λ	11.5E6	15.4E6	17.8E6	18.1E6	17.2E6	17.8E6
μ	4.9E6	6.9E6	8.4E6	9.0E6	9.0E6	9.8E6
K_o	59292	91505	251886	95631	75631	50931
n^{-1}	.223	.195	.244	.079	.059	.059
A_1	1.0E6	5.0E6	2.0E7	1.5E7	6.0E7	30.0E7
A_2	243	14.96	1.54	.66	1.79E-3	.59
A_3	1.0E-12	1.0E-12	1.0E-12	1.0E-12	1.0E-12	1.0E-12
A_4	0	0	0	0	0	0
A_5	0	0	0	0	0	0

Thus, for very small values of n_2 the theories predict a viscoelastic material behavior and the stress-strain curve again exhibits a relatively "square" behavior. Numerical results for the functional theory are exhibited in Figs. 36 and 37 when $n_1 = 0$ and $n_2 = 0.8E7$ and $n_2 = 5.0E7$, respectively. The "square" behavior for large values on n_2 is apparent in Fig. 37. In changing the value of n_2 from $0.8E7$ to $5.0E7$, it is necessary to adjust the material constant n_3 in the dynamic recovery term in order to obtain the same saturated value of the equilibrium stress.

6.2 Strain Rate Behavior

Figures 38 - 58 depict the steady state hysteresis loops obtained with the functional theory, Miller's theory, and Krieg, Swearengen and Rohde's theory at temperatures ranging from 648°C (1200°F) to 982°C (1800°F) in 38°C (100°F) intervals. These loops represent the predicted behavior of the material for triangular strain histories in which the magnitudes of the strain rates are 3.9×10^{-3} sec^{-1}, 3.7×10^{-4} sec^{-1}, 3.7×10^{-5} sec^{-1}, 1.1×10^{-5} sec^{-1} and 1.2×10^{-6} sec^{-1} and in which the strain amplitude is ± 0.6 percent. Tri-linear material behavior is observed in Miller's theory in the temperature range extending from 648°C (1200°F) to 816°C (1500°F), whilst the functional theory and Krieg, Swearengen and Rohde's theory produce rounder stress-strain hysteresis loops.

Figures 59 and 60 facilitate a comparison between the functional theory and the experimental hysteresis loops at 871°C (1600°F) and 982°C (1800°F). The peak stresses in the loops are well predicted, but at the lower strain rates the theoretical predictions of the stress-strain behavior are too "square". This "squareness" at the lower strain rates is common to each of the theories and arises from the fact that the equilibrium stress saturates to a smaller value at low strain rates due to static thermal recovery. For a given hardening rate of the equilibrium stress, the saturated value is achieved more rapidly at low strain rates, and this produces the "square" stress-strain loops. The theoretical loops at low strain rates could be made rounder by assuming that the constants which govern the hardening of the equilibrium stress, viz. $(n_1 + n_2)$, H_1 and A_1, decrease in magnitude in proportion to the decrease in the saturated value of the equilibrium stress. This is equivalent to the assumption that these hardening constants depend on the magnitude of the inelastic strain rate, $\dot{c}_{ij}$.

Figures 61 and 62 show the results of a MARC axisymmetric finite element analysis of a cylindrical specimen of Hastelloy-X using the functional theory. This specimen was cycled under fully reversed strain controlled conditions with a strain amplitude of ± 0.6 percent at 982°C (1800°F) at a constant strain rate magnitude of 1.1×10^{-5} sec^{-1}. The MARC plots represent loading the specimen to $+0.6$ percent strain, unloading and compressing the specimen to -0.6 percent strain, and finally reloading the specimen to $+0.6$ percent strain. In Fig. 61 sixty (60) MARC increments were used to load from 0 to $+0.6$ percent strain, one hundred and twenty (120) MARC increments to load from $+0.6$ to -0.6 percent strain, and one hundred and twenty (120) MARC increments to reload from -0.6 percent to $+0.6$ percent strain,

with one subincrement per MARC increment in subroutine HYPELA. The reason for using a large number of increments to traverse the hysteresis cycle was simply to obtain good definition of the stress-strain hysteresis loops in the plotted output from MARC. Figure 62 shows the same hysteresis loop in which three (3) MARC increments were used to load the specimen from 0 to +0.6 percent strain, six (6) MARC increments to unload from +0.6 percent to -0.6 percent strain, and six (6) MARC increments to reload from -0.6 percent to +0.6 percent strain. Thirty (30) subincrements were used per MARC increment in subroutine HYPELA. A comparison of Figs. 61 and 62 shows that even with the large MARC increments used in Fig. 62 the stress at the end of the MARC increment lies on the stress-strain hysteresis loop. Experience with the algorithm shows that even if only one sub-increment per MARC increment is used, the stress at the end of the MARC increment lies on the stress-strain hysteresis loop.

6.3 Creep and Relaxation Behavior

A comparison of experimental and theoretical creep predictions using the functional theory is shown in Figs. 17 and 18. The experimental results were generated by traversing a steady state hysteresis loop carried out under fully reversed strain controlled conditions at a strain amplitude of +0.6 percent at a constant strain rate magnitude of 3.7×10^{-4} sec^{-1} at temperatures of 871°C (1600°F) and 982°C (1800°F). At various points on both the tension going and compression going loading branches of the hysteresis loops, the stress was held at a constant value and the creep results were recorded on a strip chart. After each creep test was completed the material was cycled again at +0.6 percent strain amplitude at a strain rate magnitude of 3.7×10^{-4} sec^{-1}. After a few cycles the material will cycle around the original steady state hysteresis loop and the effects of the previous creep tests are wiped from the materials memory.

The functional theory was integrated around the hysteresis loops at 871°C (1600°F) and 982°C (1800°F). At various points on the hysteresis loops the stress was held at a constant value and the resulting creep strain produced by the viscoplastic theory was computed. The dots in Figs. 17 and 18 represent the predictions of the functional theory. Since the theoretical hysteresis loops are too "square" in comparison with the experimental curves, the initial strain at which creep commences differs in the experimental and theoretical creep curves. To avoid this discrepancy the theoretical and experimental creep curves in Figs. 17 and 18 have been normalized to a zero initial strain.

According to the theoretical formulation, steady state creep is indistinguishable from the stress-strain behavior at large strain values on a hysteresis loop executed at a constant strain rate, since at large strain values the stress saturates to a constant value. This conclusion is supported by the close agreement between the theoretical and experimental creep behavior, since the material constants were determined from the hysteresis loops and not from the creep curves. A difference in the compressive and tensile hysteresis behavior found in the stress-strain loops is also evident in the creep behavior, the material being stronger in

compression than in tension. The introduction of the constant, $\overset{o}{\Omega}$, into the functional theory to account for the different tensile and compressive hysteresis behavior also accounts for the difference between the tensile and compressive creep behavior shown in Fig. 18.

Figure 63 depicts the creep response obtained with Miller's theory at 1600°F. Since Miller's theory predicts equal response in tension and compression, only the results for the compressive calculations are given. At low stress levels the predictions are not as good as the functional theory predictions. However, a reasonable creep prediction is obtained at the highest compressive stress level of -197 MPa (-28,600 psi). These creep predictions have been made at a temperature where Miller's theory should be at its most accurate. The accuracy obtained at other temperatures will decrease because the material constants provide a best fit at 1600°F and give considerable scatter in attempting to correlate the behavior at other temperatures.

The creep behavior obtained with Krieg, Swearengen and Rohde's theory at 871°C (1600°F) and 982°C (1800°F) is very similar to the creep behavior of the functional theory in the case of tensile creep. It predicts equal tensile and compressive creep behavior.

Stress relaxation data was obtained at temperatures varying from 648°C (1200°F) to 982°C (1800°F). In the tests stress relaxation was initiated at a zero strain value on the compressive loading branches of three steady state hysteresis loops carried out at constant strain rate magnitudes of 3.9×10^{-3} sec^{-1}, 3.7×10^{-4} sec^{-1} and 3.7×10^{-5} sec^{-1} with strain amplitudes of ± 0.6 percent. After each stress relaxation test the material was cycled several times around the steady state hysteresis loops to erase the preceding hysteresis and relaxation tests from the memory of the material.

Since the relaxation data was not used in the determination of the material constants, very little of the experimental relaxation data has been compared with the theoretical predictions to date.

In Figs. 20 - 22 the dots represent calculations of the stress relaxation obtained by integrating the functional theory around steady state hysteresis loops executed at strain rates of 3.9×10^{-3} sec^{-1}, 3.7×10^{-4} sec^{-1} and 3.7×10^{-5} sec^{-1} under strain controlled conditions with strain amplitudes of ± 0.6 percent at 982°C (1800°F). At zero strain values on the compressive portions of these loops the strain was held at zero and the resulting stress relaxation produced by the theory was computed. The agreement between the theoretical predictions and the experimental relaxation tests show satisfactory agreement.

6.4   Thermomechanical Behavior

The thermomechanical loops predicted by the functional theory, Miller's theory and Krieg, Swearengen and Rohde's theory are displayed in Figs. 64 - 66. These hysteresis loops are produced by integrating the theories over the temperature and mechanical strain histories depicted in Figs. 25 - 27.

From Fig. 64 it is evident that the functional theory prediction exhibits a relatively small amount of stress relaxation at the maximum temperature of 954°C (1750°F) in Fig. 25. Note from Fig. 26 that the maximum temperature hold period does not correspond to the maximum compressive mechanical strain. In fact the strain is held constant on the unloading branch of the thermomechanical hysteresis loop. The hysteresis loops show a progressive overall stress relaxation in the positive stress direction and the loops stabilize after about three cycles in conformity with experimental observations.

Figure 65 shows the thermomechanical loop predicted by Miller's theory. The theory predicts a large amount of stress relaxation at the maximum temperature hold period and the loop stabilizes in one cycle. In the tensile portion of the thermomechanical loop the theory exhibits an elastic behavior and does not predict the tensile yield which is observed experimentally in Fig. 24.

Figure 66 shows the thermomechanical loop predicted by Krieg, Swearengen and Rohde's theory. The theory predicts a relatively small amount of stress relaxation at the maximum temperature hold period and the loop stabilizes in one cycle. In the tensile portion of the thermomechanical loop the theory exhibits tensile yielding with a slight stress dip at the top of the tensile portion of the loop.

By changing the material constants by a small amount in the functional theory and in Krieg, Swearengen and Rohde's theory, it is possible to produce pronounced stress dips at the top of the tensile portion of the thermomechanical loop similar to that predicted in Fig. 69. This predicted dip in the stress response at the maximum tensile position in the thermomechanical hysteresis loop may be due to two factors. First, the strain rate at the maximum tensile stress is very small and the material may be relaxing. Experimentally the material exhibits a relatively rate-insensitive response at the temperature corresponding to the maximum tensile stress, so that experimental relaxation should not be, and is not, observed. However, the theoretical models cannot reproduce a rate-insensitive response, so that the theoretical models respond to a small strain rate by producing a stress relaxation. The amount and rate of relaxation depend on how far the stress at the maximum tensile position exceeds the equilibrium stress. Secondly, the theoretical models predict that during elastic deformation the equilibrium stress remains constant. During the initial compression phase of the cycle, the equilibrium stress is negative. At the maximum temperature of 954°C (1750°F) the hysteresis response starts to elastically unload. As the stress increases elastically into the tensile region of the hysteresis loop, the equilibrium stress remains constant at its maximum negative value, since the equilibrium stress state variable changes only with inelastic deformation. However, if the equilibrium stress increased due to changes in temperature as the stress increases elastically, the difference between the actual stress σ_{ij} and the equilibrium stress Ω_{ij} would remain relatively small and the inelastic strain rate expression $\dot{\epsilon}_{ij}$, which depends on the difference between σ_{ij} and Ω_{ij}, would provide a gradual growth in the inelastic strain, similar to that observed in an isothermal hysteresis loop. But if Ω_{ij} "sticks" at its maximum negative value during an elastic excursion in which the stress σ_{ij} is increasing, the inelastic strain will grow very rapidly. This rapid growth in inelastic strain will also produce a stress dip in the hysteresis loop.

The equation governing the growth of the equilibrium stress Ω_{ij} in the functional theory may be written in the form

$$\Omega_{ij}(t) = \overset{\scriptscriptstyle 0}{\Omega}_{ij}(t) + n_1(\Theta(t)) c_{ij}(t) + n_2(\Theta(t)) \int_0^t e^{-\{G(t)-G(\xi)\}} \frac{\partial c_{ij}}{\partial \xi} d\xi \ . \tag{6.4}$$

On differentiation with respect to time, t, the following relation is obtained:

$$\dot{\Omega}_{ij} = (n_1 + n_2)\dot{c}_{ij} + \frac{\partial n_1}{\partial \Theta} \dot{\Theta} c_{ij} - \left(\dot{G} - \frac{1}{n_2} \frac{\partial n_2}{\partial \Theta} \dot{\Theta} \right) \left(\Omega_{ij} - \overset{\scriptscriptstyle 0}{\Omega}_{ij} - n_1 c_{ij} \right). \tag{6.5}$$

If the material constant n_2 $(\Theta(t))$ appears inside the integral in the form n_2 $(\Theta(\xi))$ the terms involving $\dot{\Theta}$ in the preceding expression do not appear. However, with the $\dot{\Theta}$ terms, the equilibrium stress can grow with temperature during an elastic excursion (in which $\dot{c}_{ij} = 0$ and $\dot{G} = 0$) according to the relationship

$$\dot{\Omega}_{ij} = \frac{\partial n_1}{\partial \Theta} \dot{\Theta} c_{ij} + \frac{1}{n_2} \frac{\partial n_2}{\partial \Theta} \dot{\Theta} (\Omega_{ij} - \overset{\scriptscriptstyle 0}{\Omega}_{ij} - n_1 c_{ij}). \tag{6.6}$$

In the FORTRAN subroutine HYPELA the functional theory has been implemented with the equilibrium stress having the form

$$\Omega_{ij}(t) = \overset{\scriptscriptstyle 0}{\Omega}_{ij}(t) + \int_0^t n_1(\Theta(\xi)) \frac{\partial c_{ij}}{\partial \xi} d\xi + \int_0^t n_2(\Theta(\xi)) e^{-\{G(t)-G(\xi)\}} \frac{\partial c_{ij}}{\partial \xi} d\xi, \tag{6.7}$$

so that the $\dot{\Theta}$ terms will not be present in the corresponding differential equation. This form of the equilibrium stress equation prohibits the equilibrium stress from changing during elastic excursions and was used in the computation of the thermo-mechanical loop in Fig. 64. It is thought that the expression in (6.4), which has been written as part of the functional theory in Appendix 1, will give a better representation of the thermomechanical hysteresis response. Future investigations will implement Eq. (6.4).

Stress dip anomalies due to relaxation at the maximum tensile position in the thermomechanical hysteresis loop can also be avoided if the instantaneous response of the material is assumed to be inelastic. At present the instantaneous response is elastic. If the instantaneous response is given by $\sigma_{ij} = \Xi_{ij}$ and the equilibrium response by $\sigma_{ij} = \Omega_{ij}$, then by adjusting the growth laws for Ξ_{ij} and Ω_{ij} so that at any time their magnitudes in the inelastic region are close to one another ($\Xi_{ij} \approx \Omega_{ij}$), the response can be made rate-insensitive at lower temperatures and the relaxation in the tensile poriton of the thermomechanical hysteresis loop can be avoided.

53

Based on the favorable comparison of the experimental and theoretical hysteresis loops, together with good short time creep predictions, at temperatures ranging from 800°F (427°C) to 1800°F (982°C), the functional theory was chosen to perform the cumbustor liner rig analysis.

6.5 Combustor Liner Rig Analysis

A three dimensional inelastic finite element analysis of the induction rig specimen described in Section 4.4 was undertaken in Ref. [8] under contract NAS3-21836 with the NASA-Lewis Research Center. This analysis was conducted with constitutive models currently available in the MARC program. The analysis has been repeated in the present contract with the functional viscoplastic theory.

A three dimensional finite element model of the cylindrical louvered induction rig specimen is shown in Fig. 67. The model contains an included angle of 0.577° which represents the angular distance between the radial symmetry planes of two adjacent cooling holes. This small model size was selected because of the circumferentially uniform temperatures in the louver lip region and to minimize computer run time.

As shown, the model consists of thirty (30) finite elements. Twenty-one (21) of the elements are the twenty (20) node isoparametric element with reduced integration using eight (8) Gauss integration points (MARC element #57). Since it is known that some reduced integration point elements are unreliable if distorted shapes are used, the full twenty seven (27) integration point element (MARC element #21) was used around the cooling holes. Selection of the reduced integration point elements was based on initial estimates of the savings in computer run time over the full integration point element, and to minimize the required spatial temperature interpolation between the heat transfer and structural analysis meshes.

The effect of the complete shell structure was simulated by the appropriate boundary conditions. Along the radial plane AC and BD in Fig. 67, only radial displacements were permitted. This was accomplished by use of the TRANSFORMATION option in MARC to transform the global degrees of freedom in these planes to the local coordinate systems. Along the planes AB and CD the effect of the fore and aft louvers was simulated by requiring that the radial displacements, u_r, of nodal points on each plane were related by the equation

$$(u_r)_{AB} = (u_r)_{CD} \times \frac{R_{AB}}{R_{CD}} , \tag{6.8}$$

where R_{AB} is the original radial coordinate on AB and R_{CD} is the original radial coordinate on CD. An additional condition equated the axial slopes along these planes. These conditions were prescribed by means of the user subroutine UFORMS. The fact that a series of louvers may be represented by this technique had been demonstrated in previous elastic shell of revolution analyses.

Numerical accuracy problems associated with the small included angle were investigated with a simple two element model having an included angle equal to that of the louver model. An initial analysis with this model produced stresses on the order of 69 MPa (10000 psi) when run in an isothermal condition in which the stresses should have been zero. In this model the radial displacements, due to the free thermal growth, were serveral orders of magnitude larger than the circumferential displacements. Circumferential (hoop) stresses were produced as a result of numerical round-off during the single precision solution on the IBM 370/3033 computer. Using a double precision version of MARC significantly reduced the round-off error to produce an acceptable isothermal solution.

The thermal increment file generated in Ref. [8] was used to drive the structural analysis. A small mechanical pressure load was applied initially followed by sixty-one (61) thermal load increments per hysteresis cycle. Two hysteresis cycles were completed in the analysis. The transient temperature at the integration point closest to the end of the louver lip (the fatigue critical location) is shown in Fig. 68. Figure 69 depicts the hoop stress vs. hoop mechanical strain hysteresis loop at the corresponding integration point for two thermal loading cycles consisting of one hundred and twenty-one (121) MARC thermal load increments. Thirty (30) subincrements per MARC increment were used to ensure an accurate description of the viscoplastic behavior in the subroutine HYPELA. With the new integration algorithm the two thermal loading cycles could have been traversed with much less than one hundred and twenty-one (121) MARC thermal load increments; this number of increments was used, however, because of the availability of the thermal load increment file from the analysis conducted in Ref. [8].

The thermomechanical response shown in Fig. 69 exhibits an apparent ratchetting in the negative strain direction. This ratchetting is believed to be due to the elastic behavior observed in the low temperature tensile portion of the thermomechanical hysteresis loop. A stress dip phenomenon is also observed at the maximum tensile stress obtained in the loop. Neither the excessive elastic behavior, nor the stress dip phenomenon, is observed in the experimental thermomechanical response shown in Fig. 24. Note, however, that no ratchetting is observed in the experimental thermomechanical response in Fig. 24 because the maximum mechanical strain amplitude is kept constant at -0.45 percent.

The ratchetting of the thermomechanical hysteresis loop with its associated tensile elastic response and stress dip phenomenon, coupled with the generally poor predictions of the thermomechanical response produced by the viscoplastic constitutive theories, points to a need for further research on the thermomechanical behavior of Hastelloy-X and other high temperature structural materials. In general, the isothermal predictions of the theories with respect to strain rate, creep and relaxation behavior, is good. Further analysis, along the lines suggested in Section 6.4, is required to improve the thermomechanical predictions.
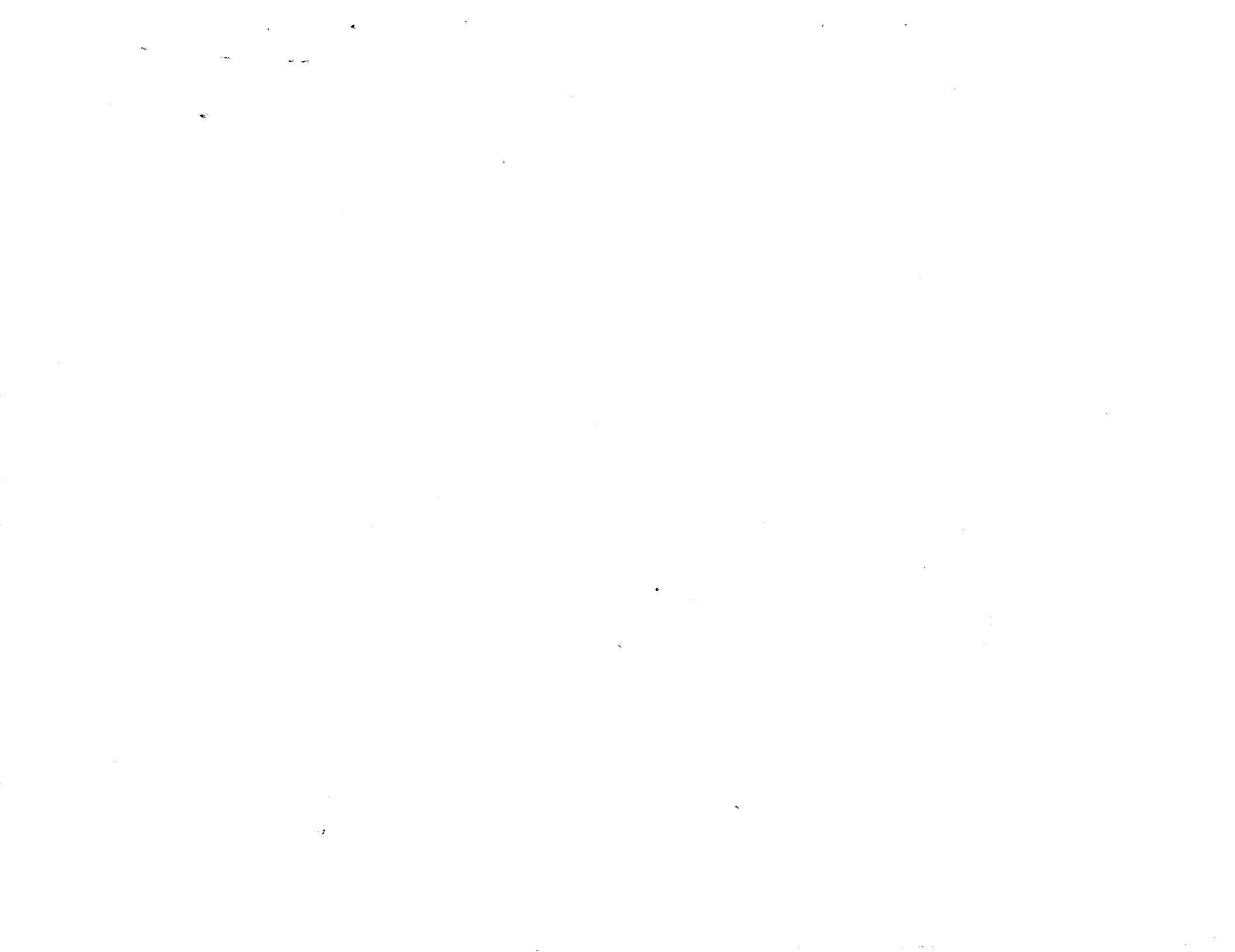
7.0 DISCUSSION OF RESULTS AND CONCLUSIONS

The unified viscoplastic constitutive theories of Walker (Appendix 1), Miller (Appendix 4), and Krieg, Swearengen & Rohde (Appendix 8), were installed for use in the MARC nonlinear finite element program by means of an initial stress method. An experimental program on Hastelloy-X material supplied the material constants for each of the theories at temperatures varying between 800°F (427°C) and 1800°F (982°C). General conclusions and observations concerning the work performed in this contract are:

1. The unified viscoplastic theories are represented by systems of "stiff" differential equations. In order to integrate such theories over the finite element load increment, it is necessary to split the finite element increment into a number of subincrements and integrate the constitutive theories over the subincrements. By using a large number of subincrements the constitutive theories can be integrated accurately over arbitrarily large finite element load increments. The size of the finite element load increments is limited only by the fact that proportional loading (strain increments are proportional during the finite element load increment) is assumed to occur over the increment. Consequently, the finite element load increments must be small enough to ensure that the strain history at any point in the structure can be represented by increments of proportional loading. The strain history, at any point in the structure, which in general is nonproportional, is then represented by a series of proportional strain increments in which the constant of proportionality changes from increment to increment.

   The solution time required for a complete load increment in a finite element program is linearly related to the number of subincrements used in the integration of the constitutive equations. A reduction in the number of subincrements can be effected if the viscoplastic constitutive theories are written in an integral form and the theories are integrated over the subincrements by means of a suitable recursive algorithm. By means of the recursive algorithm developed in this contract the number of subincrements can be reduced to one. This corresponds to integrating the constitutive equations directly over the finite element load increment. Because the recursive algorithm is stable and accurate, even when the integration increment is large, the computer time required to integrate these "stiff" viscoplastic formulations can be substantially reduced.

2. The viscoplastic constitutive theories examined give adequate accuracy in predicting the rate-dependent response of Hastelloy-X under uniaxial isothermal loading conditions. It appears that tabulating the material constants as a function of temperature provides improved accuracy over that obtained by assuming that strain rate effects and temperature effects are coupled by the Arrhenius type of exponential relation used in Miller's theory. Care must be taken, when tabulating the material constants as a function of temperature, to ensure that a reasonable asymptotic stress-strain response is obtained. Some of the material

constants, such as the inelastic strain rate exponent, n, control the magnitude of the computed stress at large strain values. The best way to obtain an interpolated value of n is to interpolate the asymptotic stress-strain response and then to determine the value of n from the interpolated response. In this contract the reciprocal, n^{-1}, is interpolated in the temperature tables, since this gives an adequate representation of the asymptotic stress-strain response at a given temperature.

3. Relatively poor accuracy is obtained when the viscoplastic theories are used to predict the uniaxial thermomechanical behavior of Hastelloy-X. It appears that improved accuracy can be obtained by assuming that the state variables can change with temperature during "elastic" excursions and by assuming that the instantaneous material response is inelastic, rather than elastic.

4. The computer time required for the three dimensional structural analysis of the combustor liner induction rig test specimen was about the same as that required by the conventional yield surface plasticity theories available within the MARC program. This structural analysis was performed by integrating the functional theory over thirty (30) subincrements for every MARC load increment. Since the number of subincrements can be decreased by a factor of thirty and the number of MARC load increments can also be substantially reduced compared with the number of increments required to preserve accuracy and stability with the conventional yield surface plasticity theories, the new integration algorithm will cut the cost of nonlinear finite element analyses substantially over the cost required for conventional plasticity analyses.

8.0 RECOMMENDATIONS

This contract has provided an enhanced capability for analyzing structural components which operate under cyclic elevated temperature conditions. Further work is necessary in order to:

1. Improve the uniaxial thermomechanical response of the constitutive theories. Improvements can be effected by: (a) allowing the state variables to change with temperature during "elastic" excursions in a thermomechanical simulation; and (b) by allowing the instantaneous response, $\sigma_{ij} = E_{ij}$, to be inelastic by specifying suitable growth laws for the variable E_{ij}.

2. Verify, and modify if necessary, the constitutive response under multiaxial loading conditions.

3. Apply the constitutive theories to other materials, both isotropic and aniso-tropic.
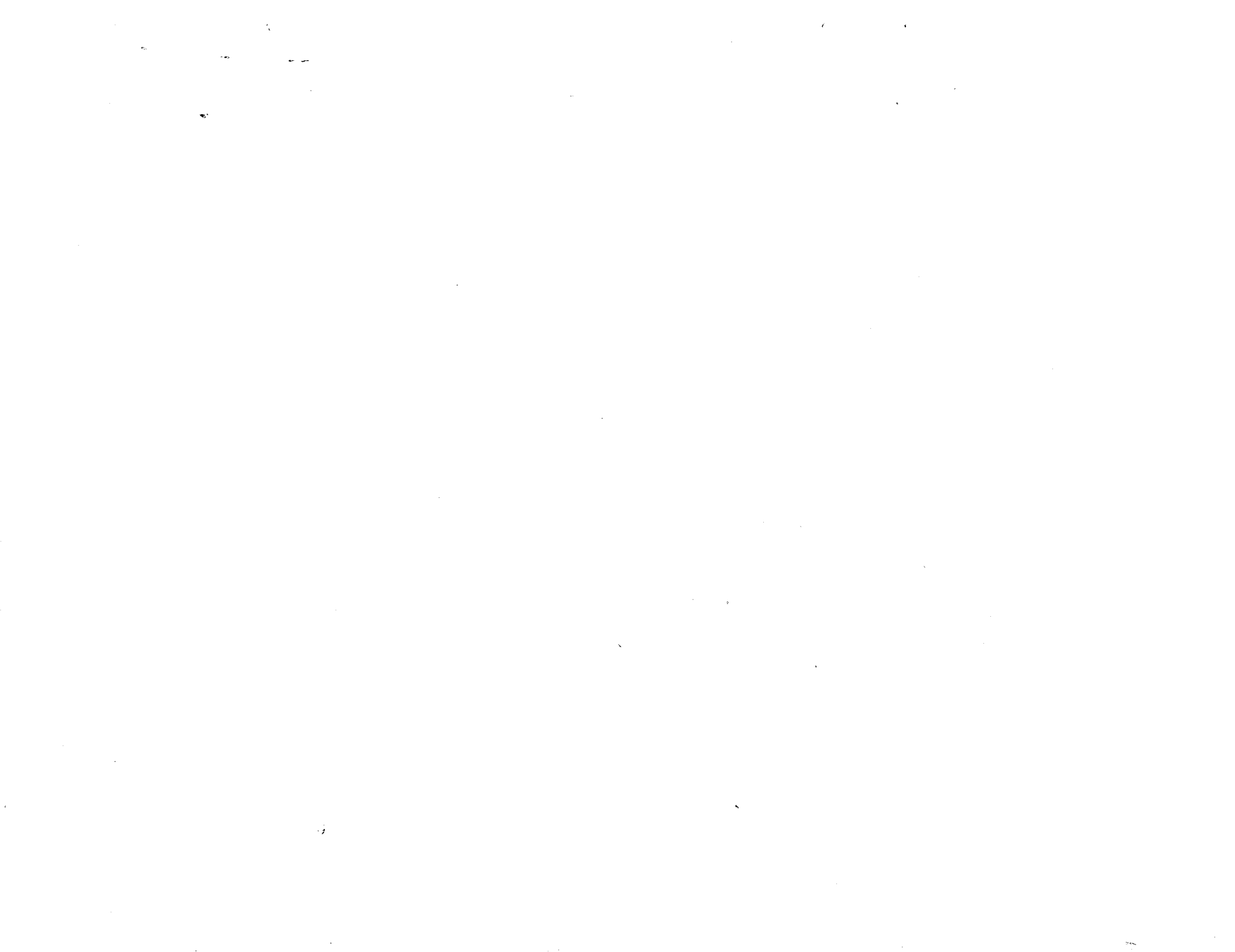
9.0 REFERENCES

1. MARC-CDC General-Purpose Finite Element Program. Volumes 1-4.

2. Argon, A. S.: Constitutive Equations in Plasticity. MIT Press, 1975.

3. Valanis, K. C.: Constitutive Equations in Viscoplasticity: Phenomenological and Physical Aspects. AMD, Vol. 21, ASME, 1976.

4. Nemat-Nasser, S.: Proceedings of the Workshop in Applied Thermoviscoplasticity. Technological Institute, Northwestern University, 1975.

5. Krempl, E., C. H. Wells and Z. Zudans: Workshop on Inelastic Constitutive Equations for Metals: Experimentation-Computation-Representation. Rensselaer Polytechnic Institute, Troy, New York, 1975.

6. Saczalski, K., and J. A. Stricklin: The Office of Naval Research Plasticity Workshop. Report 75-51, Texas A&M University, 1975.

7. Krempl, E.: Cyclic Creep - An Interpretive Literature Survey. Welding Research Council Bulletin No. 195, 1974.

8. Moreno, V.: Combustor Liner Durability Analysis. Report NASA CR 165250, prepared for NASA-Lewis Research Center under Contract NAS3-21836, 1981.

9. Krempl, E., and P. Hewelt: The Constant Volume Hypothesis for the Inelastic Deformation of Metals in the Small Strain Range. Mechanics Research Communications, Vol. 7, No. 5, pp. 283-288, 1980.

10. Krempl, E.: The Role of Servocontrolled Testing in the Development of the Theory of Viscoplasticity Based on Total Strain and Overstress. Presented at the ASTM Symposium on Mechanical Testing for Deformation Model Development, Bal Harbour, Florida, November 12-13, 1980.

11. Walker, K. P.: Representation of Hastelloy-X Behavior at Elevated Temperature with a Functional Theory of Viscoplasticity. Presented at ASME/PVP Century 2 Emerging Technology Conference, San Francisco, California, August 1980. To appear in ASME J. of Eng. Mat. & Technology, 1981.

12. Chaboche, J. L.: Viscoplastic Constitutive Equations for the Description of Cyclic and Anisotropic Behavior of Metals. Bulletin de L'Academie des Sciences, Serie des Sciences Techniques, Vol. XXV, No. 1, pp. 33-42, 1977.

REFERENCES (Cont'd)

13. Chaboche, J. L.: Thermodynamic and Phenomenological Description of Cyclic Viscoplasticity with Damage. Translation of Publication No. 1978-3 of the Office National d'Etudes et de Researches Aerospatiales, France, by the European Space Agency Technical Translation Service, Publication Number ESA-TT-548, May 1979.

14. Miller, A. K.: An Inelastic Constitutive Model for Monotonic, Cyclic and Creep Deformation: Part I - Equations Development and Analytical Procedures and Part II - Application to Type 304 Stainless Steel. ASME J. Eng. Mat. and Tech., Vol. 98, pp. 97-113, 1976.

15. Lee, D., and F. Zaverl, Jr.: A Generalized Strain Rate-Dependent Constitutive Equation for Anisotropic Metals. Acta Met., Vol. 26, No. 11, pp. 1771-1780, 1978.

16. Bodner, S. R., and Y. Partom: Constitutive Equations for Elastic-Viscoplastic Strain Hardening Materials. ASME J. of Applied Mechanics, Vol. 42, pp. 385-389, 1975.

17. Stouffer, D. C., and S. R. Bodner: A Constitutive Model for the Deformation Induced Anisotropic Plastic Flow of Metals. Int. J. Eng. Sci., Vol. 17, pp. 757-764, 1979.

18. Young, R. W.: A Note on the Stouffer-Bodner Constitutive Model for Anisotropic Plastic Flow. Lett. Appl. Eng. Sci., Vol. 18, pp. 1091-1093, 1980.

19. Krieg, R. D., J. C. Swearengen, and R. W. Rohde: A Physically Based Internal Variable Model for Rate-Dependent Plasticity. In Inelastic Behavior of Pressure Vessel and Piping Components. PVP-PB-028 (ASME), pp. 15-28, 1978.

20. Cernocky, E. P., and E. Krempl: A Nonlinear Uniaxial Integral Constitutive Equation Incorporating Rate Effects, Creep and Relaxation. Int. J. of Nonlinear Mechanics, Vol. 14, pp. 183-203, 1979.

21. Krempl, E.: On the Interaction of Rate and History Dependence in Structural Metals. Acta Mechanica, Vol. 22, pp. 53-90, 1975.

22. Hart, E. W.: Constitutive Relations for the Nonelastic Deformation of Metals. ASME J. Eng. Mat. & Technology, Vol. 98, pp. 193-202, 1976.

23. Delph, T. J.: A Comparative Study of Two State-Variable Constitutive Theories. ASME J. Eng. Mat. & Technology, Vol. 102, pp. 327-336, 1980.

REFERENCES (Cont'd)

24. Valanis, K. C.: On the Foundations of the Endochronic Theory of Viscoplasticity.
    Archiwum Mechaniki Stosowanej, Vol. 27, pp. 857-868, 1968.

25. Wu, H.-C., and L. Chen: Endochronic Theory of Transient Creep and Creep
    Recovery. Report G302-79-001 or NASA-CR-158487, NASA-Langley Research Center,
    1979.

26. Miller, A. K.: Development of the Materials Code, MATMOD. Constitutive
    Equations for Zircaloy. EPRI Report Number EPRI NP-567, Project 456-1,
    December 1977.

27. Hopkins, S. W.: Low Cycle Thermal Mechanical Fatigue Testing. ASTM STP 612,
    American Society for Testing and Materials, pp. 157-169, 1976.

28. Stouffer, D. C., L. Papernik and H. L. Bernstein: Prediction of the Mechanical
    Response of a High Temperature Superalloy Rene 95. Interim Report for the
    period September 1978 - July 1980. For Air Force Contract F33615-78-C-5199.

NOZZLE

COMBUSTOR

TURBINE

HOT COMBUSTION GAS ,

A

COOLING AIR

B

METAL
TEMPERATURE

MAXIMUM
POWER

A

IDLE

IDLE

B

TYPICAL ENGINE CYCLE
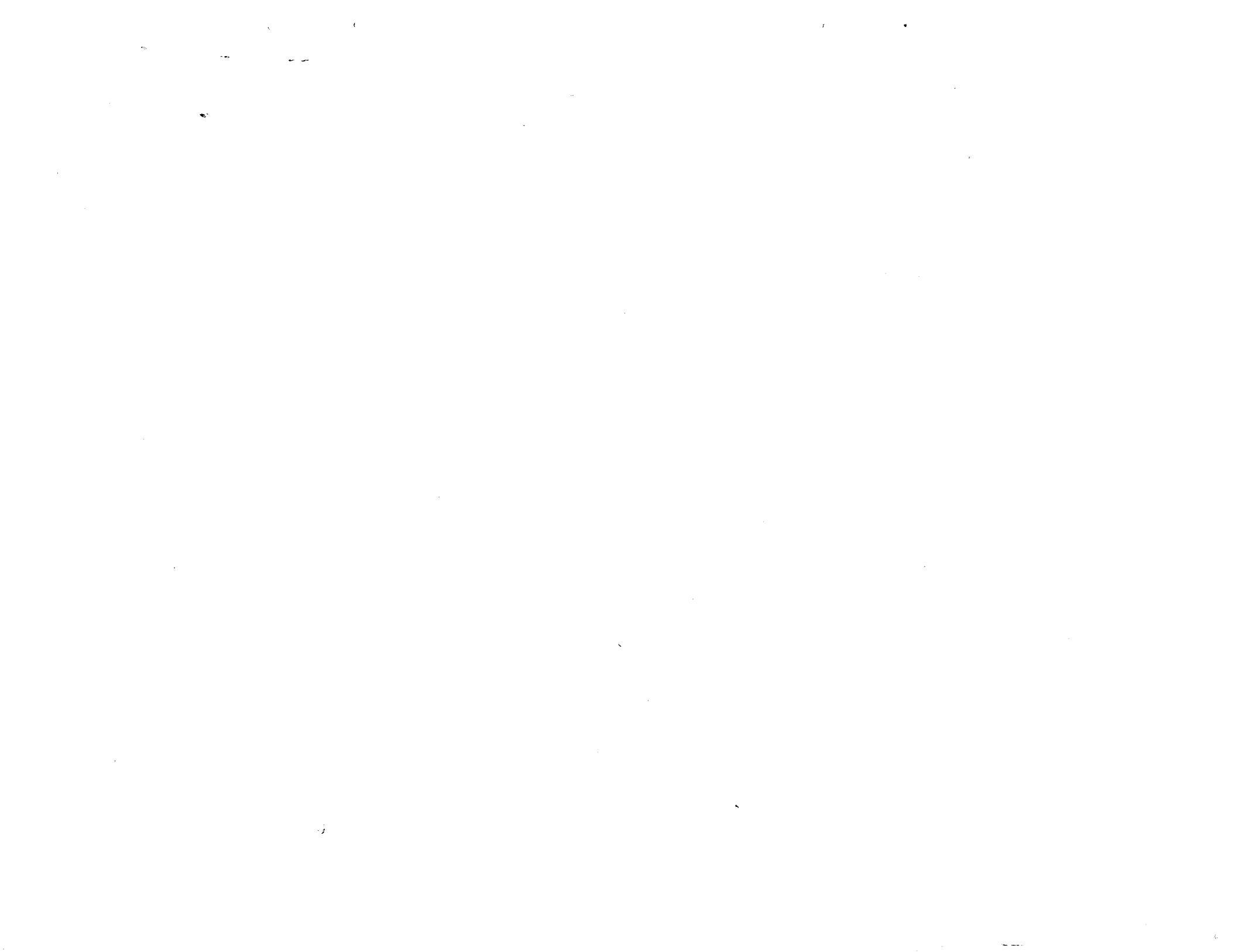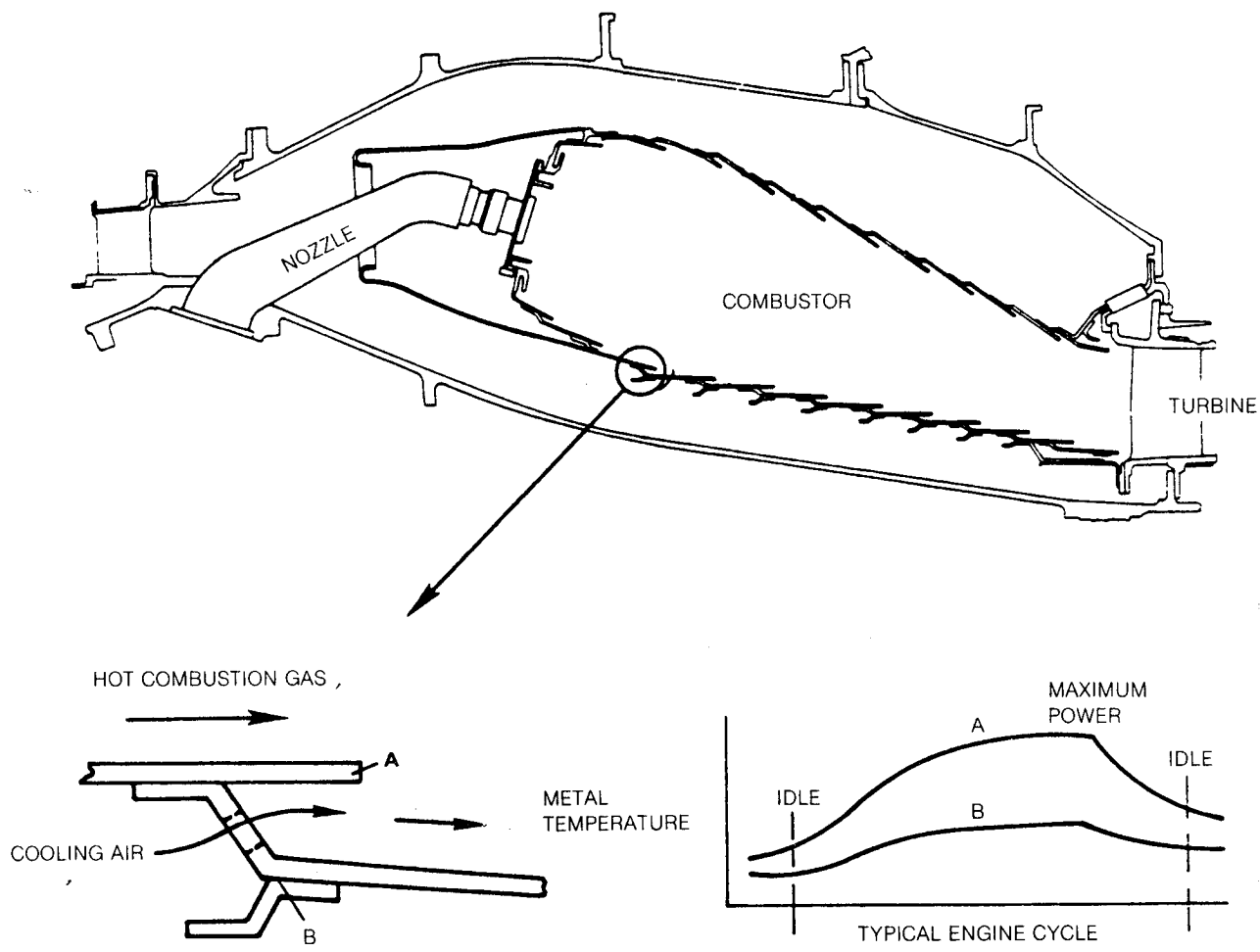
Figure 1. Typical Combustor Construction Showing Predicted Temperature Distribution

81—9—103—35
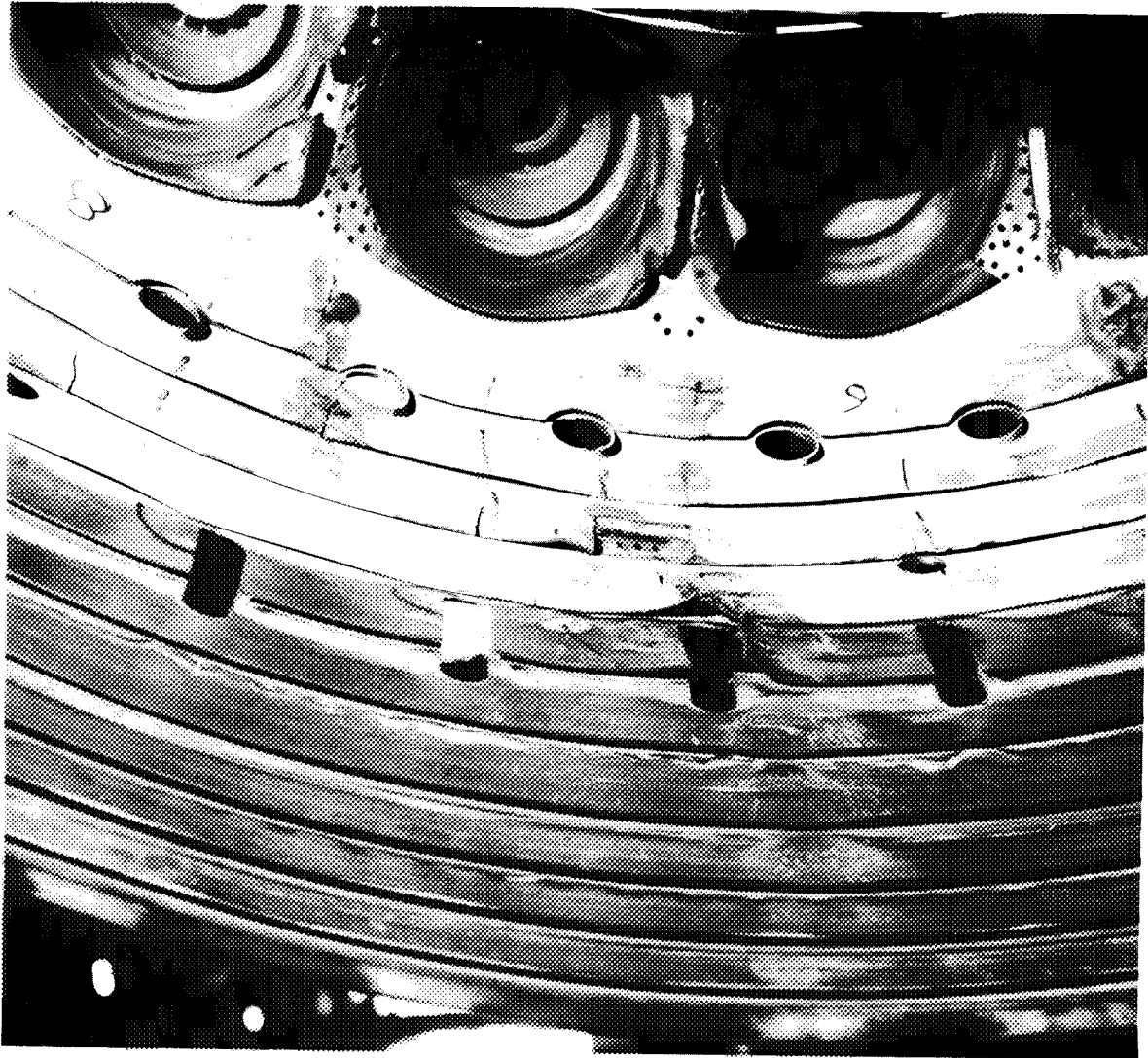
Figure 2. Typical Axial Cracks in Annular Liner

81—9—103—23

63
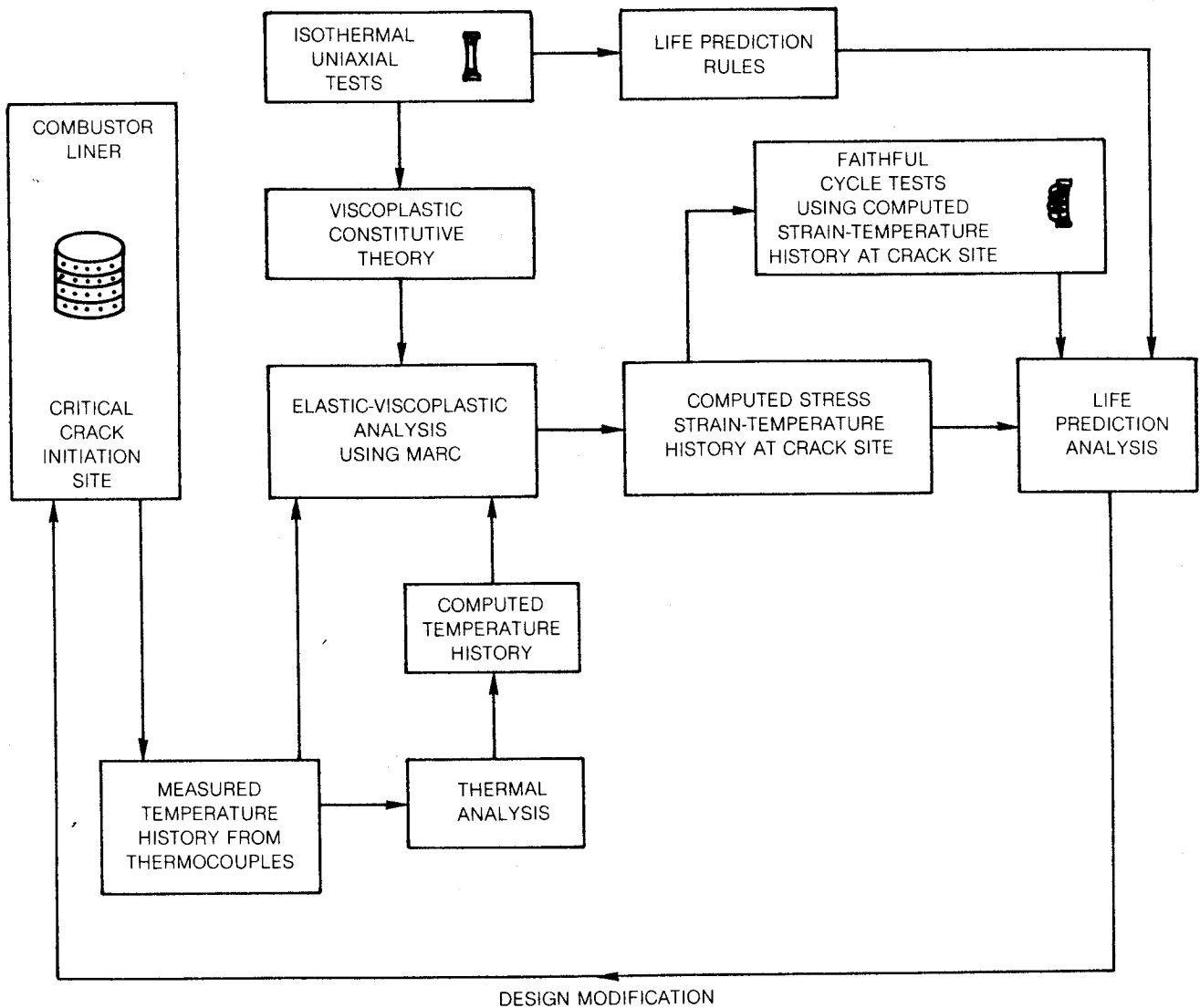
Figure 3. **Current Structural Technology is Limited by Inaccuracies in the Viscoplastic Constitutive Equation and Life Prediction Rules**
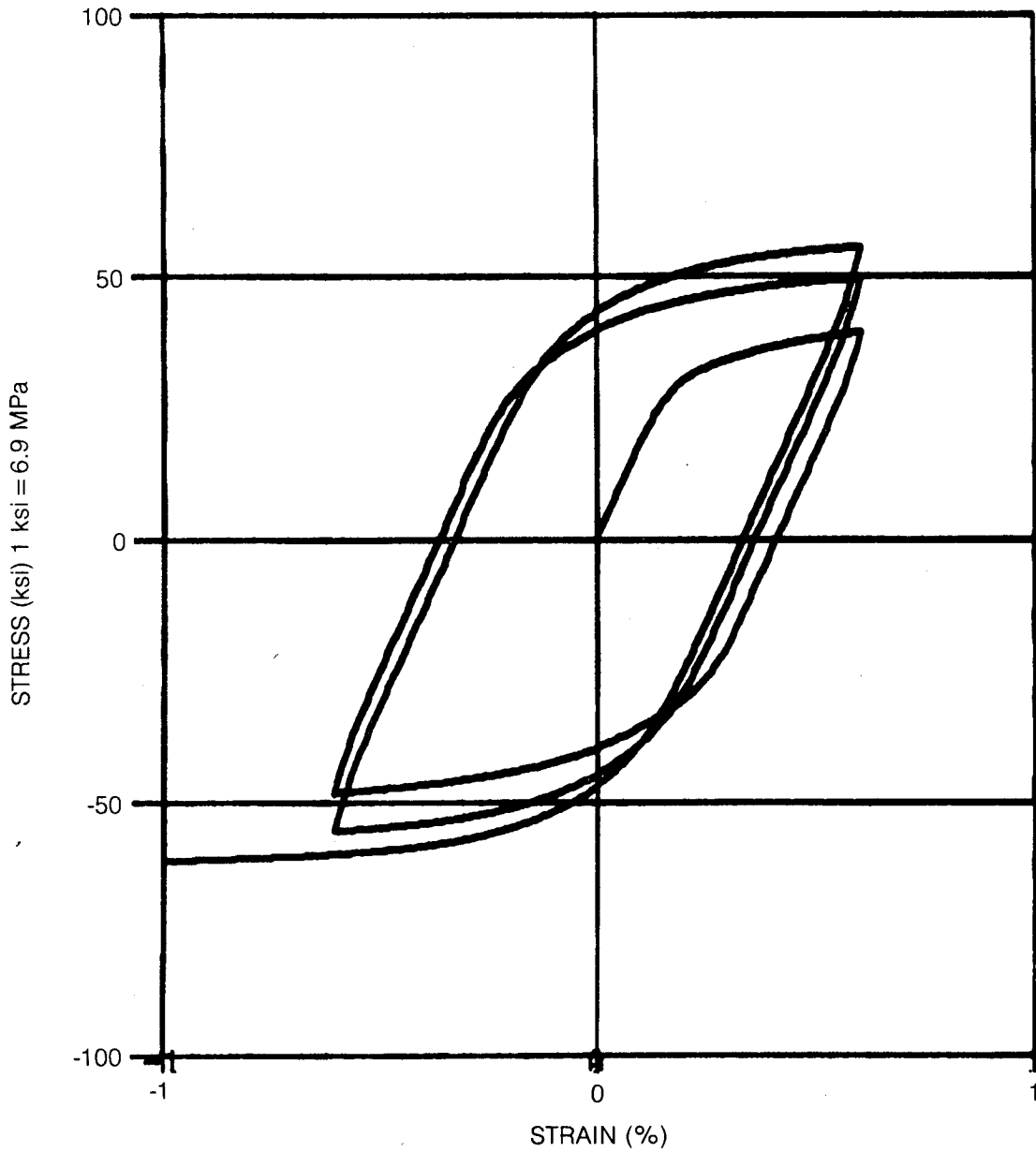
Figure 4. Hardening of Hysteresis Loop Due to Hardening of Drag Stress
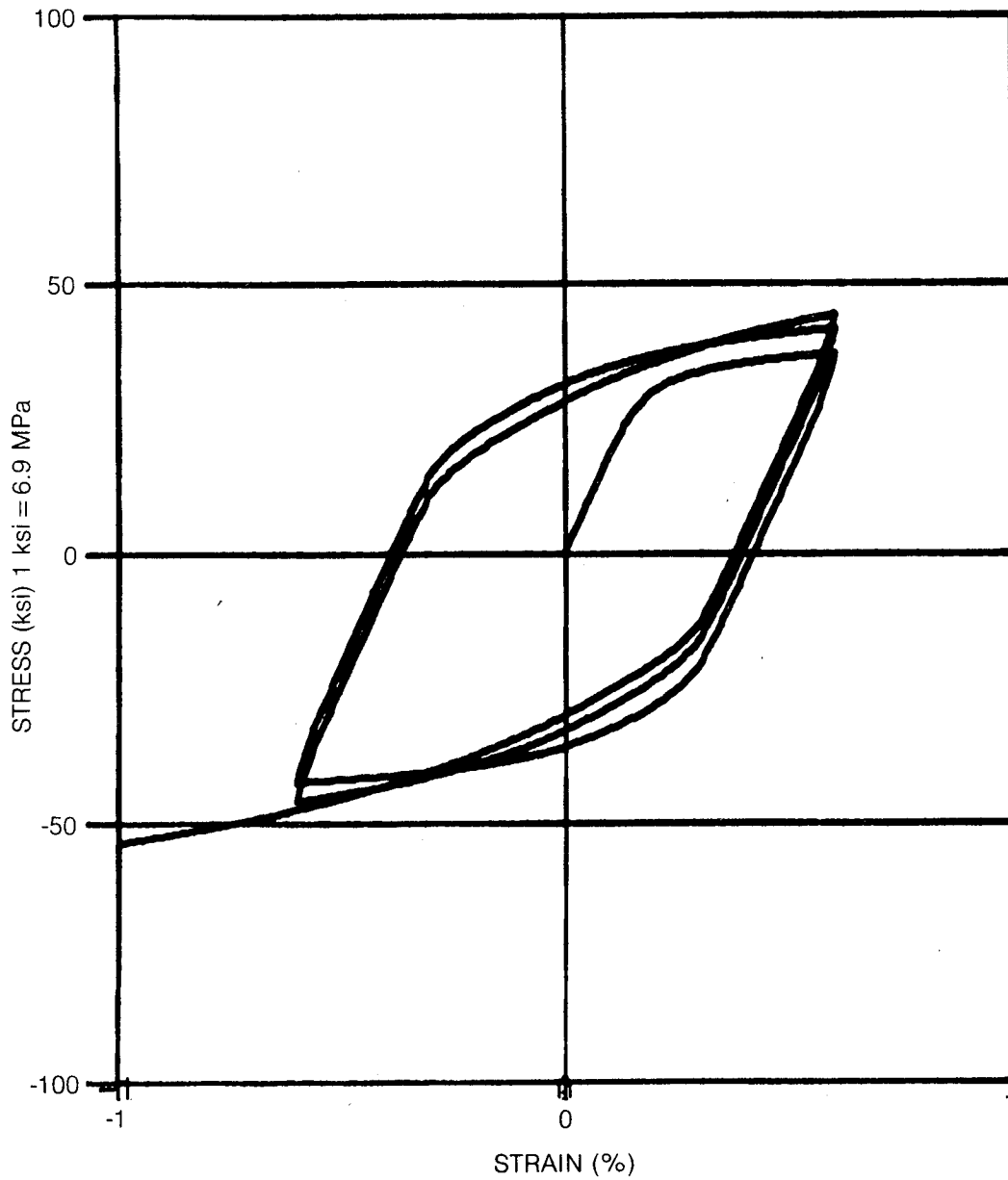
Figure 5. Hardening of Hysteresis Loop Due to Hardening of Equilibrium Stress
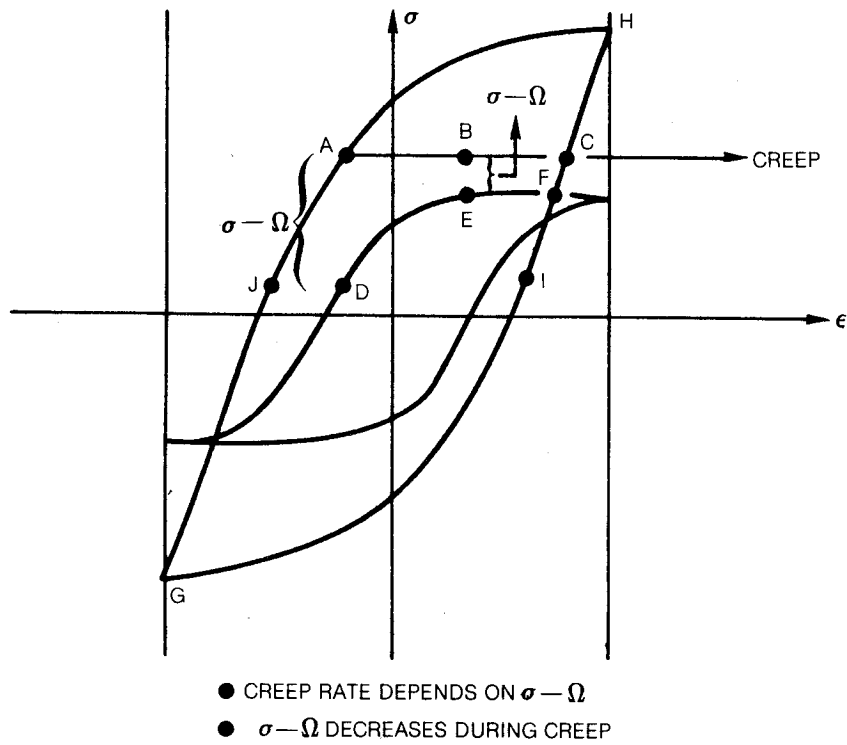
Figure 6. Creep and Relaxation Rates Depend on the "Overstress." Different Behavior is Observed on the Loading and Unloading Branches of the Hysteresis Loop.
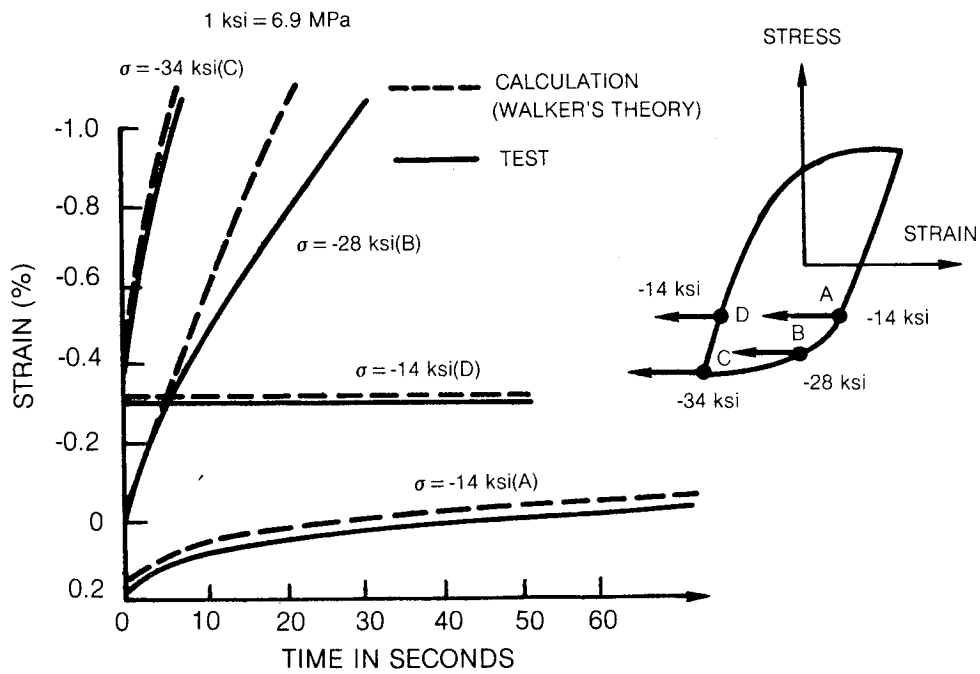
Figure 7. Comparison of Creep Response of Hastelloy-X at 871°C (1600°F) on the Loading and Unloading Branches of a Steady State Hysteresis Loop Executed at a Constant Strain Rate of $\pm 1.4 \times 10^{-3}$ sec^{-1} with a Strain Amplitude of $\pm 0.4\%$
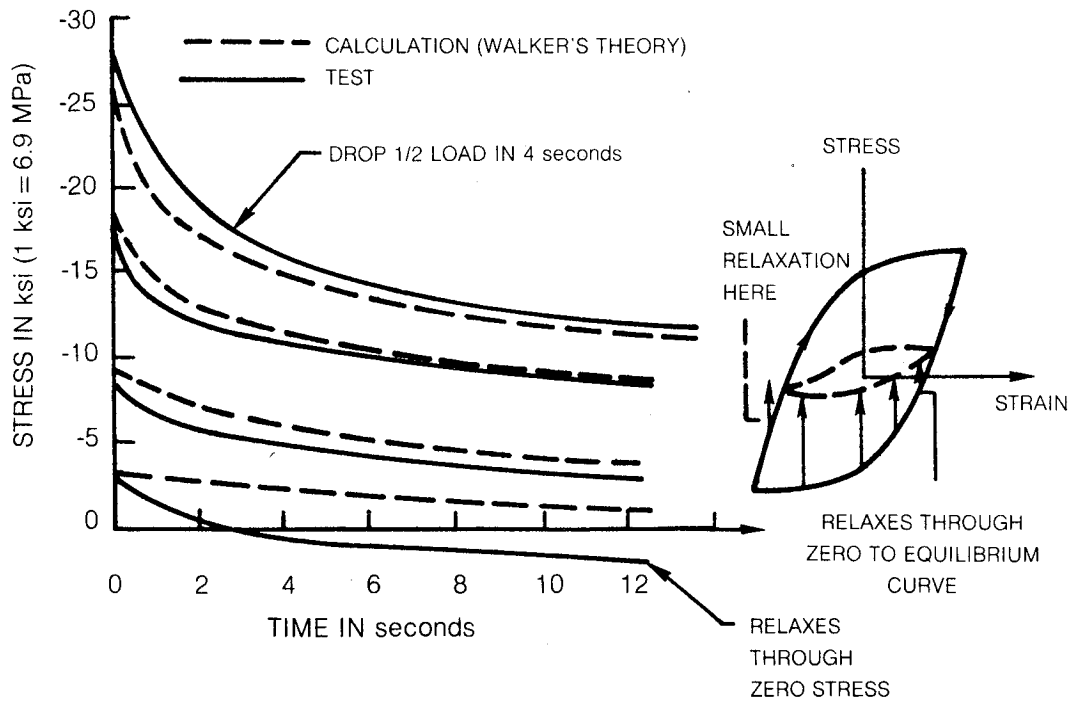
Figure 8. Negative Stress Relaxation Response of Hastelloy-X at 871°C (1600°F) Initiated from a Steady State Hysteresis Loop Executed at a Constant Strain Rate of ±1.36 × 10⁻³ sec⁻¹ with a Strain Amplitude of ±0.4%

81−9−103−3
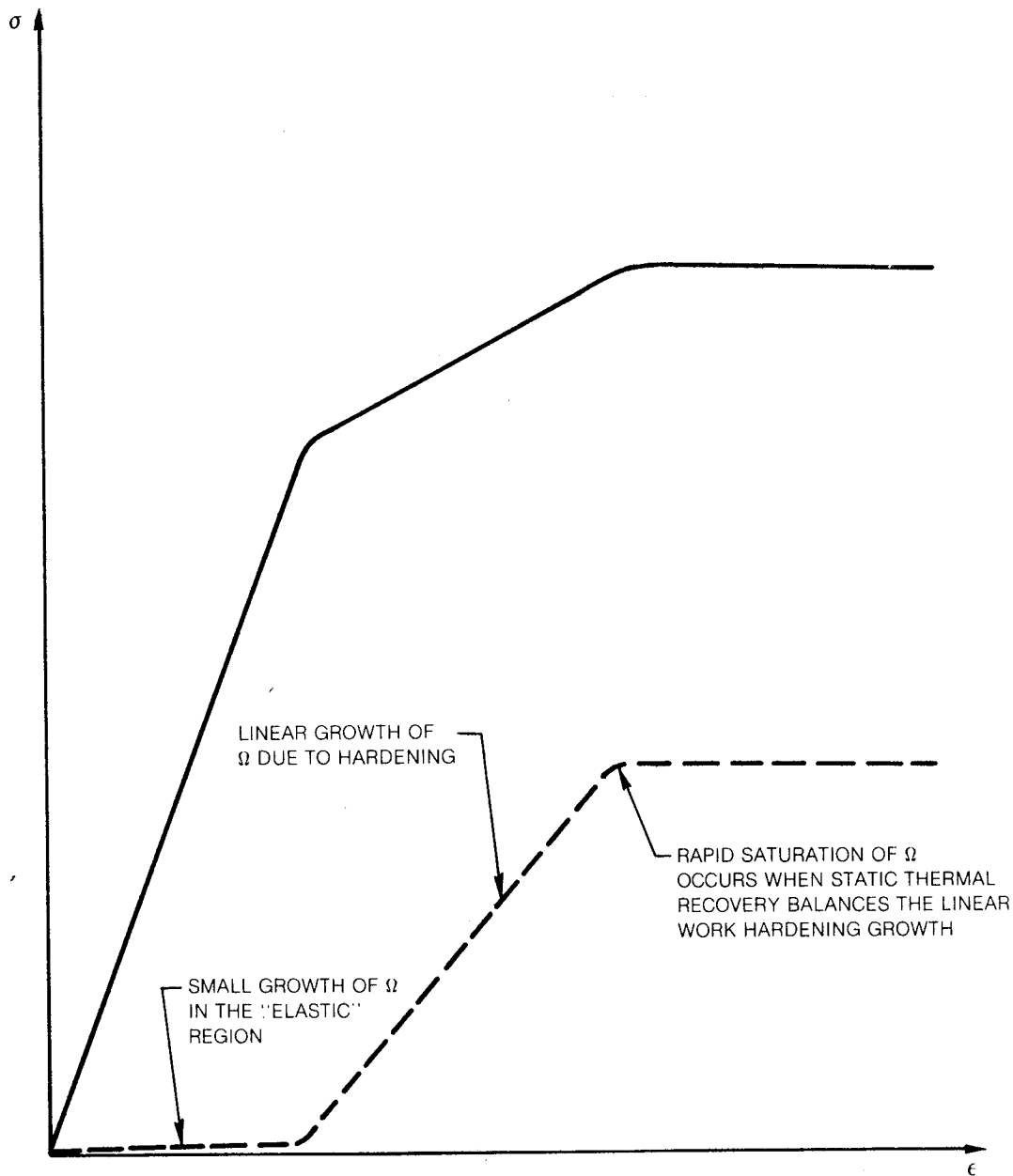
Figure 9. Characteristic Tri-Linear Stress-Strain Behavior Exhibited by those Theories (Miller; Hart; Krieg, Swearengen and Rohde) in which the Equilibrium Stress Grows Linearly with Inelastic Strain and Reaches a Saturation Limit in which Hardening and Static Thermal Recovery are Balanced

70

EXTENSOMETRY
RIDGES
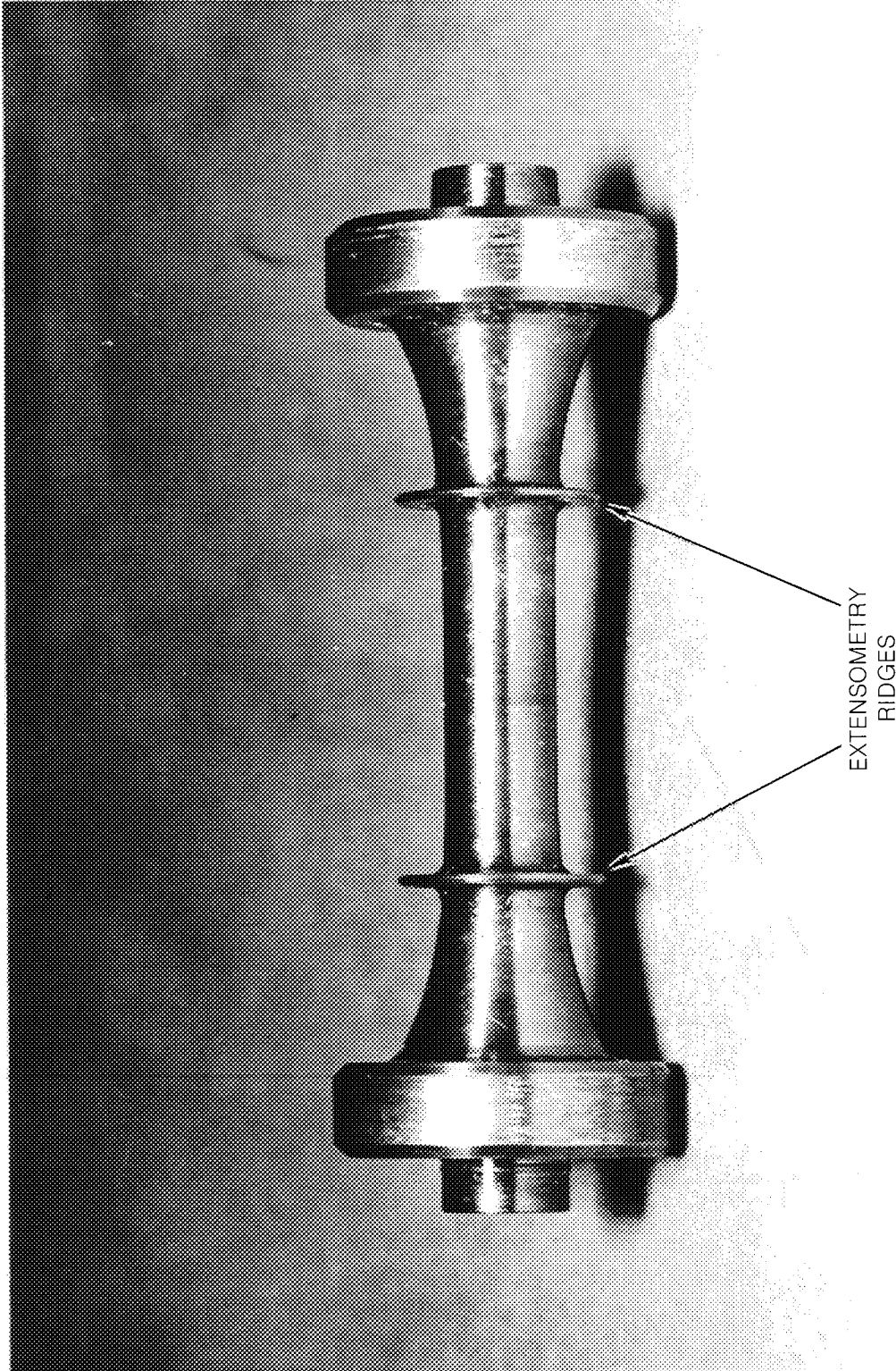
Figure 10. Strain Controlled (SC) Specimen

81-9-103-36
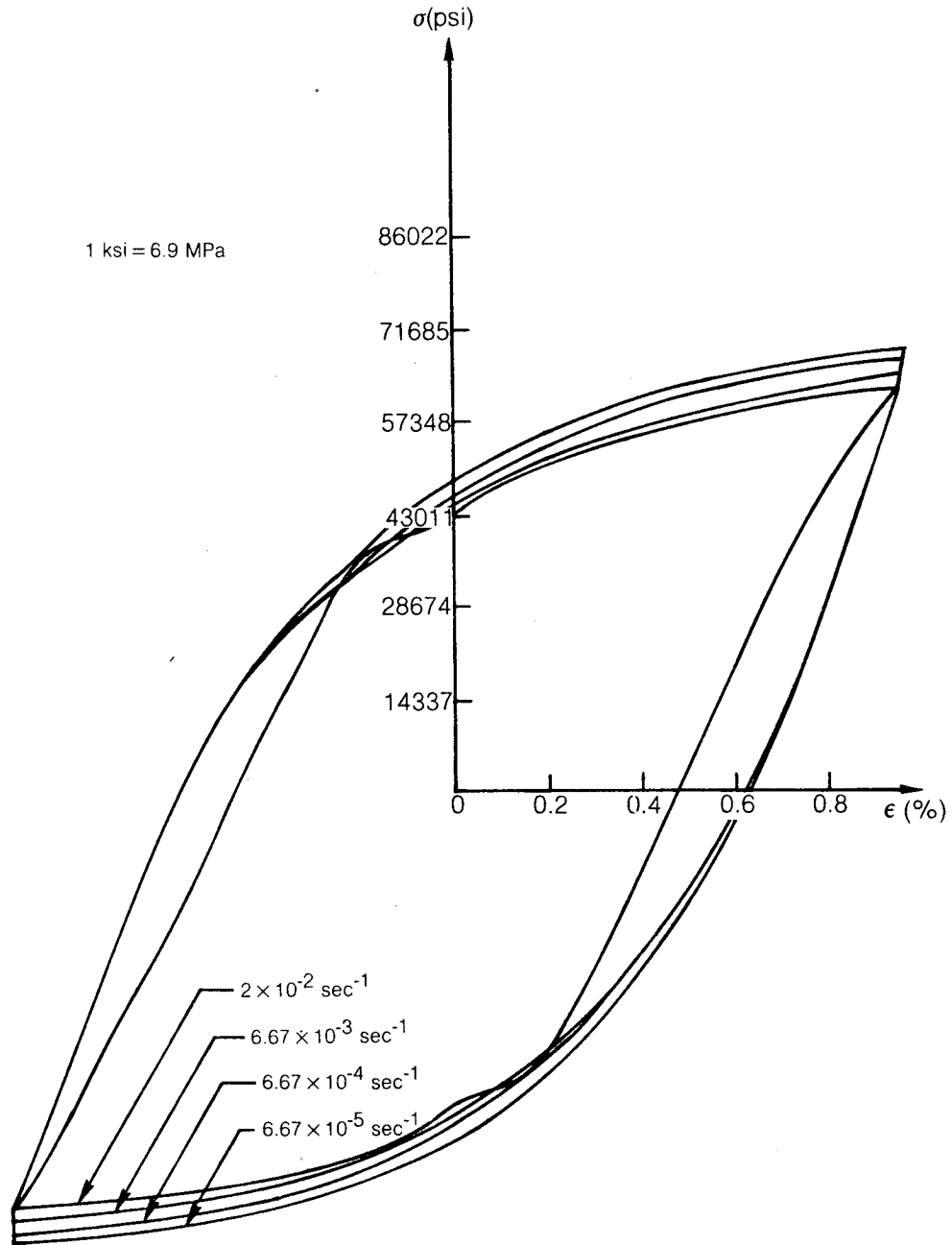
Figure 11. Experimental Steady State Hysteresis Loops for Hastelloy-X Showing Inverse Strain Rate Sensitivity at 800°F (427°C)
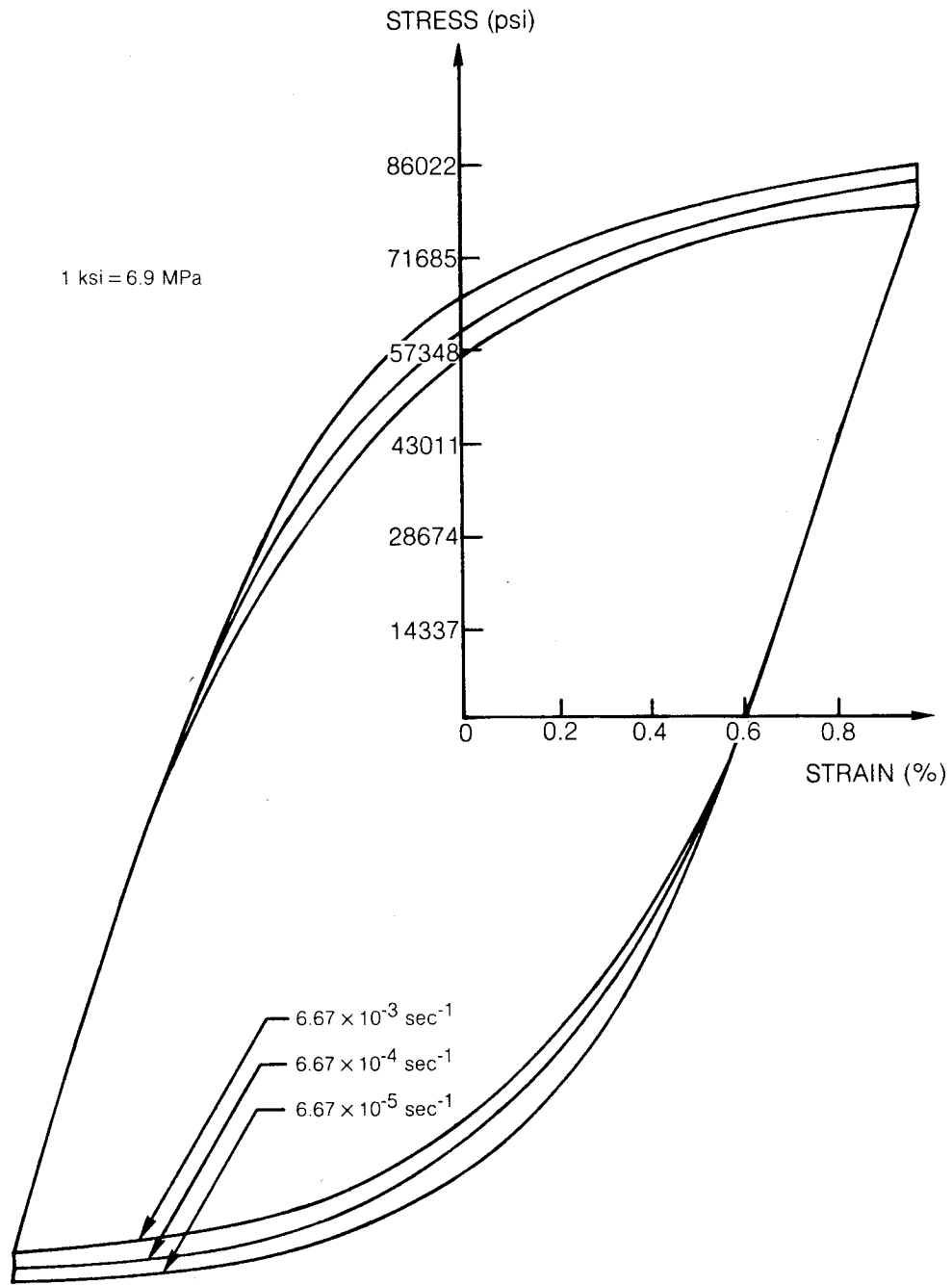
Figure 12. **Experimental Steady State Hysteresis Loops for Hastelloy-X Showing Inverse Strain Rate Sensitivity at 1000°F (538°C)**

80—8—82—2
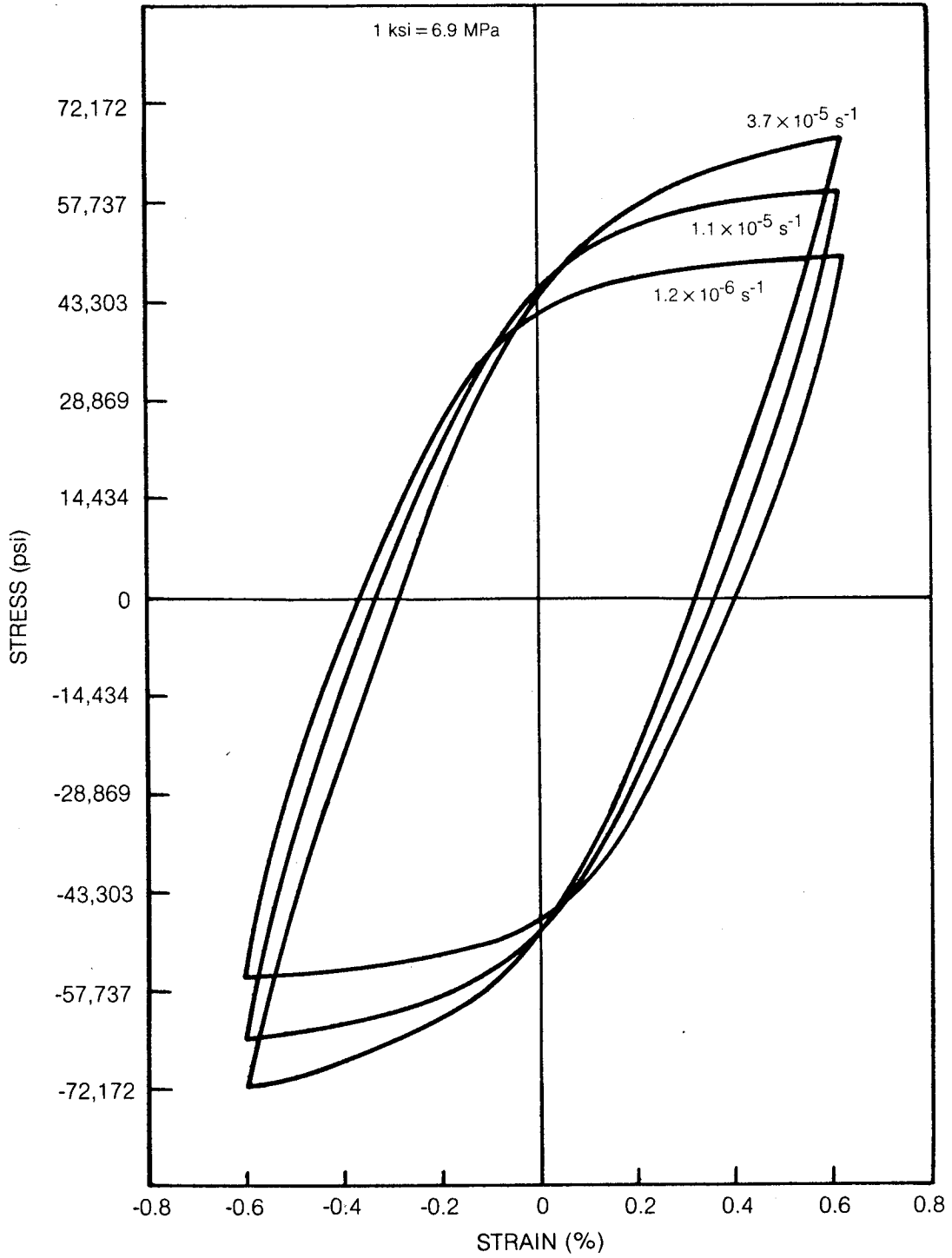
Figure 13. Experimental Steady State Hysteresis Loops for Hastelloy-X at 649°C (1200°F)

74
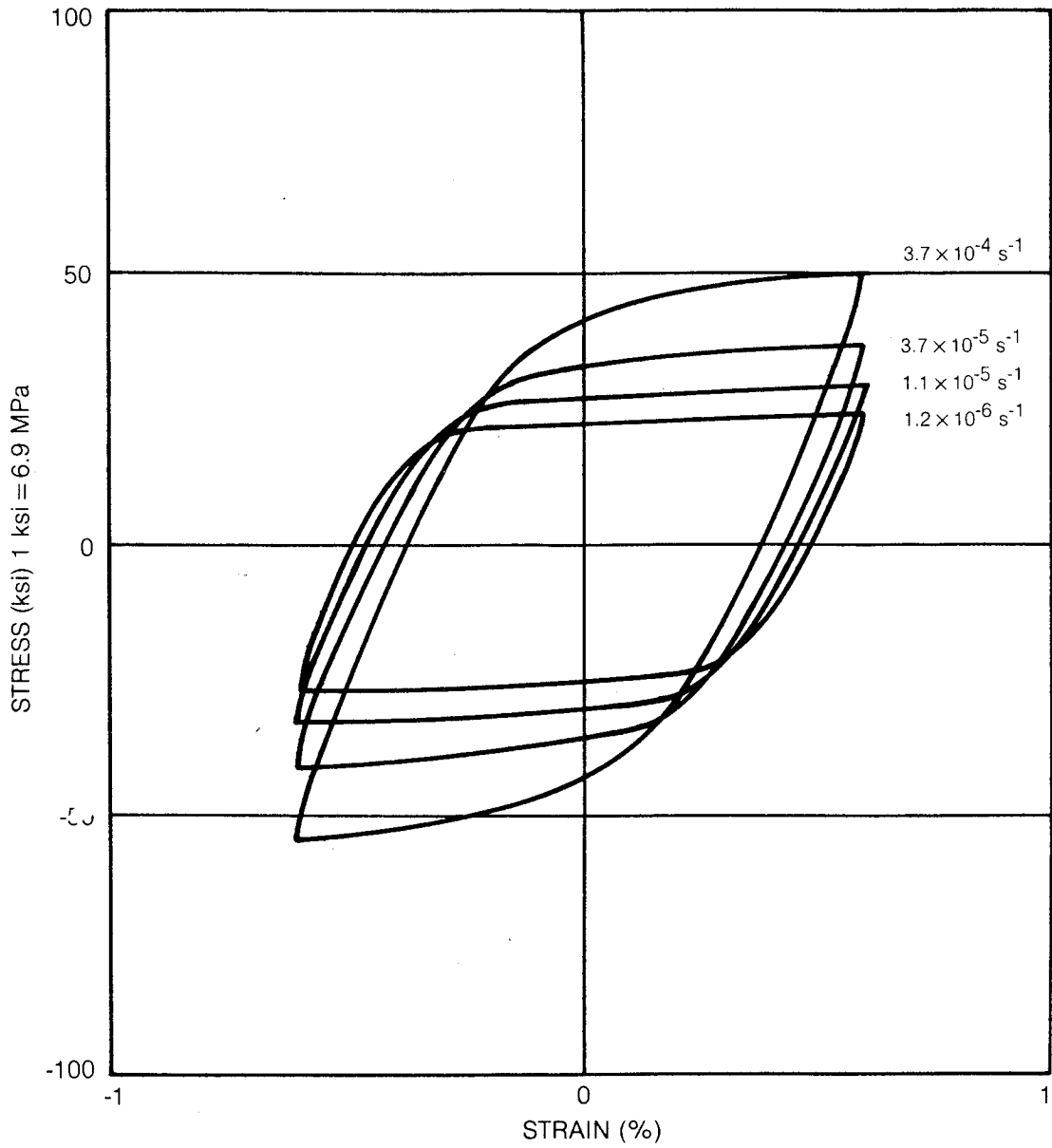
Figure 14. Experimental Steady State Hysteresis Loops for Hastelloy·X at 760 °C (1400 °F)
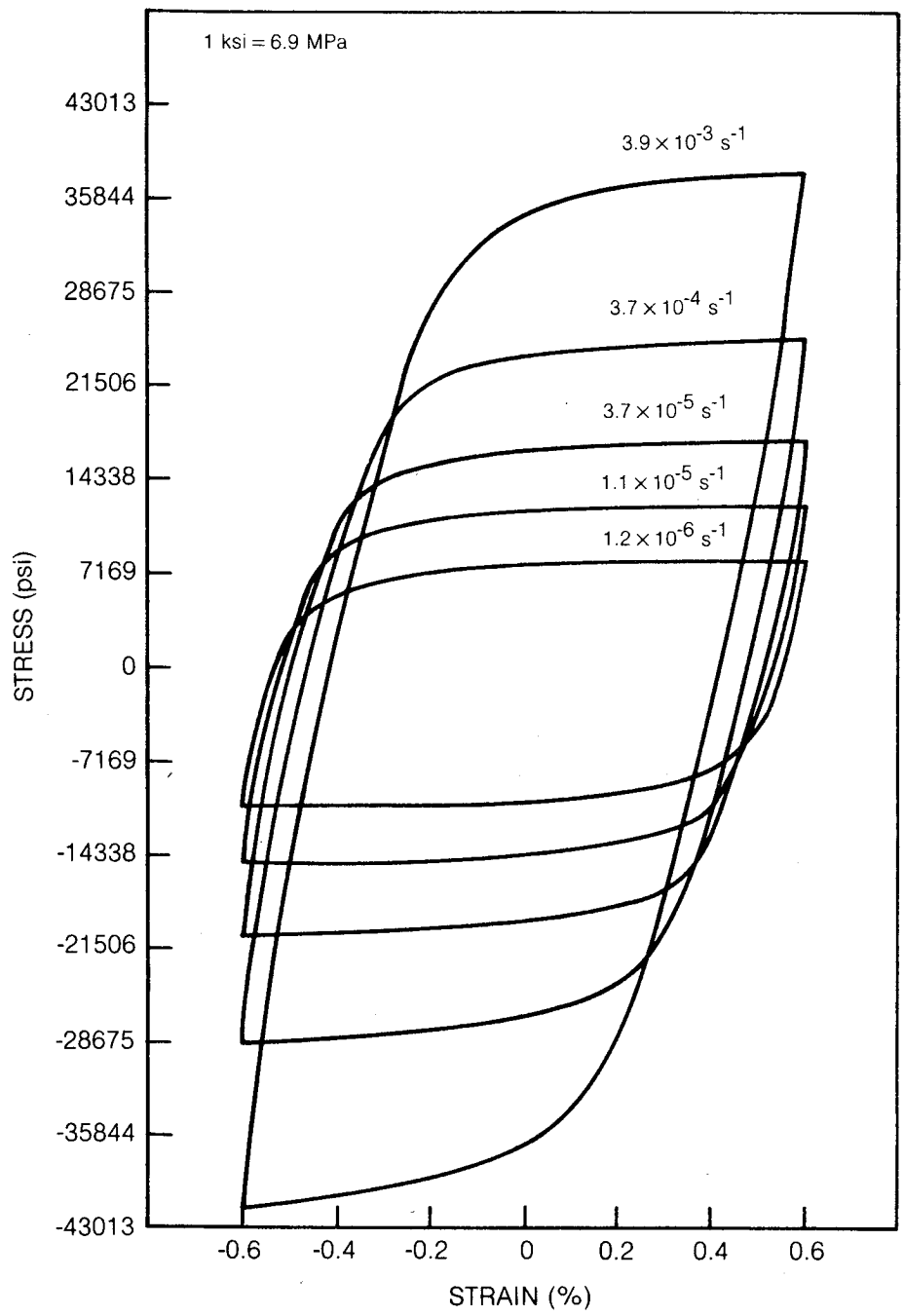
Figure 15. Experimental Hysteresis Loops for Hastelloy-X at 871 °C (1600 °F)

80—11—72—2
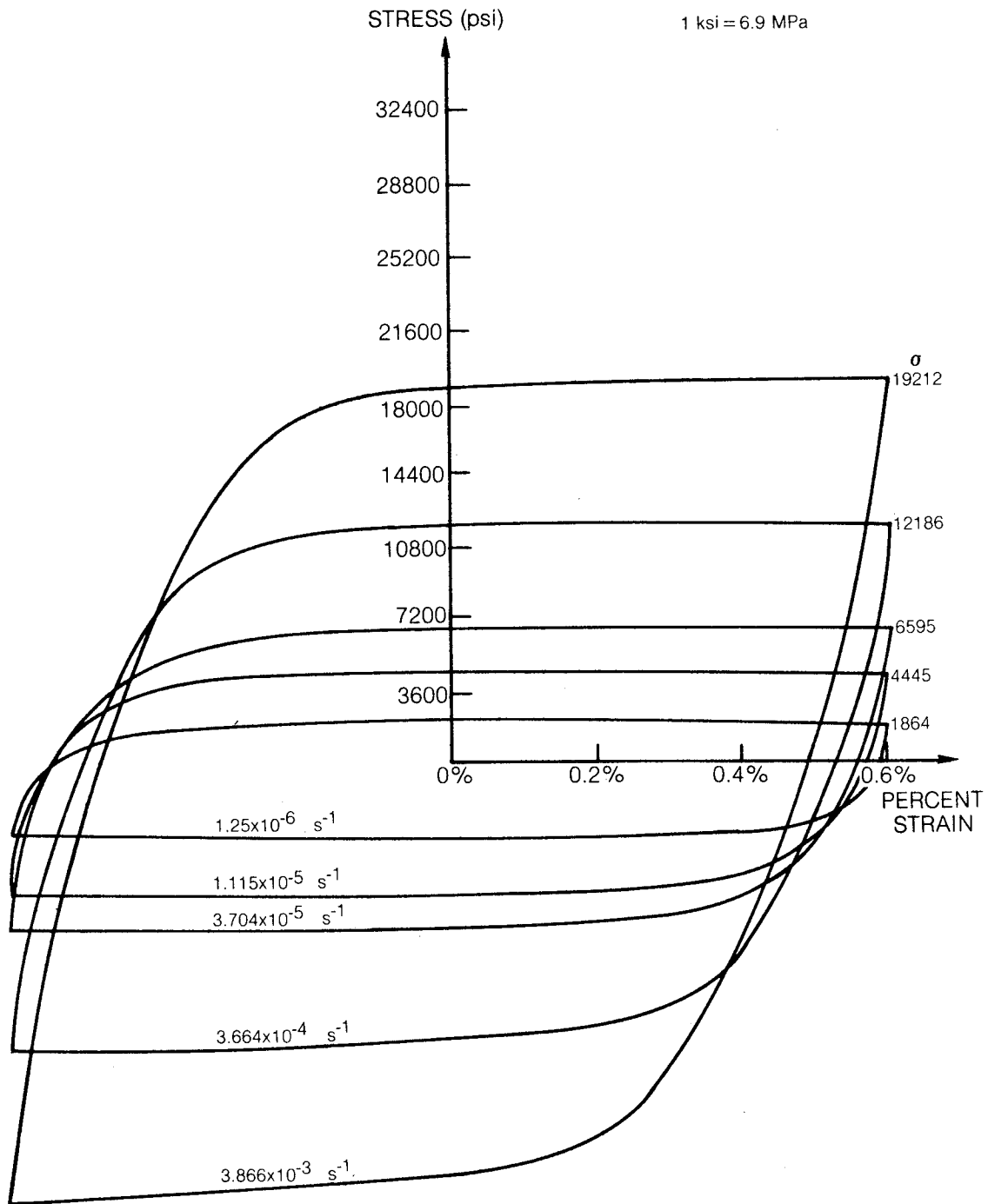
Figure 16. Experimental Hysteresis Loops for Hastelloy-X at 1800°F at ±0.6% Strain Amplitude

77
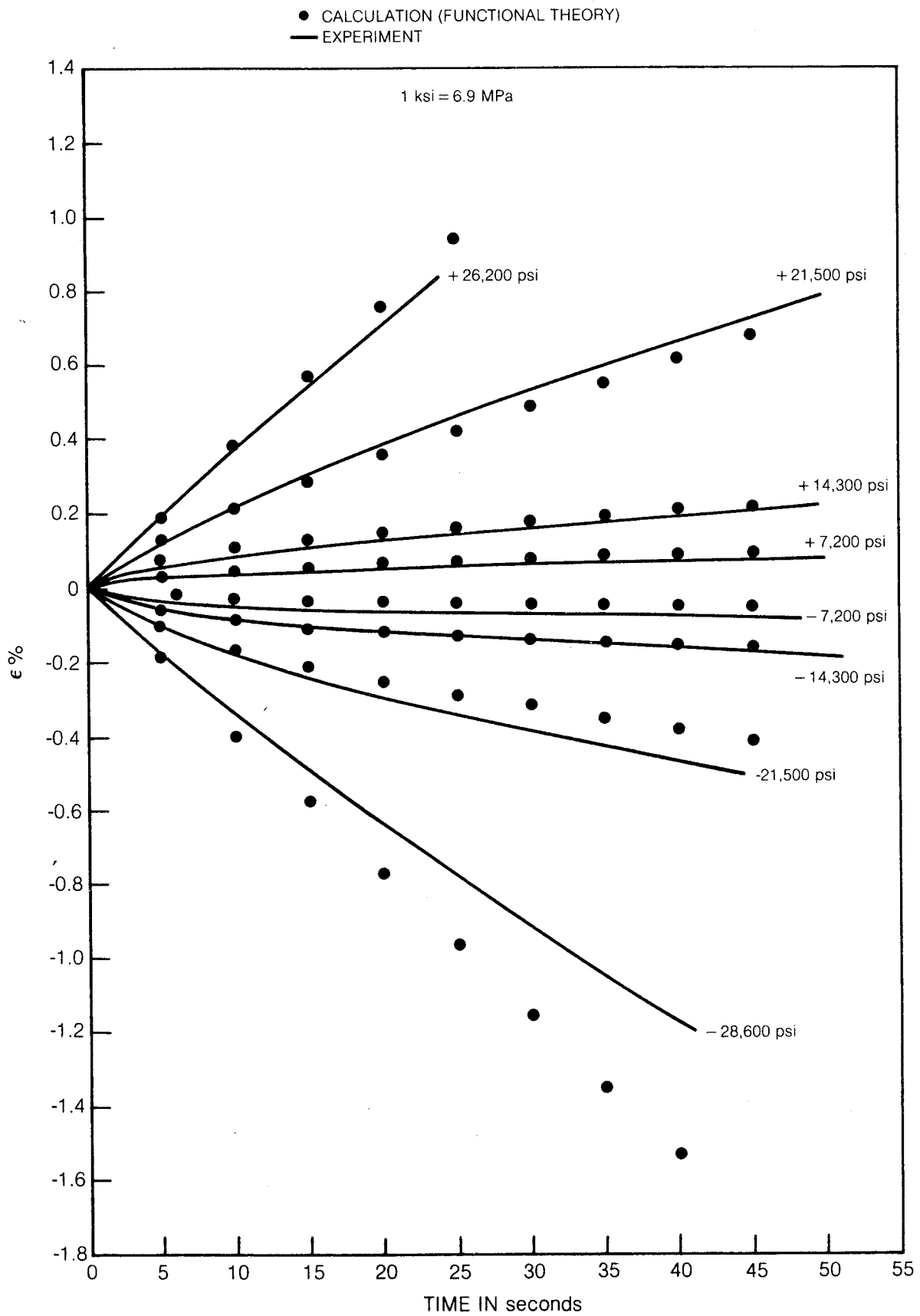
Figure 17. Creep Response of Hastelloy-X at 1600°F

80—11—72—1
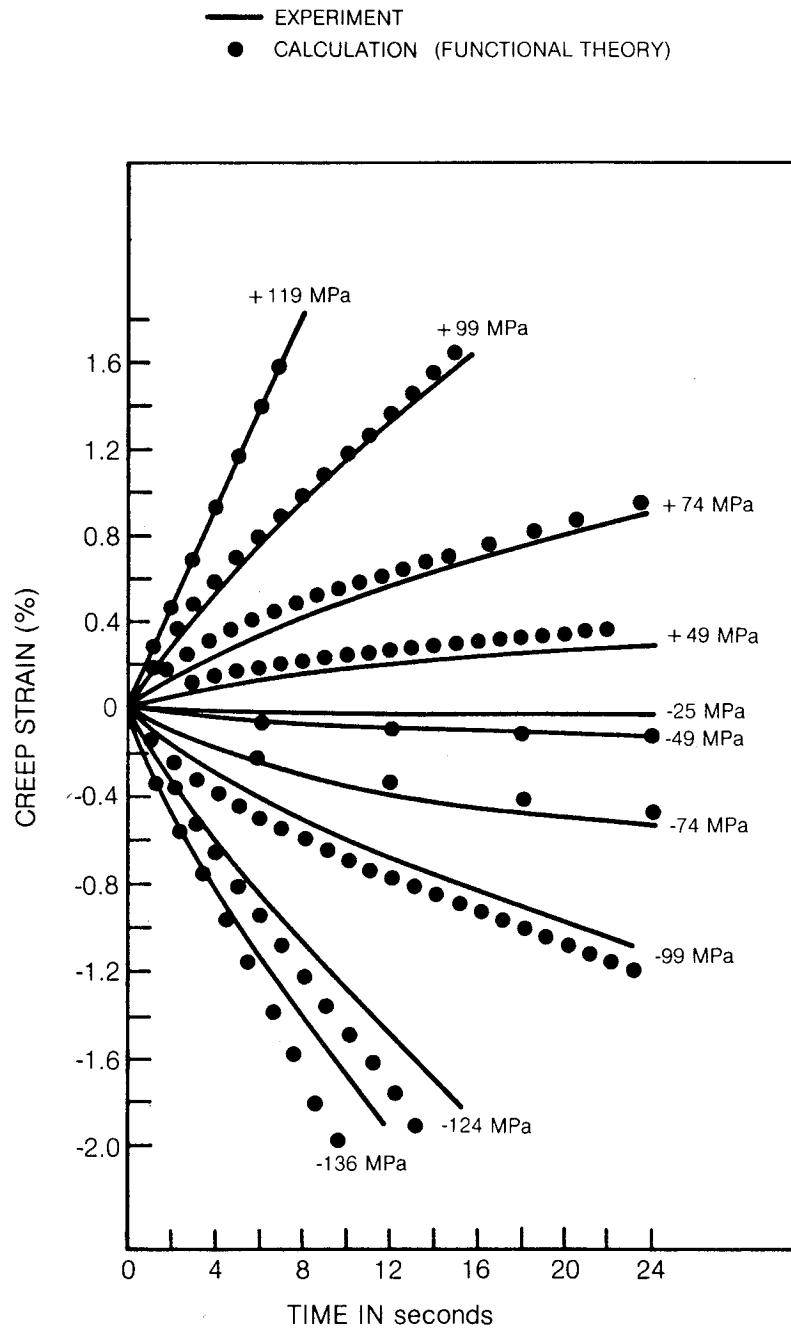
Figure 18. Theoretical and Experimental Creep Behavior for Hastelloy-X at 982°C (1800°F) Starting from Various Points on the Tensile and Compressive Loading Branches of a Steady State Hysteresis Loop Executed at a Strain Rate of 3.66×10^{-4} sec^{-1} at ±0.6% Strain Amplitude
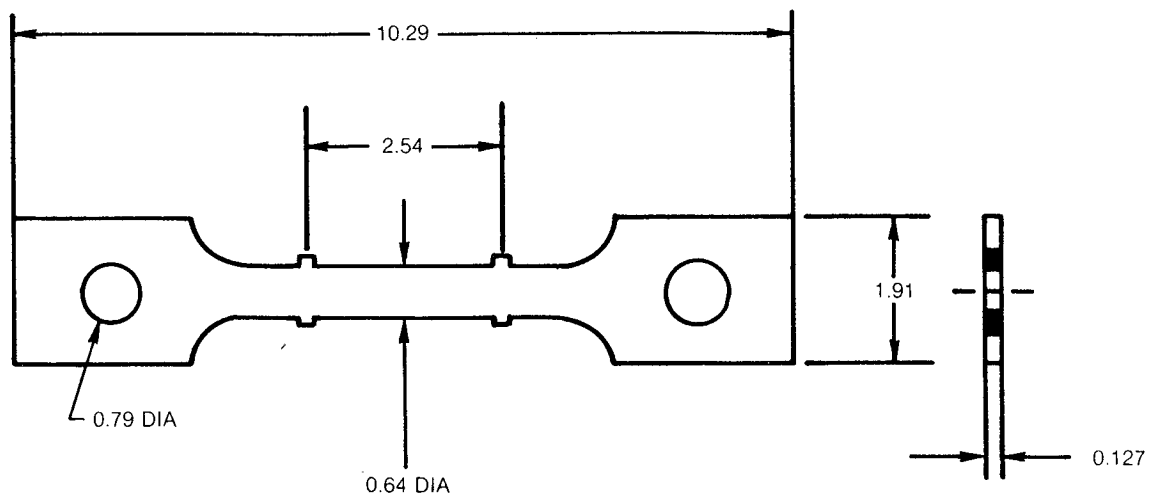
Figure 19. Standard Tensile and Creep Sheet Specimen (Units in cm)
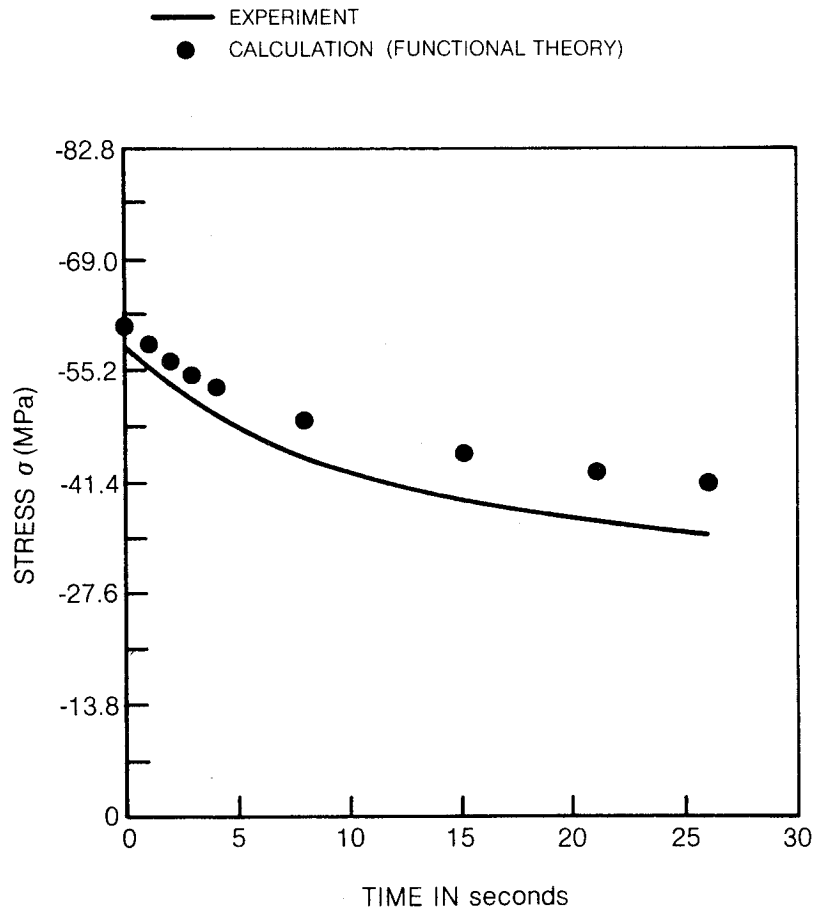
Figure 20. Theoretical and Experimental Relaxation Behavior for Hastelloy-X at 982°C (1800°F) Starting at a Zero Strain Value on the Compressive Branch of a Steady State Hysteresis Loop Executed at a Strain Rate of 3.70×10^{-5} sec^{-1} at ±0.6% Strain Amplitude
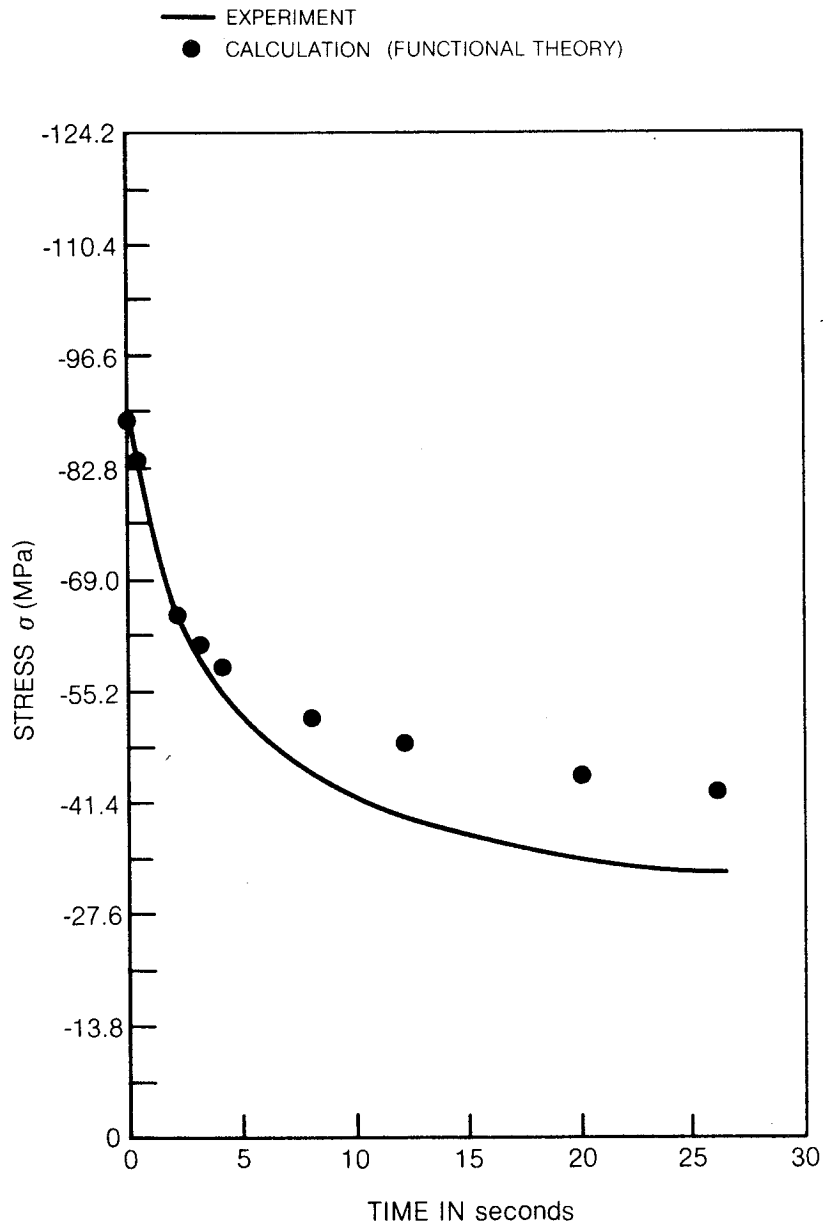
Figure 21. Theoretical and Experimental Relaxation Behavior for Hastelloy-X at 982°C (1800°F) Starting at a Zero Strain Value on the Compressive Branch of a Steady State Hysteresis Loop Executed at a Strain Rate of 3.66 × 10⁻⁴ sec⁻¹ at ±0.6% Strain Amplitude
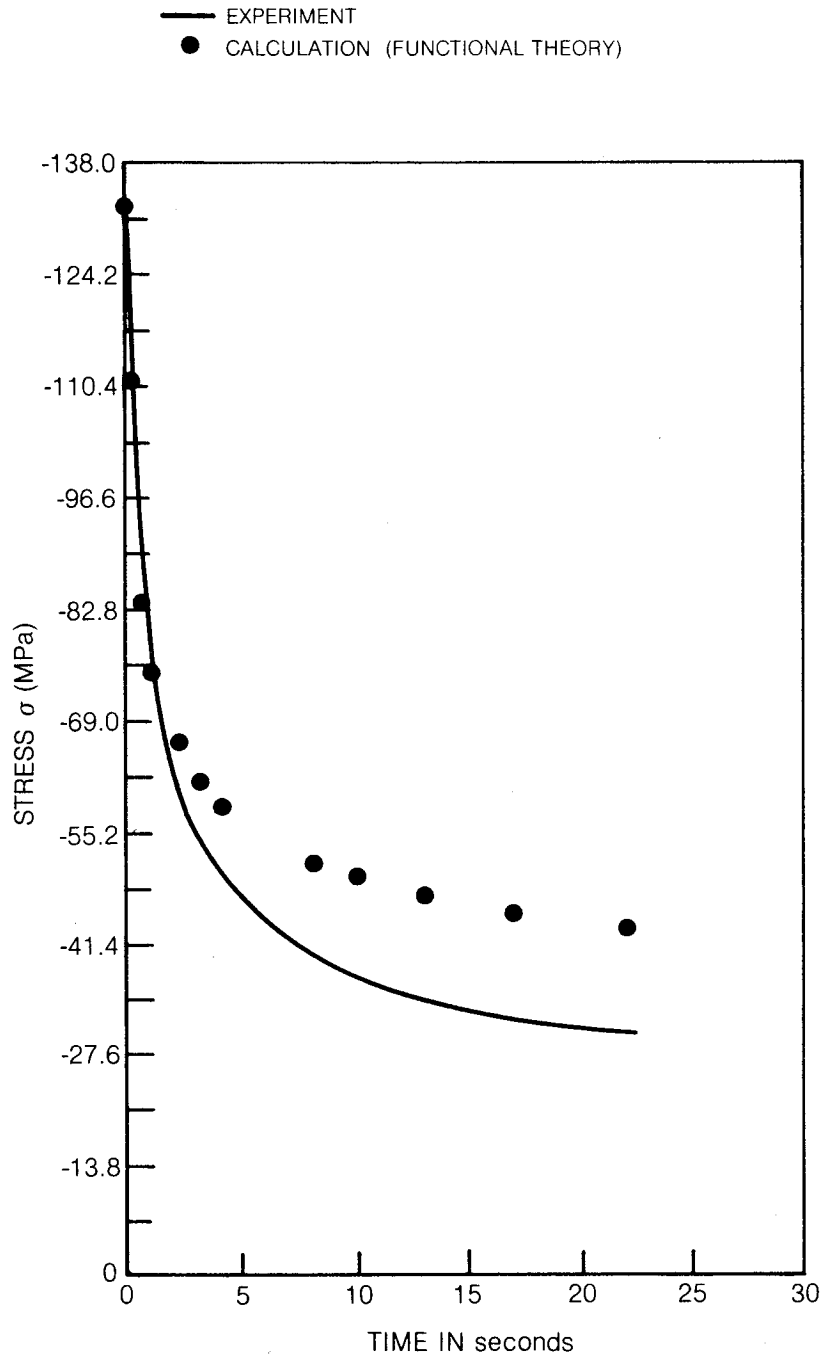
Figure 22. Theoretical and Experimental Relaxation Behavior for Hastelloy-X at 982°C (1800°F) Starting at a Zero Strain Value on the Compressive Branch of a Steady State Hysteresis Loop Executed at a Strain Rate of 3.87×10^{-3} sec^{-1} at ±0.6% Strain Amplitude

80—7—40—3
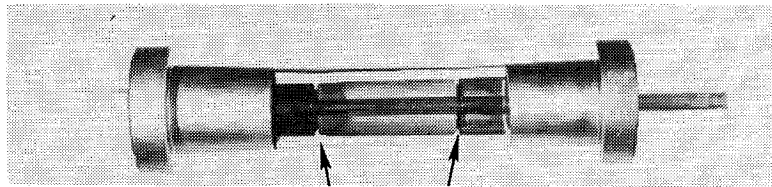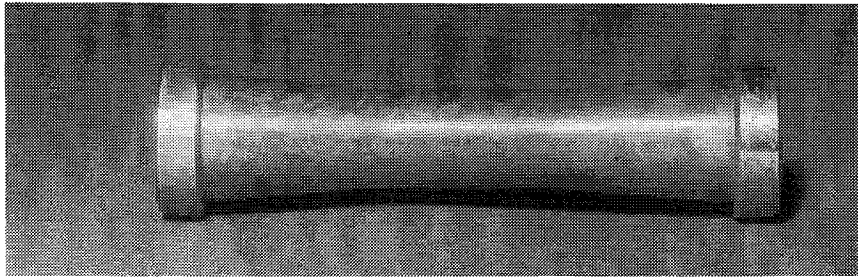
EXTENSOMETRY
RIDGES

Figure 23. Tubular Specimen for Thermomechanical Testing

84

81—9—103—7
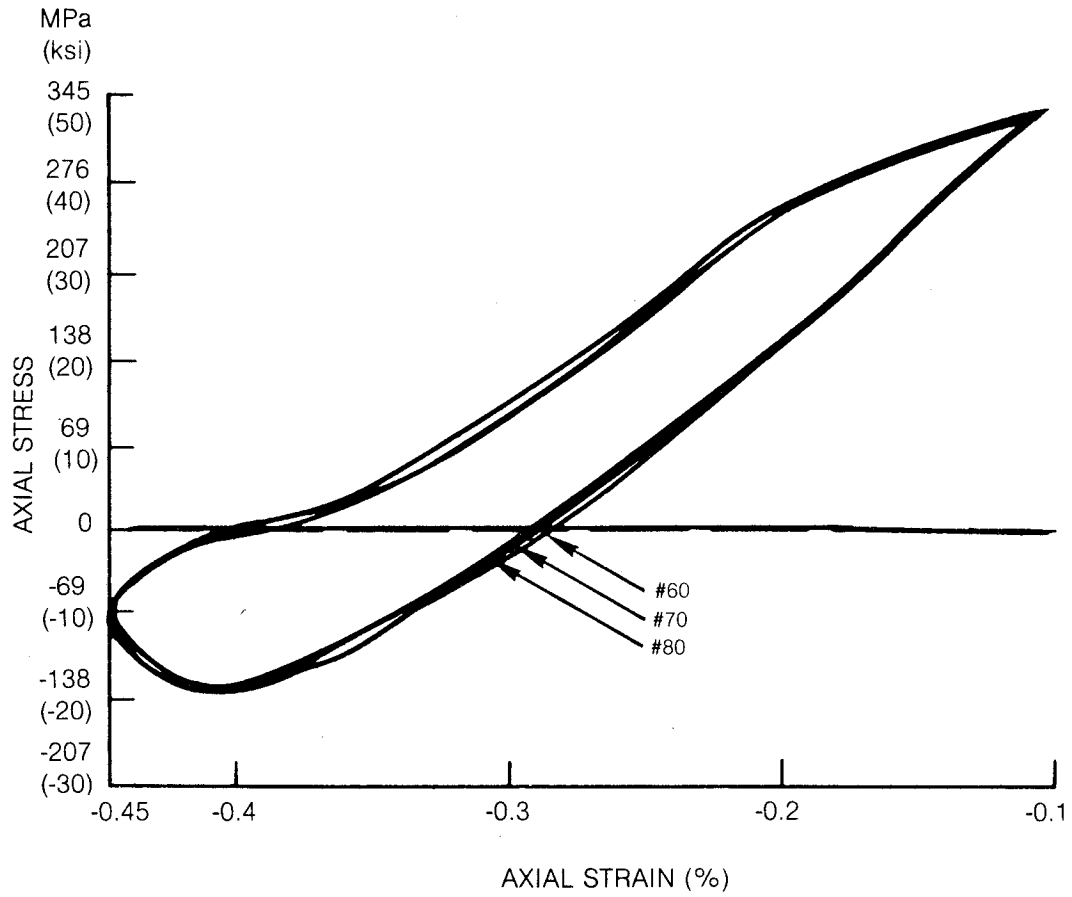
Figure 24. Test Specimen Response at Cycles 60, 70 & 80

81−9−103−1
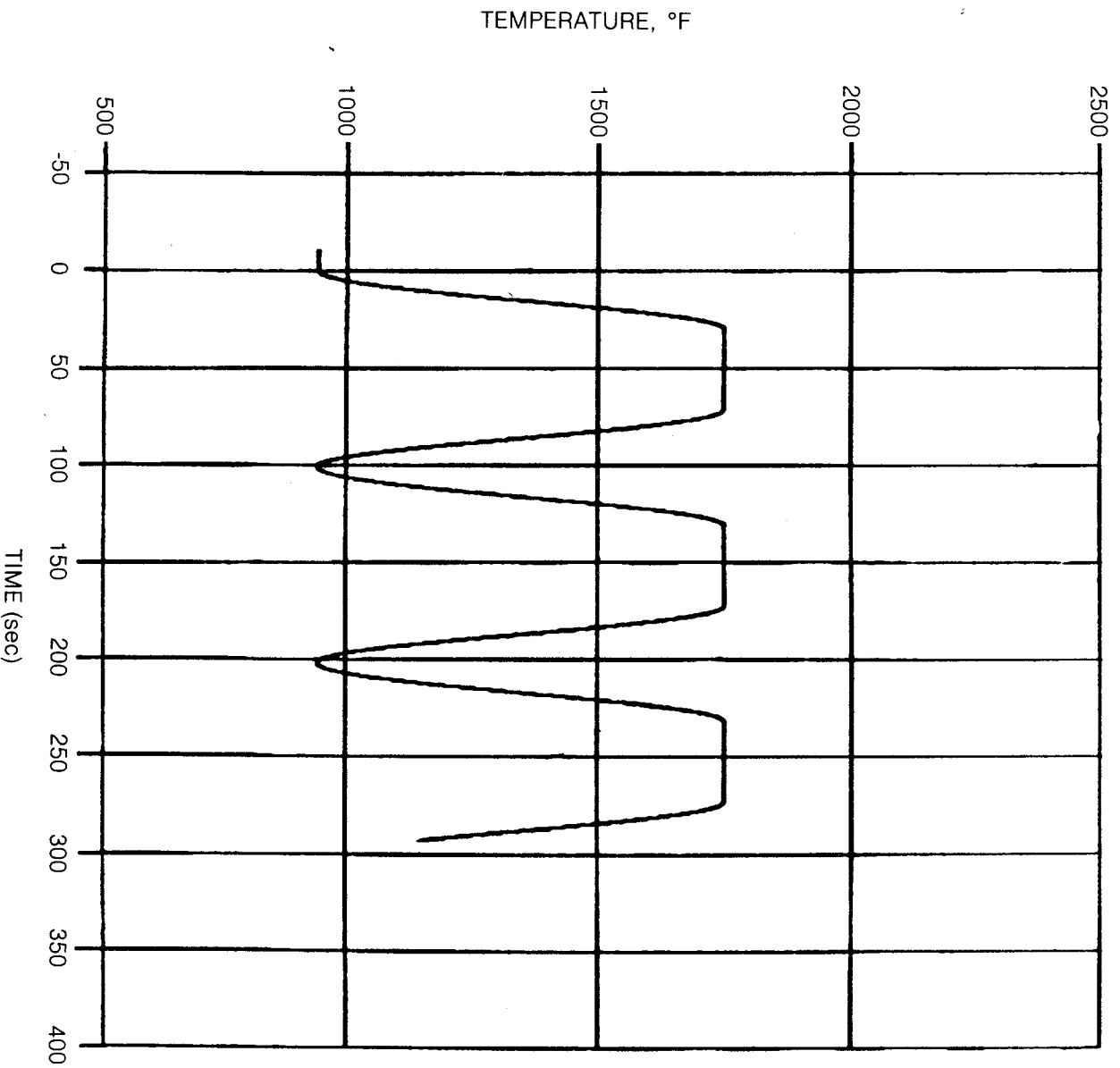
Figure 25. Thermomechanical Temperature History

86

80—11—72—23
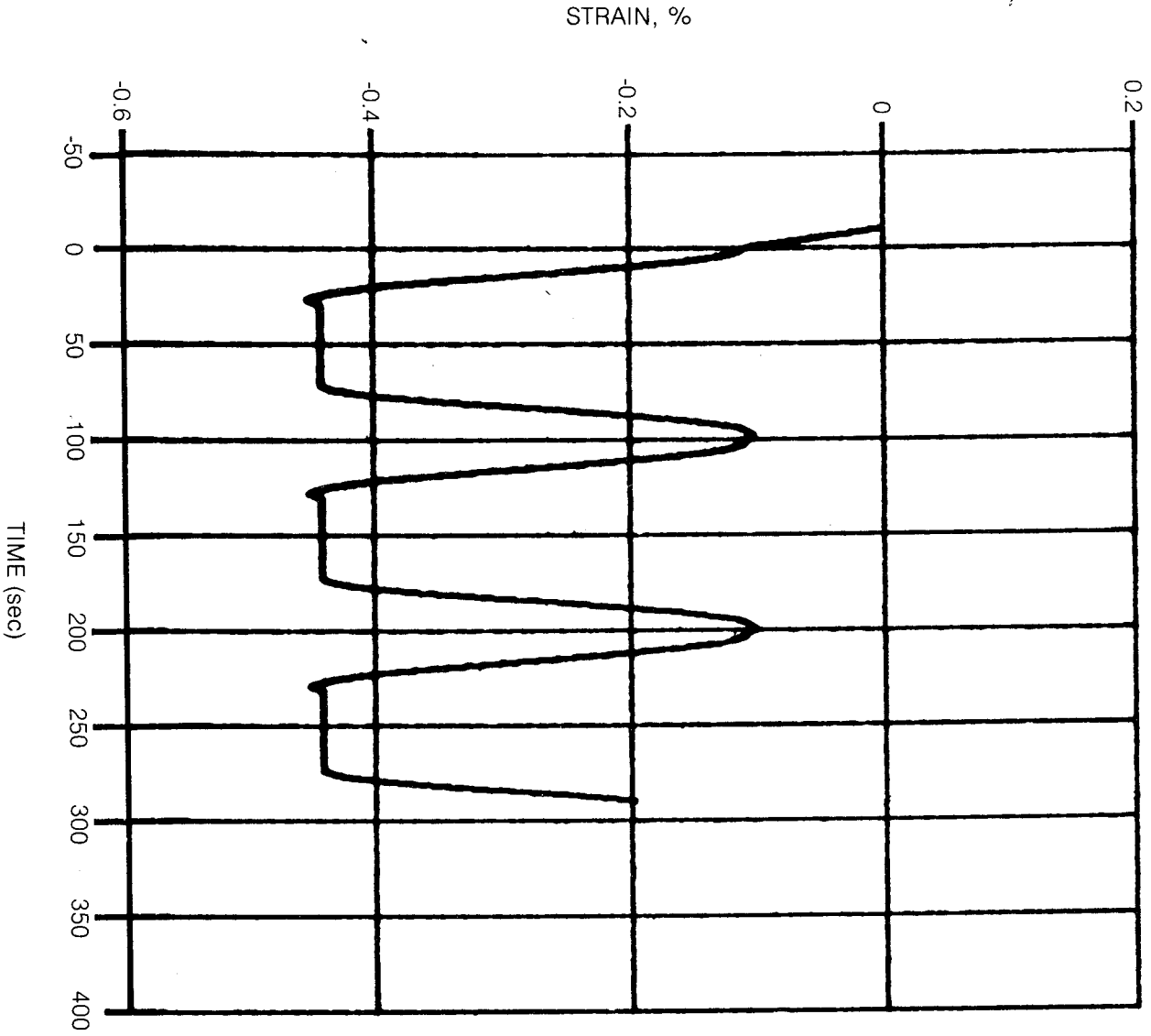
Figure 26. Thermomechanical Strain History
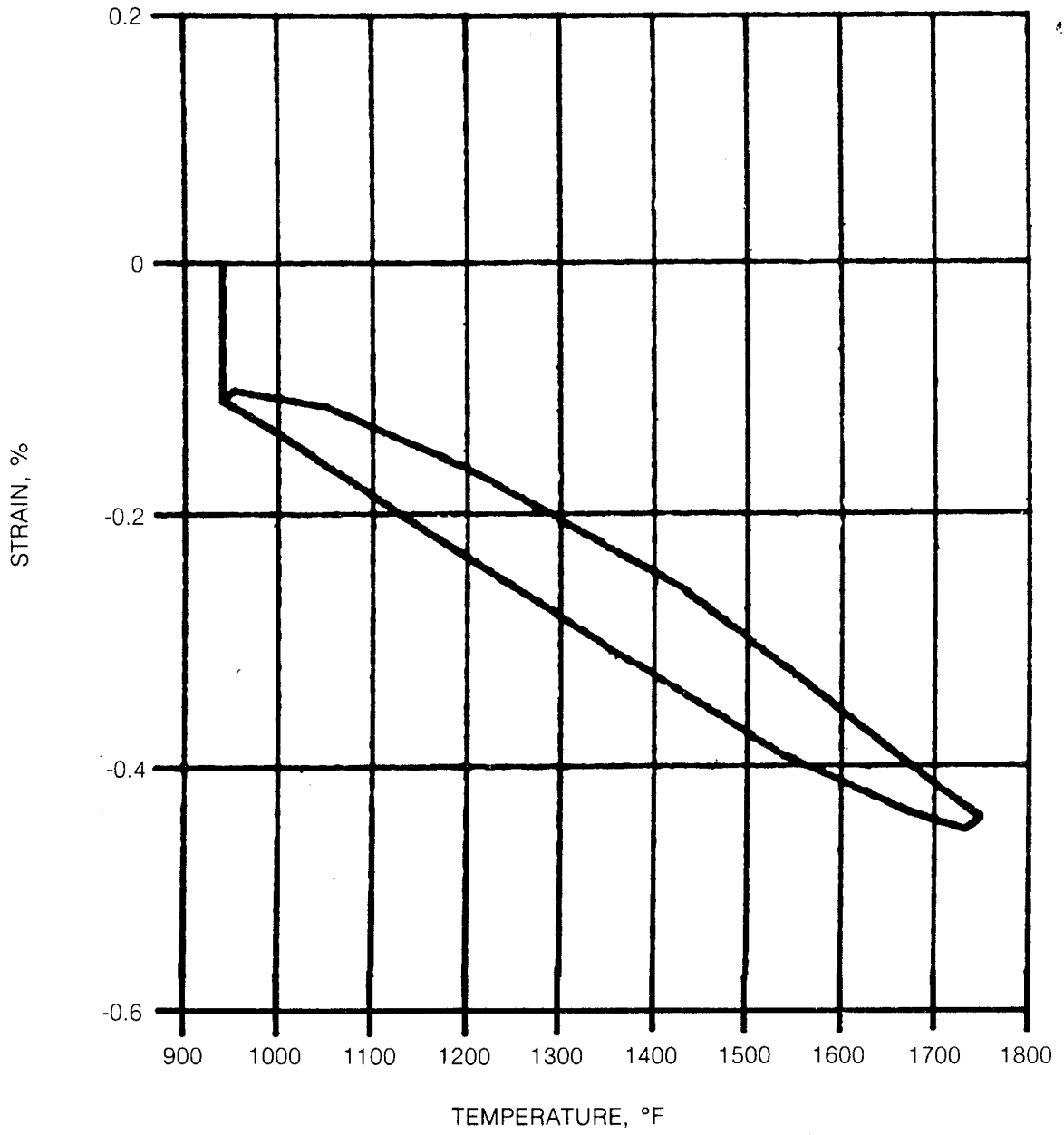
Figure 27. Thermomechanical Strain Temperature History

88
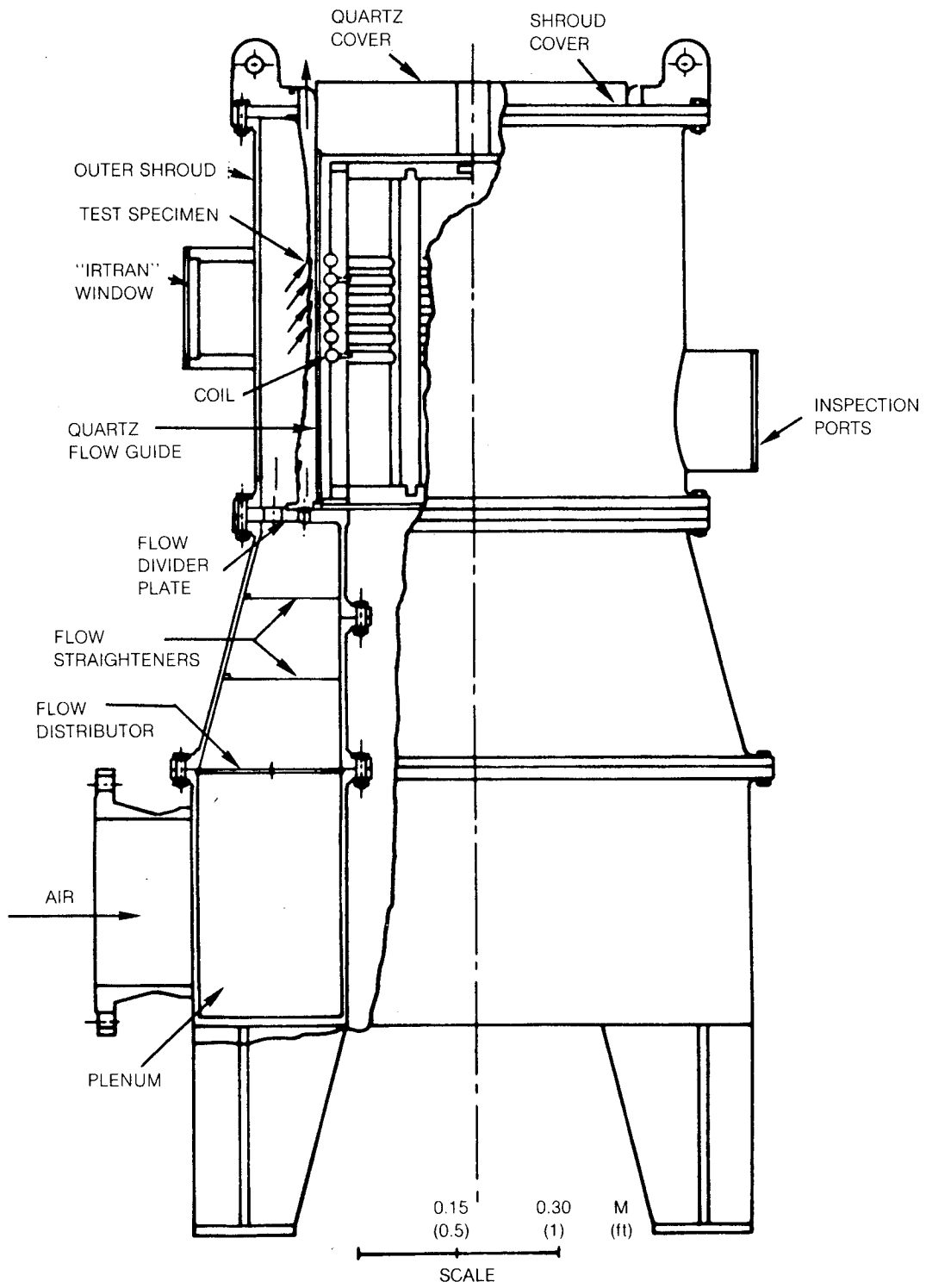
Figure 28. Combustor Liner Induction Heating Test Rig

81−9−103−8

SPECIMEN
$\mathdollar$

REPRESENTATIVE
THERMOCOUPLE
LOCATIONS*

(a)   (b)
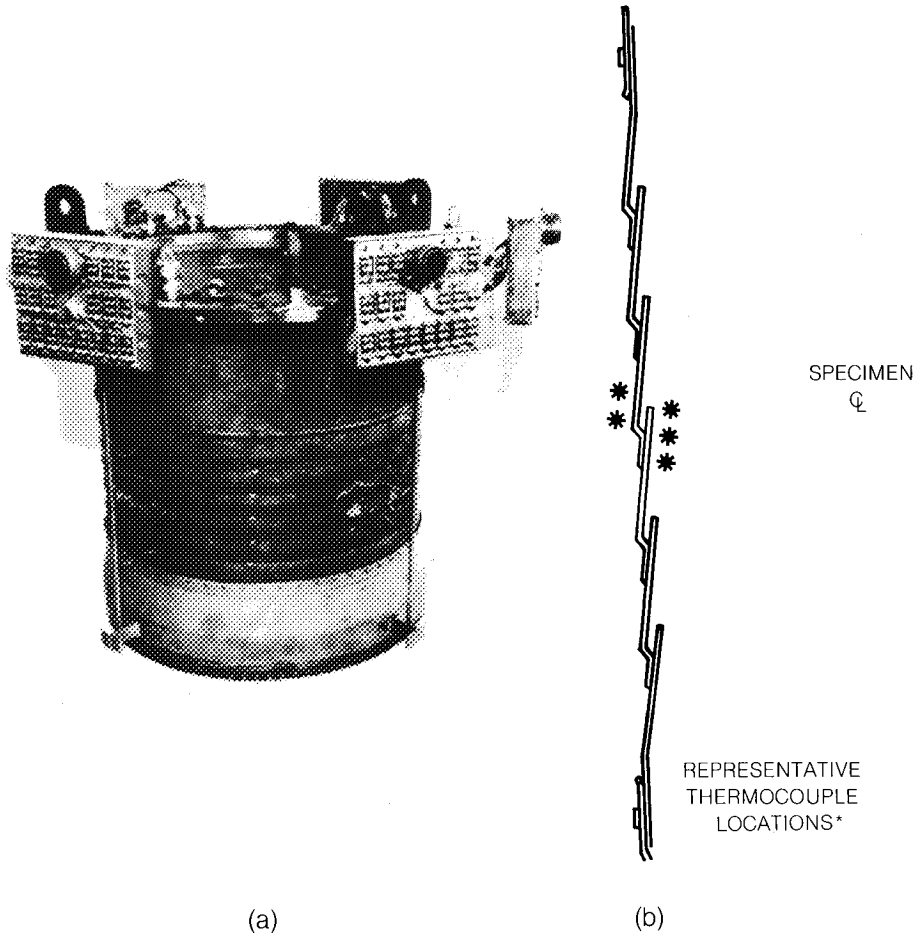
Figure 29. Assembled Liner Test Specimen and Cover (a) and 5-Louver Test Section (b)

81—9—103—15
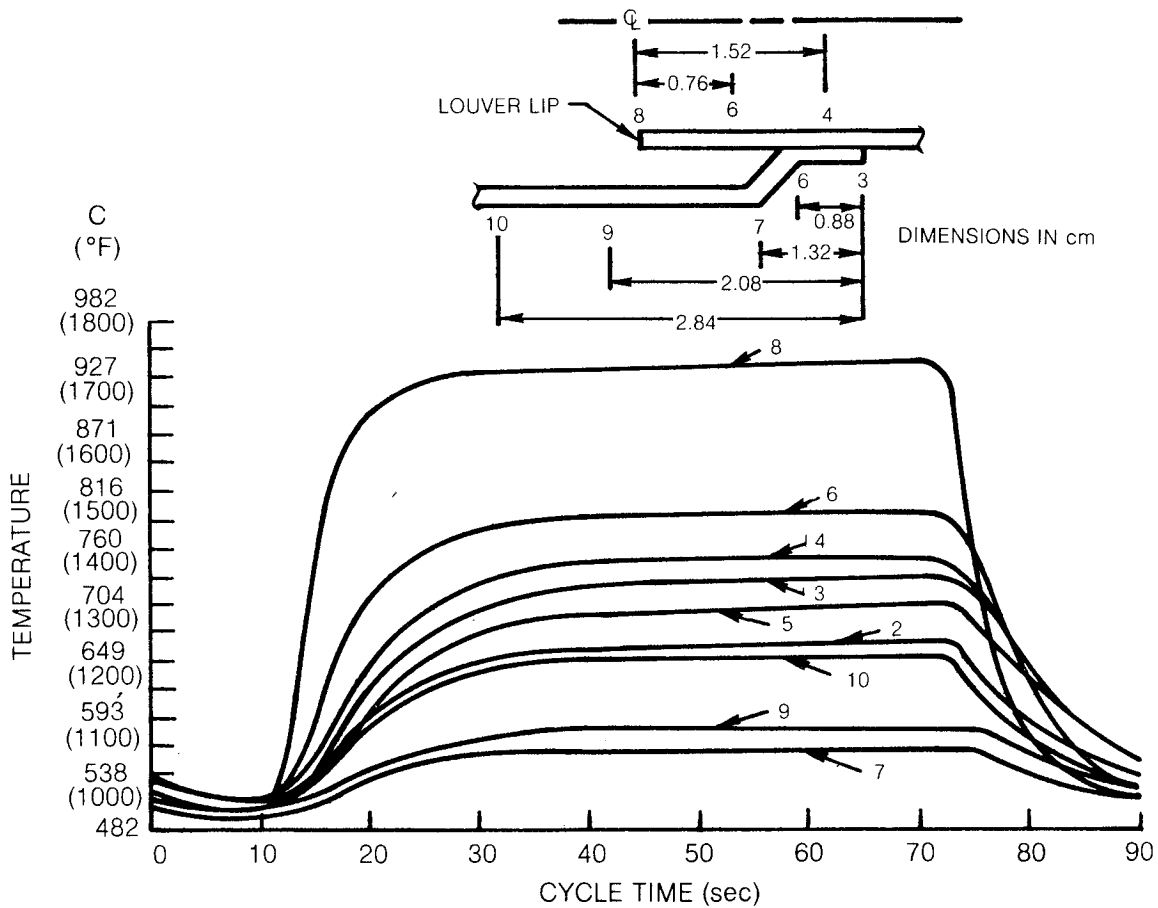
Figure 30. Measured Thermal Response

START INCREMENT n

ASSUME $\Delta\epsilon_i$, FROM INCREMENT n-1.
READ LOAD INCREMENT ΔP_i OR DISPLACEMENT
INCREMENT Δu_i, TEMPERATURE INCREMENT $\Delta\Theta$,
AND TIME INCREMENT Δt FOR INCREMENT n

ENTER SUBROUTINE HYPELA FOR EACH INTEGRATION
POINT IN EACH ELEMENT. INTEGRATE CONSTITUTIVE
THEORY OVER SUBINCREMENTS TO OBTAIN ACCURATE
VALUES OF D_{ij} AND $\Delta\zeta_i$ IN THE CONSTITUTIVE RELATION

$$\Delta\sigma_i = D_{ij}\,(\Delta\epsilon_j - \delta_j\alpha\Delta\Theta) - \Delta\zeta_i$$

WHERE

$$\Delta\zeta_i = \Delta\zeta_i\,(\Delta\epsilon_j)$$

SET $\Delta E = \sum\limits_{i=1}^{6} \sigma_i\Delta\epsilon_i$

AFTER D_{ij}, B_{ij} AND $\Delta\zeta_i$ HAVE BEEN COMPUTED AT EACH INTEGRATION
POINT, CALCULATE THE INTEGRALS

$$K_{ij} = \Sigma\!\!\int_V B_{ik}{}^T D_{kl}B_{lj}dV,$$

$$\Delta P_i{}^* = \Sigma\int_V B_{ij}{}^T\,(\Delta\zeta_j + \delta_j\alpha\Delta\Theta)\,dV$$

$$\Delta R_i = P_i - \Sigma\!\!\int_V B_{ij}{}^T\sigma_j\,dV$$

AND SOLVE THE EQUILIBRIUM EQUATIONS

$$K_{ij}\Delta u_j = \Delta P_i + \Delta P_i{}^* + \Delta R_i$$

CALCULATE $\Delta\epsilon_i = B_{ij}\Delta u_j$

CONVERGED?

$$\left|\frac{\sum\limits_{i=1}^{b}\sigma_i\Delta\epsilon_i - \Delta E}{\Delta E}\right| < \text{TOLERANCE}$$

NO

MAXIMUM NUMBER OF
ITERATIONS EXCEEDED?

NO

YES

ERROR EXIT

YES

UPDATE STRESS, STRAIN, TEMPERATURE
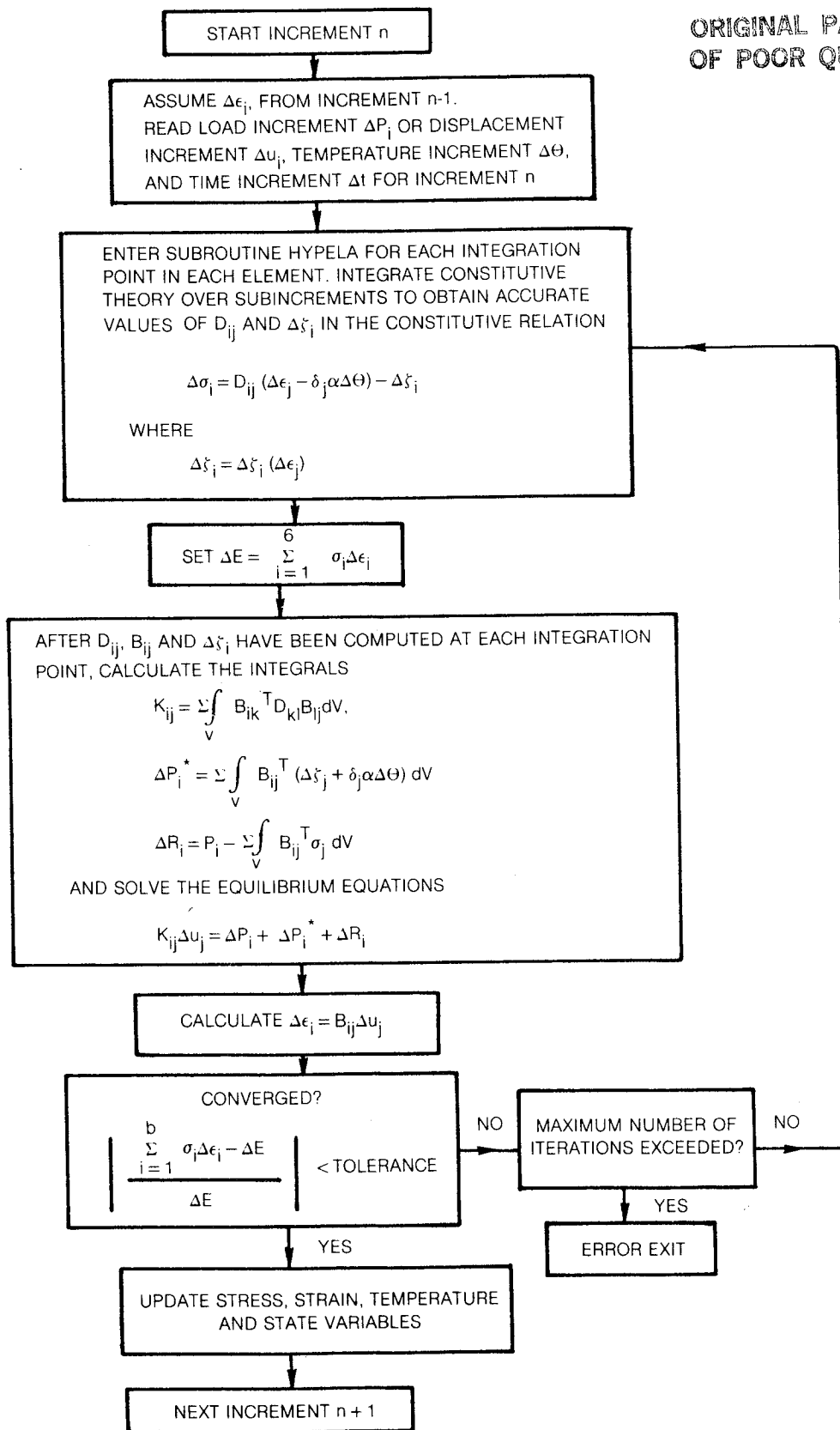AND STATE VARIABLES

NEXT INCREMENT n + 1

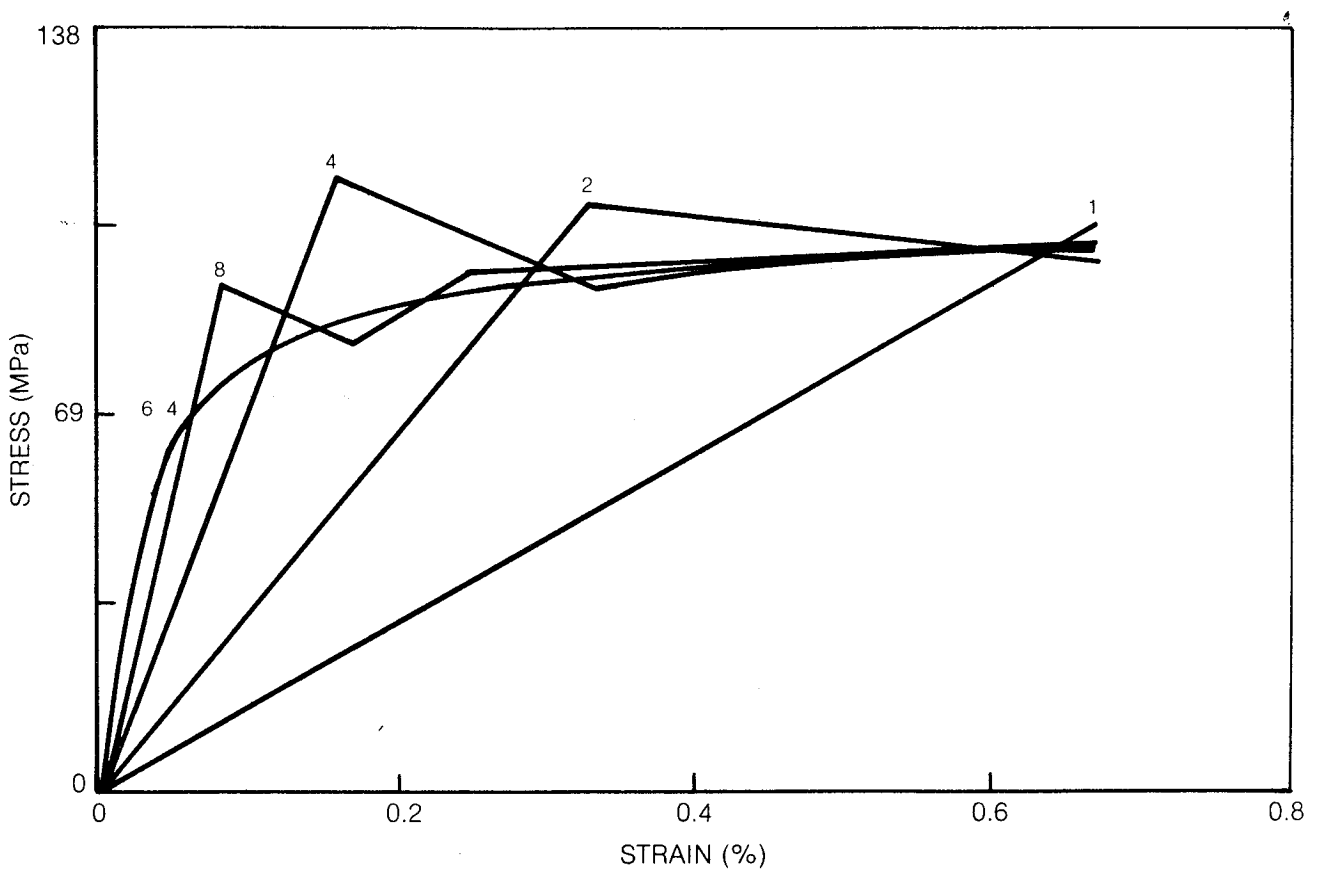**Figure 31. Flow Chart of MARC Iteration Procedure**

81–9–103–9

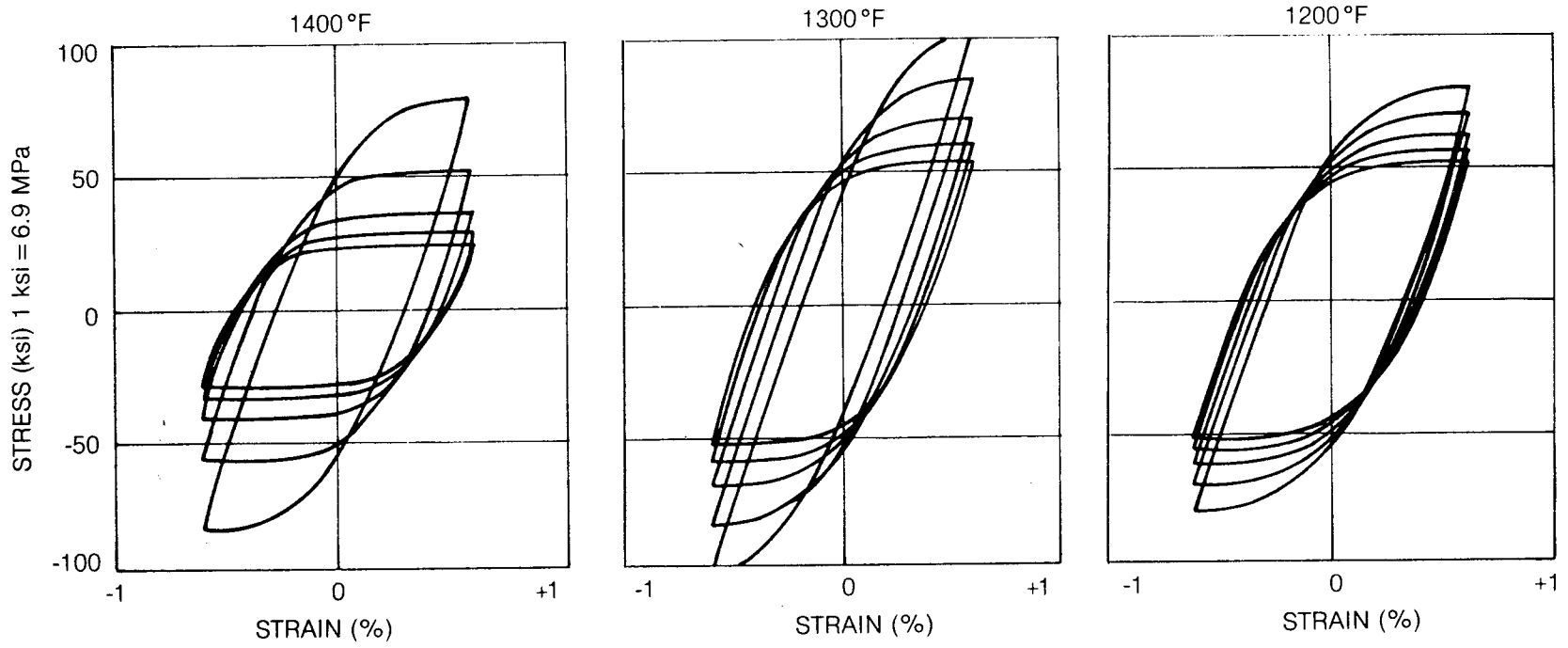Figure 32. Integration Algorithm is Stable and Accurate

Figure 33. Theoretical Hysteresis Loops for Hastelloy-X Predicted with Linearly Interpolated Material Constants
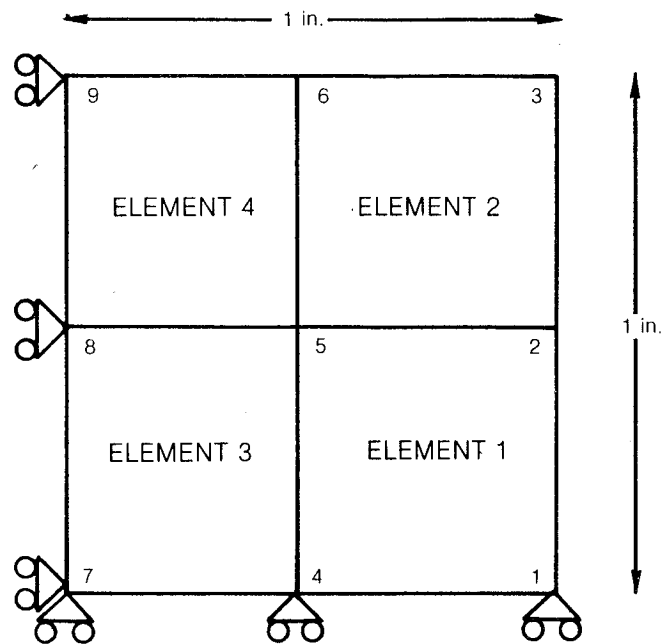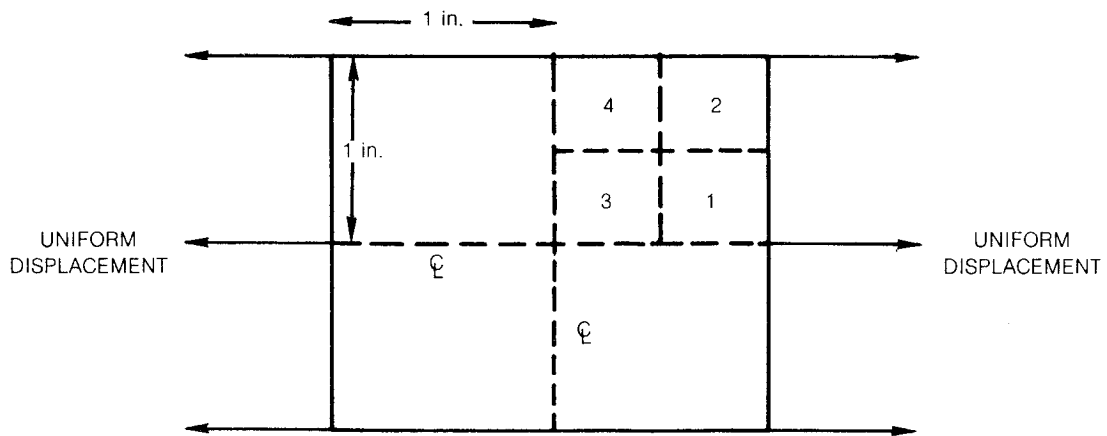
Figure 34. Axisymmetric Finite Element Model Used in the Thermomechanical History Simulation Models One Quarter of the Problem Using Roller Boundary Conditions
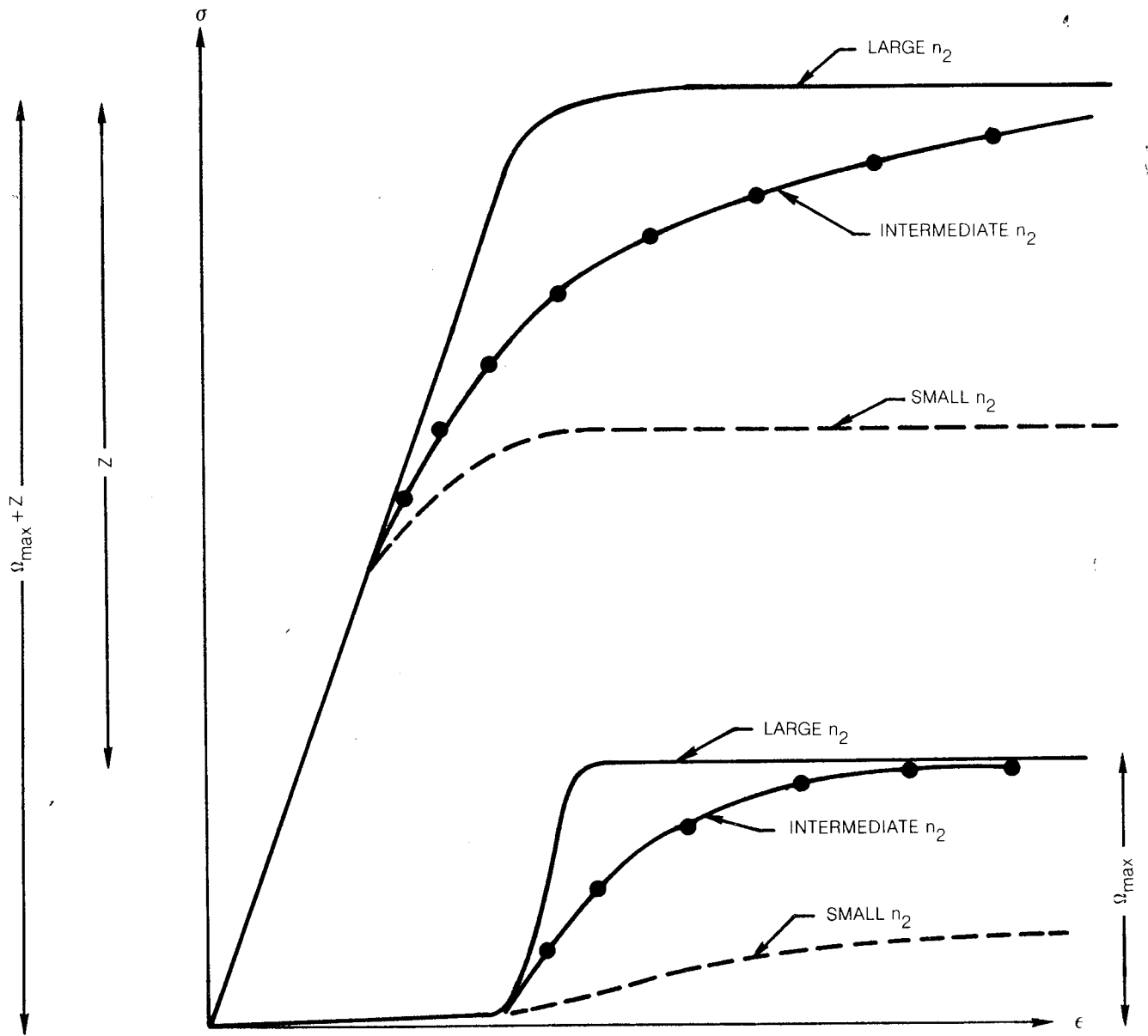
81—9—103—11

95

Figure 35. For Large and Small Work Hardening Rates the Stress-Strain Curves are Relatively "Square". For Intermediate Work Hardening Rates the Stress-Strain Curves are Rounded
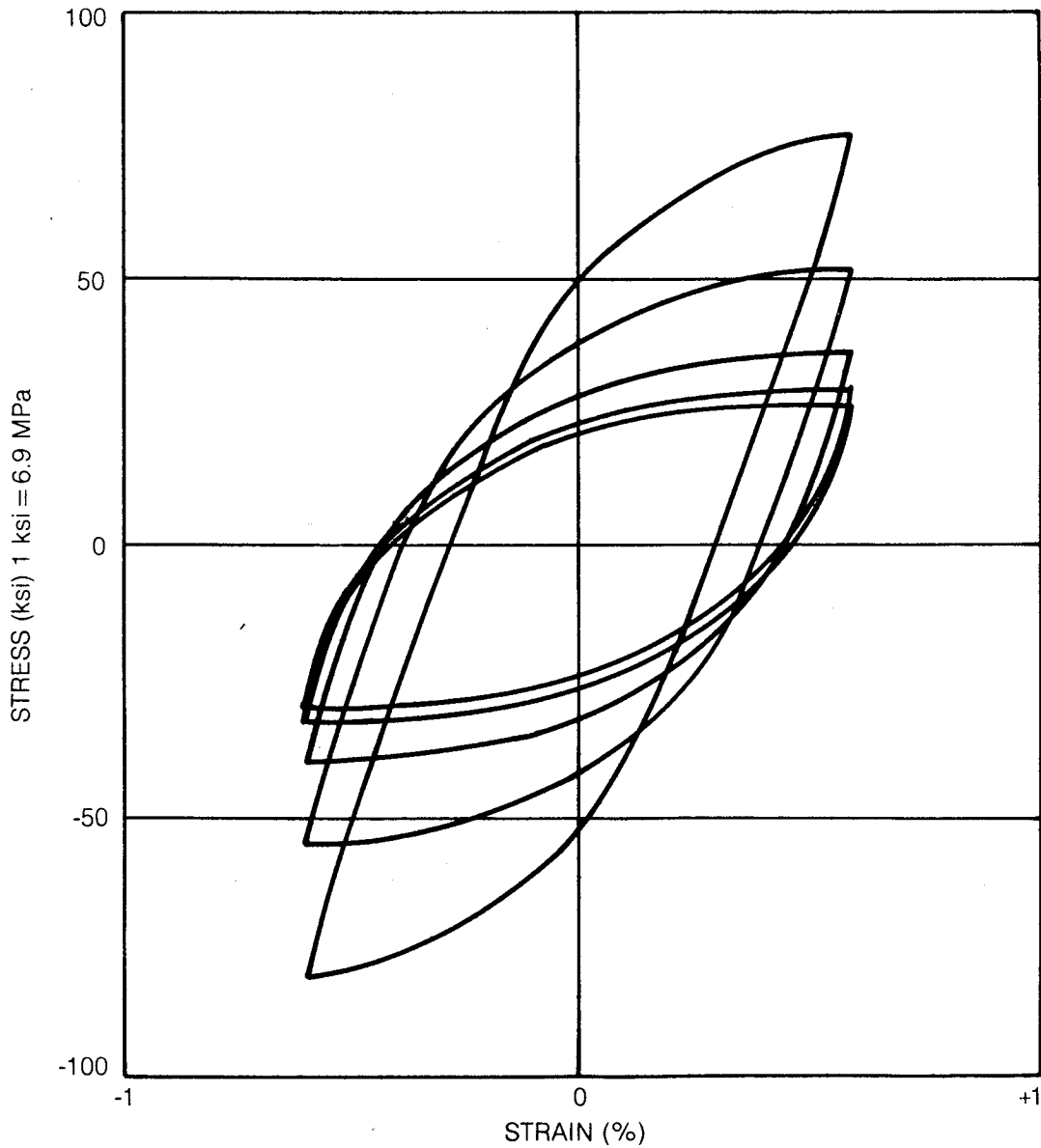
Figure 36. Hysteresis Loops for Hastelloy-X at 760°C (1400°F) Generated with the Functional Theory with $n_2 = 0.8 \times 10^7$
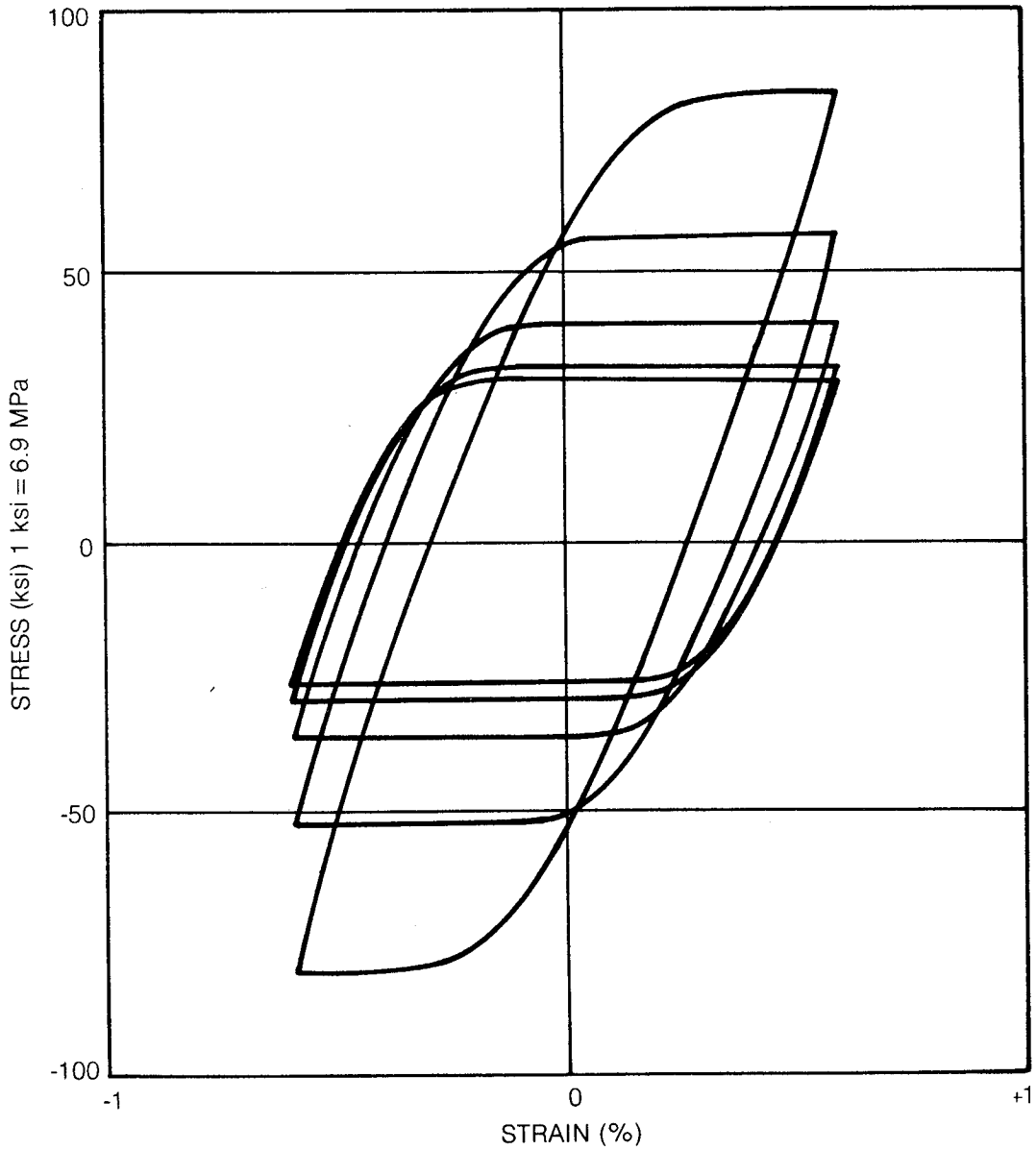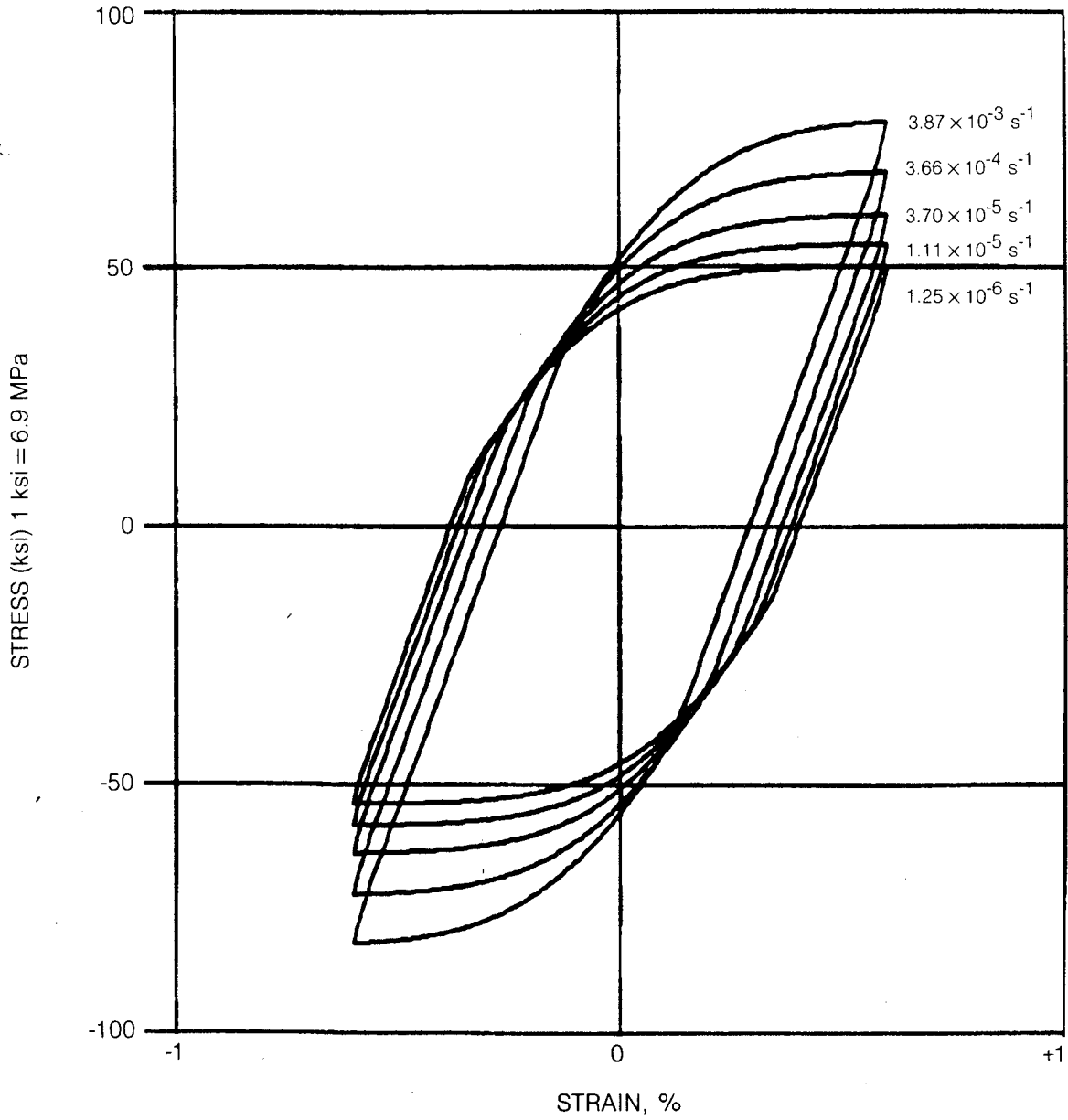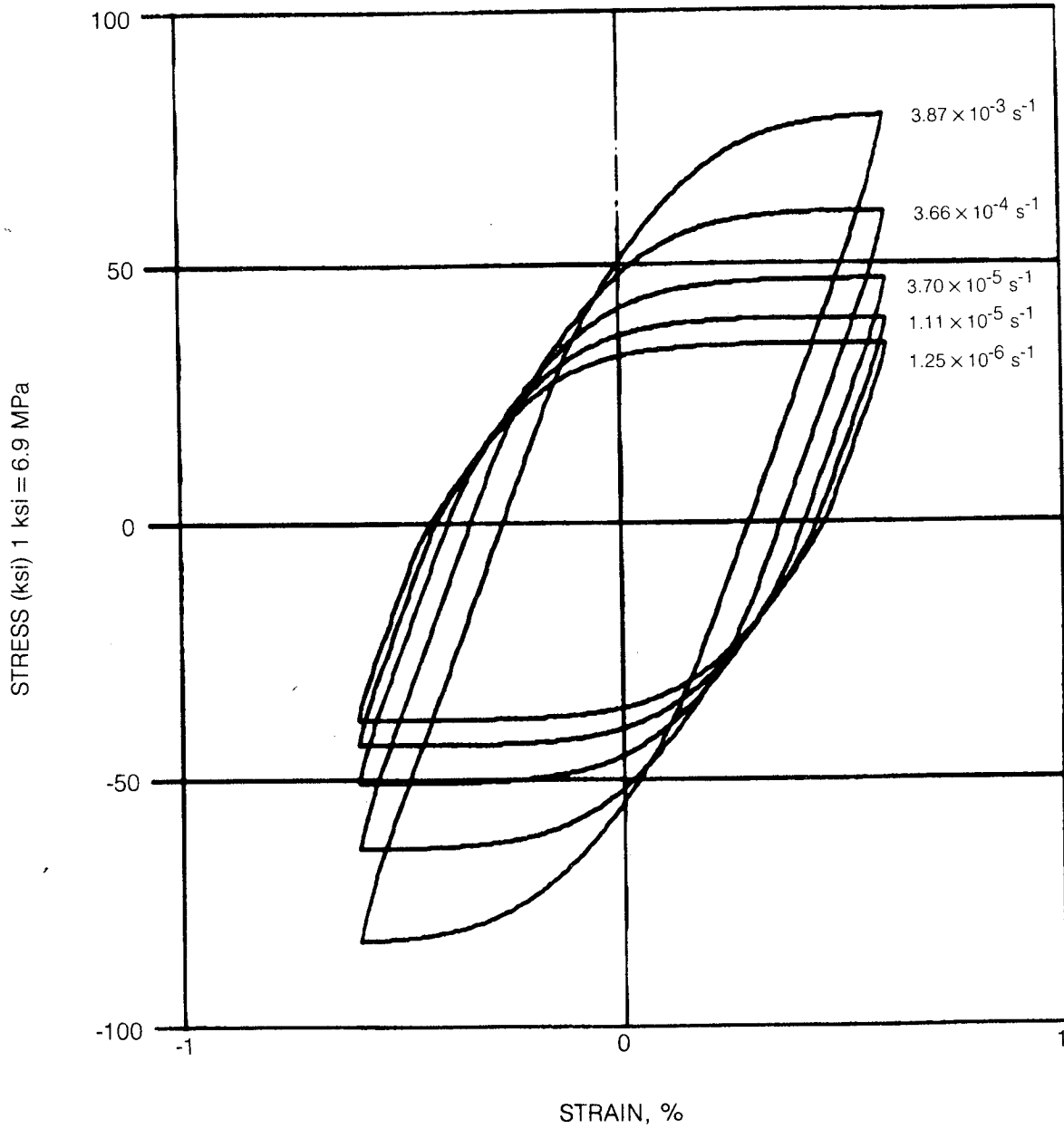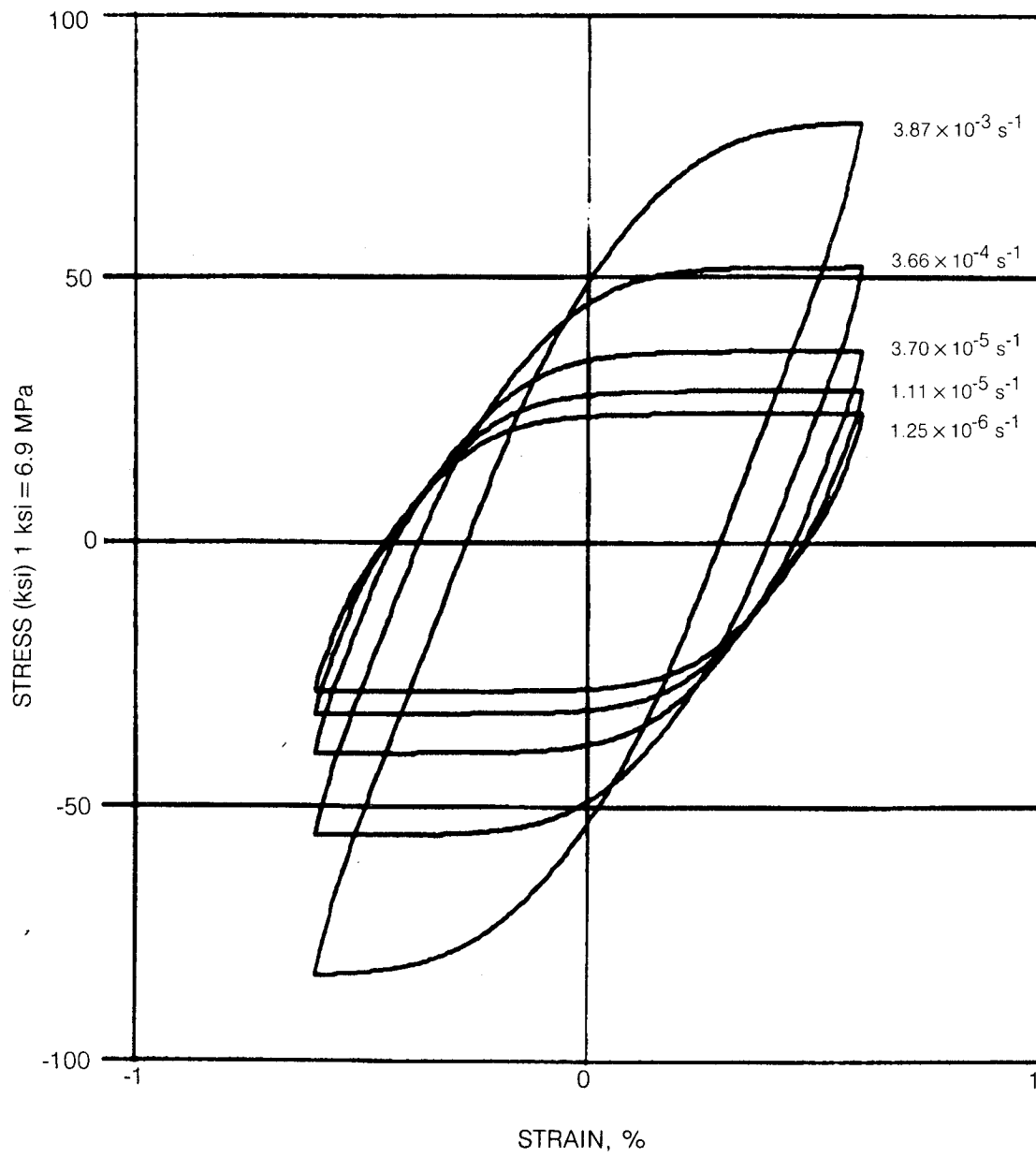
Figure 37. Hysteresis Loops for Hastelloy-X at 760°C (1400°F) Generated
by the Functional Theory   with $n_2 = 5.0 \times 10^7$

Figure 38. Theoretical Hysteresis Loops at 649°C (1200°F)
Generated with Functional Theory

80—11—72—6

Figure 39. Theoretical Hysteresis Loops at 704 °C (1300 °F)
Generated with Functional Theory

Figure 40. Theoretical Hysteresis Loops at 760 °C (1400 °F)
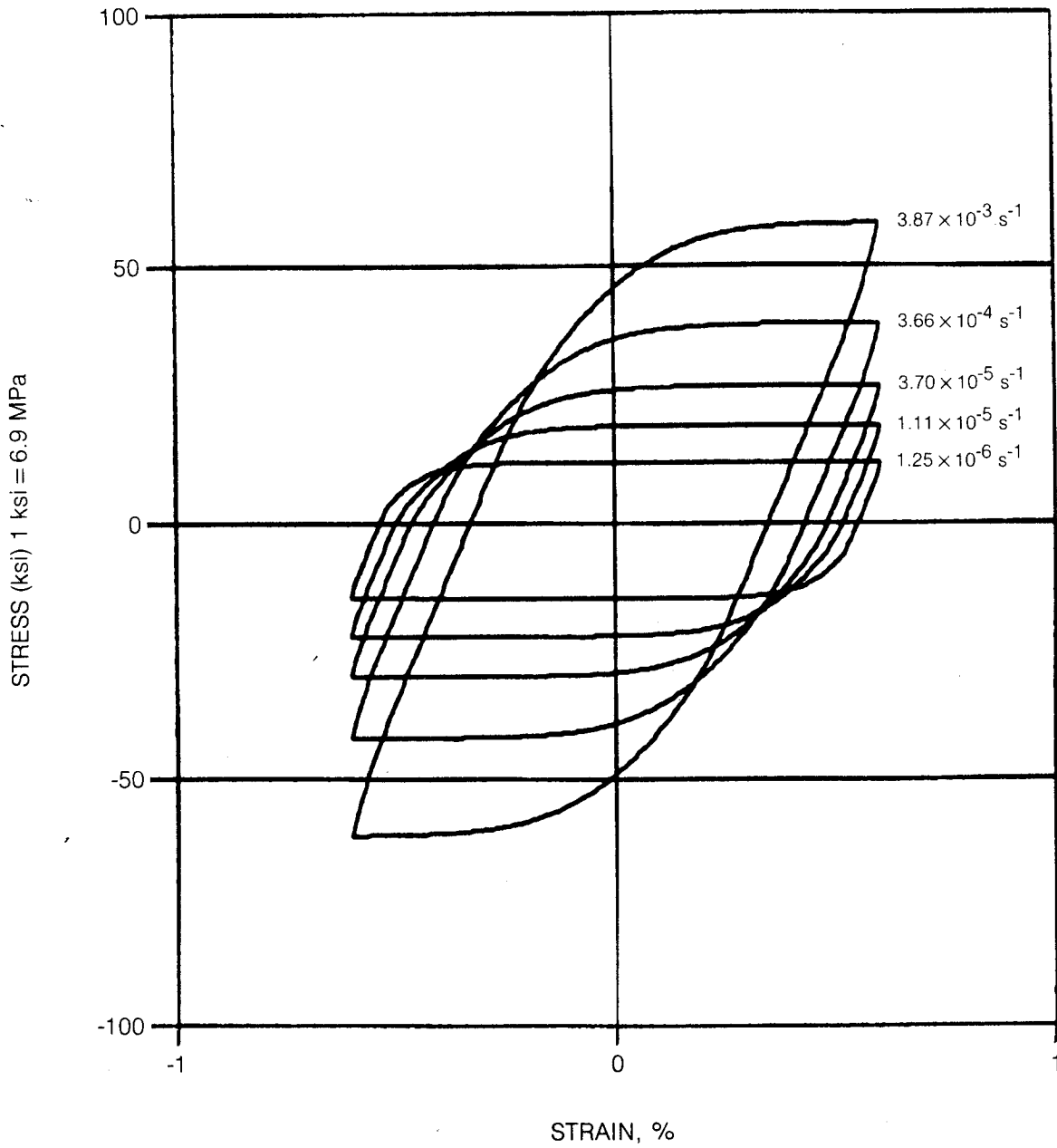Generated with Functional Theory

Figure 41. Theoretical Hysteresis Loops at 816°C (1500°F) Generated with Functional Theory
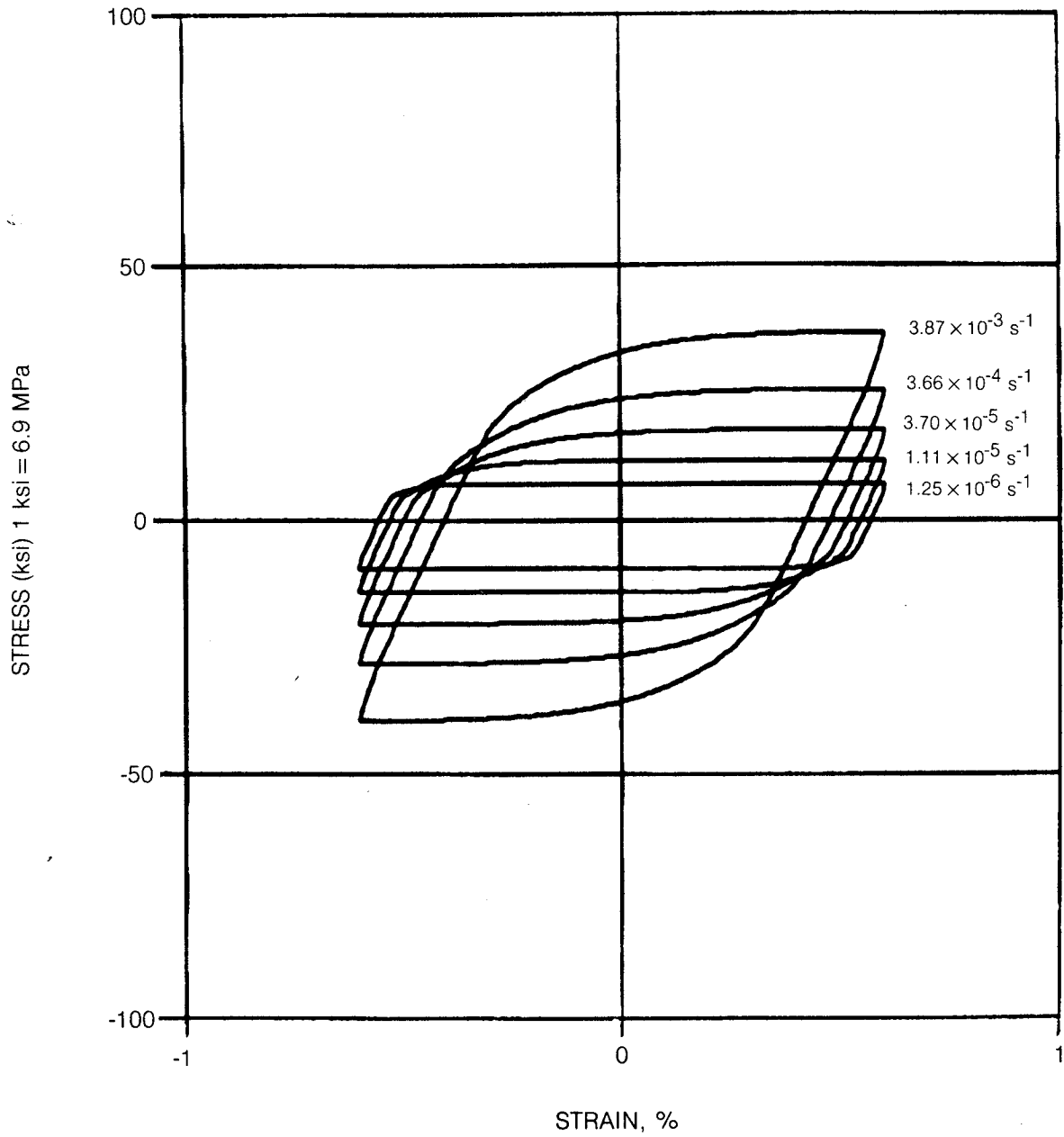
Figure 42. Theoretical Hysteresis Loops at 871°C (1600°F) Generated with Functional Theory

80—11—72—10

103

Figure 43. Theoretical Hysteresis Loops at 927 °C (1700 °F) Generated with Functional Theory

100

50

STRESS (ksi) 1 ksi = 6.9 MPa

3.87×10^{-3} s^{-1}
3.66×10^{-4} s^{-1}
3.70×10^{-5} s^{-1}
1.11×10^{-5} s^{-1}
1.25×10^{-6} s^{-1}
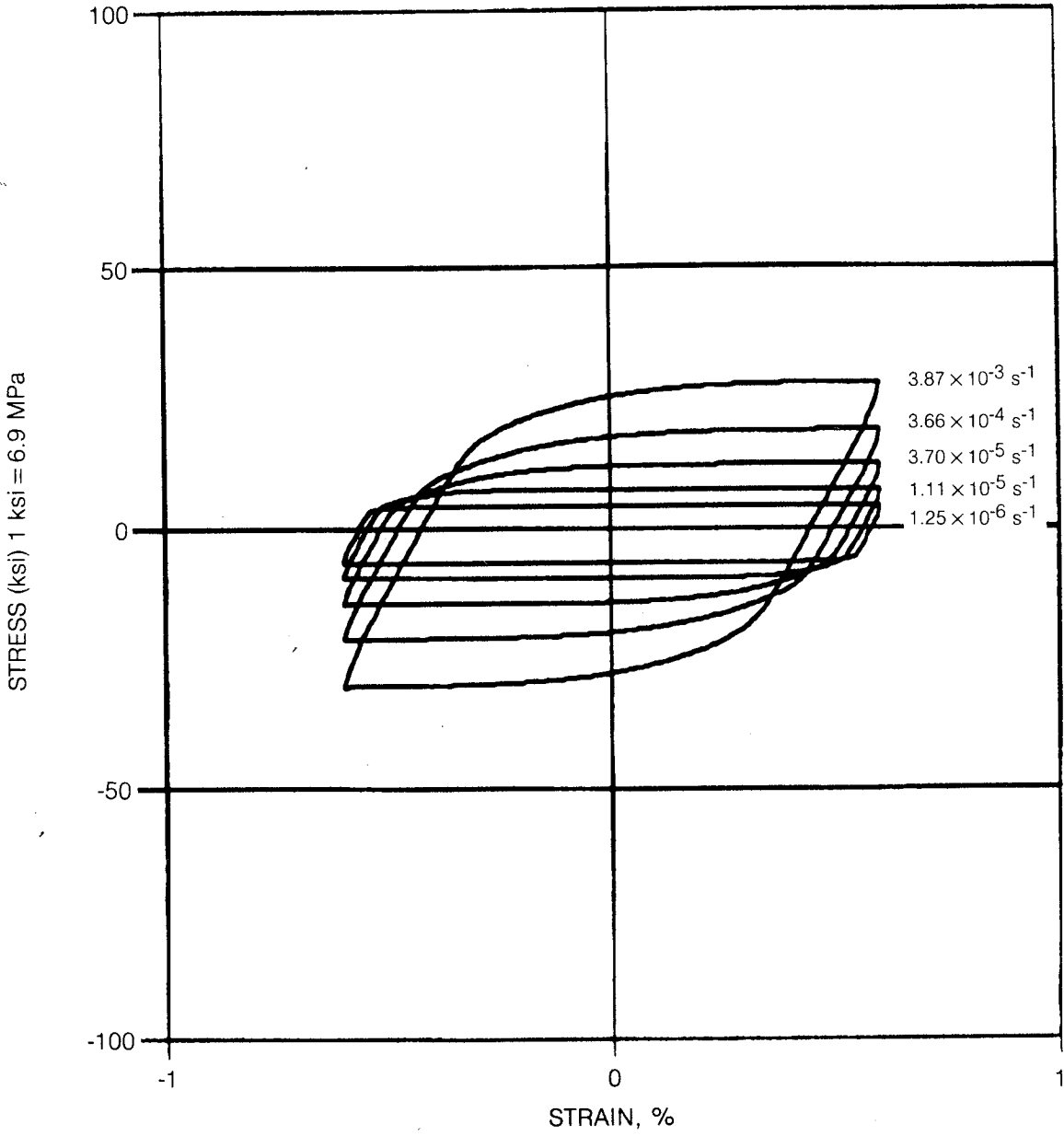
0

-50

-100

-1

0

1

STRAIN, %
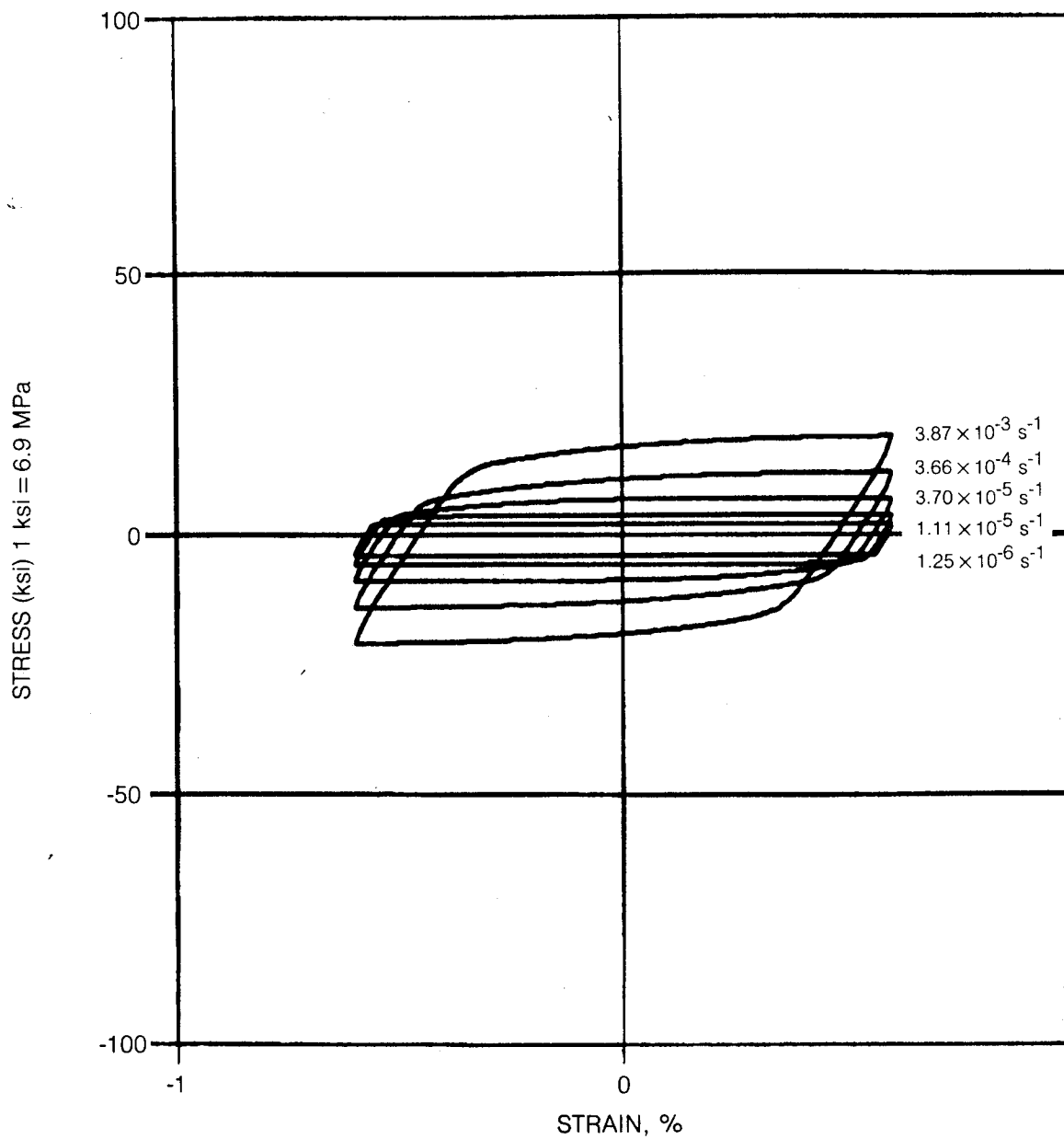
Figure 44. Theoretical Hysteresis Loops at 982°C (1800°F) Generated with Functional Theory

80—11—72—12

105

Figure 45. Theoretical Hysteresis Loops at 649°C (1200°F) Generated
with Krieg, Swearengen & Rohde's Theory

Figure 46. Theoretical Hysteresis Loops at 704°C (1300°F) Generated with Krieg, Swearengen & Rohde's Theory

81—9—103—14

107

Figure 47. Theoretical Hysteresis Loops at 760°C (1400°F) Generated with Krieg, Swearengen & Rohde's Theory

Figure 48. **Theoretical Hysteresis Loops at 816°C (1500°F) Generated with Krieg, Swearengen & Rohde's Theory**

Figure 49. Theoretical Hysteresis Loops at 871°C (1600°F) Generated with Krieg, Swearengen & Rohde's Theory

81−9−103−29

110

Figure 50. Theoretical Hysteresis Loops at 927°C (1700°F) Generated with Krieg, Swearengen & Rohde's Theory

The y-axis is labeled "STRESS (ksi) 1 ksi = 6.9 MPa" with values 100, 50, 0, -50, -100. The x-axis is labeled "STRAIN (%)" with values -1, 0, +1. The curves are labeled:

$3.87 \times 10^{-3} \text{ s}^{-1}$
$3.66 \times 10^{-4} \text{ s}^{-1}$
$3.70 \times 10^{-5} \text{ s}^{-1}$
$1.11 \times 10^{-5} \text{ s}^{-1}$
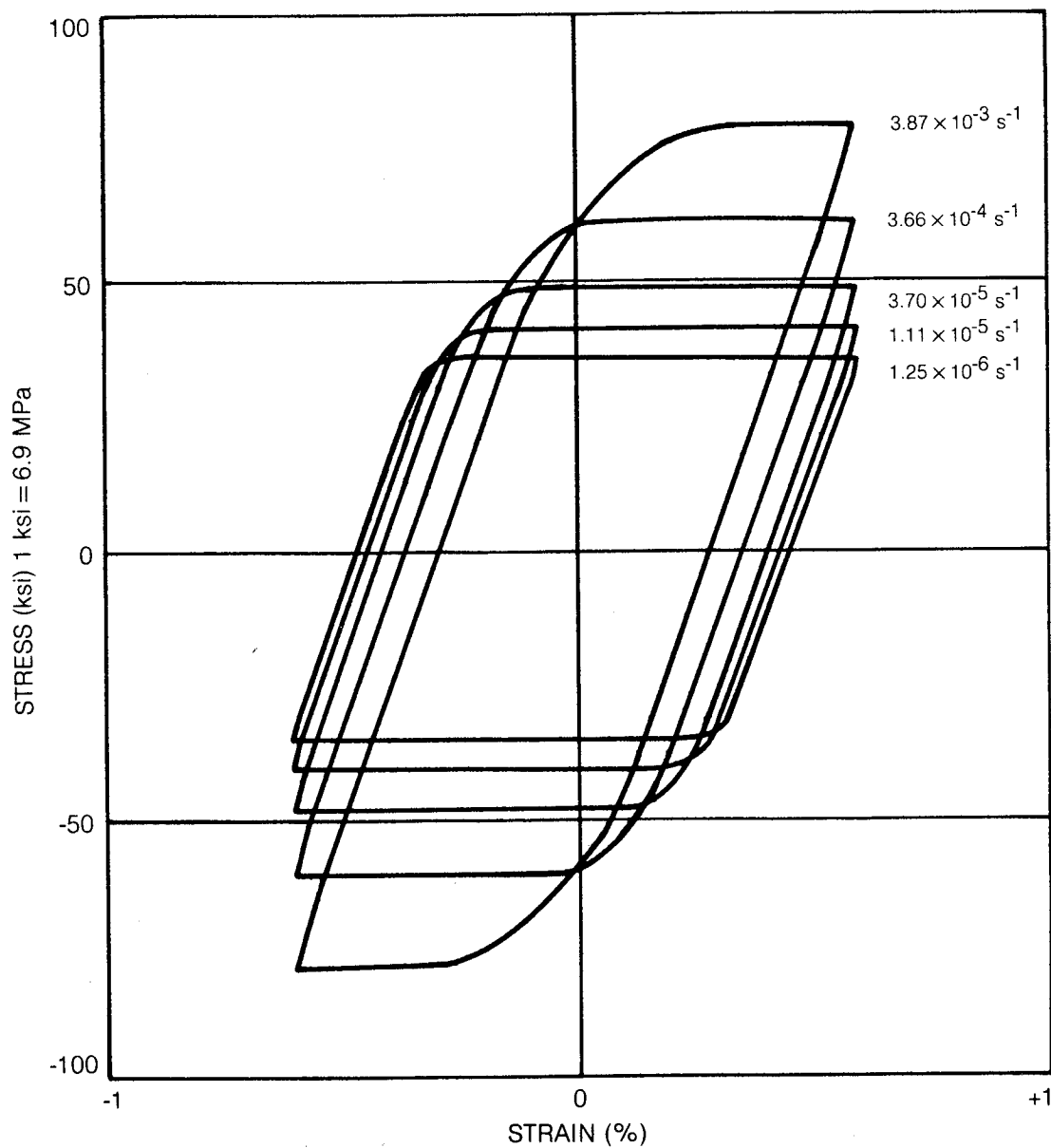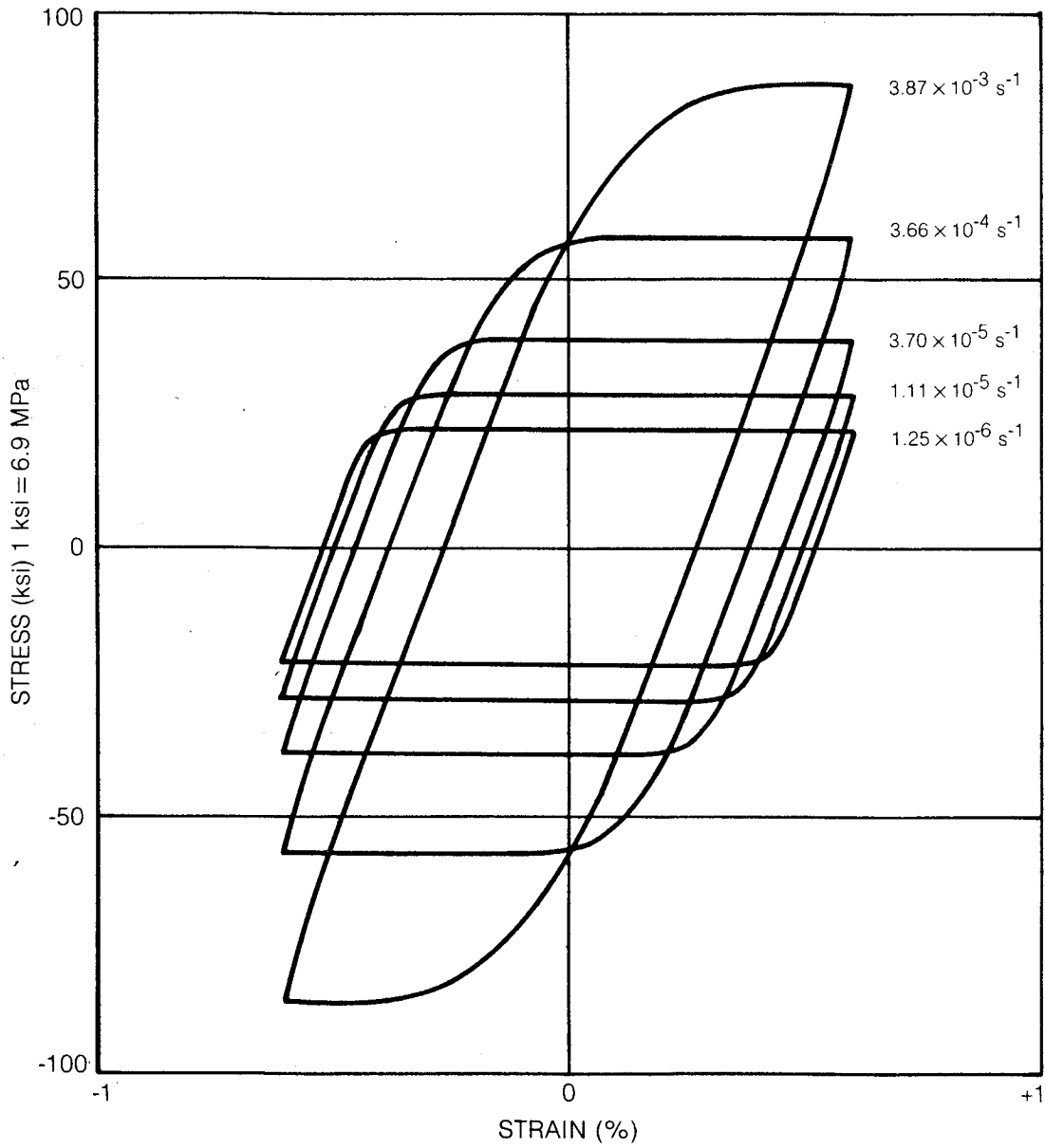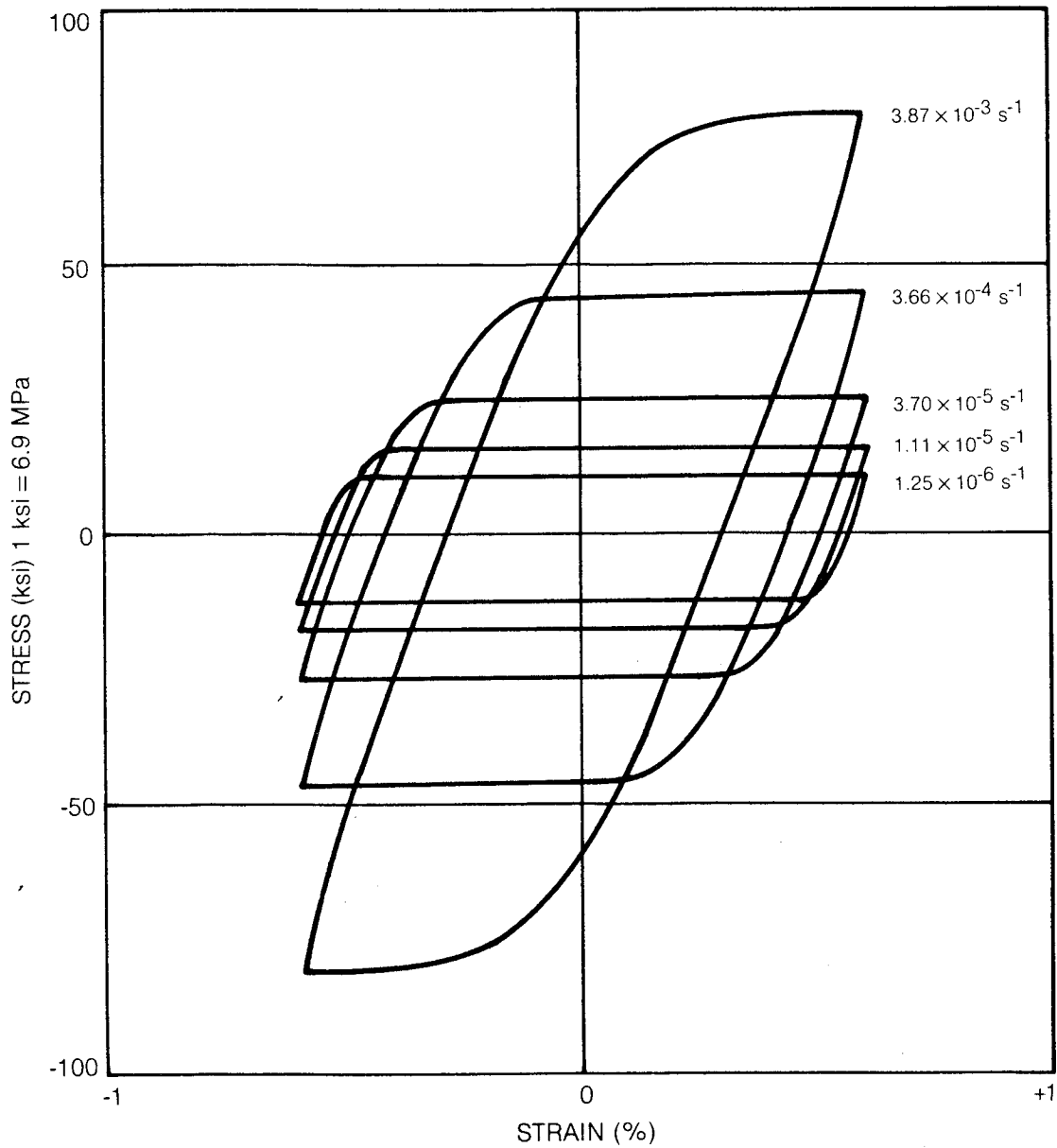$1.25 \times 10^{-6} \text{ s}^{-1}$

81-9-103-28
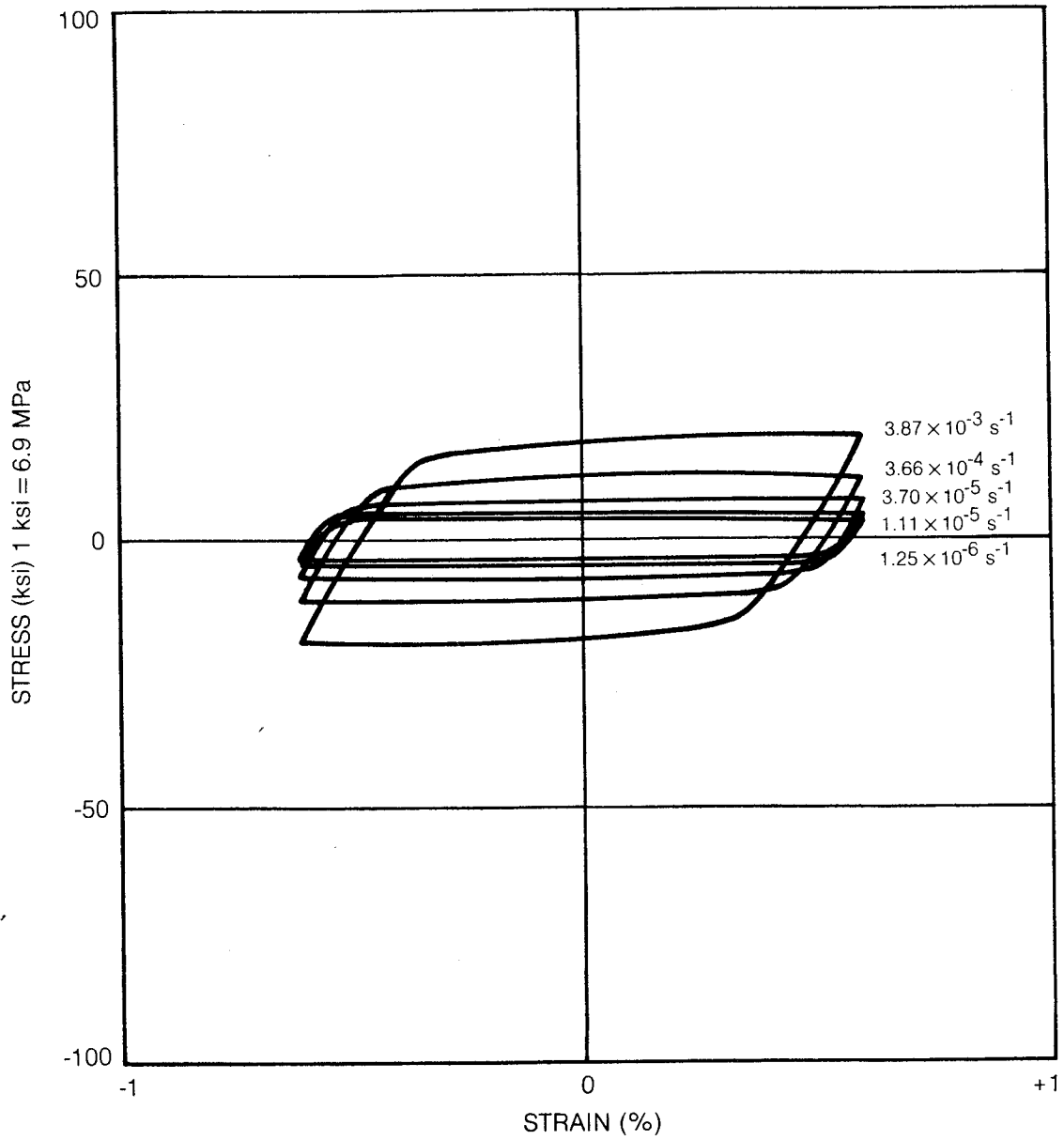
Figure 51. Theoretical Hysteresis Loops at 982°C (1800°F) Generated with Krieg, Swearengen & Rohde's Theory
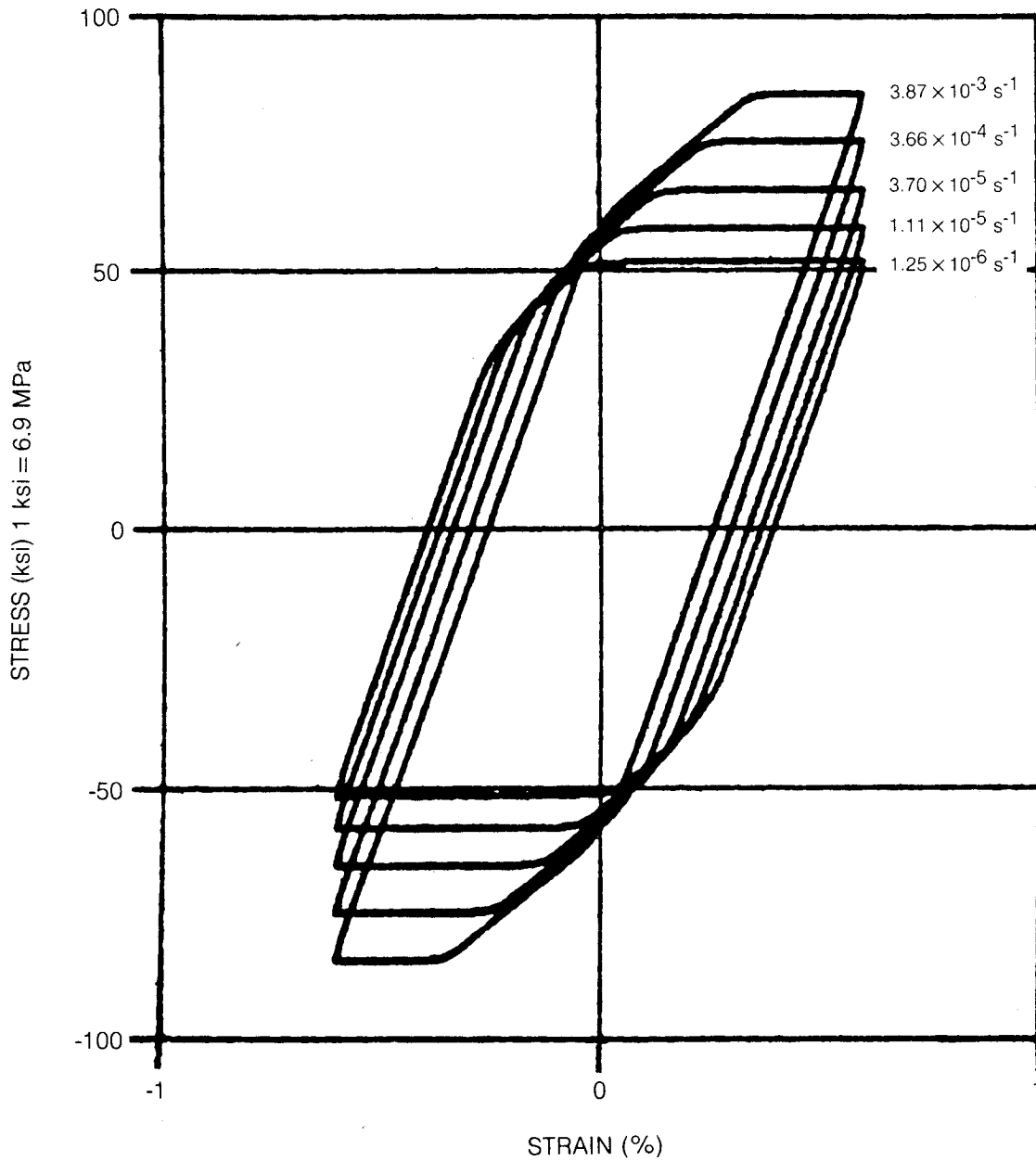
Figure 52. Theoretical Hysteresis Loops at 649°C (1200°F) Generated with Miller's Theory
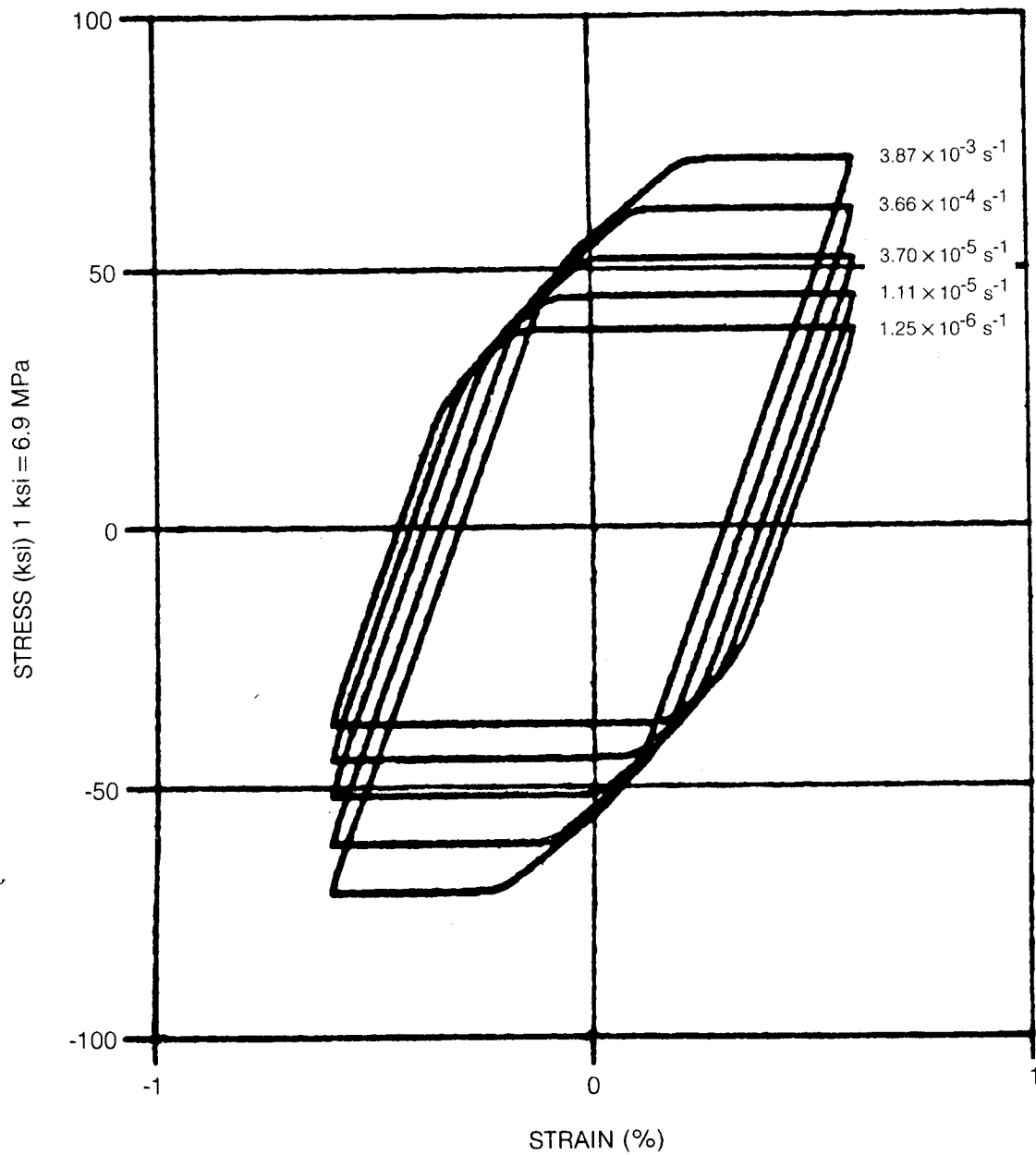
Figure 53. Theoretical Hysteresis Loops at 704°C (1300°F) Generated with Miller's Theory
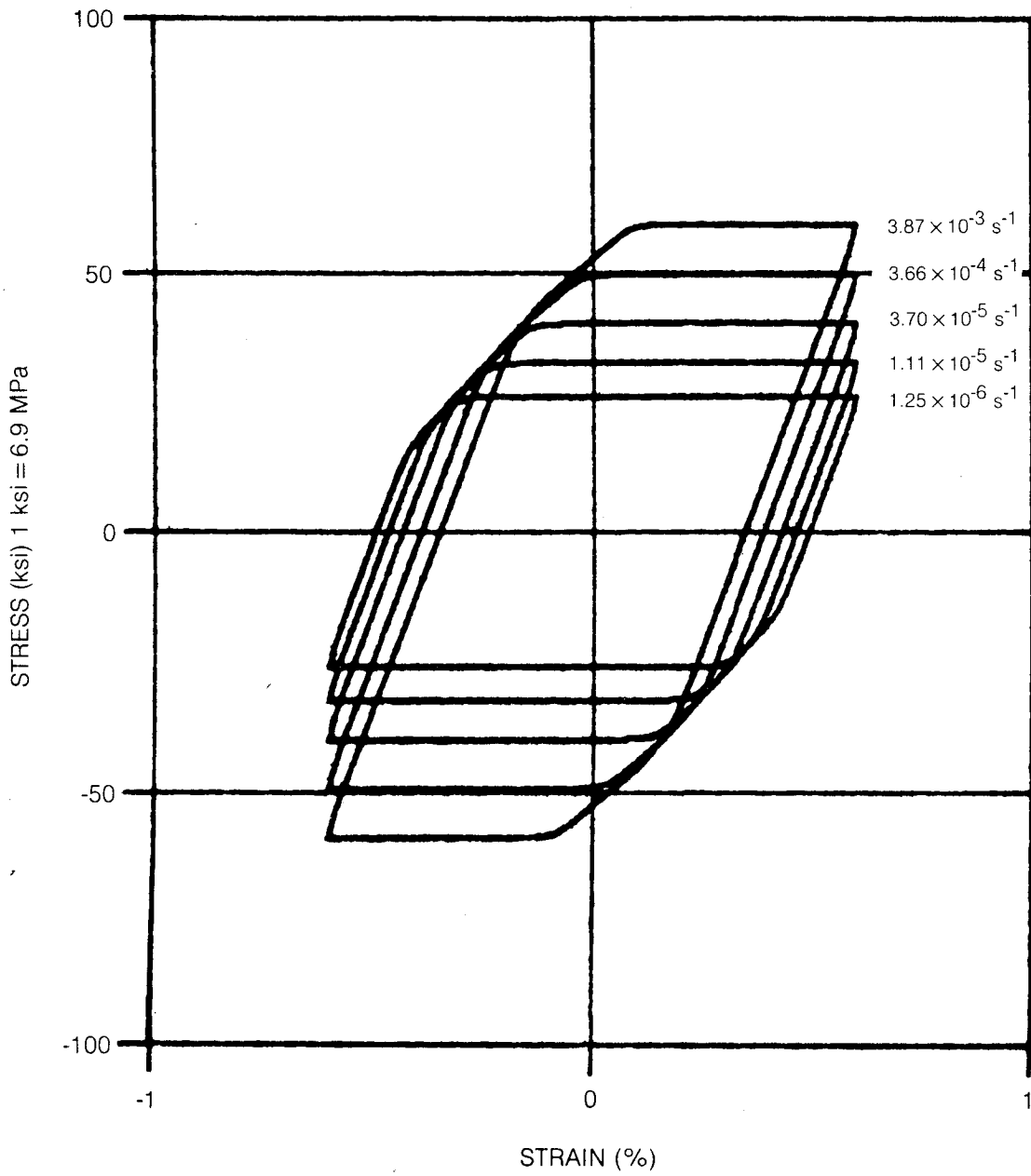
Figure 54. Theoretical Hysteresis Loops at 760°C (1400°F) Generated with Miller's Theory
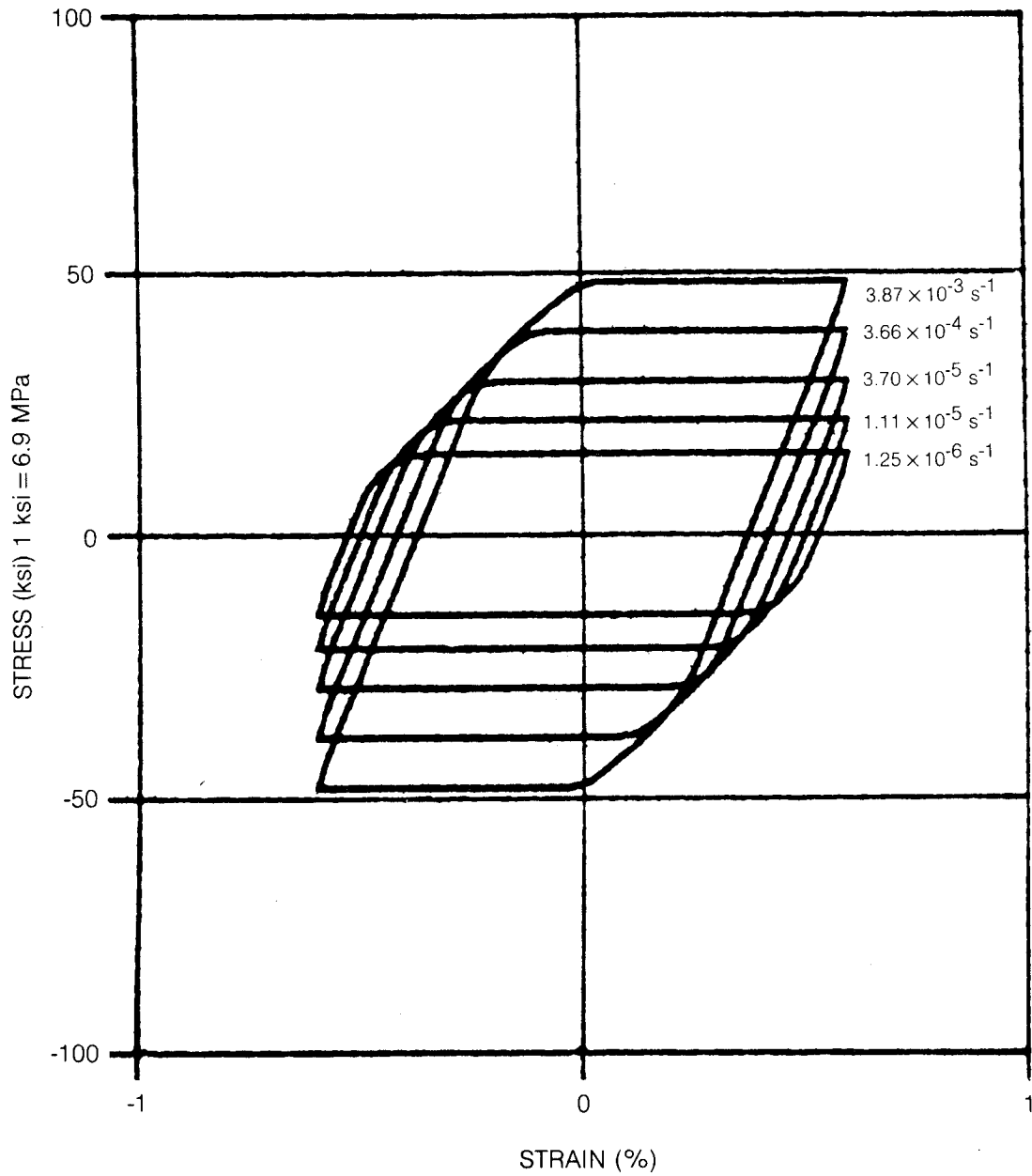
**Figure 55. Theoretical Hysteresis Loops at 816°C (1500°F)
Generated with Miller's Theory**

116
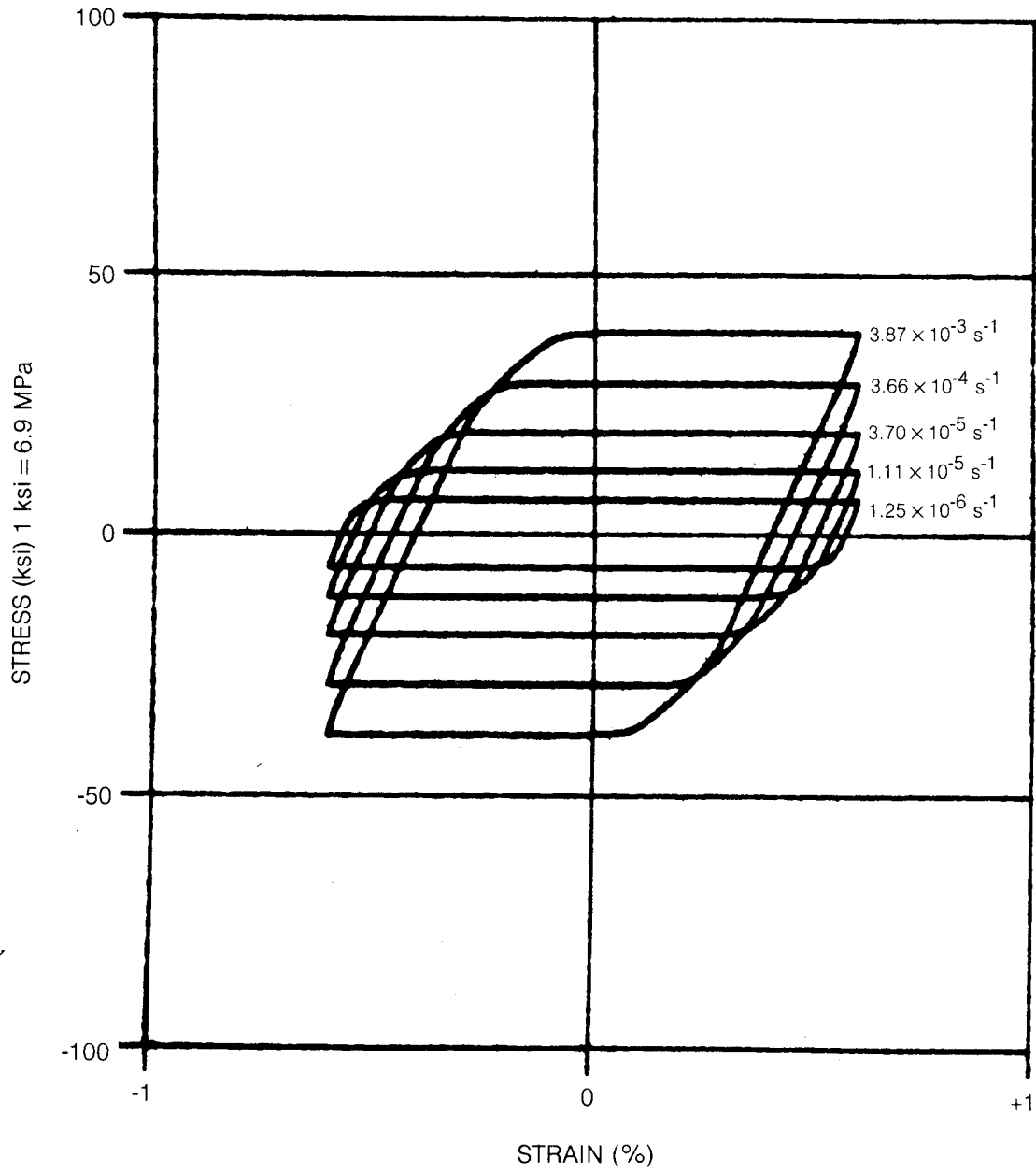
Figure 56. Theoretical Hysteresis Loops at 871 °C (1600 °F)
Generated with Miller's Theory

117

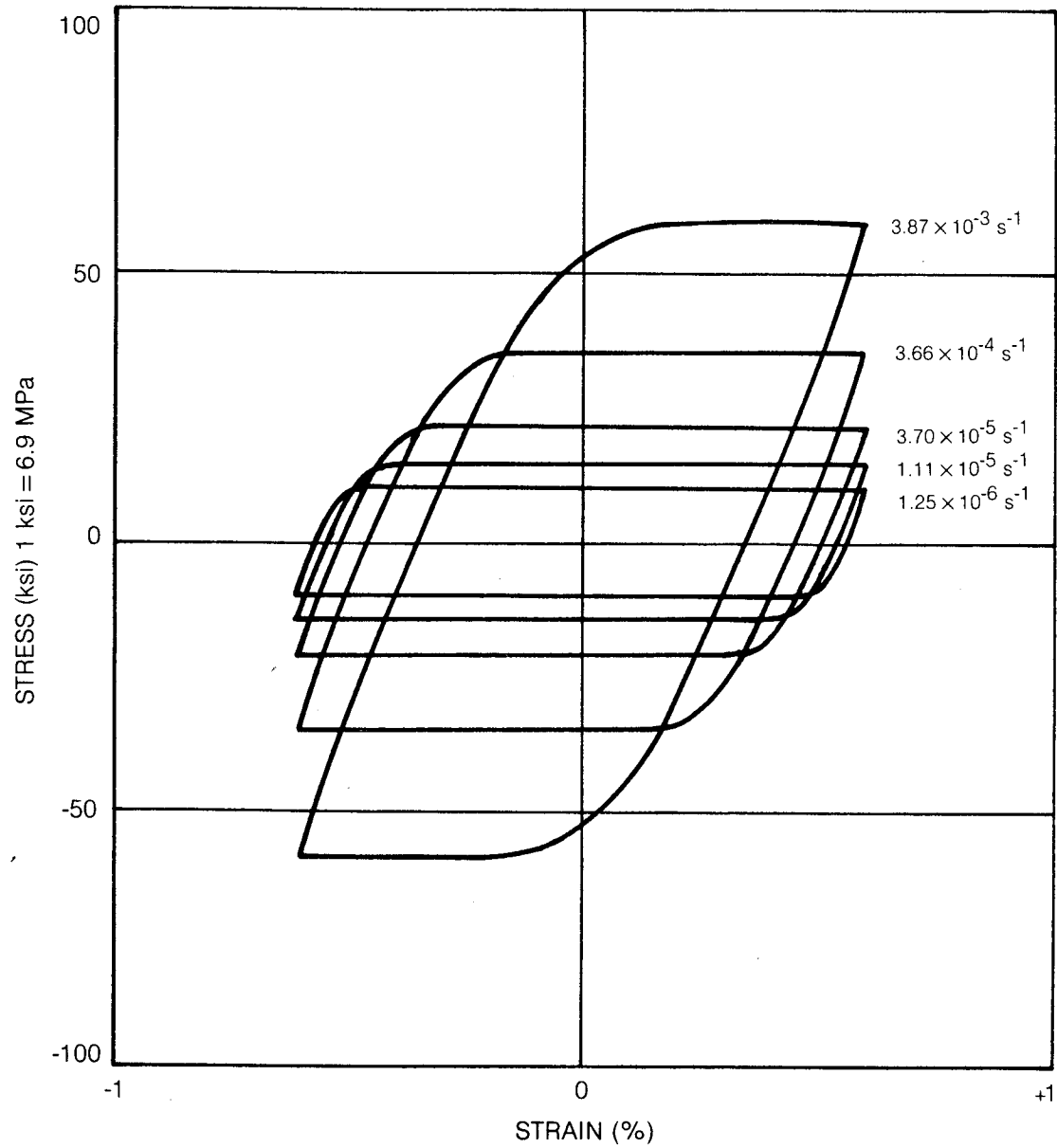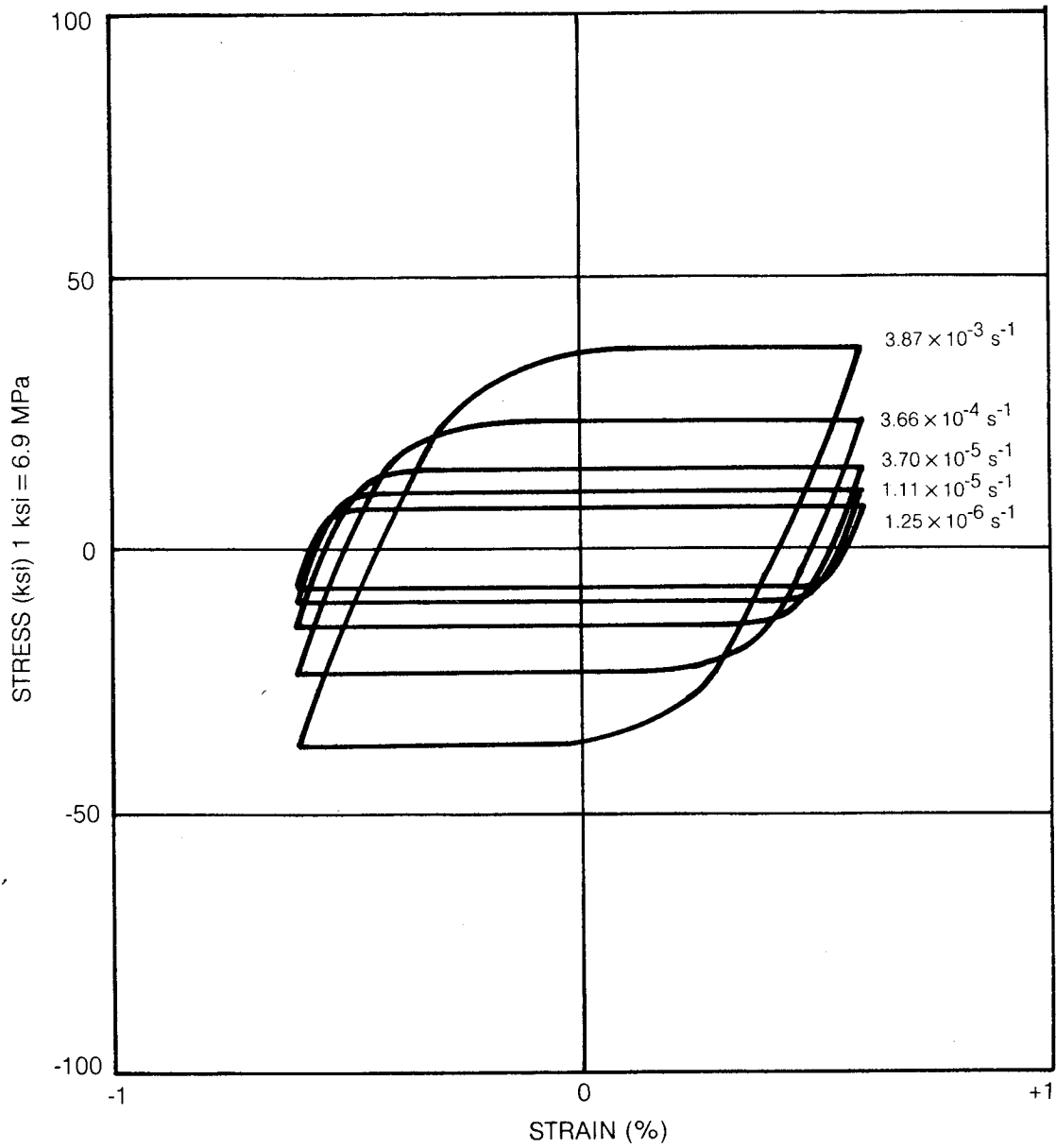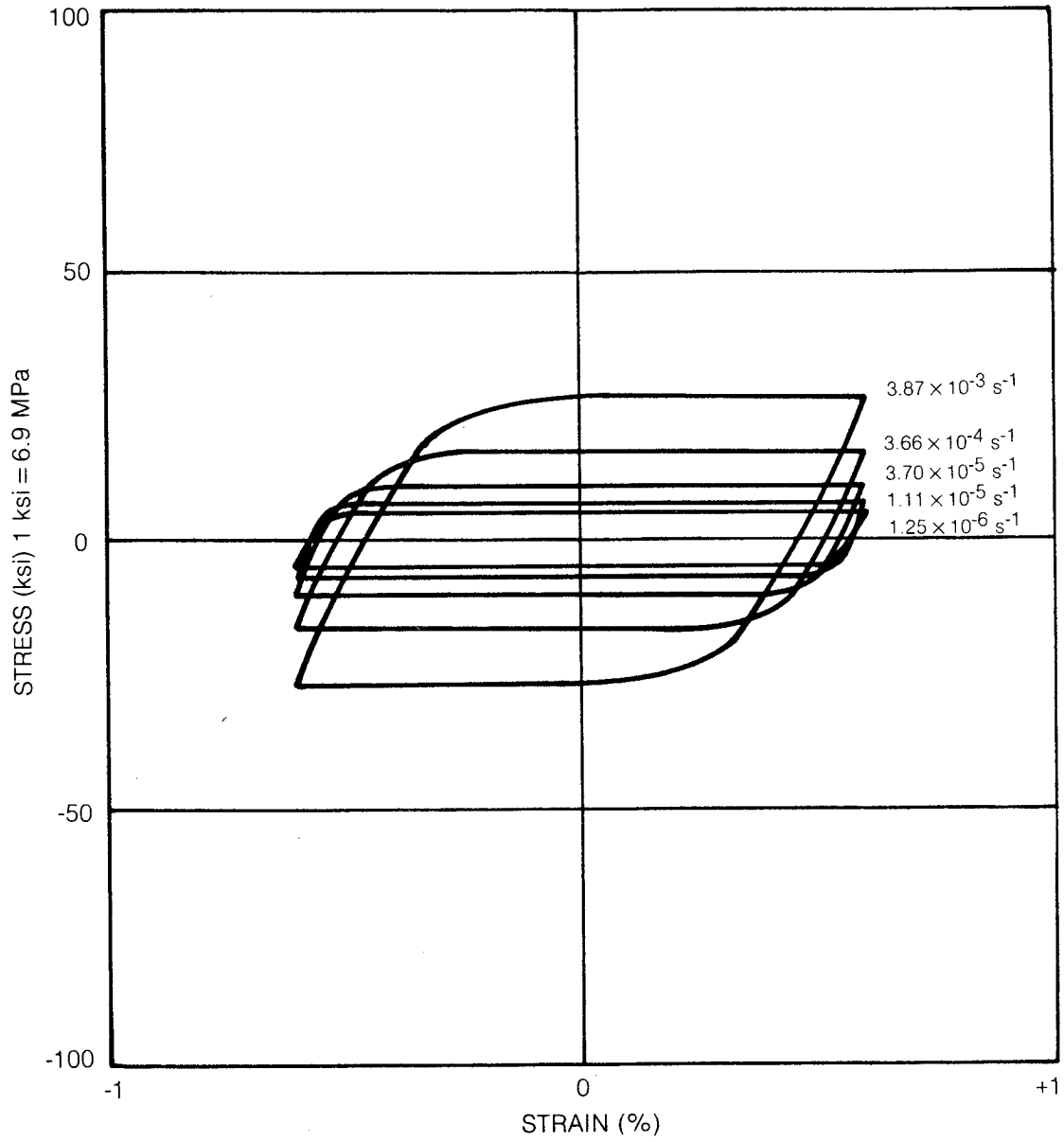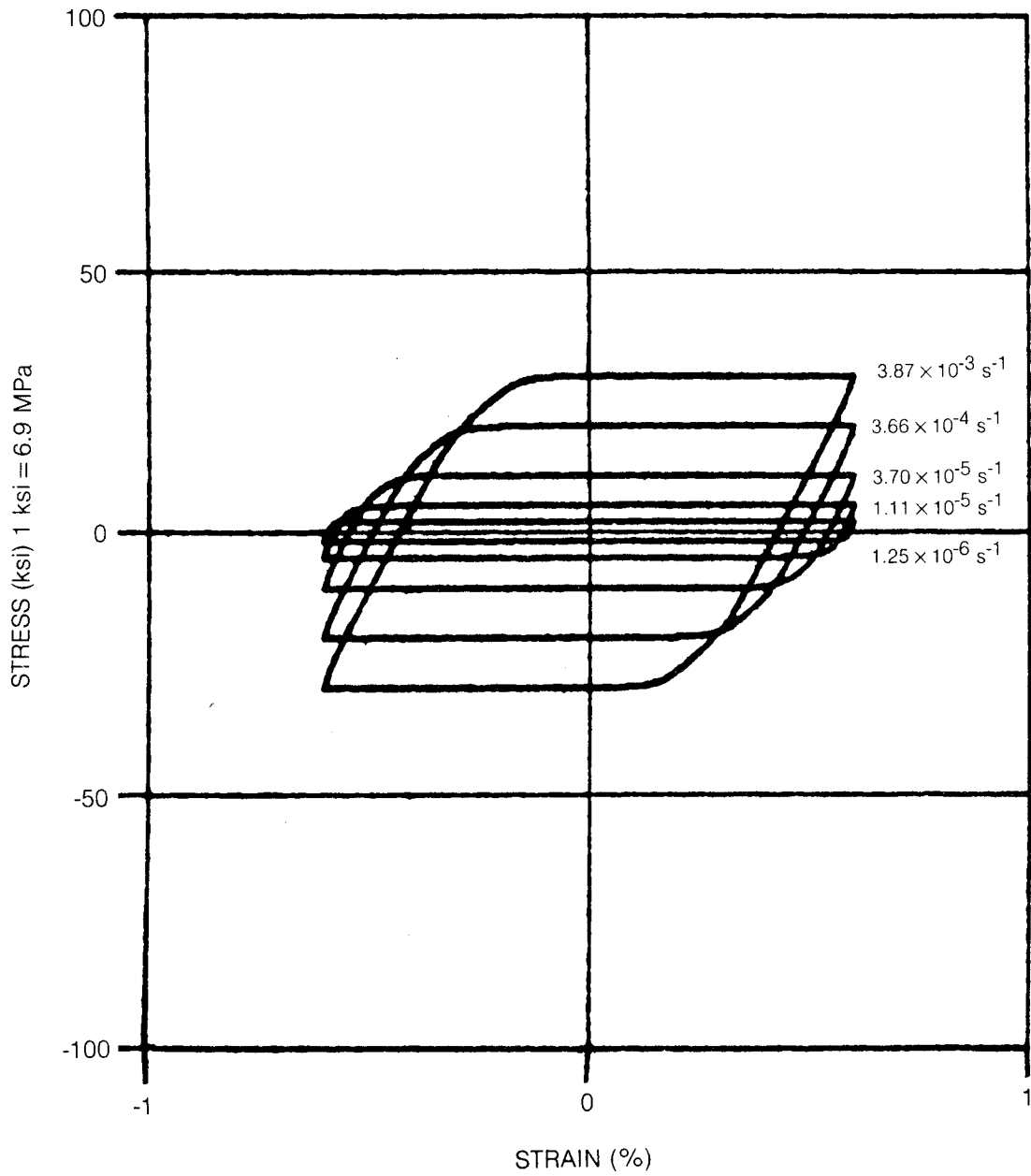**Figure 57. Theoretical Hysteresis Loops at 927°C (1700°F) Generated with Miller's Theory**
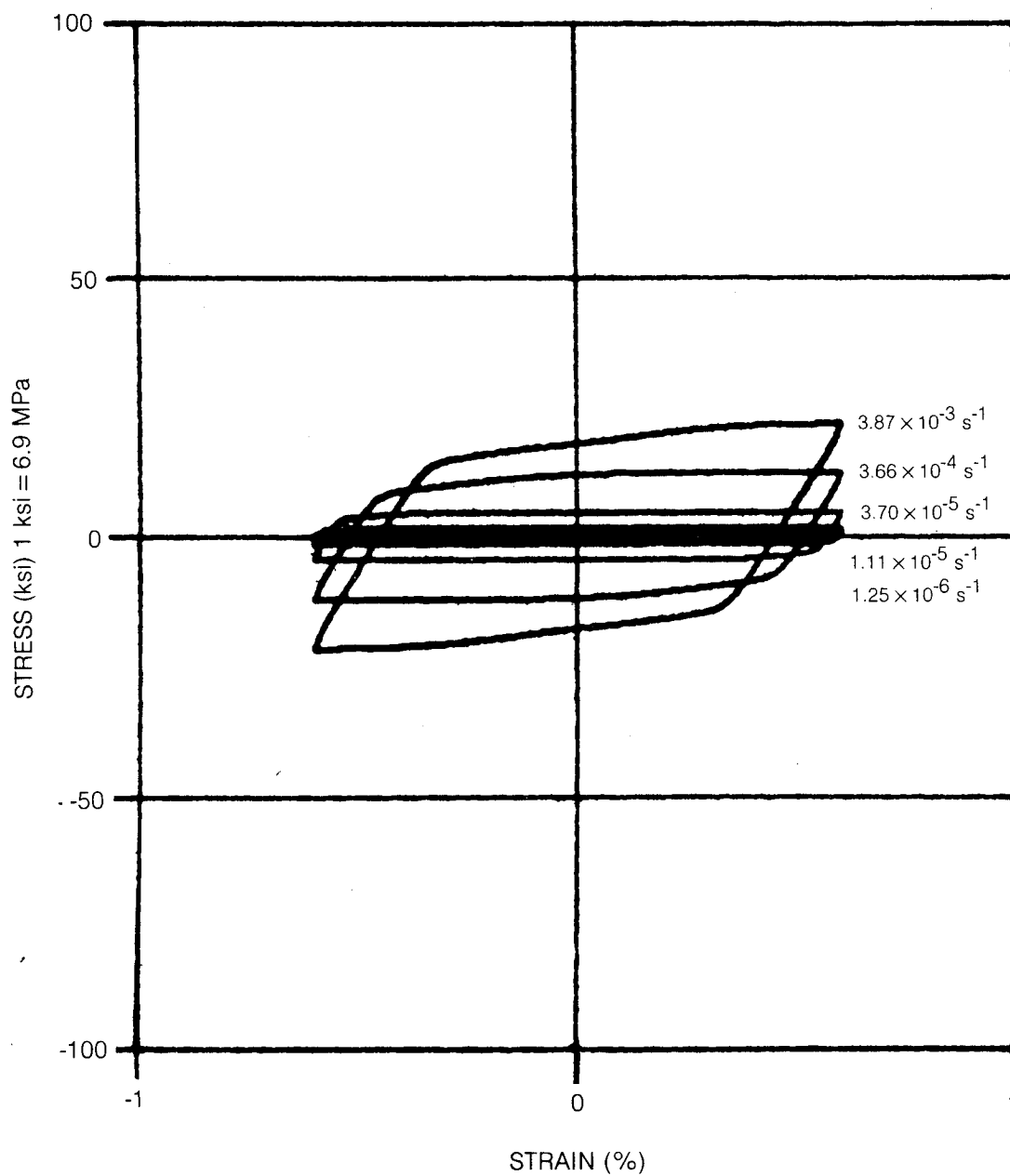
Figure 58. Theoretical Hysteresis Loops at 982°C (1800°F)
Generated with Miller's Theory
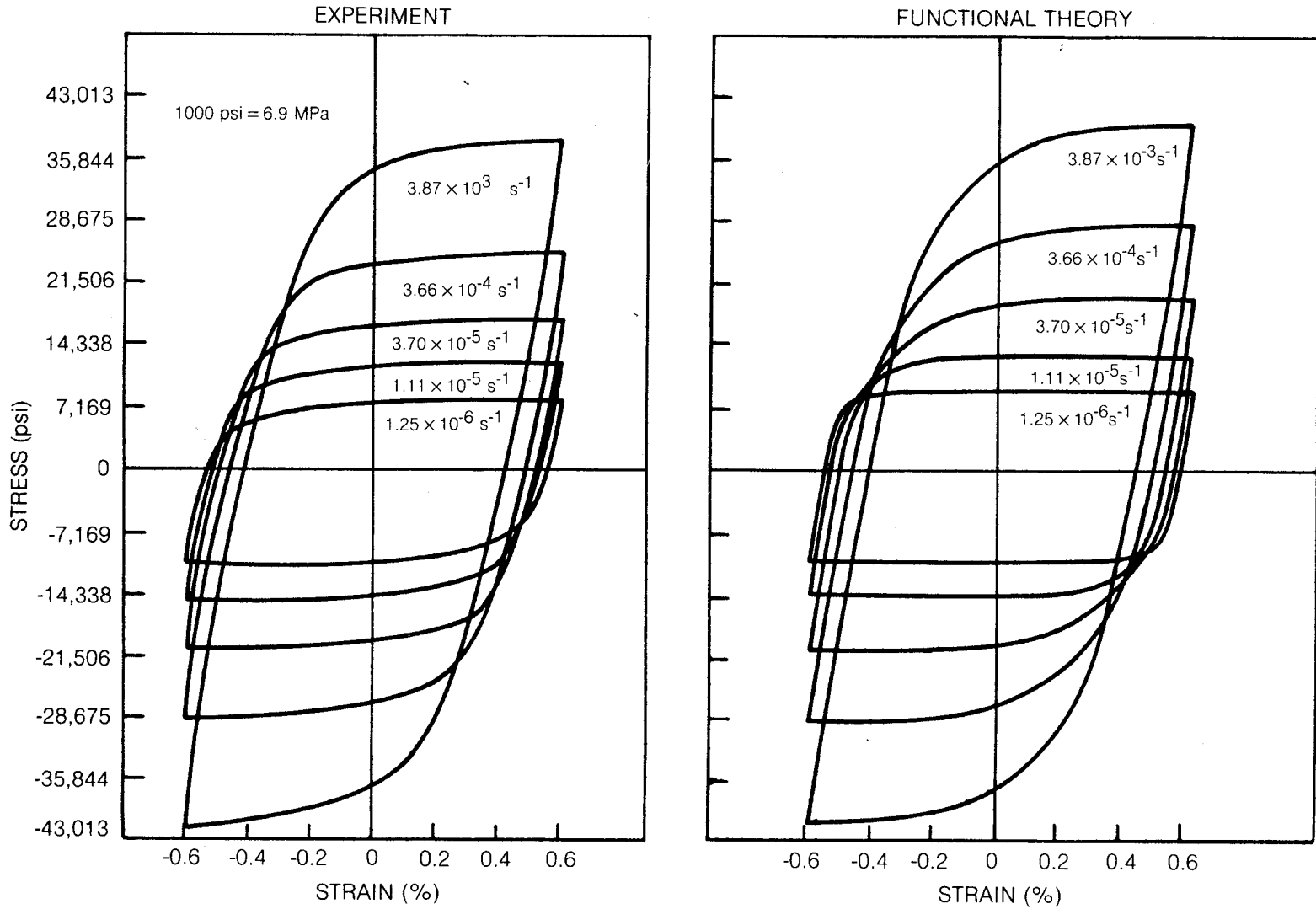
Figure 59. Comparison of Experimental and Functional Theory Predictions for Hastelloy-X at   871°C (1600°F)

EXERIMENTAL

FUNCTIONAL THEORY

$\dot{\epsilon}$ (sec^{-1})

3.87×10^{-3}
3.66×10^{-4}
3.70×10^{-5}
1.11×10^{-5}
1.25×10^{-6}
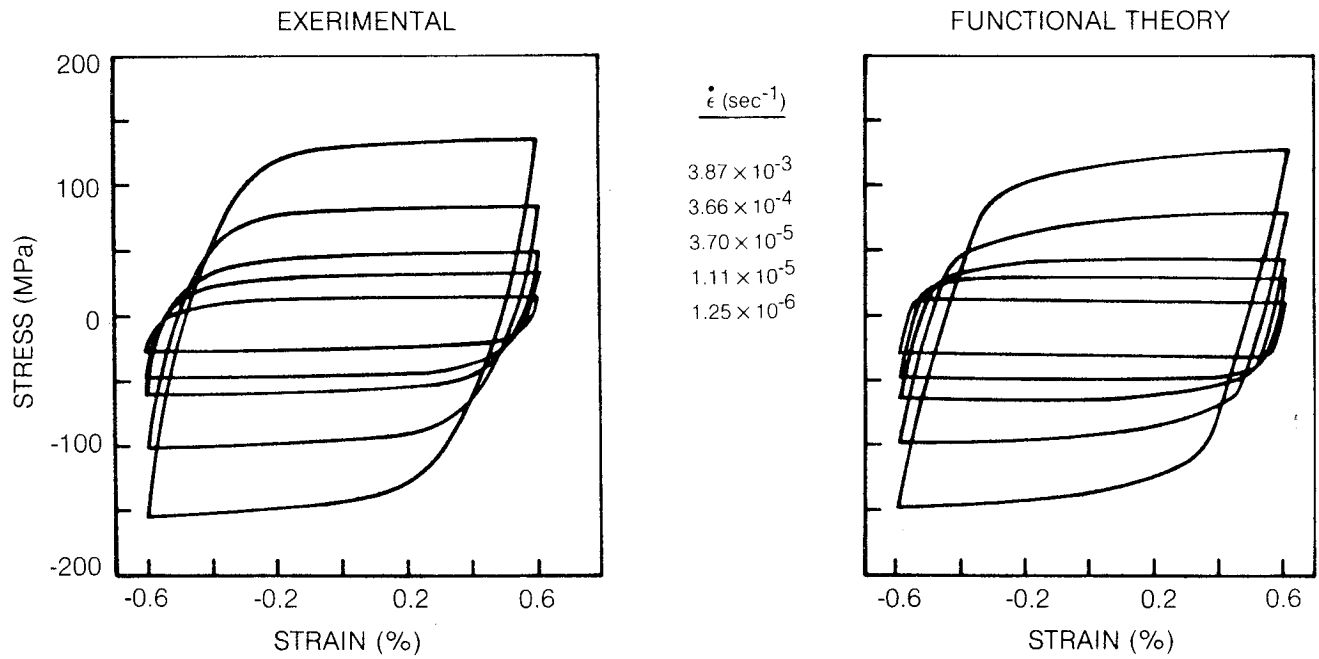
Figure 60. Comparison of Experimental and Functional Theory Predictions for Hastelloy-X at 982°C (1800°F)

81—9—103—19
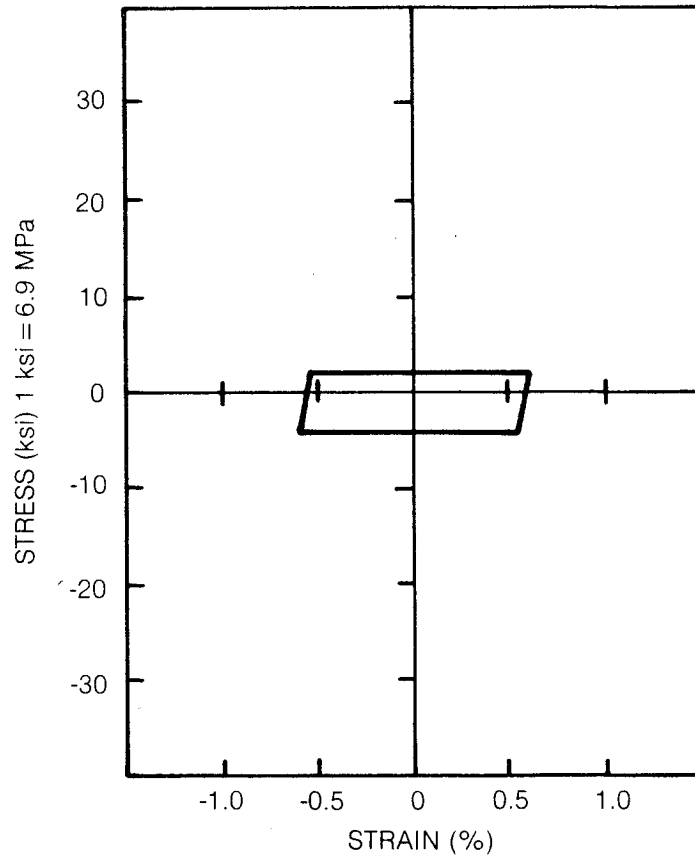
Figure 61. Hysteresis Loop Predicted by Functional Theory at 982°C (1800°F) for Strain Rate of 1.25 × 10⁻⁶ sec⁻¹. Output from MARC

122
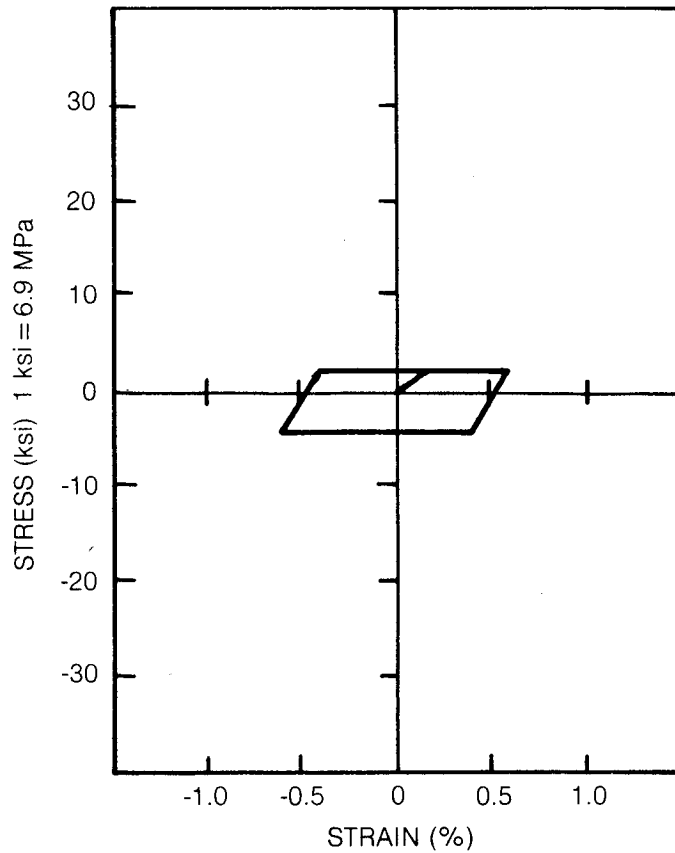
Figure 62. Hysteresis Loop Predicted by Functional Theory at 982°C (1800°F) for Strain Rate of 1.25 × 10^{-6} sec^{-1}. Three MARC Increments were used to Load from Zero Strain to 0.6% Strain with Thirty Subincrements per MARC Increment
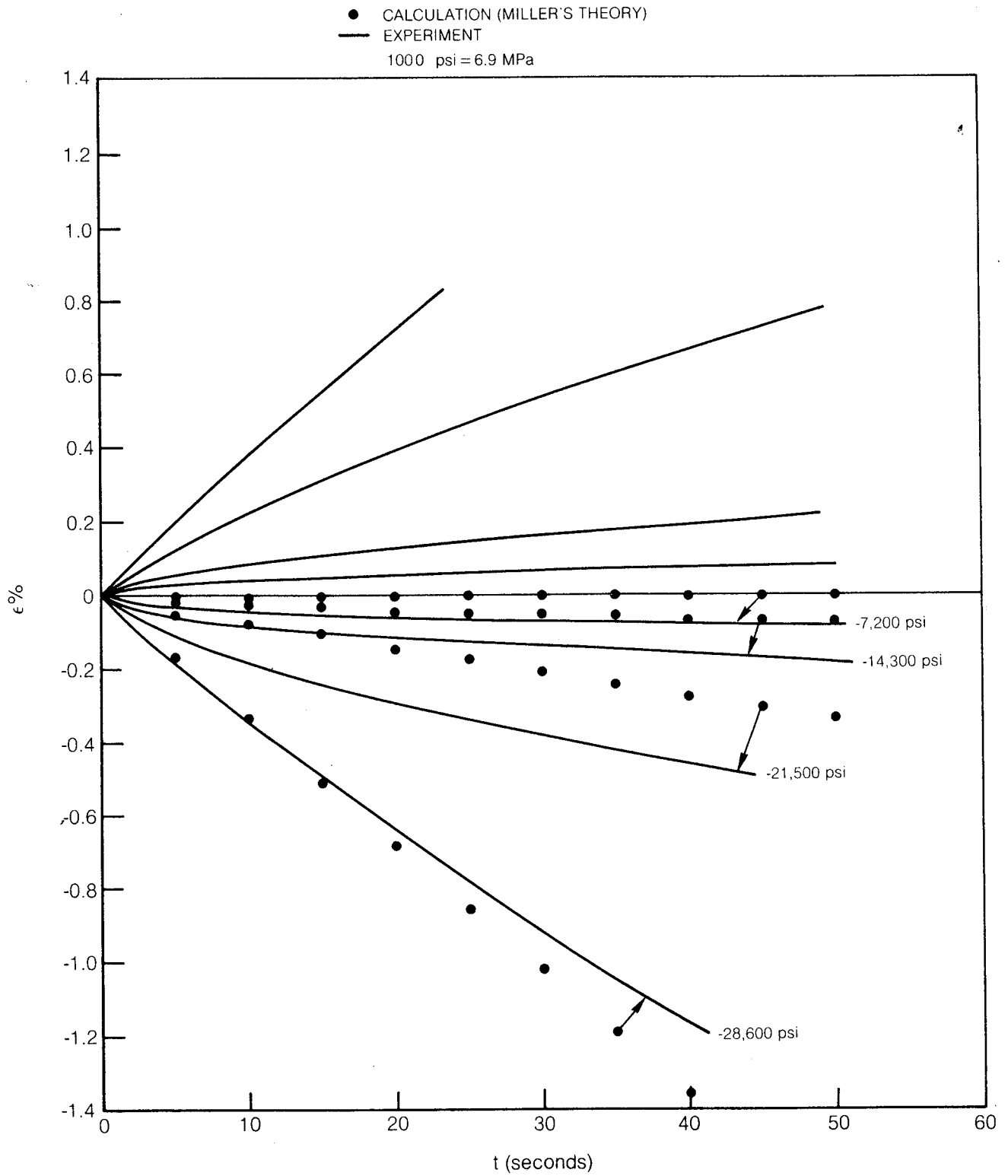
Figure 63. Creep Response of Hastelloy-X at 1600°F
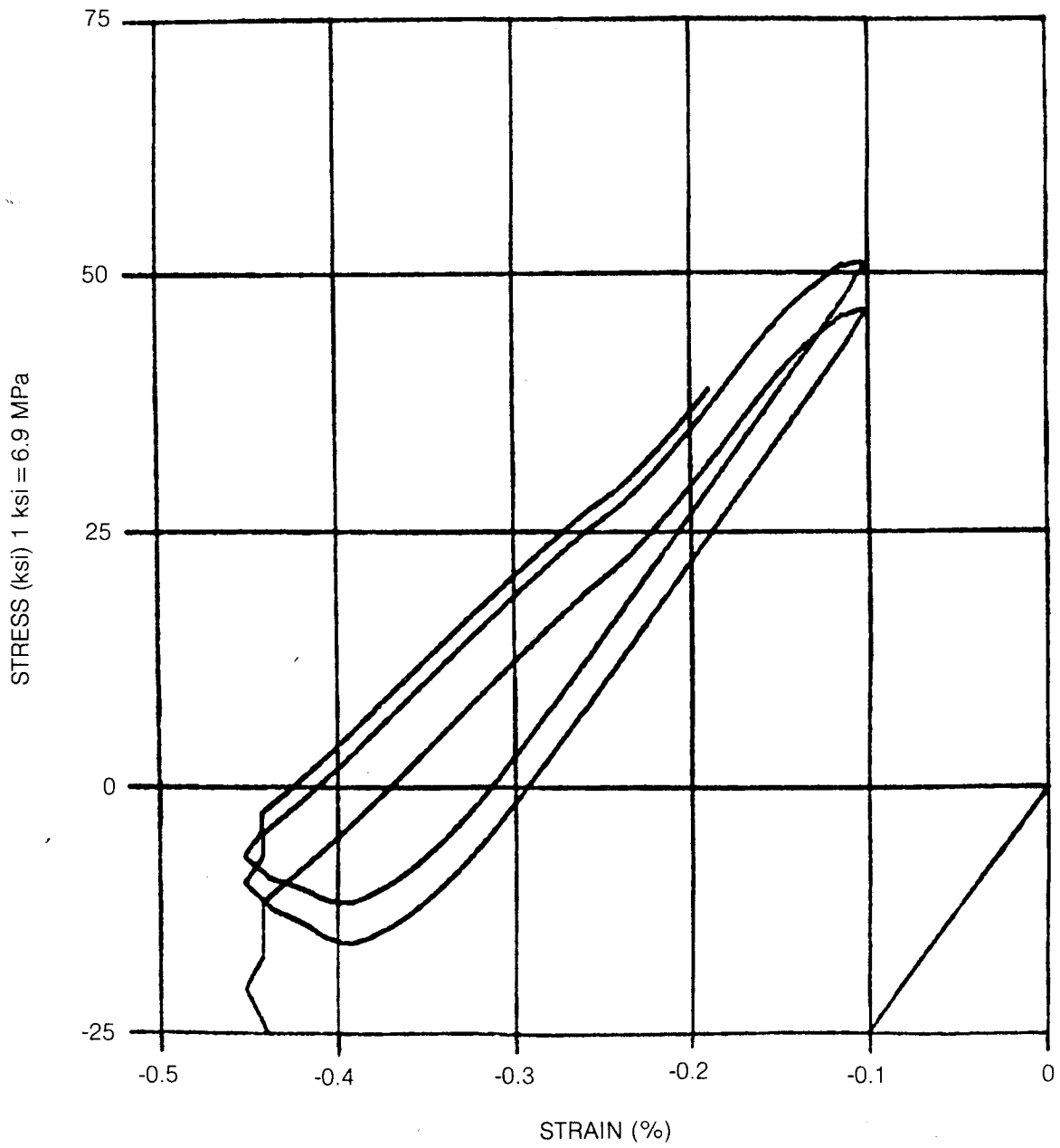
Figure 64. Thermomechanical Loop Predicted by Functional Theory

125
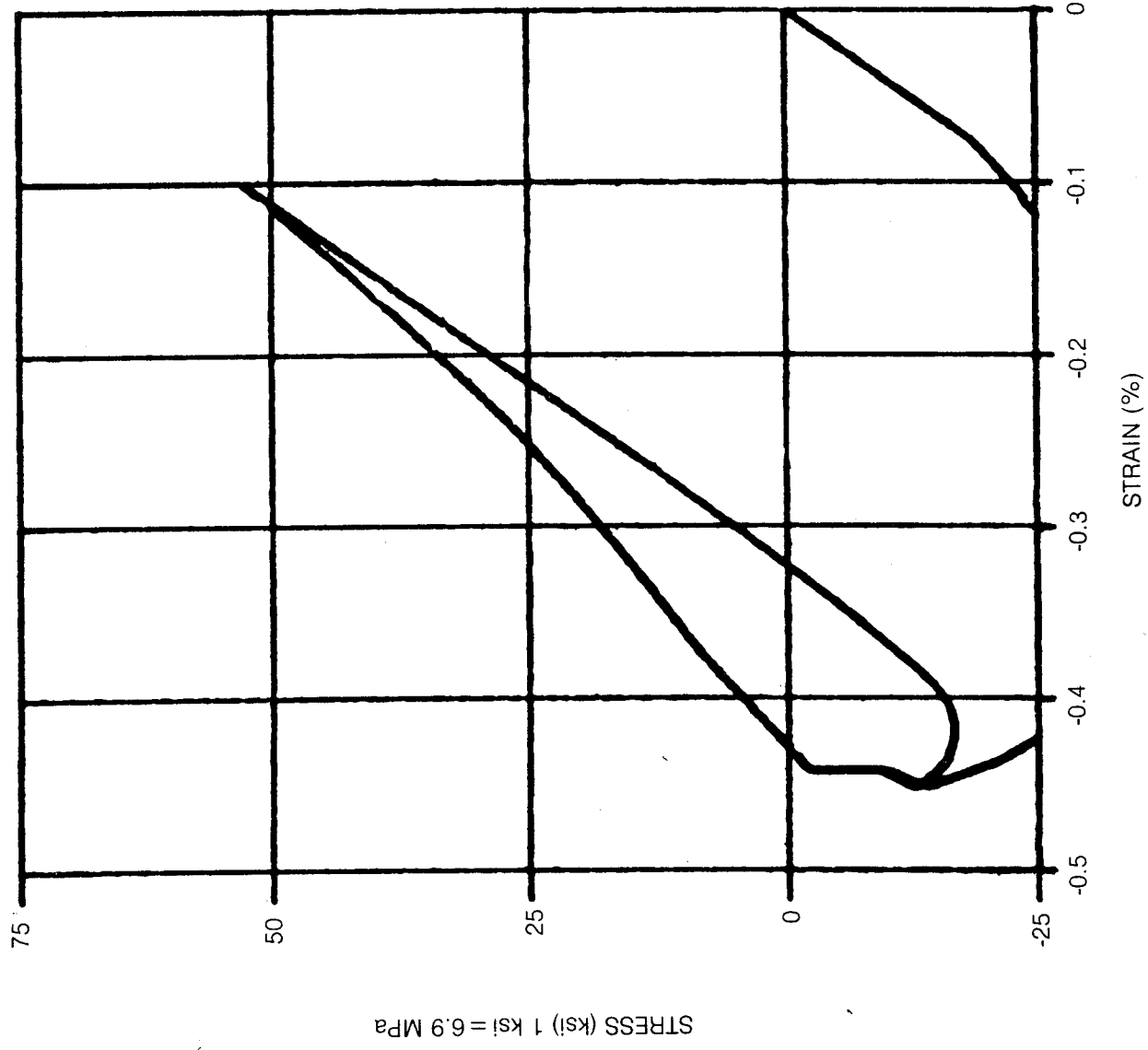
Figure 65. Thermomechanical Loop Predicted by Miller's Theory
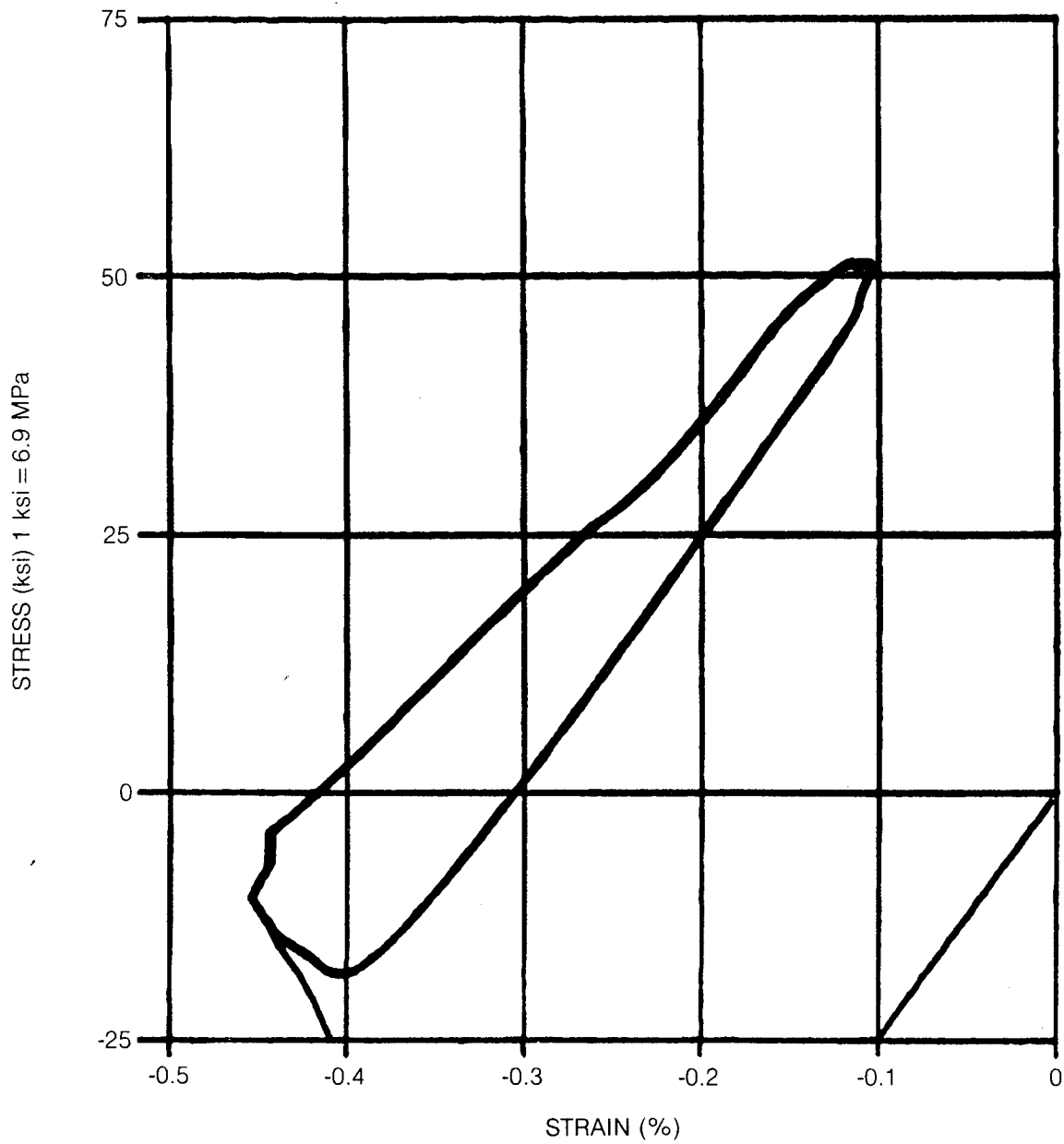
Figure 66. Thermomechanical Loop Predicted by Krieg, Swearengen & Rohde's Theory

81—4—42—1

COOLING HOLES

LIP

WELD

R

ENGINE
℄

SYMMETRY BOUNDARY
CONDITIONS

A

B

SYMMETRY BOUNDARY
CONDITIONS

C

D

0.577°

R
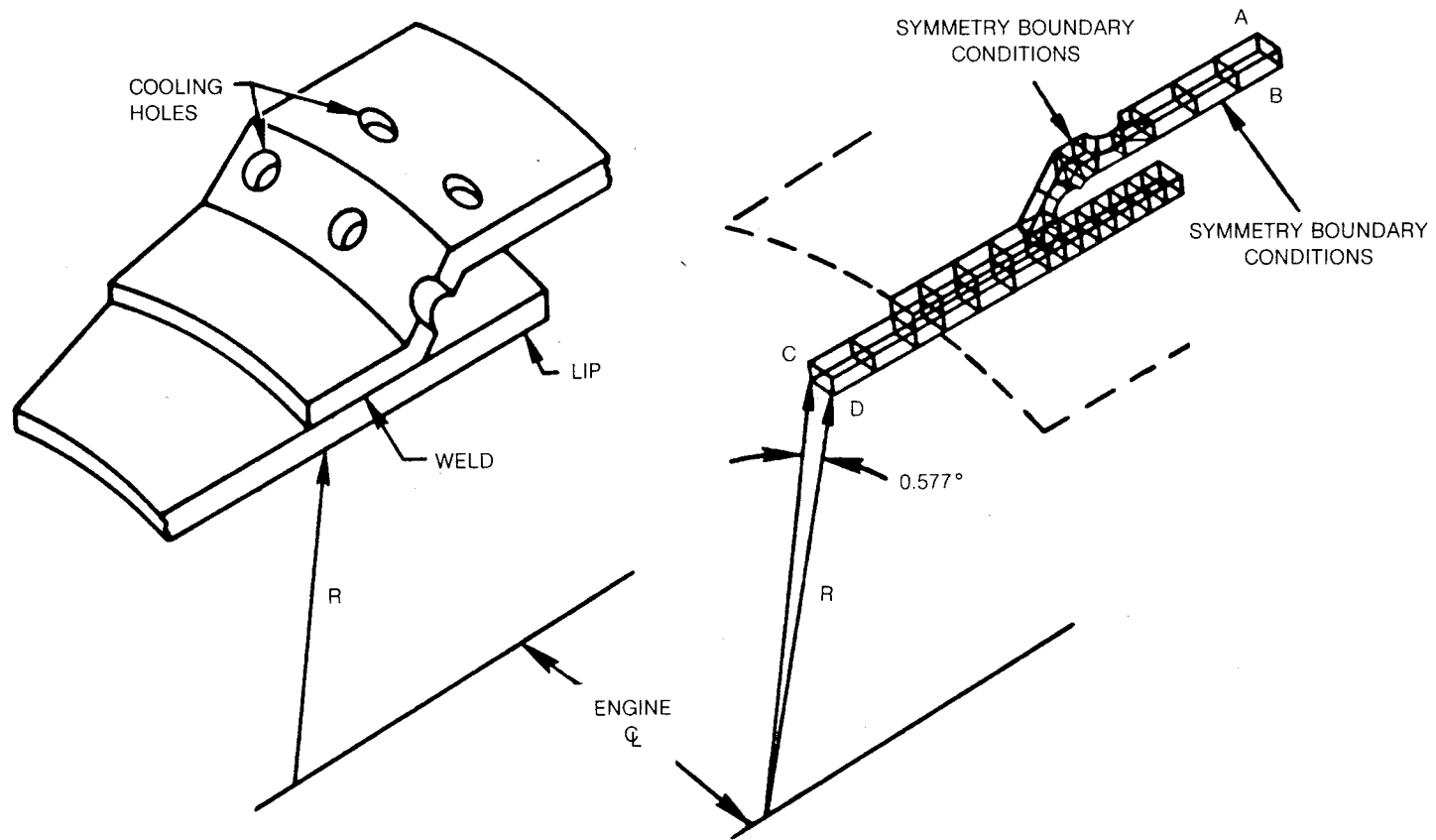
Figure 67. MARC Finite Element Breakup of Combustor for Liner Specimen
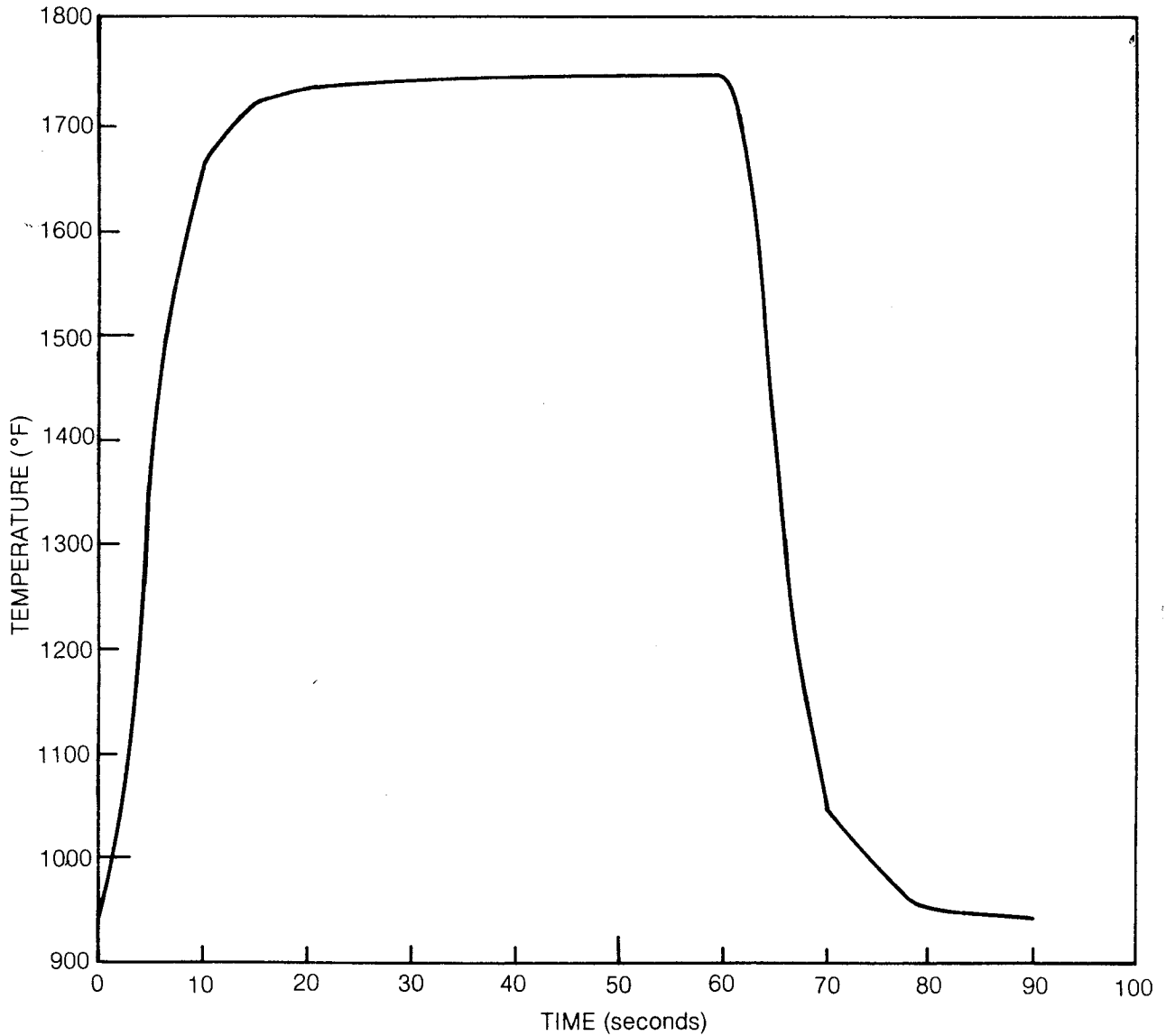
**Figure 68. Transient Temperature Response at Integration
Point Closest to the Louver Lip**

81—3—74—2

129
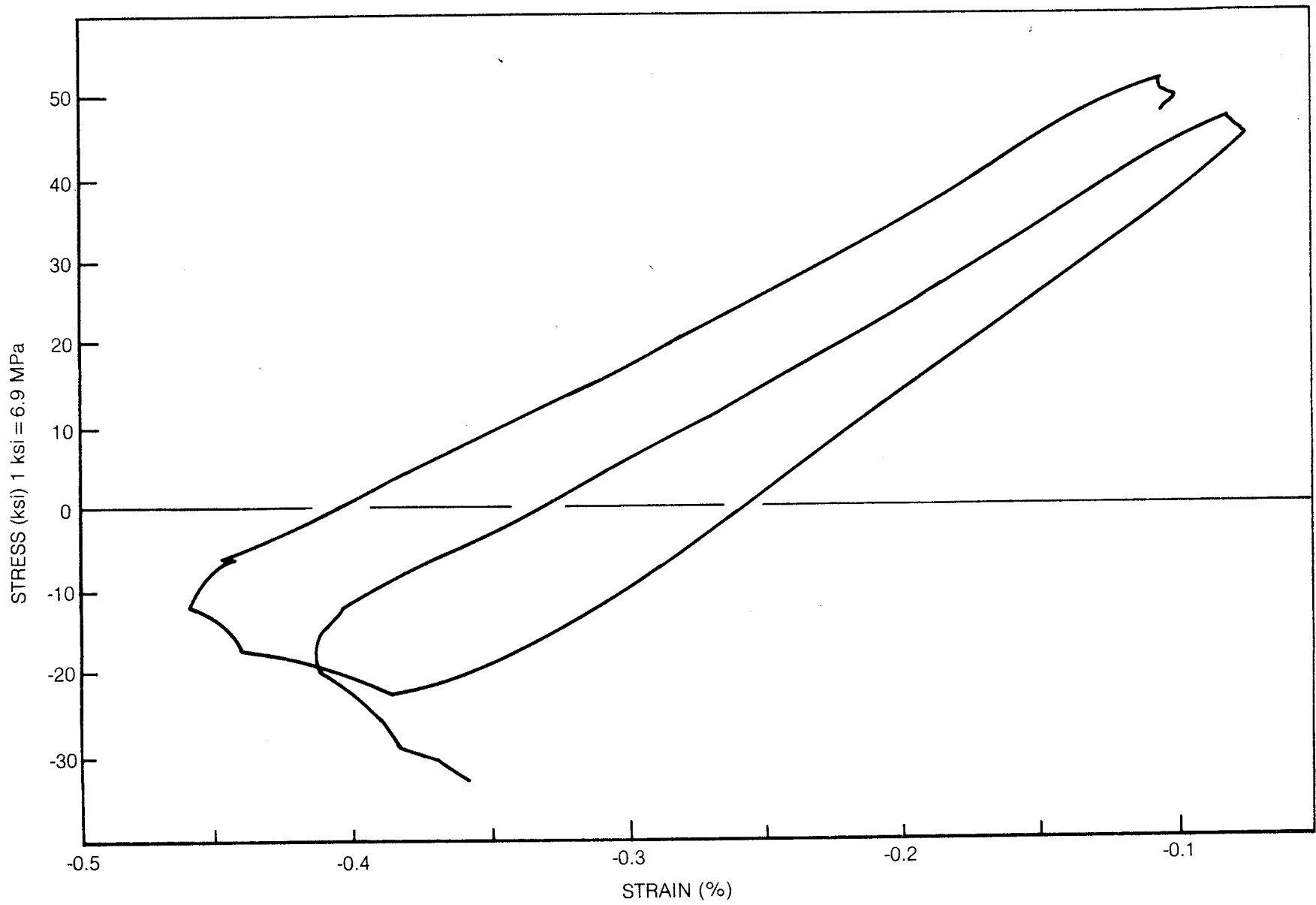
Figure 69. Hoop Stress Hoop Strain Hysteresis Response at Integration
Point Closest to the Louver Lip

81—3—74—1
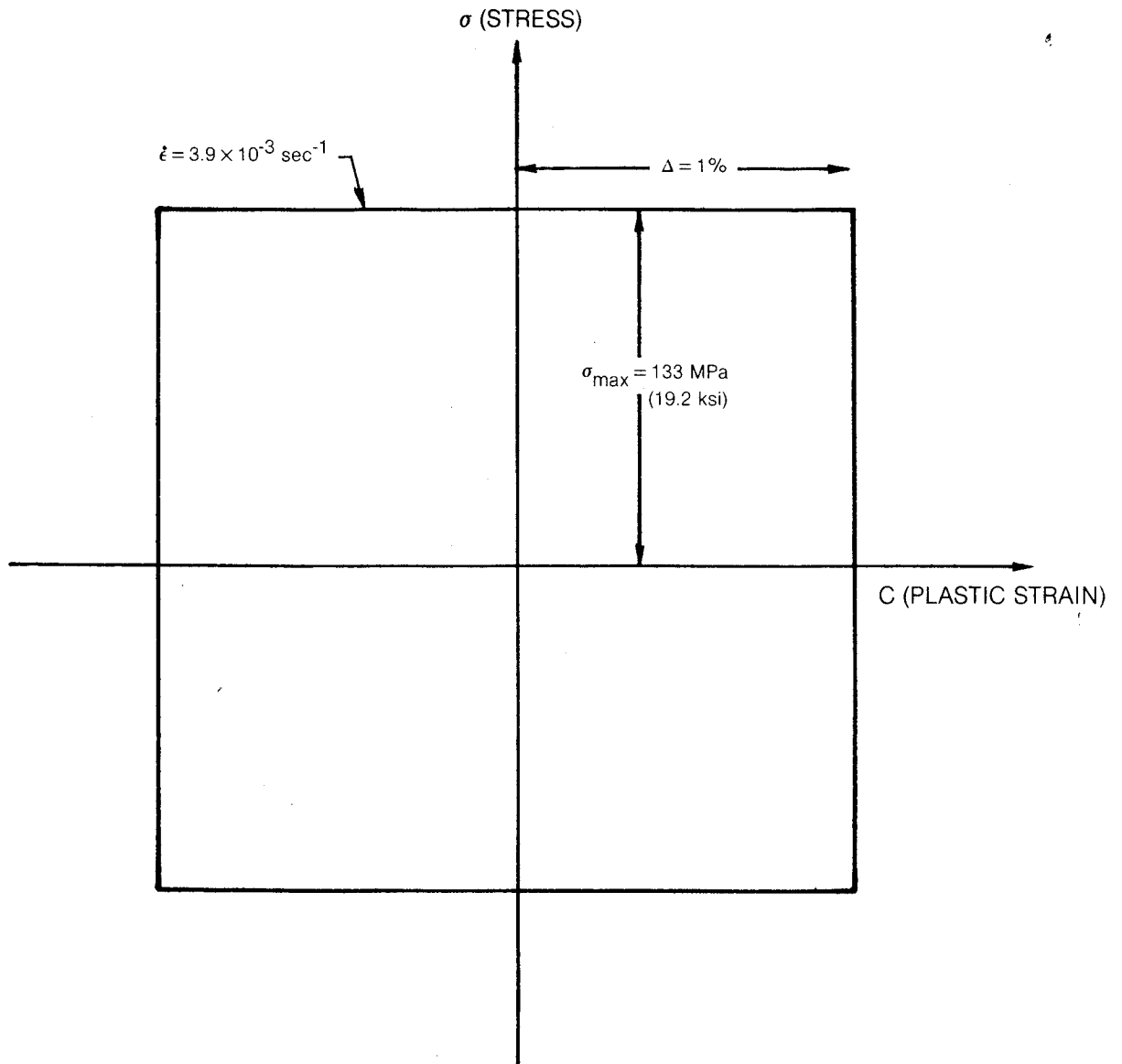
Figure 70. Elastic-Perfectly Plastic Hysteresis Loop Approximation for Hastelloy-X at 982°C (1800°F)

81—9—103—24
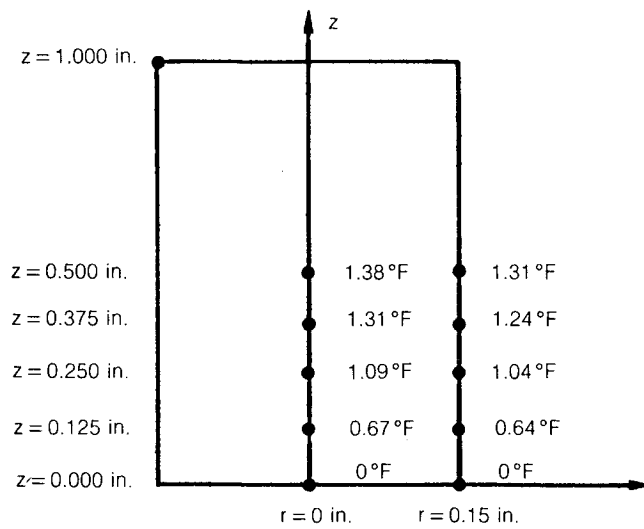
Figure 71. Temperature Rise in Hastelloy-X Specimen at 982 °C (1800 °F) Due to Plastic Deformation

132

Appendix 1. Walker's Theory (Integral Form)

$$\sigma_{ij}(t) = \frac{2}{3}\,\Omega_{ij}(t) + \delta_{ij}\int_0^t \left(\lambda(\Theta(t)) + \frac{2}{3}\,\mu(\Theta(t))\right)\left(\frac{\partial \epsilon_{kk}}{\partial \xi} - 3\alpha(\Theta(\xi))\,\frac{\partial \Theta}{\partial \xi}\right)d\xi + \int_0^t e^{-\{Q(t)-Q(\xi)\}}\left(2\mu(\Theta(t))\frac{\partial \epsilon_{ij}}{\partial \xi} - \delta_{ij}\frac{2}{3}\,\mu(\Theta(t))\frac{\partial \epsilon_{kk}}{\partial \xi} - \frac{2}{3}\,\frac{\partial \Omega_{ij}}{\partial \xi}\right)d\xi , \quad (1)$$

$$\Omega_{ij}(t) = \overset{0}{\Omega}_{ij}(t) + n_1(\Theta(t))c_{ij}(t) + n_2(\Theta(t))\int_0^t e^{-\{G(t)-G(\xi)\}}\,\frac{\partial c_{ij}}{\partial \xi}\,d\xi , \tag{2}$$

$$K(t) = K_1(\Theta(t)) - K_2(\Theta(t))\,e^{-n_7(\Theta(t))R(t)} , \tag{3}$$

$$c_{ij}(t) = \int_0^t \left(\delta_{ij}\lambda(\Theta(t))\frac{\partial \epsilon_{kk}}{\partial \xi} + 2\mu(\Theta(t))\frac{\partial \epsilon_{ij}}{\partial \xi} - \frac{\partial \sigma_{ij}}{\partial \xi} - \delta_{ij}\,\alpha(\Theta(\xi))\left(3\lambda(\Theta(\xi)) + 2\mu(\Theta(\xi))\right)\frac{\partial \Theta}{\partial \xi}\right)d\xi , \tag{4}$$

$$\overset{0}{\Omega}_{ij}(t) = -\delta_{ij}\overset{0}{\Omega}(\Theta(t)) + 3\overset{0}{\Omega}(\Theta(t))\frac{c_{ik}(t)c_{kj}(t)}{c_{pq}(t)c_{pq}(t)} , \tag{5}$$

$$Q(t) = \int_0^t \frac{3\mu(\Theta(\xi))}{K(\xi)}\left(\frac{\partial R}{\partial \xi}\right)^{1-1/n(\Theta(\xi))}d\xi , \tag{6}$$

$$G(t) = \int_0^t \left\{\left(n_3(\Theta(\xi)) + n_4(\Theta(\xi))\,e^{-n_5(\Theta(\xi))R(\xi)}\right)\frac{\partial R}{\partial \xi} + n_6(\Theta(\xi))\left(\frac{2}{3}\,\Omega_{ij}(\xi)\,\Omega_{ij}(\xi)\right)^{\frac{m(\Theta(\xi))-1}{2}}\right\}d\xi , \tag{7}$$

$$R(t) = \int_0^t \sqrt{\frac{2}{3}\,\frac{\partial c_{ij}}{\partial \xi}\,\frac{\partial c_{ij}}{\partial \xi}}\;\;d\xi . \tag{8}$$

Material constants: $\lambda,\mu,\overset{0}{\Omega},n,m,n_1,n_2,n_3,n_4,n_5,n_6,n_7,K_1,K_2$ depend on temperature.

133

Appendix 2. Walker's Theory (Differential Form)

$$\dot{c}_{ij} = \left(\frac{\sqrt{\frac{2}{3}\left(\frac{3}{2}s_{ij} - \Omega_{ij}\right)\left(\frac{3}{2}s_{ij} - \Omega_{ij}\right)}}{K} \right)^{n} \frac{\left(\frac{3}{2}s_{ij} - \Omega_{ij}\right)}{\sqrt{\frac{2}{3}\left(\frac{3}{2}s_{ij} - \Omega_{ij}\right)\left(\frac{3}{2}s_{ij} - \Omega_{ij}\right)}} \tag{1}$$

$$\dot{\Omega}_{ij} = (n_1 + n_2)\dot{c}_{ij} + \dot{c}_{ij}\frac{\partial n_1}{\partial \Theta}\dot{\Theta} - \left(\Omega_{ij} - \overset{0}{\Omega}_{ij} - n_1 c_{ij}\right)\left(\dot{G} - \frac{1}{n_2}\frac{\partial n_2}{\partial \Theta}\dot{\Theta}\right) \tag{2}$$

$$K = K_1 - K_2 e^{-n_7 R}, \tag{3}$$

$$\dot{c}_{ij} = \left(\delta_{ij}\lambda\dot{\epsilon}_{kk} + 2\mu\dot{\epsilon}_{ij} - \dot{\sigma}_{ij} - \delta_{ij}(3\lambda + 2\mu)\alpha\dot{\Theta}\right)/2\mu, \tag{4}$$

$$\dot{G} = \left(n_3 + n_4 e^{-n_5 R}\right)\dot{R} + n_6\left(\frac{2}{3}\Omega_{ij}\Omega_{ij}\right)^{\frac{m-1}{2}}, \tag{5}$$

$$\dot{R} = \sqrt{\frac{2}{3}\dot{c}_{ij}\dot{c}_{ij}}, \tag{6}$$

$$s_{ij} = \sigma_{ij} - \frac{1}{3}\delta_{ij}\sigma_{kk}.$$

Material constants: $\lambda, \mu, \overset{0}{\Omega}, n, m, n_1, n_2, n_3, n_4, n_5, n_6, n_7, K_1, K_2$ depend on temperature.

134

Appendix 3. Chaboche's Theory

$$\dot{c}_{ij} = \left\langle \frac{\sqrt{\frac{2}{3}\left(\frac{3}{2}s_{ij}-\Omega_{ij}\right)\left(\frac{3}{2}s_{ij}-\Omega_{ij}\right)}-Y-k}{K} \right\rangle^{n} \frac{\left(\frac{3}{2}s_{ij}-\Omega_{ij}\right)}{\sqrt{\frac{2}{3}\left(\frac{3}{2}s_{ij}-\Omega_{ij}\right)\left(\frac{3}{2}s_{ij}-\Omega_{ij}\right)}} , \tag{1}$$

$$\text{where } \langle x \rangle = \begin{cases} 0 & \text{if } x \leq 0 \\ x & \text{if } x > 0 , \end{cases}$$

$$\dot{\Omega}_{ij} = cf(R)\left[a\dot{c}_{ij} - \dot{R}\,\Omega_{ij} - b\left(\frac{2}{3}\Omega_{ij}\Omega_{ij}\right)^{\frac{m-1}{2}}\Omega_{ij}\right] + \left[\frac{1}{c}\frac{\partial c}{\partial\Theta} + \frac{1}{a}\frac{\partial a}{\partial\Theta} + \frac{1}{f}\frac{\partial f}{\partial\Theta}\right]\dot{\Theta}\,\Omega_{ij} , \tag{2}$$

$$Y = \frac{1}{2ca}\frac{\frac{\partial f(R)}{\partial R}}{f^{2}(R)}\left(\frac{2}{3}\Omega_{ij}\Omega_{ij}\right) + g(R) , \tag{3}$$

$$\dot{c}_{ij} = \left(\delta_{ij}\lambda\dot{\epsilon}_{kk} + 2\mu\dot{\epsilon}_{ij} - \dot{\sigma}_{ij} - \delta_{ij}(3\lambda+2\mu)\alpha\dot{\Theta}\right)/2\mu , \tag{4}$$

$$f(R) = \ell + (1-\ell)e^{-\beta R} , \tag{5}$$

$$g(R) = h(1-e^{-\gamma R}) , \tag{6}$$

$$\dot{R} = \sqrt{\frac{2}{3}\dot{c}_{ij}\dot{c}_{ij}} , \tag{7}$$

$$s_{ij} = \sigma_{ij} - \frac{1}{3}\delta_{ij}\sigma_{kk} . \tag{8}$$

Material constants: $\lambda, \mu, K, k, n, m, a, b, c, \ell, h, \beta, \gamma$ depend on temperature.

Appendix 4. Miller's Theory (Differential Form)

$$\dot{c}_{ij} = B\theta' \left\{ \sinh \left(\frac{\sqrt{\frac{2}{3}\left(\frac{3}{2}s_{ij} - \Omega_{ij}\right)\left(\frac{3}{2}s_{ij} - \Omega_{ij}\right)}}{K} \right)^{\frac{3}{2}} \right\}^{n} \frac{\left(\frac{3}{2}s_{ij} - \Omega_{ij}\right)}{\sqrt{\frac{2}{3}\left(\frac{3}{2}s_{ij} - \Omega_{ij}\right)\left(\frac{3}{2}s_{ij} - \Omega_{ij}\right)}} \quad , \tag{1}$$

$$\dot{\Omega}_{ij} = H_1 \dot{c}_{ij} - H_1 B\theta' \left\{ \sinh \left(A_1 \sqrt{\frac{2}{3}\Omega_{ij}\Omega_{ij}} \right) \right\}^{n} \frac{\Omega_{ij}}{\sqrt{\frac{2}{3}\Omega_{ij}\Omega_{ij}}} \quad , \tag{2}$$

$$\dot{K} = H_2 \dot{R} \left(C_2 + \sqrt{\frac{2}{3}\Omega_{ij}\Omega_{ij}} - \frac{A_2}{A_1}K^3 \right) - H_2 C_2 B\theta' \left\{ \sinh \left(A_2 K^3 \right) \right\}^{n} \quad , \tag{3}$$

$$\dot{c}_{ij} = (\delta_{ij}\lambda\dot{\epsilon}_{kk} + 2\mu\dot{\epsilon}_{ij} - \dot{\sigma}_{ij} - \delta_{ij}(3\lambda + 2\mu)\alpha\dot{\Theta})/2\mu \tag{4}$$

$$\dot{R} = \sqrt{\frac{2}{3}\dot{c}_{ij}\dot{c}_{ij}} \quad , \tag{5}$$

$$s_{ij} = \sigma_{ij} - \frac{1}{3}\delta_{ij}\sigma_{kk} \quad , \tag{6}$$

$$\theta' = \exp \left\{ \frac{-Q^*}{kT} \right\} \quad \text{for } T \geq 0.6T_m \quad , \tag{7}$$

$$\theta' = \exp \left\{ \frac{-Q^*}{0.6\,kT} \ln \left(1 + \frac{0.6T_m}{T} \right) \right\} \quad \text{for } T < 0.6T_m \tag{8}$$

Material constants: $n, H_1, H_2, A_1, A_2, C_2, Q^*, k$ are independent of temperature.

Material constants: $\lambda, \mu, K_0, \theta'$ depend on temperature, where K_0 is the initial value of K, and T is the temperature in °K.

Appendix 5. Miller's Theory (Integral Form)

$$\sigma_{ij}(t) = \frac{2}{3}\Omega_{ij}(t) + \delta_{ij}\int_0^t \left(\lambda(\Theta(\xi)) + \frac{2}{3}\mu(\Theta(\xi))\right)\left(\frac{\partial\epsilon_{kk}}{\partial\xi} - 3\alpha(\Theta(\xi))\frac{\partial\Theta}{\partial\xi}\right)d\xi + \int_0^t e^{-\{Q(t)-Q(\xi)\}}\left(2\mu(\Theta(\xi))\frac{\partial\epsilon_{ij}}{\partial\xi} - \delta_{ij}\frac{2}{3}\mu(\Theta(\xi))\frac{\partial\epsilon_{kk}}{\partial\xi} - \frac{2}{3}\frac{\partial\Omega_{ij}}{\partial\xi}\right)d\xi, \tag{1}$$

$$\Omega_{ij}(t) = H_1\int_0^t e^{-\{G(t)-G(\xi)\}}\frac{\partial c_{ij}}{\partial\xi}d\xi, \tag{2}$$

$$K(t) = K_0 + H_2\int_0^t \left(C_2 + \sqrt{\frac{2}{3}\Omega_{ij}(\xi)\Omega_{ij}(\xi)} - A_2 K^3(\xi)/A_1\right)e^{-\{J(t)-J(\xi)\}}\frac{\partial R}{\partial\xi}d\xi, \tag{3}$$

$$c_{ij}(t) = \int_0^t \left(\delta_{ij}\lambda(\Theta(\xi))\frac{\partial\epsilon_{kk}}{\partial\xi} + 2\mu(\Theta(\xi))\frac{\partial\epsilon_{ij}}{\partial\xi} - \frac{\partial\sigma_{ij}}{\partial\xi} - \delta_{ij}\alpha(\Theta(\xi))\left(3\lambda(\Theta(\xi)) + 2\mu(\Theta(\xi))\right)\frac{\partial\Theta}{\partial\xi}\right)d\xi, \tag{4}$$

$$Q(t) = \int_0^t \frac{3\mu(\Theta(\xi))}{K(\xi)}\left\{\sinh^{-1}\left(\frac{1}{B\theta'(\Theta(\xi))}\frac{\partial R}{\partial\xi}\right)^{\frac{1}{n}}\right\}^{-\frac{2}{3}}\frac{\partial R}{\partial\xi}d\xi, \tag{5}$$

$$G(t) = H_1\int_0^t B\theta'(\Theta(\xi))\frac{\left\{\sinh\left(A_1\sqrt{\frac{2}{3}\Omega_{ij}(\xi)\Omega_{ij}(\xi)}\right)\right\}^n}{\sqrt{\frac{2}{3}\Omega_{ij}(\xi)\Omega_{ij}(\xi)}}d\xi, \tag{6}$$

$$J(t) = H_2 C_2\int_0^t B\theta'(\Theta(\xi))\frac{\left\{\sinh(A_2 K^3(\xi))\right\}^n}{K(\xi) - K_0}d\xi, \tag{7}$$

$$R(t) = \int_0^t \sqrt{\frac{2}{3}\frac{\partial c_{ij}}{\partial\xi}\frac{\partial c_{ij}}{\partial\xi}}d\xi \tag{8}$$

137

Appendix 6. Lee and Zaverl's Theory (Isotropic Form)

For $\dfrac{2}{3}\left(\dfrac{3}{2}s_{ij}-\Omega_{ij}\right)\left(\dfrac{3}{2}s_{ij}-\Omega_{ij}\right)>Y^2$,

$$\dot{c}_{ij}=\left(\frac{\sqrt{\frac{2}{3}\left(\frac{3}{2}s_{ij}-\Omega_{ij}\right)\left(\frac{3}{2}s_{ij}-\Omega_{ij}\right)}}{K}\right)^n\left\{\exp\left[-\frac{B}{k\Theta}\left(-\sqrt{\frac{\sqrt{\frac{2}{3}\left(\frac{3}{2}s_{ij}-\Omega_{ij}\right)\left(\frac{3}{2}s_{ij}-\Omega_{ij}\right)}}{K}}\right)\right]+\exp\left[-\frac{D}{k\Theta}\right]\right\}\frac{\left(\frac{3}{2}s_{ij}-\Omega_{ij}\right)}{\sqrt{\frac{2}{3}\left(\frac{3}{2}s_{ij}-\Omega_{ij}\right)\left(\frac{3}{2}s_{ij}-\Omega_{ij}\right)}} \quad , \tag{1}$$

$$\dot{\Omega}_{ij}=\frac{q\dot{R}\left(cs_{ij}+\sigma_{ij}^{s}-\Omega_{ij}\right)}{\sqrt{\frac{2}{3}\left(\frac{3}{2}s_{ij}-\Omega_{ij}\right)\left(\frac{3}{2}s_{ij}-\Omega_{ij}\right)}}\quad\text{where}\quad\dot{\sigma}_{ij}^{s}=\frac{g\dot{R}s_{ij}}{\sqrt{\frac{2}{3}\left(\frac{3}{2}s_{ij}-\Omega_{ij}\right)\left(\frac{3}{2}s_{ij}-\Omega_{ij}\right)}}\quad , \tag{2}$$

$$\dot{Y}=\frac{q\dot{R}\left(Y^{s}-Y\right)}{\sqrt{\frac{2}{3}\left(\frac{3}{2}s_{ij}-\Omega_{ij}\right)\left(\frac{3}{2}s_{ij}-\Omega_{ij}\right)}}\quad\text{where}\quad\dot{Y}^{s}=\frac{h\dot{R}}{\sqrt{\frac{2}{3}\left(\frac{3}{2}s_{ij}-\Omega_{ij}\right)\left(\frac{3}{2}s_{ij}-\Omega_{ij}\right)}}\quad , \tag{3}$$

$$K=\alpha Y ,$$

$$\dot{c}_{ij}=\left(\delta_{ij}\lambda\dot{\epsilon}_{kk}+2\mu\dot{\epsilon}_{ij}-\dot{\sigma}_{ij}-\delta_{ij}(3\lambda+2\mu)\alpha\dot{\Theta}\right)/2\mu \quad , \tag{4}$$

$$\dot{R}=\sqrt{\frac{2}{3}\dot{c}_{ij}\dot{c}_{ij}} \quad , \qquad s_{ij}=\sigma_{ij}-\frac{1}{3}\delta_{ij}\sigma_{kk} \quad .$$

Material constants: $\lambda,\mu,K_0,Y_0,n,q,c,g,h,\alpha$ depend on temperature, where K_0 and Y_0 are the initial values of K and Y.

Material constants: B,D,k are temperature independent.

Appendix 7. Bodner, Partom and Stouffer's Theory (Isotropic Form)

$$\dot{c}_{ij} = D_0 \exp\left[-\frac{1}{2}\left(\frac{Z_{ij}^2}{\sqrt{\frac{3}{2}s_{ij}s_{ij}}}\right)^n\right] \frac{s_{ij}}{\sqrt{\frac{3}{2}s_{ij}s_{ij}}}, \tag{1}$$

$$Z_{ij} = \overset{o}{Z} + \int_0^t q\frac{\partial Z}{\partial \xi}\,d\xi + \frac{\dot{c}_{ij}}{|\dot{c}_{ij}|}\int_0^t (1-q)\frac{\partial Z}{\partial \xi}\frac{\dot{c}_{ij}(\xi)}{|\dot{c}_{ij}(\xi)|}\,d\xi, \tag{2}$$

$$\dot{Z} = m(z_1 - z_0)e^{-m\int_0^t s_{ij}\frac{\partial c_{ij}}{\partial \xi}\,d\xi}\, s_{ij}\dot{c}_{ij}, \tag{3}$$

$$\dot{c}_{ij} = (\delta_{ij}\lambda\dot{\epsilon}_{kk} + 2\mu\dot{\epsilon}_{ij} - \dot{\sigma}_{ij} - \delta_{ij}(3\lambda + 2\mu)\alpha\dot{\Theta})/2\mu, \tag{4}$$

$$s_{ij} = \sigma_{ij} - \frac{1}{3}\delta_{ij}\sigma_{kk}. \tag{5}$$

Material constants: $\lambda, \mu, D_0, \overset{o}{Z}, q, m, n, z_1, z_0$ depend on temperature

The quantity Z_{ij} is not a tensor, but depends on the sign of the ij^{th} component of the inelastic strain rate.

Appendix 8. Krieg, Swearengen and Rohde's Theory (Differential Form)

$$\dot{c}_{ij} = \left(\frac{\sqrt{\frac{2}{3}\left(\frac{3}{2}s_{ij}-\Omega_{ij}\right)\left(\frac{3}{2}s_{ij}-\Omega_{ij}\right)}}{K} \right)^n \; \frac{\left(\frac{3}{2}s_{ij}-\Omega_{ij}\right)}{\sqrt{\frac{2}{3}\left(\frac{3}{2}s_{ij}-\Omega_{ij}\right)\left(\frac{3}{2}s_{ij}-\Omega_{ij}\right)}} \tag{1}$$

$$\dot{\Omega}_{ij} = A_1 \dot{c}_{ij} - A_2 \Omega_{ij} \sqrt{\frac{2}{3}\Omega_{pq}\Omega_{pq}} \left(e^{A_3 \frac{2}{3}\Omega_{pq}\Omega_{pq}} - 1 \right), \tag{2}$$

$$\dot{K} = A_4 \dot{R} - A_5 (K-K_0)^n, \tag{3}$$

$$\dot{c}_{ij} = (\delta_{ij}\lambda\dot{\epsilon}_{kk} + 2\mu\dot{\epsilon}_{ij} - \dot{\sigma}_{ij} - \delta_{ij}(3\lambda+2\mu)\alpha\dot{\Theta})/2\mu, \tag{4}$$

$$\dot{R} = \sqrt{\frac{2}{3}\dot{c}_{ij}\dot{c}_{ij}}, \tag{5}$$

$$s_{ij} = \sigma_{ij} - \frac{1}{3}\delta_{ij}\sigma_{kk}. \tag{6}$$

Material constants: $\lambda, \mu, n, A_1, A_2, A_3, A_4, A_5, K_0$ depend on temperature, where K_0 is the initial value of K.

Appendix 9. Krieg, Swearengen and Rohde's Theory (Integral Form)

$$\sigma_{ij}(t) = \frac{2}{3}\,\Omega_{ij}(t) + \delta_{ij}\int_0^t \left(\lambda(\Theta(\xi)) + \frac{2}{3}\,\mu\,(\Theta(\xi))\right)\left(\frac{\partial\epsilon_{kk}}{\partial\xi} - 3\alpha(\Theta(\xi))\frac{\partial\Theta}{\partial\xi}\right)d\xi + \int_0^t e^{-\{Q(t)-Q(\xi)\}}\left(2\mu(\Theta(\xi))\frac{\partial\epsilon_{ij}}{\partial\xi} - \delta_{ij}\frac{2}{3}\,\mu\,(\Theta(\xi))\frac{\partial\epsilon_{kk}}{\partial\xi} - \frac{2}{3}\frac{\partial\Omega_{ij}}{\partial\xi}\right)d\xi, \tag{1}$$

$$\Omega_{ij}(t) = \int_0^t A_1(\Theta(\xi))e^{-\{G(t)-G(\xi)\}}\frac{\partial c_{ij}}{\partial\xi}\,d\xi, \tag{2}$$

$$K(t) = K_0(\Theta(t)) + \int_0^t A_3(\Theta(\xi))e^{-\{J(t)-J(\xi)\}}\frac{\partial R}{\partial\xi}\,d\xi, \tag{3}$$

$$c_{ij}(t) = \int_0^t \left(\delta_{ij}\lambda(\Theta(\xi))\frac{\partial\epsilon_{kk}}{\partial\xi} + 2\mu\,(\Theta(\xi))\frac{\partial\epsilon_{ij}}{\partial\xi} - \frac{\partial\sigma_{ij}}{\partial\xi} - \delta_{ij}\alpha(\Theta(\xi))\left(3\lambda(\Theta(\xi)) + 2\mu(\Theta(\xi))\right)\frac{\partial\Theta}{\partial\xi}\right)d\xi, \tag{4}$$

$$Q(t) = \int_0^t \frac{3\mu(\Theta(\xi))}{K(\xi)}\left(\frac{\partial R}{\partial\xi}\right)^{1-1/n(\Theta(\xi))}d\xi, \tag{5}$$

$$G(t) = \int_0^t A_2(\Theta(\xi))\sqrt{\frac{2}{3}\,\Omega_{ij}(\xi)\,\Omega_{ij}(\xi)}\left(e^{A_3(\Theta(\xi))\frac{2}{3}\Omega_{ij}(\xi)\Omega_{ij}(\xi)} - 1\right)d\xi, \tag{6}$$

$$J(t) = \int_0^t A_4(\Theta(\xi))\left(K(\xi) - K_0(\Theta(\xi))\right)^{n(\Theta(\xi))-1}d\xi, \tag{7}$$

$$R(t) = \int_0^t \sqrt{\frac{2}{3}\frac{\partial c_{ij}}{\partial\xi}\frac{\partial c_{ij}}{\partial\xi}}\,d\xi. \tag{8}$$

Appendix 10. Cernocky and Krempl's Theory (Integral Form)

$$\sigma_{ij}(t) = \Omega_{ij}(t) + \int_0^t e^{-\{Q(t) - Q(\xi)\}} \left(2\mu(\Theta(\xi)) \frac{\partial \epsilon_{ij}}{\partial \xi} + \delta_{ij} \lambda(\Theta(\xi)) \frac{\partial \epsilon_{kk}}{\partial \xi} - \frac{\partial \Omega_{ij}}{\partial \xi} - \delta_{ij} \alpha(\Theta(\xi)) \left(3\lambda(\Theta(\xi)) + 2\mu(\Theta(\xi)) \right) \frac{\partial \Theta}{\partial \xi} \right) d\xi, \tag{1}$$

$$\Omega_{ij}(t) = \frac{\Psi_{ij}(t)}{\sqrt{\Psi_{ij}(t)\Psi_{ij}(t)}} \left\{ E_t(\Theta(t)) \sqrt{\Psi_{ij}(t)\Psi_{ij}(t)} + \frac{(E(\Theta(t)) - E_t(\Theta(t)))}{2a(\Theta(t)) \tanh[b(\Theta(t))]} \ln \left(\frac{\cosh\left(b(\Theta(t)) + a(\Theta(t))\sqrt{\Psi_{ij}(t)\Psi_{ij}(t)}\right)}{\cosh\left(b(\Theta(t)) - a(\Theta(t))\sqrt{\Psi_{ij}(t)\Psi_{ij}(t)}\right)} \right) \right\}, \tag{2}$$

$$\Psi_{ij}(t) = \left[\delta_{ij} \lambda(\Theta(t)) \epsilon_{kk}(t) + 2\mu(\Theta(t)) \epsilon_{ij}(t) - \delta_{ij} \alpha(\Theta(t)) \left(3\lambda(\Theta(t)) + 2\mu(\Theta(t)) \right) \right] / E(\Theta(t)), \tag{3}$$

$$Q(t) = \int_0^t \frac{d\xi}{J(\xi)}, \tag{4}$$

$$J(t) = K(\Theta(t)) \exp\left\{ \delta(\Theta(t)) \exp\left[-\zeta(\Theta(t)) \sqrt{(\sigma_{ij}(t) - \Omega_{ij}(t))(\sigma_{ij}(t) - \Omega_{ij}(t))'} \right] \right\}. \tag{5}$$

Material "constants": $\lambda, \mu, E_t, a, b, K, \delta, \zeta$ depend on temperature, $E = $ Young's modulus $= \dfrac{\mu(3\lambda + 2\mu)}{\lambda + \mu}$.

Material "constants": $E_t, a, b, K, \delta, \zeta$ are updated under cyclic loading conditions.

In this particular formulation it is assumed that Poisson's ratio is constant. This assumption can easily be relaxed.

Appendix 11. Hart's Theory

$$\dot{c}_{ij} = \dot{a}^* \left(\frac{\sqrt{\frac{2}{3}\left(\frac{3}{2}s_{ij}-\Omega_{ij}\right)\left(\frac{3}{2}s_{ij}-\Omega_{ij}\right)}}{K} \right)^n \frac{\left(\frac{3}{2}s_{ij}-\Omega_{ij}\right)}{\sqrt{\frac{2}{3}\left(\frac{3}{2}s_{ij}-\Omega_{ij}\right)\left(\frac{3}{2}s_{ij}-\Omega_{ij}\right)}} \quad , \tag{1}$$

$$\dot{\Omega}_{ij} = K\dot{c}_{ij} - Kf \frac{(\sigma^*)^m \, \Omega_{ij}}{\sqrt{\frac{2}{3}\Omega_{pq}\Omega_{pq}} \left(\ell n \frac{\sigma^*}{\sqrt{\frac{2}{3}\Omega_{pq}\Omega_{pq}}}\right)^{1/\beta}} \quad , \tag{2}$$

$$\dot{\sigma}^* = \frac{Cf(\sigma^*)^{m+1}\Gamma(\sigma^*,\Omega)}{\left(\ell n \frac{\sigma^*}{\sqrt{\frac{2}{3}\Omega_{pq}\Omega_{pq}}}\right)^{1/\beta}} \quad , \tag{3}$$

$$\Gamma(\sigma^*,\Omega) = \left(\frac{\gamma}{\sigma^*}\right)^\delta , \quad \text{(other forms were also considered in Delph's review paper [23]} \tag{4}$$

$$\dot{c}_{ij} = (\delta_{ij}\lambda\dot{\epsilon}_{kk} + 2\mu\dot{\epsilon}_{ij} - \dot{\sigma}_{ij} - \delta_{ij}(3\lambda+2\mu)\alpha\dot{\Theta})/2\mu \quad ,$$

$$s_{ij} = \sigma_{ij} - \frac{1}{3}\delta_{ij}\sigma_{kk} . \tag{5}$$

Material constants: $\lambda, \mu, \dot{a}^*, K, n, f, \sigma_0^*, m, \beta, C, \gamma, \delta$ depend on temperature where σ_0^* is the initial value of σ^*

Appendix 12. Valanis' Theory (Isothermal Form)

$$\sigma_{ij}(t) = \delta_{ij}\left(\lambda + \frac{2}{3}\mu\right)\epsilon_{kk}(t) + \int_0^t G\left[z(t) - z(\xi)\right]\left\{\frac{\partial\epsilon_{ij}}{\partial\xi} - \frac{1}{3}\delta_{ij}\frac{\partial\epsilon_{kk}}{\partial\xi}\right\}d\xi ,\tag{1}$$

$$G\left[z(t) - z(\xi)\right] = G_1 e^{-\alpha_1\left[z(t) - z(\xi)\right]} + G_2 e^{-\alpha_2\left[z(t) - z(\xi)\right]} ,\tag{2}$$

$$z(t) = \frac{1}{\beta}\ln\left(1 - \beta R(t)\right),\tag{3}$$

$$R(t) = \int_0^t \frac{\partial\theta}{\partial\xi} f\left(\frac{\partial\theta}{\partial\xi}\right) d\xi ,\tag{4}$$

$$\frac{\partial\theta}{\partial\xi} = \sqrt{\frac{2}{3}\frac{\partial c_{ij}}{\partial\xi}\frac{\partial c_{ij}}{\partial\xi}} ,\tag{5}$$

$$f\left(\frac{\partial\theta}{\partial\xi}\right) = \text{a function of } \frac{\partial\theta}{\partial\xi} \text{ which varies [25] according to the type of deformation (creep, relaxation),}\tag{6}$$

$$\frac{\partial c_{ij}}{\partial\xi} = \delta_{ij}\lambda\frac{\partial\epsilon_{kk}}{\partial\xi} + 2\mu\frac{\partial\epsilon_{ij}}{\partial\xi} - k\frac{\partial\sigma_{ij}}{\partial\xi} , \quad (0 < k < 1).\tag{7}$$

Material constants: $\lambda, \mu, G_1, G_2, \alpha_1, \alpha_2, \beta, k$. Further constants are needed to define $f\left(\dfrac{\partial\theta}{\partial\xi}\right)$

144

A question naturally arises as to how much heat is generated in uniaxial Hastelloy-X specimens when they are subjected to cyclic, triangular strain histories, at strain amplitudes of about $\pm$ 1 percent. The specimens are cycled at a given temperature which is monitored by thermocouples attached to the grips at the ends of the specimen. If heat is generated by the dissipation of inelastic work during cyclic loading of the specimen, the temperature of the specimen will increase above that of the oven temperature until a steady state is reached. Under steady state conditions, the rate at which heat is produced by inelastic working of the cylindrical specimen is equal to the rate at which this heat is conducted through the grips at the ends of the specimen and through radiation and conduction at the cylindrical surface of the specimen. The following calculations show that at 982°C (1800°F), for a strain rate magnitude of 3.9×10^{-3} sec^{-1}, the steady state temperature in the central part of a Hastelloy-X cylindrical button head bar specimen exceeds the oven temperature by about 0.8°C (1.4°F) due to inelastic working. At room temperature, the temperature rise in the specimen does not exceed 22°C (40°F) at a strain rate of 3.9×10^{-3} sec^{-1}, whilst at 3.9×10^{-4} sec^{-1} it does not exceed 2°C (4°F). Hence, the effects of inelastic dissipation of work into heat can be neglected in the data reduction of the Hastelloy-X tests.

The coupled heat conduction equation for a cylindrical rod under uniaxial loading may be written in the form

$$\rho s \frac{\partial^2 \Theta}{\partial r^2} = k \left(\frac{\partial^2 \Theta}{\partial r^2} + \frac{1}{r} \frac{\partial \Theta}{\partial r} + \frac{\partial^2 \Theta}{\partial z^2} \right) + D ,$$ (1)

where ρ is the density, s is the specific heat, Θ is the temperature in the specimen, and D is the rate of dissipation of work into heat due to inelastic working. In formulating Eq. (1), small heat source terms, such as that arising from the expansion and compression of the material, have been neglected in comparison with the inelastic dissipation.

Under cyclic loading, about 90 percent of the work in typical metals is dissipated as heat whilst the remainder is used to produce microstructural changes (evidenced by working hardening). Since Hastelloy-X does not work harden at elevated temperature, one may assume that all of the work is dissipated as heat and take D in the form $D = \sigma \dot{c}$ where $\dot{c}$ is the inelastic strain rate. The average dissipation rate over a hysteresis cycle is then obtained in the form

$$\overline{D} = \frac{1}{T} \oint_0^T \sigma \frac{\partial c}{\partial \xi} d\xi$$ (2)

where T is the time for one cycle.

The value of $\bar{D}$ may be found by noting that the stress-strain hysteresis loop for Hastelloy-X at 982°C (1800°F) may be represented fairly well by an elastic-perfectly plastic loop. Hence,

$$\bar{D} = \frac{1}{T} \oint_0^T \sigma \frac{\partial c}{\partial \xi} \, d\xi = \frac{\text{area of loop in fig. 70}}{T} \tag{3}$$

or

$$\bar{D} = \frac{4\sigma_{max}\Delta}{T} \, ,$$

where σ_{max} is the maximum stress in the hysteresis loop.

At large strain values ($\sim 1\%$), the total strain is approximately equal to the plastic strain, $\varepsilon \approx c$, so that the magnitude of the total strain rate is given by $|\dot{\varepsilon}| \approx 4\Delta/T$. The average dissipation rate then becomes

$$\bar{D} = \sigma_{max}|\dot{\varepsilon}| \, . \tag{4}$$

Since σ and $|\dot{\varepsilon}|$ are spatially constant throughout the rod, the average dissipation rate, given by $\bar{D}$ in Eq. (4), represents a constant source of heat.

The steady state equations governing heat conduction in the rod are:

$$\frac{\partial^2 \Theta}{\partial r^2} + \frac{1}{r} + \frac{\partial^2 \Theta}{\partial z^2} + Q = 0, \quad Q = \frac{\bar{D}}{k} \, , \tag{5}$$

$$k\frac{\partial \Theta}{\partial r} + h(\Theta - \Theta_0) = 0 \quad \text{at } r = a, \tag{6}$$

$$\Theta = \Theta_0 \quad \text{at } z = 0 \text{ and } z = \ell, \tag{7}$$

where Θ_0 is the temperature of the end grips and the oven (as measured by thermocouples on the grips).

Choosing

$$\Theta = \Theta_0 + v(r, z) + \phi(z), \tag{8}$$

146

Eqs. (5)-(7) become

$$\frac{\partial^2 v}{\partial r^2} + \frac{1}{r} \frac{\partial v}{\partial r} + \frac{\partial^2 v}{\partial v^2} + \frac{\partial^2 \phi}{\partial z^2} + Q = 0, \tag{9}$$

$$k \frac{\partial v}{\partial r} + hv = -h\phi \text{ at } r = a, \tag{10}$$

$$v = -\phi \text{ at } z = 0 \text{ and } z = \ell. \tag{11}$$

Equation (9) can be made homogeneous by choosing

$$\frac{\partial^2 \phi}{\partial z^2} + Q = 0.$$

Choosing $\phi = 0$ at $z = 0$ and $z = \ell$ then gives

$$\phi = \frac{1}{2} Q z(\ell - z), \tag{12}$$

and Eqs. (9)-(11) become:

$$\frac{\partial^2 v}{\partial r^2} + \frac{1}{r} \frac{\partial v}{\partial r} + \frac{\partial^2 v}{\partial z^2} = 0, \tag{13}$$

$$k \frac{\partial v}{\partial r} + hv = -\frac{1}{2} hQz(\ell - z) \text{ at } r = a, \tag{14}$$

$$v = 0 \text{ at } z = 0 \text{ and } z = \ell. \tag{15}$$

The solution to Eq. (13) which is finite at $r = 0$ and satisfies the boundary condition in Eq. (15) is

$$v = \sum_{n=1}^{\infty} a_n \sin \frac{n\pi z}{\ell} I_0\left(\frac{n\pi r}{\ell}\right), \tag{16}$$

where $I_0(x)$ is the Bessel function of order zero with imaginary argument given by

$$I_0(x) = J_0(ix) = \sum_{n=0}^{\infty} \frac{\left(\frac{x}{2}\right)^{2n}}{(n!)^2}.$$

147

Satisfaction of boundary condition (Eq. (14)) requires that

$$\sum_{n=1}^{\infty}\left\{\frac{kn\Pi}{\ell}I_1\left(\frac{n\Pi a}{\ell}\right)+hI_0\left(\frac{n\Pi a}{\ell}\right)\right\}a_n\sin\frac{n\Pi z}{\ell}=-\frac{1}{2}hQz(\ell-z),\qquad(17)$$

where

$$I_1(x)=\frac{dI_0(x)}{dx}=\sum_{n=0}^{\infty}\frac{\left(\frac{x}{2}\right)^{2n+1}}{n!(n+1)!}\ .$$

The Fourier expansion of $z(\ell-z)$ on the interval $(0,\ell)$ is given by

$$z(\ell-z)=\sum_{n=1}^{\infty}B_n\sin\frac{n\Pi z}{\ell}\quad\text{where}\quad B_n=\frac{2}{\ell}\int_0^{\ell}z(\ell-z)\sin\frac{n\Pi z}{\ell}\ z,$$

or

$$z(\ell-z)=\sum_{n=1}^{\infty}\frac{4\ell^2}{n^3\Pi^3}\left\{(-1)^{n+1}+1\right\}\sin\frac{n\Pi z}{\ell}.\qquad(18)$$

Comparing coefficients in Eqs. (17) and (18) gives

$$a_n=-\frac{2hQ\ell^2}{n^3\Pi^3}\ \frac{\left\{(-1)^{n+1}+1\right\}}{\left[\frac{kn\Pi}{\ell}I_0\left(\frac{n\Pi a}{\ell}\right)+hI_0\left(\frac{n\Pi a}{\ell}\right)\right]}\ .\qquad(19)$$

For $n = 2,4,6,\ldots$ the coefficients a_n in Eq. (19) are zero. Equations (8), (12), (16), and (19) then give the temperature in the rod in the form

$$\Theta=\Theta_0+\frac{1}{2}Qz(\ell-z)-\frac{4hQ\ell^2}{\Pi^3}\sum_{n=0}^{\infty}\frac{1}{(2n+1)^3}\ \frac{\sin\frac{(2n+1)\Pi z}{\ell}I_0\left[\frac{(2n+1)\Pi r}{\ell}\right]}{\left\{\frac{k(2n+1)\Pi}{\ell}I_1\left[\frac{(2n+1)\Pi a}{\ell}\right]+hI_0\left[\frac{(2n+1)\Pi a}{\ell}\right]\right\}}\ .\qquad(20)$$

The maximum excess temperature occurs in the middle of the rod where $r = 0$ and $z = \ell/2$, and is given by

$$\Theta - \Theta_0 = \Delta\Theta = \frac{Q\ell^2}{8} - \frac{4hQ\ell^2}{\Pi^3}\sum_{n=0}^{\infty}\frac{1}{(2n+1)^3}\cdot\frac{(-1)^n}{\left\{\frac{k(2n+1)\Pi}{\ell}I_1\left[\frac{(2n+1)\Pi a}{\ell}\right]+hI_0\left[\frac{(2n+1)\Pi a}{\ell}\right]\right\}}$$

From the relation $Q = \bar{D}/k = \sigma_{max}|\dot\epsilon|$, this becomes

$$\Delta\Theta = \frac{\sigma_{max}|\dot\epsilon|\ell^2}{8k} - \frac{4h\sigma_{max}|\dot\epsilon|\ell^2}{k\Pi^3}\left\{\frac{1}{\frac{k\Pi}{\ell}I_1\left(\frac{\Pi a}{\ell}\right)+hI_0\left(\frac{\Pi a}{\ell}\right)} + \frac{1}{3^3}\frac{1}{\frac{3k\Pi}{\ell}I_1\left(\frac{3\Pi a}{\ell}\right)+hI_0\left(\frac{3\Pi a}{\ell}\right)}\right.$$

$$\left. + \frac{1}{5^3}\cdot\frac{1}{\frac{5k\Pi}{\ell}I_1\left(\frac{5\Pi a}{\ell}\right)+hI_0\left(\frac{5\Pi a}{\ell}\right)} - \cdots\right\} \qquad (21)$$

The thermal conductivity k for Hastelloy-X at 982°C (1800°F) is

$$k = 195\ \frac{Btu\cdot in}{ft^2\cdot hr\cdot°F} = \frac{195 \times 778 \times 12}{144 \times 3600}\ \frac{in^2\cdot lb}{in^2\cdot sec\cdot°F} = 3.51\ \frac{lb}{sec\cdot°F}$$

The value of h is given by

$$h \approx 135\ \frac{Btu}{hr\cdot ft^2\cdot°F} = \frac{135 \times 778 \times 12}{144 \times 3600}\ \frac{in\cdot lb}{in^2\cdot sec\cdot°F} = 2.43\ \frac{lb}{in\cdot sec\cdot°F}$$

At a strain rate of $|\dot\epsilon| = 3.866 \times 10^{-3}\ sec^{-1}$ (10 cycles per minute at $\pm$ 0.6 percent strain amplitude), $\sigma_{max} = 19212$ psi. The length of the specimen is $\ell=1$ in. and its radius is $a = 0.15$ in.

Substitution of these values into Eq. (21) gives the excess temperature at the center of the rod as

From this result it can be seen that only the first term in the infinite series contributes significantly to the result. Figure 71 shows the computed steady state temperature excess, $\Delta\Theta$, in various parts of the specimen obtained by keeping only the first term in the series expansion in Eq. (20). The radial distribution of temperature in the bar is almost uniform and the axial distribution is the difference between a parabolic and sine function.

At room temperature σ_{max} = 100,000 psi at 10 cycles per minute and k = 60 Btu in./ft^2. hr. °F. The constant h is probably small, ~ 1 Btu/ft^2.hr.°F. Neglecting the series terms which account for the radial outflow of heat, one obtains $\Delta\Theta \approx$ 45°F at 10 cycles/minute and $\Delta\Theta \approx$ 4.5°F at 1 cycle/minute at room temperature.

RECURSIVE INTEGRATION METHOD FOR FUNCTIONAL THEORY

The uniaxial form of the function theory in Appendix 1 may be written, for isothermal deformations ($\dot{\Theta} = 0$), as

$$\sigma(t) = \Omega(t) + \int_0^t e^{-\left\{Q(t) - Q(\xi)\right\}} \left(E \frac{\partial \epsilon}{\partial \xi} - \frac{\partial \Omega}{\partial \xi}\right) d\xi, \tag{1}$$

$$c(t) = \int_0^t \left(\frac{\partial \epsilon}{\partial \xi} - \frac{1}{E} \frac{\partial \sigma}{\partial \xi}\right) d\xi, \tag{2}$$

$$\Omega(t) = \overset{0}{\Omega} + n_1 c(t) + n_2 \int_0^t e^{-\left\{G(t) - G(\xi)\right\}} \frac{\partial c}{\partial \xi} d\xi, \tag{3}$$

$$K(t) = K_1 - K_2 e^{-n_7 R(t)}, \tag{4}$$

$$Q(t) = \int_0^t \frac{E}{K} \left(\frac{\partial R}{\partial \xi}\right)^{1 - 1/n} d\xi, \tag{5}$$

$$G(t) = \int_0^t \left\{\left(n_3 + n_4 e^{-n_5 R(\xi)}\right) \frac{\partial R}{\partial \xi} + n_6 |\Omega(\xi)|^{m-1}\right\} d\xi, \tag{6}$$

$$R(t) = \int_0^t \left|\frac{\partial c}{\partial \xi}\right| d\xi. \tag{7}$$

The decreasing exponential function in Eq. (1) implies that most of the contribution to the integral comes from the region about the upper limit, t, where $Q(\xi) \approx Q(t)$. For general integrals of the form

$$I = \int_0^t e^{-\left\{Q(t) - Q(\xi)\right\}} \frac{\partial m(\xi)}{\partial \xi} d\xi, \tag{8}$$

it may be shown that the asymptotic expansion of the integral for large values of t is given by the relation

$$I \sim \frac{\dot{m}}{\dot{Q}} - \frac{\ddot{m}}{\dot{Q}^2} + \frac{(\dot{m}\ddot{Q} + \dddot{m})}{\dot{Q}^3} - \cdots ,$$ (9)

where dots denote differentiation with respect to time.

The first term of Eq. (9) may be applied to the integral in Eq. (1) to give an asymptotic expression for the stress well into the plastic region at large values of strain and time in the form

$$\sigma = \Omega + \frac{E\dot{\epsilon} - \dot{\Omega}}{\dot{Q}} ,$$ (10)

where

$$\dot{Q} = \frac{E}{K} \left(\frac{\partial R}{\partial t} \right)^{1-1/n} = \frac{E}{K} \left| \frac{\partial C}{\partial t} \right| = \frac{E}{K} \left| \frac{\partial \epsilon}{\partial t} - \frac{1}{E} \frac{\partial \sigma}{\partial t} \right|^{1-1/n}$$ (11)

Since $\dot{\epsilon} \gg \dot{\sigma}/E$ and $E\dot{\epsilon} \gg \dot{\Omega}$ in this large strain region, the asymptotic expression for the stress takes the form

$$\sigma = \Omega + K\dot{\epsilon}^{1/n} .$$ (12)

This relation can also be derived by assuming that $\dot{\epsilon} \gg \dot{\sigma}/E$ and $E\dot{\epsilon} \gg \dot{\Omega}$ in the uniaxial differential equation appropriate to monotonic loading, viz.,

$$\dot{C} = \dot{\epsilon} - \frac{\dot{\sigma}}{E} = \left(\frac{\sigma - \Omega}{K} \right)^n$$ (13)

In a finite element solution the strain increment $\Delta\epsilon$ is supplied to the subroutine at the beginning of each load increment, and it is assumed that the strain rate $\Delta\epsilon/\Delta t$ during the load increment is constant. It is, therefore, constant during each subincrement in a multi-step technique.

152

The integrals in Eqs. (1) and (2) contain the expressions $(E\, \partial\epsilon/\partial\xi - \partial\Omega/\partial\xi)$ and $(\partial c/\partial\xi = \partial\epsilon/\partial\xi - \partial\sigma/E\partial\xi)$. In an asymptotic expansion of these integrals (valid for large values of t) the strain rate $\partial\epsilon/\partial\xi$ is the dominant term in the two preceding expressions. Since the strain rate term is constant during the finite element load increment, it is therefore permissible, in an asymptotic expansion of the integrals, to assume that the expressions $(E\, \partial\epsilon/\partial\xi - \partial\Omega/\partial\xi)$ and $(\partial c/\partial\xi)$ are constant during the integration.

Consider the value of the stress σ_{n+1} at time t_{n+1}, assuming that the values of the stress σ_n and equilibrium stress Ω_n are known at time t_n. Then, from Eq. (1)

$$\sigma_{n+1} - \Omega_{n+1} = \int_0^{t_n} e^{-\{Q_{n+1} - Q(\xi)\}} \left(E\, \frac{\partial\epsilon}{\partial\xi} - \frac{\partial\Omega}{\partial\xi} \right) d\xi$$

$$= \int_0^{t} e^{-\{Q_{n+1} - Q(\xi)\}} \left(E\, \frac{\partial\epsilon}{\partial\xi} - \frac{\partial\Omega}{\partial\xi} \right) d\xi + \int_{t_n}^{t_{n+1}} e^{-\{Q_{n+1} - Q(\xi)\}} \left(E\, \frac{\partial\epsilon}{\partial\xi} - \frac{\partial\Omega}{\partial\xi} \right) d\xi$$

$$= (\sigma_n - \Omega_n) e^{-\{Q_{n+1} - Q_n\}} + \int_{t_n}^{t_{n+1}} e^{-\{Q_{n+1} - Q(\xi)\}} \left(E\, \frac{\partial\epsilon}{\partial\xi} - \frac{\partial\Omega}{\partial\xi} \right) d\xi .$$

$$(14)$$

For small time increments the exponential term in the integral is approximately equal to one and the integrand $(E\, \partial\epsilon/\partial\xi - \partial\Omega/\partial\xi)$ may be assumed constant in the integration over the small time interval. It is also permissible to assume that $(E\, \partial\epsilon/\partial\xi - \partial\Omega/\partial\xi)$ is constant in the asymptotic integration appropriate to large time increments. Hence, for both large and small time increments, the integral may be approximated in the form:

$$\int_{t_n}^{t_{n+1}} e^{-\{Q_{n+1} - Q(\xi)\}} \left(E\, \frac{\partial\epsilon}{\partial\xi} - \frac{\partial\Omega}{\partial\xi} \right) d\xi \approx \left[\frac{E(\epsilon_{n+1} - \epsilon_n) - (\Omega_{n+1} - \Omega_n)}{t_{n+1} - t_n} \right] \int_{t_n}^{t_{n+1}} e^{-\{Q_{n+1} - Q(\xi)\}} d\xi , \quad (15)$$

where the subscripts n and n+1 refer to the values of the variables at the times t_n and t_{n+1}.

The preceding integral may be written

$$\int_{t_n}^{t_{n+1}} e^{-\{Q_{n+1} - Q(\xi)\}} d\xi = \int_{t_n}^{t_{n+1}} \frac{e^{-\{Q_{n+1} - Q(\xi)\}}}{\dfrac{dQ(\xi)}{d\xi}} dQ(\xi), \quad (16)$$

and since

$$\frac{dQ(\xi)}{d\xi} = \frac{E}{K}\left|\frac{\partial c}{\partial \xi}\right|^{1-1/n}$$

may be assumed to be constant in the integral for both large and small time increments, the integral on the right-hand side of Eq. (9) takes the form:

$$\int_{t_n}^{t_{n+1}} e^{-\{Q_{n+1}-Q(\xi)\}} d\xi \approx \frac{e^{-Q_{n+1}}}{\left(\frac{Q_{n+1}-Q_n}{t_{n+1}-t_n}\right)} \int_{t_n}^{t_{n+1}} e^{Q(\xi)} dQ(\xi) = \left(\frac{1-e^{-\{Q_{n+1}-Q_n\}}}{\frac{Q_{n+1}-Q_n}{t_{n+1}-t_n}}\right) .$$

Equation (15) may thus be integrated in the approximate form:

$$\int_{t_n}^{t_{n+1}} e^{-\{Q_{n+1}-Q(\xi)\}}\left(E\frac{\partial \epsilon}{\partial \xi} - \frac{\partial \Omega}{\partial \xi}\right) d\xi \approx \left[E(\epsilon_{n+1}-\epsilon_n)-(\Omega_{n+1}-\Omega_n)\right]\left(\frac{1-e^{-\{Q_{n+1}-Q_n\}}}{Q_{n+1}-Q_n}\right) \quad (17)$$

For large time increments the exponential term vanishes and the integral takes the asymptotic form $(E \Delta\epsilon - \Delta\Omega)/\Delta Q = (E\dot{\epsilon} - \dot{\Omega})/\dot{Q}$, in agreement with the result in Eq. (12). For small time increments the integral assumes the approximate value $(E \Delta\epsilon - \Delta\Omega)$.

Substitution of Eq. (17) into Eq. (14) gives the recurrence relation

$$\sigma_{n+1} = \Omega_{n+1} + (\sigma_n - \Omega_n)e^{-\{Q_{n+1}-Q_n\}} + \left[E(\epsilon_{n+1}-\epsilon_n)-(\Omega_{n+1}-\Omega_n)\right]\left(\frac{1-e^{-\{Q_{n+1}-Q_n\}}}{Q_{n+1}-Q_n}\right) . \quad (18)$$

Similarly, the recurrence relation for the equilibrium stress integral in Eq. (13) may be written in the form:

$$\Omega_{n+1} = \overset{o}{\Omega} + n_1 c_{n+1} + (\Omega_n - \overset{o}{\Omega} - n_1 c_n)e^{-\{G_{n+1}-G_n\}} + n_2(c_{n+1}-c_n)\left(\frac{1-e^{-\{G_{n+1}-G_n\}}}{G_{n+1}-G_n}\right) . \quad (19)$$

In the recurrence relations in Eqs. (18) and (19), the values of Q_{n+1} and G_{n+1} at the end of the increment may be determined by the approximate relations

$$Q_{n+1} - Q_n = \Delta Q = \frac{E}{K}\left(\frac{\Delta R}{\Delta t}\right)^{1-1/n} \Delta t = \frac{E}{K}\left|\frac{\Delta c}{\Delta t}\right|^{1-1/n} \Delta t \qquad (19)$$

and

$$G_{n+1} - G_n = \Delta G = (n_3 + n_4 e^{-n_5 R_{n+1}})\, \Delta R + n_6\left|\Omega_{n+1}\right|^{m-1} \Delta t, \qquad (20)$$

where ΔR and Δc are defined by the relations

$$c_{n+1} - c_n = \Delta c = (\epsilon_{n+1} - \epsilon_n) - \frac{(\sigma_{n+1} - \sigma_n)}{E} \qquad (21)$$

and

$$R_{n+1} - R_n = \Delta R = |\Delta c|. \qquad (22)$$

Evidently, the values of σ_{n+1} and Ω_{n+1} depend on $|\Delta c|$ and are therefore implicitly defined in Eqs. (19) and (20), since $|\Delta c|$ depends on σ_{n+1}, and σ_{n+1} depends on Ω_{n+1}. An iterative technique is therefore required to resolve these equations. This iterative technique is described in Appendix 15.
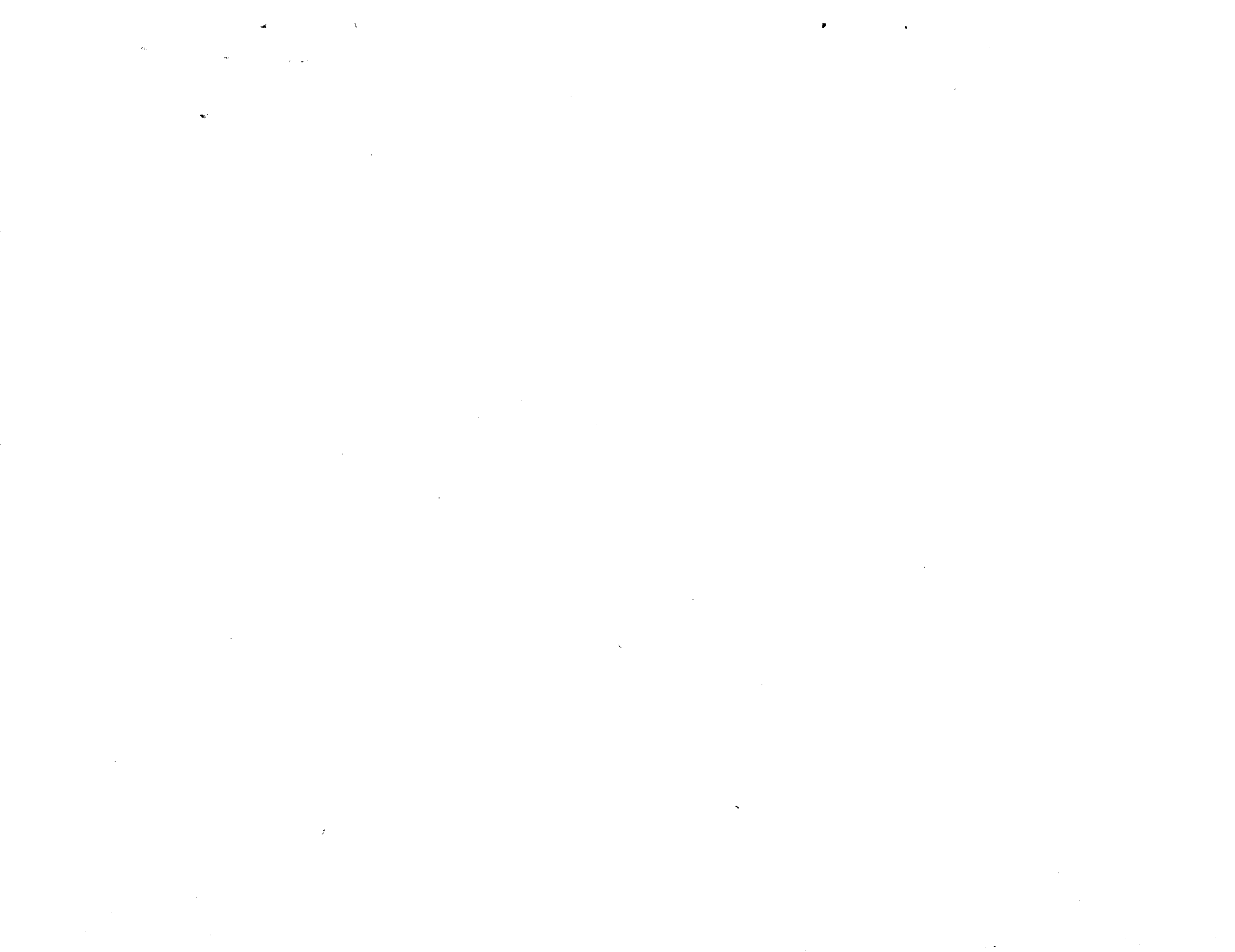
APPENDIX 15

RECURSIVE INTEGRATION METHOD FOR FUNCTIONAL THEORY
USED IN SUBROUTINE HYPELA

The integration algorithm developed in Appendix 14 is now used to integrate the three dimensional equations of Appendix 1. The solution to the implicit recursive relations is obtained by means of a Newton-Raphson technique.

In the following algorithm the symbol "Δ" in front of a variable refers to the difference in the variable between the beginning and end of the increment. The time at the beginning of the increment is denoted by t and at the end of the increment by $t + \Delta t$.

Since the stress tensor for non-polar media is symmetric, the constitutive relations are written in vector form, so that $\sigma_1 = \sigma_{11}$, $\sigma_2 = \sigma_{22}$, $\sigma_3 = \sigma_{33}$, $\sigma_4 = \sigma_{12}$, $\sigma_5 = \sigma_{23}$, $\sigma_6 = \sigma_{13}$ with similar definitions applying to c_{ij}, ε_{ij} and Ω_{ij}.

In the following algorithm the symbol $\varepsilon_i(t)$ refers to the mechanical strain, so that

$$\Delta \epsilon_i(t) = \Delta \epsilon_i^T(t) - \delta_i \alpha \Delta \Theta, \quad \delta_i = \begin{cases} 1 & \text{if } i \leq 3 \\ 0 & \text{if } i > 3 \end{cases}.$$

where, $\Delta \varepsilon_i^T(t)$ is the total strain increment. It is assumed that $\sigma_i(t)$, $\varepsilon_i(t)$, $c_i(t)$, $\Omega_i(t)$, $R(t)$, $Q(t)$ and $G(t)$ are known at the beginning of the increment. Initially, at time $t = 0$, $\sigma_i(t) = \varepsilon_i(t) = c_i(t) = 0$ and $R(t) = Q(t) = G(t) = 0$, whilst $\Omega_i(t) = \overset{\circ}{\Omega}_i(t)$.

To integrate the constitutive equations from time t to time $t + \Delta t$, the following operations are required.

Step #1. Compute the values of the material constants at the temperature $\Theta(t + 1/2 \Delta t)$ corresponding to the middle of the subincrement.

Step #2. Assume an initial guess for the inelastic strain increment Δc_i. In a subincrement method this guess is taken equal to the deviatoric strain increment in the first subincrement of the current load step. In subsequent subincrements the guess is taken from the preceding subincrement of the current load step.

156

Step #3. Compute the inelastic strain at the end of the subincrement from
the relation

$$c_i(t+\Delta t) = c_i(t) + \Delta c_i$$

Step #4. Set $\Omega_i(t + \Delta t) = \Omega_i(t)$ as a first guess for the equilibrium
stress at the end of the subincrement.

Step #5. Compute the initial values of the equilibrium stress at the end of
the subincrement from the relations

$$\overset{0}{\Omega}_1(t+\Delta t) = -\overset{0}{\Omega} + 2\overset{0}{\Omega}\left\{c_1^2(t+\Delta t) + c_4^2(t+\Delta t) + c_6^2(t+\Delta t)\right\}/\overset{0}{\Omega}_{II}\,,$$

$$\overset{0}{\Omega}_2(t+\Delta t) = -\overset{0}{\Omega} + 2\overset{0}{\Omega}\left\{c_2^2(t+\Delta t) + c_4^2(t+\Delta t) + c_6^2(t+\Delta t)\right\}/\overset{0}{\Omega}_{II}\,,$$

$$\overset{0}{\Omega}_3(t+\Delta t) = -\overset{0}{\Omega} + 2\overset{0}{\Omega}\left\{c_3^2(t+\Delta t) + c_5^2(t+\Delta t) + c_6^2(t+\Delta t)\right\}/\overset{0}{\Omega}_{II}\,,$$

$$\overset{0}{\Omega}_4(t+\Delta t) = 2\overset{0}{\Omega}\left\{c_1(t+\Delta t)\,c_4(t+\Delta t) + c_2(t+\Delta t)\,c_4(t+\Delta t) + c_5(t+\Delta t)\,c_6(t+\Delta t)\right\}/\overset{0}{\Omega}_{II}\,,$$

$$\overset{0}{\Omega}_5(t+\Delta t) = 2\overset{0}{\Omega}\left\{c_4(t+\Delta t)\,c_6(t+\Delta t) + c_2(t+\Delta t)\,c_5(t+\Delta t) + c_3(t+\Delta t)\,c_5(t+\Delta t)\right\}/\overset{0}{\Omega}_{II}\,,$$

$$\overset{0}{\Omega}_6(t+\Delta t) = 2\overset{0}{\Omega}\left\{c_1(t+\Delta t)\,c_6(t+\Delta t) + c_4(t+\Delta t)\,c_5(t+\Delta t) + c_3(t+\Delta t)\,c_6(t+\Delta t)\right\}/\overset{0}{\Omega}_{II}\,,$$

where

$$\overset{0}{\Omega}_{II} = \frac{2}{3}\left\{c_1^2(t+\Delta t) + c_2^2(t+\Delta t) + c_3^2(t+\Delta t) + 2\left[c_4^2(t+\Delta t) + c_5^2(t+\Delta t) + c_6^2(t+\Delta t)\right]\right\}.$$

Step #6. Compute the cumulative inelastic strain increment from the relation

$$\Delta R = \sqrt{\sum_{i=1}^{6}\frac{2}{3}\beta_i(\Delta c_i)^2} \quad \text{where } \beta_i = \begin{cases} 1 \text{ if } i \le 3 \\ 2 \text{ if } i > 3 \end{cases}.$$

157

Step #7.   Let subscript m refer to the number of iterations.

Set $m = 0$.

Step #8.   Set $m = m + 1$.   This is the start of the iteration loop.

Step #9.   Set $\Delta R_m = \Delta R$.   Compute the cumulative inelastic strain at the end of the subincrement from the relation

$$R(t+\Delta t) = R(t) + \Delta R$$

Step #10. Evaluate the drag stress at the end of the subincrement from the relation

$$K(t+\Delta t) = K_1 - K_2 \, e^{-n_7 R(t+\Delta t)} .$$

Step #11. Evaluate the mth guess for ΔG from the relation

$$\Delta G_m = \left[n_3 + n_4 \, e^{-n_5 R(t+\Delta t)} \right] \Delta R + n_6 \, \Delta t \left[\sum_{i=1}^{6} \frac{2}{3} \, \beta_i \, \Omega_i^2 \, (t+\Delta t) \right]^{\frac{m-1}{2}} .$$

Step #12. Compute the inelastic strain at the end of the subincrement from the relation

$$c_i (t+\Delta t) = c_i (t) + \Delta c_i .$$

Step #13. Compute the equilibrium stress at the end of the subincrement from the recursive relation

$$\Omega_i (t+\Delta t, \Delta G_m) = \overset{o}{\Omega}_i (t+\Delta t) + n_1 \, c_i (t+\Delta t) + (\Omega_i(t) - \overset{o}{\Omega}_i(t) - n_1 c_i(t)) \, e^{-\Delta G_m} + \Delta c_i \left(\frac{1 - e^{-\Delta G_m}}{\Delta G_m} \right) .$$

Note that this is an implicit relation for the determination of $\Omega_i(t + \Delta t)$ since ΔG_m depends on $\Omega_i(t + \Delta t)$ if the recovery term involving n_6 is present (cf. Step #11).   If $n_6 = 0$ and there is no recovery, this relation for $\Omega_i(t + \Delta t)$ is explicit and no iteration is required for its determination.

Step #15. Compute equilibrium stress increment from the relation

$$\Delta \Omega_i = \Omega_i (t+\Delta t, \Delta G_m) - \Omega_i (t) .$$

If $n_6 = 0$, skip the Newton–Raphson iteration for $\Omega_i(t + \Delta t)$ and go to step #20.

Step #16. Compute the function $f(\Delta G_m)$ where

$$f(\Delta G_m) = \Delta G_m - \left[n_3 + n_4 \, e^{-n_5 R(t+\Delta t)} \right] \Delta R - n_6 \, \Delta t \left[\sum_{i=1}^{6} \frac{2}{3} \, \beta_i \, \Omega_i^2 (t+\Delta t, \Delta G_m) \right]^{\frac{m-1}{2}} .$$

Note that if ΔG_m, the guess for ΔG computed in Step #11, is exact, then $f(\Delta G_m) = 0$. In general $f(\Delta G_m) \neq 0$ and a Newton–Raphson iteration is required to improve the value of ΔG_m. (Note that the exact ΔG_m satisfies both Step #13 and the relation $f(\Delta G_m) = 0$.)

Step #17. Compute the derivative

$$\frac{\partial f(\Delta G_m)}{\partial (\Delta G_m)} = 1 - \frac{1}{2}(m-1) n_6 \Delta t \left[\sum_{i=1}^{6} \frac{2}{3} \, \beta_i \, \Omega_i^2 (t+\Delta t, \Delta G_m) \right]^{\frac{m-3}{2}}$$

$$\left[\sum_{i=1}^{6} \frac{4}{3} \, \beta_j \, \Omega_j(t+\Delta t, \Delta G_m) \, \frac{\partial \Omega_j(t+\Delta t, \Delta G_m)}{\partial (\Delta G_m)} \right]$$

where

$$\frac{\partial \Omega_j(t+\Delta t, \Delta G_m)}{\partial (\Delta G_m)} = -(\Omega_j(t) - \overset{o}{\Omega}_j(t) - n_1 c_j(t)) e^{-\Delta G_m} + n_2 \Delta c_j \left(\frac{\Delta G_m e^{-\Delta G_m} + e^{-\Delta G_m} - 1}{(\Delta G_m)^2} \right)$$

by differentiation of the relation in Step #13.

Step #18. Refine ΔG_m with a Newton–Raphson iteration

$$\Delta G_{m+1} = \Delta G_m - \frac{f(\Delta G_m)}{\dfrac{\partial f(\Delta G_m)}{\partial (\Delta G_m)}} .$$

Step #19. Compute refined value for the equilibrium stress at the end of the subincrement from the relation

$$\Omega_i(t+\Delta t, \Delta G_{m+1}) = \overset{o}{\Omega}_i(t+\Delta t) + n_1 c_i(t+\Delta t) + (\Omega_i(t) - \overset{o}{\Omega}_i(t) - n_1 c_i(t)) e^{-\Delta G_{m+1}} + \Delta c_i \left(\frac{1 - e^{-\Delta G_{m+1}}}{\Delta G_{m+1}} \right) .$$

159

Compute equilibrium stress increment from the relation

$$\Delta \Omega_i = \Omega_i(t + \Delta t, \Delta G_{m+1}) - \Omega_i(t) .$$

Step #20. Compute the mth guess for ΔQ from the relation

$$\Delta Q_m = \frac{3\mu}{K(t + \Delta t)} \left(\frac{\Delta R}{\Delta t}\right)^{1-1/n} \Delta t .$$

Note that ΔQ_m depends on $\sigma_i(t + \Delta t)$ through its dependence on ΔR (cf. Steps #'s 22 and 24).

Step #21. Compute the stress at the end of the subincrement from the recursive relation

$$\sigma_i(t+\Delta t, \Delta Q_m) = \frac{2}{3}\Omega_i(t+\Delta t) + \alpha_i \left(\sum_{j=1}^{3} \frac{1}{3}\sigma_j(t) + \left(\lambda + \frac{2}{3}\mu\right)\sum_{j=1}^{3}\Delta\epsilon_j\right)$$

$$+ \left(\sigma_i(t) - \frac{2}{3}\Omega_i(t) - \alpha_i \sum_{j=1}^{3}\frac{1}{3}\sigma_j(t)\right) e^{-\Delta Q_m} + \left(2\mu\Delta\epsilon_i - \alpha_i \frac{2}{3}\mu\sum_{j=1}^{3}\Delta\epsilon_j \frac{2}{3}\Delta\Omega_i\right)\left(\frac{1 - e^{-\Delta Q_m}}{\Delta Q_m}\right)$$

where $\alpha_i = \begin{cases} 1 & \text{if } i \leq 3 \\ 0 & \text{if } i > 3 \end{cases}$.

This is an implicit relation for $\sigma_i(t + \Delta t, \Delta Q_m)$, since ΔQ_m depends on $\sigma_i(t + \Delta t)$, which must be resolved by Newton-Raphson iteration.

Step #22. Compute the inelastic strain increment from the relation

$$\Delta c_i(\Delta Q_m) = \left\{\alpha_i \lambda \sum_{j=1}^{3} \Delta\epsilon_j + 2\mu\Delta\epsilon_i - \sigma_i(t+\Delta t, \Delta Q_m) + \sigma_i(t)\right\} / 2\mu .$$

Step #23. Compute inelastic strain at the end of the subincrement from the relation

$$c_i(t + \Delta t) = c_i(t) + \Delta c_i(\Delta Q_m).$$

Step #24. Compute the cumulative inelastic strain increment

$$\Delta R(\Delta Q_m) = \sqrt{\sum_{i=1}^{6} \frac{2}{3} \beta_i \left[\Delta c_i(\Delta Q_m)\right]^2} .$$

Step #24. Compute the function $F(\Delta Q_m)$ where

$$F(\Delta Q_m) = \Delta Q_m - \frac{3\mu}{K(t+\Delta t)} \left[\frac{\Delta R(\Delta Q_m)}{\Delta t}\right]^{1-1/n} \Delta t .$$

Note that ΔQ_m was evaluated in Step #20 and is used to evaluate $\Delta R(\Delta Q_m)$ in Step #24. If the exact value of ΔQ_m is known, then $F(\Delta Q_m) = 0$. In general, $F(\Delta Q_m) \neq 0$ and ΔQ_m must be refined by a Newton-Raphson iteration. (Note that the exact ΔQ_m satisfies both Step #21 and the relation $F(\Delta Q_m) = 0$.)

Step #26. Compute the derivative

$$\frac{\partial F(\Delta Q_m)}{\partial(\Delta Q_m)} = 1 - \frac{3\mu}{K(t+\Delta t)} \left(1 - \frac{1}{n}\right)\left[\frac{\Delta R(\Delta Q_m)}{\Delta t}\right]^{-1/n} \frac{\partial(\Delta R(\Delta Q_m))}{\partial(\Delta Q_m)} \Delta t$$

where

$$\frac{\partial(\Delta R(\Delta Q_m))}{\partial(\Delta Q_m)} = \frac{\partial}{\partial(\Delta Q_m)} \sqrt{\sum_{i=1}^{6} \frac{2}{3} \beta_i \left[\Delta c_i(\Delta Q_m)\right]^2} = \frac{1}{\Delta R(\Delta Q_m)} \sum_{i=1}^{6} \frac{2}{3} \beta_i \Delta c_i(\Delta Q_m) \frac{\partial(\Delta c_i(\Delta Q_m))}{\partial(\Delta Q_m)}$$

The derivative $\partial(\Delta c_i(\Delta Q_m))/\partial(\Delta Q_m)$ is obtained from differentiation of the relation for $\Delta c_i(\Delta Q_m)$ in Step #22 in the form

$$\frac{\partial(\Delta c_i(\Delta Q_m))}{\partial(\Delta Q_m)} = -\frac{1}{2\mu} \frac{\partial \sigma_i(t+\Delta t, \Delta Q_m)}{\partial(\Delta Q_m)}$$

$$= \frac{1}{2\mu} \left\{ \left(\sigma_i(t) - \frac{2}{3}\Omega_i(t) - \alpha_i \sum_{j=1}^{3} \frac{1}{3}\sigma_j(t)\right) e^{-\Delta Q_m} - \left(2\mu\Delta\epsilon_i - \sigma_i\frac{2}{3}\mu\sum_{j=1}^{3}\Delta\epsilon_j - \frac{2}{3}\Delta\Omega_i\right) \left(\frac{\Delta Q_m e^{-\Delta Q_m} + e^{-\Delta Q_m} - 1}{(\Delta Q_m)^2}\right) \right\} .$$

161

Step #27. Refine ΔQ_m with a Newton-Raphson iteration

$$\Delta Q_{m+1} = \Delta Q_m - \frac{F(\Delta Q_m)}{\dfrac{\partial F(\Delta Q_m)}{\partial (\Delta Q_m)}} \ .$$

Step #28. Compute refined value of stress at the end of the subincrement from the relation

$$\sigma_i(t+\Delta t, \Delta Q_{m+1}) = \frac{2}{3}\Omega_i(t+\Delta t) + \alpha_i\left(\sum_{j=1}^{3}\frac{1}{3}\sigma_j(t) + \left(\lambda + \frac{2}{3}\mu\right)\sum_{j=1}^{3}\Delta\epsilon_j\right)$$

$$+\left(\sigma_i(t) - \frac{2}{3}\Omega_i(t) - \alpha_i\sum_{j=1}^{3}\frac{1}{3}\sigma_j(t)\right)e^{-\Delta Q_{m+1}} + \left(2\mu\Delta\epsilon_i - \alpha_i\frac{2}{3}\mu\sum_{j=1}^{3}\Delta\epsilon_j - \frac{2}{3}\Delta\Omega_i\right)\left(\frac{1-e^{-\Delta Q_{m+1}}}{\Delta Q_{m+1}}\right) \ .$$

Step #29. Compute refined value of inelastic strain increment from the relation

$$\Delta c_i(\Delta Q_{m+1}) = \left\{\alpha_i\lambda\sum_{j=1}^{3}\Delta\epsilon_j + 2\mu\Delta\epsilon_i - \sigma_i(t+\Delta t, \Delta Q_{m+1}) + \sigma_i(t)\right\}/2\mu \ .$$

Step #30. Compute refined value of cumulative inelastic strain increment

$$\Delta R = \sqrt{\sum_{i=1}^{6}\frac{2}{3}\beta_i\left[\Delta c_i(\Delta Q_{m+1})\right]^2} \ .$$

Step #31. If increment is elastic after two Newton-Raphson iterations, exit from the iteration loop:

$$\text{If } \Delta R < \frac{1}{100}\sqrt{\sum_{i=1}^{6}\frac{2}{3}\beta_i\left[\Delta\epsilon_i\right]^2} \text{ and } m=2, \text{ go to Step } \#35 \ .$$

Step #32. If m = maximum number of iterations allowed, go to Step #35.

Step #33. If m < maximum number of iterations allowed, go to Step #8.

162

Step #34.   If $\left| \dfrac{\Delta R - \Delta R_m}{\Delta R_m} \right| > \dfrac{1}{100}$, go to step #8.

Step #35. The iterative loop is now complete. The state variables at the end
of the subincrement are now given by the values of the quantities
$\Theta(t + \Delta t)$, $R(t + \Delta t)$, $c_i(t + \Delta t)$, $\Omega_i(t + \Delta t)$, $\varepsilon_i(t + \Delta t)$, $\sigma_i(t + \Delta t)$
at the updated time increment $t + \Delta t$.

Step #36. Go to Step #1 for next time increment.

Appendix 16. MARC Input History for Thermomechanical Hysteresis Loop

```
 1  TITLE
 2  SIZING                THERMOMECHANICAL LOOP WITH FUNCTIONAL THEORY
 3  POST                         15000          4        9     2    10
 4  ALL POINTS          2
 5  INPUT TAPE          1
 6  HYPOELAS
 7  STATE VARS         16
 8  NO LOADCOR          1
 9  RESTART
10  END
11  MESH2D
12  BLOCKS
13  DEFINE             4      10     1     1     9       6
14  DEFINE             1
15  BOUNDARY           2       2     1     2     3       4
16  BOUNDARY
17           1         1.
18           2         1.            1.
19           3         0.            1.
20           4
21  CONSTRAINT
22           2         1
23           1         3
24           1         4            2
25  MERGE
26  .GOOS
27  GENERATE           1
28  CONNECTIVITY       1
29  CONNECTIVITY
30  COORDINATES        1
31  BOUNDARY CONDITIONS          1
32  BOUNDARY CONDITIONS          1
33  BOUNDARY CONDITIONS          0
34           1,3,1,1,1.E-8
35  THERMAL LOADS
36           1,
37           0.,1.E-6
38  
39  PROPERTY           1
40           1         3.2E6              .3       0.E-5
41                     4
42  POST               2      16    16
43           1
44           1
45  PRINT CHOICE       1
46           1
47  CONTROL            1
48           500,15,1,05
49           .05
50  RESTART            .05
51           1,1,0,8,8
52  END OPTION
53  BOUNDARY CHANGE
54           3,
```

Appendix 16. MARC Input History for Thermomechanical Hysteresis Loop (Continued)

```
60    7,1,1,-.000088
61    8,2,1,-.000088
62    9,3,1,-.000088
63    THERMAL LOADS
64    1,,.1
65    0.,,1
66
67    CONTINUE
68    BOUNDARY CHANGE
69    3,
70    7,1,1,-.001000
71    8,2,1,-.001000
72    9,3,1,-.001000
73    THERMAL LOADS
74    1,,
75    0.,10.
76
77    CONTINUE
78    BOUNDARY CHANGE
79    3,
80    7,1,1,-.000506
81    8,2,1,-.000506
82    9,3,1,-.000506
83    THERMAL LOADS
84    1,,
85    105.,5.125
86
87    CONTINUE
88    BOUNDARY CHANGE
89    3,
90    7,1,1,-.000506
91    8,2,1,-.000506
92    9,3,1,-.000506
93    THERMAL LOADS
94    1,,
95    105.,5.125
96
97    CONTINUE
98    BOUNDARY CHANGE
99    3,
100   7,1,1,-.000475
101   8,2,1,-.000475
102   9,3,1,-.000475
103   THERMAL LOADS
104   1,,
105   100.,2.5
106
107   CONTINUE
108   BOUNDARY CHANGE
109   3,
110   7,1,1,-.000475
111   8,2,1,-.000475
112   9,3,1,-.000475
113   THERMAL LOADS
114   1,,
115   100.,2.5
116
117   CONTINUE
118   BOUNDARY CHANGE
119   3,
```

```
120  7,1,1,-.000419
121  8,2,1,-.000419
122  9,3,1,.000419
123  THERMAL LOADS
124  1,
125  91.,2.25
126  CONTINUE
127  BOUNDARY CHANGE
128  3,
129  7,1,1,-.000419
130  8,2,1,-.000419
131  9,3,1,.000419
132  THERMAL LOADS
133  1,
134  91.,2.25
135  CONTINUE
136  BOUNDARY CHANGE
137  3,
138  7,1,1,-.000234
139  8,2,1,-.000234
140  9,3,1,.000234
141  THERMAL LOADS
142  1,
143  69.,2.125
144  CONTINUE
145  BOUNDARY CHANGE
146  3,
147  7,1,1,-.000234
148  8,2,1,-.000234
149  9,3,1,.000234
150  THERMAL LOADS
151  1,
152  69.,2.125
153  CONTINUE
154  BOUNDARY CHANGE
155  3,
156  7,1,1,-.000062
157  8,2,1,-.000062
158  9,3,1,.000062
159  THERMAL LOADS
160  1,
161  26.,1.625
162  CONTINUE
163  BOUNDARY CHANGE
164  3,
165  7,1,1,-.000062
166  8,2,1,-.000062
167  9,3,1,.000062
168  THERMAL LOADS
169  1,
170  26.,1.625
171  CONTINUE
172  BOUNDARY CHANGE
173  3,
174  7,1,1,-.000062
175  8,2,1,-.000062
176  9,3,1,.000062
177  THERMAL LOADS
178  1,
179  26.,1.625
```

```
180   7.,1.,1.,+.0000080
181   8.,2.,1.,+.0000080
182   9.,3.,1.,+.0000080
183   THERMAL LOADS
184   1.,
185   14.,1.375
186
187   CONTINUE
188   BOUNDARY CHANGE
189   3.,1.,1.,+.0000080
190   7.,1.,1.,+.0000080
191   8.,2.,1.,+.0000080
192   9.,3.,1.,+.0000080
193   THERMAL LOADS
194   1.,
195   14.,1.375
196
197   CONTINUE
198   BOUNDARY CHANGE
199   3.,1.,1.,1.E-7
200   7.,1.,1.,1.E-7
201   8.,2.,1.,1.E-7
202   9.,3.,1.,1.E-7
203   THERMAL LOADS
204   1.,
205   0.,20.5
206
207   CONTINUE
208   BOUNDARY CHANGE
209   3.,1.,1.,1.E-7
210   7.,1.,1.,1.E-7
211   8.,2.,1.,1.E-7
212   9.,3.,1.,1.E-7
213   THERMAL LOADS
214   1.,
215   0.,20.5
216
217   CONTINUE
218   BOUNDARY CHANGE
219   3.,1.,1.,+.0000135
220   7.,1.,1.,+.0000135
221   8.,2.,1.,+.0000135
222   9.,3.,1.,+.0000135
223   THERMAL LOADS
224   1.,
225   -25.,2.25
226
227   CONTINUE
228   BOUNDARY CHANGE
229   3.,1.,1.,+.0000135
230   7.,1.,1.,+.0000135
231   8.,2.,1.,+.0000135
232   9.,3.,1.,+.0000135
233   THERMAL LOADS
234   1.,
235   -25.,2.25
236
237   CONTINUE
238   BOUNDARY CHANGE
239   3.,
```

```
240   7,1,1,+.0004375
241   8,2,1,+.0004375
242   9,3,1,+.0004375
243   THERMAL LOADS
244   1,-75.,2.75
245   -75.,2.75
246
247   CONTINUE
248   BOUNDARY CHANGE
249   3,,1,+.0004375
250   7,1,1,+.0004375
251   8,2,1,+.0004375
252   9,3,1,+.0004375
253   THERMAL LOADS
254   1,-75.,2.75
255   -75.,2.75
256
257   CONTINUE
258   BOUNDARY CHANGE
259   3,,1,+.0003755
260   7,1,1,+.0003755
261   8,2,1,+.0003755
262   9,3,1,+.0003755
263   THERMAL LOADS
264   1,-66.5,1.5
265   -66.5,1.5
266
267   CONTINUE
268   BOUNDARY CHANGE
269   3,,1,+.0003755
270   7,1,1,+.0003755
271   8,2,1,+.0003755
272   9,3,1,+.0003755
273   THERMAL LOADS
274   1,-66.5,1.5
275   -66.5,1.5
276
277   CONTINUE
278   BOUNDARY CHANGE
279   3,,1,+.0004455
280   7,1,1,+.0004455
281   8,2,1,+.0004455
282   9,3,1,+.0004455
283   THERMAL LOADS
284   1,-106.5,2.75
285   -106.5,2.75
286
287   CONTINUE
288   BOUNDARY CHANGE
289   3,,1,+.0004455
290   7,1,1,+.0004455
291   8,2,1,+.0004455
292   9,3,1,+.0004455
293   THERMAL LOADS
294   1,-106.5,2.75
295   -106.5,2.75
296
297   CONTINUE
298   BOUNDARY CHANGE
299   3,
```

Appendix 16. MARC Input History for Thermomechanical Hysteresis Loop (Continued)

```
300   7,1,1,+.0002535
301   8,2,1,+.0002535
302   9,3,1,+.0002535
303   THERMAL LOADS
304   1,-77.5,2.125
305
306   CONTINUE
307   BOUNDARY CHANGE
308   3,
309
310   7,1,1,+.0002535
311   8,2,1,+.0002535
312   9,3,1,+.0002535
313   THERMAL LOADS
314   1,-77.5,2.125
315
316   CONTINUE
317   BOUNDARY CHANGE
318   3,
319
320   7,1,1,+.0000130
321   8,2,1,+.0000130
322   9,3,1,+.0000130
323   THERMAL LOADS
324   1,-46.5,2.375
325
326   CONTINUE
327   BOUNDARY CHANGE
328   3,
329
330   7,1,1,+.0000130
331   8,2,1,+.0000130
332   9,3,1,+.0000130
333   THERMAL LOADS
334   1,-46.5,2.375
335
336   CONTINUE
337   BOUNDARY CHANGE
338   3,
339
340   7,1,1,-.0000088
341   8,2,1,-.0000088
342   9,3,1,-.0000088
343   THERMAL LOADS
344   1,-16.,2.5
345
346   CONTINUE
347   BOUNDARY CHANGE
348   3,
349
350   7,1,1,-.0005506
351   8,2,1,-.0005506
352   9,3,1,-.0005506
353   THERMAL LOADS
354   1,105.,5.125
355
356   CONTINUE
357   BOUNDARY CHANGE
358   3,
359
```

169

```
360   7,1,1,-.000506
361   8,2,1,-.000506
362   9,3,1,-.000506
363   THERMAL LOADS
364   1,
365   105.,5.125
366
367   CONTINUE
368   BOUNDARY CHANGE
369   3,
370   7,1,1,-.000475
371   8,2,1,-.000475
372   9,3,1,-.000475
373   THERMAL LOADS
374   1,
375   100.,2.5
376
377   CONTINUE
378   BOUNDARY CHANGE
379   3,
380   7,1,1,-.000475
381   8,2,1,-.000475
382   9,3,1,-.000475
383   THERMAL LOADS
384   1,
385   100.,2.5
386
387   CONTINUE
388   BOUNDARY CHANGE
389   3,
390   7,1,1,-.000419
391   8,2,1,-.000419
392   9,3,1,-.000419
393   THERMAL LOADS
394   1,
395   91.,2.25
396
397   CONTINUE
398   BOUNDARY CHANGE
399   3,
400   7,1,1,-.000419
401   8,2,1,-.000419
402   9,3,1,-.000419
403   THERMAL LOADS
404   1,
405   91.,2.25
406
407   CONTINUE
408   BOUNDARY CHANGE
409   3,
410   7,1,1,-.000234
411   8,2,1,-.000234
412   9,3,1,-.000234
413   THERMAL LOADS
414   1,
415   69.,2.125
416
417   CONTINUE
418   BOUNDARY CHANGE
419   3,
```

```
4420   7,1,1,-.000234
4421   8,2,1,-.000234
4422   9,3,1,-.000234
4423   THERMAL LOADS
4424   1,
4425   69.,2.125
4426
4427   CONTINUE
4428   BOUNDARY CHANGE
4429   3,
4430   7,1,1,-.000062
4431   8,2,1,-.000062
4432   9,3,1,-.000062
4433   THERMAL LOADS
4434   1,
4435   26.,1.625
4436
4437   CONTINUE
4438   BOUNDARY CHANGE
4439   3,
4440   7,1,1,-.000062
4441   8,2,1,-.000062
4442   9,3,1,-.000062
4443   THERMAL LOADS
4444   1,
4445   26.,1.625
4446
4447   CONTINUE
4448   BOUNDARY CHANGE
4449   3,
4450   7,1,1,+.000080
4451   8,2,1,+.000080
4452   9,3,1,+.000080
4453   THERMAL LOADS
4454   1,
4455   14.,1.375
4456
4457   CONTINUE
4458   BOUNDARY CHANGE
4459   3,
4460   7,1,1,+.000080
4461   8,2,1,+.000080
4462   9,3,1,+.000080
4463   THERMAL LOADS
4464   1,
4465   14.,1.375
4466
4467   CONTINUE
4468   BOUNDARY CHANGE
4469   3,
4470   7,1,1,1.E-7
4471   8,2,1,1.E-7
4472   9,3,1,1.E-7
4473   THERMAL LOADS
4474   1,
4475   0.,20.5
4476
4477   CONTINUE
4478   BOUNDARY CHANGE
4479   3,
```

```
480   7.,1.,1.,1.E-7
481   8.,2.,1.,1.E-7
482   9.,3.,1.,1.E-7
483   THERMAL LOADS
484   1.,20.5
485   0.,20.5
486
487   CONTINUE
488   BOUNDARY CHANGE
489   3.,1.,1.,+.0001135
490   7.,1.,1.,+.0001135
491   8.,2.,1.,+.0001135
492   9.,3.,1.,+.0001135
493   THERMAL LOADS
494   1.25.,2.25
495   -1.25.,2.25
496
497   CONTINUE
498   BOUNDARY CHANGE
499   3.,1.,1.,+.0001135
500   7.,1.,1.,+.0001135
501   8.,2.,1.,+.0001135
502   9.,3.,1.,+.0001135
503   THERMAL LOADS
504   1.25.,2.25
505   -1.25.,2.25
506
507   CONTINUE
508   BOUNDARY CHANGE
509   3.,1.,1.,+.0004375
510   7.,1.,1.,+.0004375
511   8.,2.,1.,+.0004375
512   9.,3.,1.,+.0004375
513   THERMAL LOADS
514   1.75.,2.75
515   -1.75.,2.75
516
517   CONTINUE
518   BOUNDARY CHANGE
519   3.,1.,1.,+.0004375
520   7.,1.,1.,+.0004375
521   8.,2.,1.,+.0004375
522   9.,3.,1.,+.0004375
523   THERMAL LOADS
524   1.75.,2.75
525   -1.75.,2.75
526
527   CONTINUE
528   BOUNDARY CHANGE
529   3.,1.,1.,+.0003755
530   7.,1.,1.,+.0003755
531   8.,2.,1.,+.0003755
532   9.,3.,1.,+.0003755
533   THERMAL LOADS
534   1.66.5,1.5
535   -1.66.5,1.5
536
537   CONTINUE
538   BOUNDARY CHANGE
539   3.,
```

172

```
540   7,1,1,+.0003755
541   8,2,1,+.0003755
542   9,3,1,+.0003755
543   THERMAL LOADS
544   1,
545   -66.5,1.5
546   CONTINUE
547   BOUNDARY CHANGE
548   3,
549   7,1,1,+.0004455
550   8,2,1,+.0004455
551   9,3,1,+.0004455
552   THERMAL LOADS
553   1,
554   -106.5,2.75
555   CONTINUE
556   BOUNDARY CHANGE
557   3,
558   7,1,1,+.0004455
559   8,2,1,+.0004455
560   9,3,1,+.0004455
561   THERMAL LOADS
562   1,
563   -106.5,2.75
564   CONTINUE
565   BOUNDARY CHANGE
566   3,
567   7,1,1,+.0002535
568   8,2,1,+.0002535
569   9,3,1,+.0002535
570   THERMAL LOADS
571   1,
572   -77.5,2.125
573   CONTINUE
574   BOUNDARY CHANGE
575   3,
576   7,1,1,+.0002535
577   8,2,1,+.0002535
578   9,3,1,+.0002535
579   THERMAL LOADS
580   1,
581   -77.5,2.125
582   CONTINUE
583   BOUNDARY CHANGE
584   3,
585   7,1,1,+.0001130
586   8,2,1,+.0001130
587   9,3,1,+.0001130
588   THERMAL LOADS
589   1,
590   -46.5,2.375
591   CONTINUE
592   BOUNDARY CHANGE
593   3,
```

```
600  7.,1.,1.,+.00001.0
601  8.,2.,1.,+.00001.0
602  9.,3.,1.,+.00001.0
603  THERMAL LOADS
604  1
605  -46.5,2.375
606  CONTINUE
607  BOUNDARY CHANGE
608  3.,1.,1.,-.000008B
609  7.,1.,1.,-.000008B
610  8.,2.,1.,-.000008B
611  9.,3.,1.,-.000008B
612  THERMAL LOADS
613  1
614  -16.,2.5
615  CONTINUE
616
617
```

174

Appendix 17. Fortran Listing of Functional Theory in Subroutine HYPELA

```fortran
      SUBROUTINE HYPELA(D,G,E,DE,S,TEMP,DTEMP,NGENS,N,NN,KC,MAT,NDI,
     1NSHEAR)
      DIMENSION D(NGENS,NGENS),G(NGENS),E(NGENS),DE(NGENS),S(NGENS)
      DIMENSION TEMP(1),DTEMP(1)
      DIMENSION SIGB(6),OMEGB(6),CB(6),SIGE(6),OMEGE(6),CE(6)
      DIMENSION DC(6),DET(6),OM(6),OMEGI(6),OMEGZT(6)
      DIMENSION SUMIN(6),DSIGIN(6),DS(6),AB(6)
      DIMENSION TABT(6),EET(6),ANUT(6),ANT(6),AMT(6),ANIT(6)
      DIMENSION AN2T(6),EET(6),ANUT(6),AN4T(6),AN5T(6),AN6T(6),AN7T(6)
      DIMENSION AK1T(6),AK2T(6),ANINT(6)
      COMMON/AKEV/KEVINC
      COMMON/FAR/DUMMINC
      COMMON/CCC/DUMMY(18),NCYCLE
      DATA TABT/80.,100.,1200.,1400.,1600.,1800./
      DATA EET/26.,24.E6,22.6E6,18.6E6,13.2E6/
      DATA AK1T/0.,0.328,0.334,0.339,0.345,0.351/
      DATA AK2T/.5931,.75631,.95631,.251886,.91505,.59292./
      DATA ANINT/1.,.059,.079,.244,.195,.223/
      DATA AMT/.158,1.158,1.158,1.158,1.158,1.158/
      DATA AN2T/.30,.E7,.6E7,.5E7,.2,E7.5,E6,1.E6/
      DATA AN3T/800.,1000.,781.2,1178.6,672.6,312.5/
      DATA AN4T/0.,0.,0.,0./
      DATA AN5T/0.,0.,0.,0./
      DATA AN6T/977E-4,2.733E-3/
      DATA AN7T/0.,0.,0./
      DATA OMEGZT/0.,0.,-2000.,-1434.,-1200./
C******THIS SUBROUTINE RETURNS THE ELASTICITY MATRIX D AND INELASTIC
C******STRESS INCREMENT DG FOR THE FUNCTIONAL VISCOPLASTIC THEORY
C******USING THE INTEGRAL FORM (K.P.WALKER UTRC TEL# 203-727-7399)
C**
C******SECOND INVARIANT FUNCTION
C******SINV(A,B,C,D,E,F)=(A*A+B*B+C*C+2.*(D*D+E*E+F*F))*2./3.
C******DETERMINE IF PLANE STRESS,PLANE STRAIN,AXISYMMETRIC,OR 3-D
C******KELTYPE=1 FOR PLANE STRESS PROBLEM             KELTYPE=1
C******KELTYPE=2 FOR PLANE STRAIN PROBLEM             KELTYPE=2
C******KELTYPE=3 FOR 3-D PROBLEM                      KELTYPE=3
   33 IF(NDI.EQ.3.AND.NSHEAR.EQ.1) KELTYPE=1
      IF(NDI.EQ.2.AND.NSHEAR.EQ.1) KELTYPE=2
      IF(NDI.EQ.3.AND.NSHEAR.EQ.3) KELTYPE=3
C******SET UP CONSTANTS
      NTP=6
      NTPM1=NTP-1
      MAXIT=8
      MINIT=1
      NELPR=1
      IPRE=1
      NPRIN=1
      NSPLIT=5
      SFTEMP=940.
      TDIF=200.
C******PUT STRESSES AT BEGINNING OF MARC INCREMENT INTO SIGB ARRAY ACCORDING
C******TO ELEMENT TYPE
      GO TO(801,802,803),KELTYP
  801 CONTINUE
      SIGB(1)=S(1)
      SIGB(2)=S(2)
```

```
      SIGB(3)=S(3)
      SIGB(4)=S(4)
      SIGB(5)=0.
      SIGB(6)=0.
      GO TO 900
  802 CONTINUE
      SIGB(1)=S(1)
      SIGB(2)=S(2)
      SIGB(3)=0.*S(3)
      SIGB(4)=S(3)
      SIGB(5)=0.
      SIGB(6)=0.
      GO TO 900
  803 DO 804 J=1,6
      SIGB(J)=S(J)
  804 CONTINUE
  900 CONTINUE
C*****INITIALIZE STATE VARIABLES ON FIRST ENTRY TO SUBROUTINE. ON SECOND
C*****AND SUBSEQUENT ENTRIES SKIP INITIALIZATION.
      KEVIN=INC+NCYCLE
      IF(KEVIN.NE.0) GO TO 3
      TEMP(1)=SFTEMP
      DO 2 J=2,15
      TEMP(J)=0.
    2 CONTINUE
    3 CONTINUE
C*****SET STARTING VALUES OF STATE VARIABLES DURING PRESENT MARC INCREMENT
      C1=0.
      C2=0.
      C3=0.
      C4=0.
      C5=0.
      DEG=TEMP(1)
      TB=TEMP(2)
      RB=TEMP(3)
      DO 104 KA=1,6
      J=KA+3
      OMEGB(KA)=TEMP(J)
      CB(KA)=TEMP(J+6)
      SUMIN(KA)=0.
  104 CONTINUE
C*****SET TEMPERATURE AND TIME SUBINCREMENTS
      SPLIT=NSPLIT
      DDEG=DTEMP(1)/SPLIT
      DT=DTEMP(2)/SPLIT
C*****PUT SUBINCREMENTS OF TOTAL STRAIN INTO ARRAY DET ACCORDING
C*****TO ELEMENT TYPE
      GO TO(61,62,63),KELTYP
   61 CONTINUE
      DET(1)=DE(1)/SPLIT
      DET(2)=DE(2)/SPLIT
      DET(3)=DE(3)/SPLIT
      DET(4)=0.5*DE(4)/SPLIT
      DET(5)=0.
      DET(6)=0.
      GO TO 71
   62 DET(1)=DE(1)/SPLIT
      DET(2)=DE(2)/SPLIT
      DET(3)=-DET(1)-DET(2)
      DET(4)=0.5*DE(3)/SPLIT
```

Appendix 17. Fortran Listing of Functional Theory in Subroutine HYPELA (Continued)

```
      DET(5)=0.
      DET(6)=0.
      GO TO 71
   63 CONTINUE
      DO 64 J=1,6
      FAC=1.
      IF(J.GT.3)FAC=0.5
      DET(J)=FAC*DE(J)/SPLIT
   64 CONTINUE
   71 CONTINUE
C*****SET INITIAL GUESS FOR EQUILIBRIUM STRESS AT END
C*****OF SUBINCREMENT EQUAL TO EQUILIBRIUM STRESS AT
C*****BEGINNING OF MARC INCREMENT
      DO 2000 J=1,6
      OMEGE(J)=OMEGB(J)
 2000 CONTINUE
C*****ASSUME INITIAL GUESS FOR INELASTIC STRAIN IN FIRST SUBINCREMENT
C*****EQUAL TO DEVIATORIC STRAIN SUBINCREMENT
      DVOL=DET(1)+DET(2)+DET(3)
      DO 72 J=1,6
      ALPHA=1.
      IF(J.GT.3)ALPHA=0.
      DC(J)=DET(J)-ALPHA*DVOL/3.
   72 CONTINUE
C*****COMPUTE INELASTIC STRAINS AT END OF FIRST SUBINCREMENT
      DO 7125 J=1,6
      CE(J)=CB(J)+DC(J)
 7125 CONTINUE
C*****START INTEGRATION OVER SUBINCREMENTS
      DO 5 JA=1,NSPLIT
C*****COMPUTE TEMPERATURE DEPENDENT MATERIAL CONSTANTS
      DEGM=DEG+0.5*DDEG
      L1=DEGM
      L2=TABT(1)-TDIF
      L3=TDIF
      IT=(L1-L2)/L3
      IF(IT.LT.1)IT=1
      IF(IT.GT.NTPM1)IT=NTPM1
      FAC=(DEGM-TABT(IT))/TDIF
      EET=(EET(IT+1)-EET(IT))*FAC+EET(IT)
      ANU=(ANUT(IT+1)-ANUT(IT))*FAC+ANUT(IT)
      AK1=(AK1T(IT+1)-AK1T(IT))*FAC+AK1T(IT)
      AK2=(AK2T(IT+1)-AK2T(IT))*FAC+AK2T(IT)
      AM=(AMT(IT+1)-AMT(IT))*FAC+ANINT(IT)
      AN1=(AN1T(IT+1)-AN1T(IT))*FAC+AMT(IT)
      AN2=(AN2T(IT+1)-AN2T(IT))*FAC+AN1T(IT)
      AN3=(AN3T(IT+1)-AN3T(IT))*FAC+AN2T(IT)
      AN4=(AN4T(IT+1)-AN4T(IT))*FAC+AN3T(IT)
      AN5=(AN5T(IT+1)-AN5T(IT))*FAC+AN4T(IT)
      AN6=(AN6T(IT+1)-AN6T(IT))*FAC+AN5T(IT)
      AN7=(AN7T(IT+1)-AN7T(IT))*FAC+AN6T(IT)
      OMEGZ=(OMEGZT(IT+1)-OMEGZT(IT))*FAC+OMEGZT(IT)
      ANI=1./ANIN
      ALAM=EE*ANU/((1.-2.*ANU)*(1.+ANU))
      AMU=(1.-2.*ANU)*ALAM/(2.*ANU)
      C1=C1+2.*AMU*ALAM/((ALAM+AMU)*SPLIT)
      C2=C2+2.*AMU*(ALAM+AMU)/((ALAM+2.*AMU)*SPLIT)
      C3=C3+2.*AMU/SPLIT
      C4=C4+AMU/SPLIT
```

Appendix 17. Fortran Listing of Functional Theory in Subroutine HYPELA (Continued)

```
      C5=C5+ALAM/SPLIT
C***** SET INITIAL VALUES OF EQUILIBRIUM STRESS
      DENOM=SINV(CE(1),CE(2),CE(3),CE(4),CE(5),CE(6))
      DENOM=DENOM+1.E-30
      AB(1)=(-OMEGZ+2.*OMEGZ*(CE(1)*CE(1)+CE(4)*CE(4)+CE(6)*CE(6)
     1+1.E-30)/DENOM
      AB(2)=(-OMEGZ+2.*OMEGZ*(CE(4)*CE(4)+CE(2)*CE(2)+CE(5)*CE(5)
     1+1.E-30)/DENOM
      AB(3)=(-OMEGZ+2.*OMEGZ*(CE(6)*CE(6)+CE(5)*CE(5)+CE(3)*CE(3)+
     11.E-30)/DENOM
      AB(4)=2.*OMEGZ*(CE(1)*CE(4)+CE(4)*CE(2)+CE(5)*CE(5)+CE(6)+1.E-30)/
     1DENOM
      AB(5)=2.*OMEGZ*(CE(4)*CE(6)+CE(2)*CE(5)+CE(5)*CE(3))+1.E-30)/
     1DENOM
      AB(6)=2.*OMEGZ*(CE(1)*CE(6)+CE(4)*CE(5)+CE(6)*CE(3))+1.E-30)/
     1DENOM
      ABSUM=AB(1)+AB(2)+AB(3)
      DO 7124 J=1,6
      ALPHA=1.
      IF(J.GT.3)ALPHA=0.
      OMEGI(J)=AB(J)-ALPHA*ABSUM/3.
7124  CONTINUE
C***** COMPUTE INITIAL DR AND SAVE IN DRG
      DR=SINV(DC(1),DC(2),DC(3),DC(4),DC(5),DC(6))
      DR=SQRT(DR)
      IF(DR.LE.1.E-10)DR=1.E-10
      NIT=0
C***** START ITERATION LOOP
73    CONTINUE
      DRG=DR
      NIT=NIT+1
C***** COMPUTE DRAG STRESS
      AK=AK1-AK2*EXP(-AN7*(RB+DR))
      A=SINV(OMEGE(1),OMEGE(2),OMEGE(3),OMEGE(4),OMEGE(5),OMEGE(6))
      IF(A.LE.1.E-10)A=1.E-10
      B=0.5*(AM-1.)
      DHARD=(AN3+AN4*EXP(-AN5*(RB+DR)))*DR
      RECOV=AN6*DT*A**B
      DG=DHARD+DRECOV
C***** COMPUTE INELASTIC STRAINS AT END OF SUBINCREMENT
      DO 302 J=1,6
      CE(J)=CB(J)+DC(J)
302   CONTINUE
C***** COMPUTE EQUILIBRIUM STRESS AT END OF SUBINCREMENT
      Q1=EXP(-DG)
      IF(ABS(DG).LE.1.E-10)DG=1.E-10
      IF(ABS(DG).LE.1.E-4)Q2=AN2*(1.-.5*DG+DG*DG/6.-DG*DG*DG/12.)
      IF(ABS(DG).GT.1.E-4)Q2=AN2*(1.-Q1)/DG
      DO 303 J=1,6
      OMEGE(J)=OMEGI(J)+AN1*CE(J)+Q1*(OMEGB(J)-OMEGI(J)-AN1*CB(J))
     1+Q2*DC(J)
303   CONTINUE
C***** IF NO RECOVERY, SKIP NEWTON-RAPHSON ITERATION FOR
C***** EQUILIBRIUM STRESS
      IF(AN6.EQ.0.)GO TO 298
C***** COMPUTE FUNCTION(DG)
      A=SINV(OMEGE(1),OMEGE(2),OMEGE(3),OMEGE(4),OMEGE(5),OMEGE(6))
      IF(A.LE.1.E-10)A=1.E-10
      B=0.5*(AM-1.)
      DRECOV=AN6*DT*A**B
```

```fortran
      FDG=DG-DHARD-DRECOV
      IF(ABS(DG).LE.1.E-3)Q6=AN2*(-.5+DG/3.-DG*DG/12.+DG*DG*DG/15.)
      IF(ABS(DG).GT.1.E-3)Q6=AN2*(DG*Q1+Q1-1.)/(DG*DG)
C***** COMPUTE DERIVATIVE D(FUNCTION(DG))/DG
      DADDG=0.
      DO 304 J=1,6
      BETA=1.
      IF(J.GT.3)BETA=2.
      DOMDDG=-Q1*(OMEGB(J)-OMEGI(J)-AN1*CB(J))+Q6*DC(J)
      DADDG=DADDG+4.*BETA*DOMDDG*OMEGE(J)/3.
304   CONTINUE
      DFDFGDG=1.-.5*AN6*DT*(AM-1.)*DADDG*A**(.5*(AM-3.))
C***** REFINE DG WITH NEWTON-RAPHSON ITERATION
      IF(DFDFGDG.EQ.0.)GO TO 7126
      RATIO=FDG/DFDGDG
      IF(ABS(RATIO).GT.DG)GO TO 7126
      DG=DG-RATIO
7126  CONTINUE
C***** RECOMPUTE EQUILIBRIUM STRESS AT END OF SUBINCREMENT
      Q1=EXP(-DG)
      IF(ABS(DG).LE.1.E-10)DG=1.E-10
      IF(ABS(DG).LE.1.E-4)Q2=AN2*(1.-.5*DG+DG*DG/6.-DG*DG*DG/12.)
      IF(ABS(DG).GT.1.E-4)Q2=AN2*(1.-Q1)/DG
      DO 305 J=1,6
      OMEGE(J)=OMEGI(J)+AN1*CE(J)+Q1*(OMEGB(J)-OMEGI(J)-AN1*CB(J))
     1+Q2*DC(J)
305   CONTINUE
298   CONTINUE
C***** COMPUTE STRESS AT END OF SUBINCREMENT
C***** IF PLANE STRESS COMPUTE TOTAL STRAIN INCREMENT IN THICKNESS
C***** DIRECTION DET(3) AND VOLUMETRIC STRAIN AT END OF SUBINCREMENT
      Q3=1.-1./AN
      PRESB=(SIGB(1)+SIGB(2)+SIGB(3))/3.
      IF(DR.LE.1.E-10)DR=1.E-10
      DQ=(3.*AMU*DT/AK)*(DR/DT)**Q3
      Q4=EXP(-DQ)
      IF(ABS(DQ).LE.1.E-3)Q5=1.-.5*DQ+DQ*DQ/6.-DQ*DQ*DQ/12.
      IF(ABS(DQ).GT.1.E-3)Q5=(1.-Q4)/DQ
      IF(ABS(DQ).LE.1.E-3)Q7=-.5+DQ/3.-DQ*DQ/12.+DQ*DQ*DQ/15.
      IF(ABS(DQ).GT.1.E-3)Q7=(DQ*Q4+Q4-1.)/(DQ*DQ)
      IF(KELTYP.EQ.2)
     1DET(3)=(2.*AMU*DC(3)-ALAM*(DET(1)+DET(2)))/(ALAM+2.*AMU)
      DVOL=DET(1)+DET(2)+DET(3)
      PRESE=PRESB+(ALAM+2.*AMU/3.)*DVOL
701   CONTINUE
      DO 702 J=1,6
      ALPHA=1.
      IF(J.GT.3)ALPHA=0.
      DOM=OMEGE(J)-OMEGB(J)
      SIGE(J)=2.*OMEGE(J)-2.*OMEGB(J)/3.+ALPHA*PRESE+Q4*(SIGB(J)-2.*OMEGB(J)/3.
     1-ALPHA*PRESB)+Q5*(2.*AMU*DET(J)-ALPHA*2.*AMU*DVOL/3.-2.*DOM/3.)
C***** COMPUTE INELASTIC STRAIN SUBINCREMENT
      DO 7123 J=1,6
      ALPHA=1.
      IF(J.GT.3)ALPHA=0.
      DC(J)=(ALPHA*ALAM*DVOL+2.*AMU*DET(J)-SIGE(J)+SIGB(J))/(2.*AMU)
      CE(J)=CB(J)+DC(J)
7123  CONTINUE
      DR=SINV(DC(1),DC(2),DC(3),DC(4),DC(5),DC(6))
```

179

```fortran
      DR=SQRT(DR)
      IF(DR.LE.1.E-10)DR=1.E-10
C***** COMPUTE FUNCTION(DQ)
      FDQ=DQ-(3.*AMU*DT/AK)*(DR/DT)**Q3
C***** COMPUTE DERIVATIVE D(FUNCTION(DQ))/DQ
      DDRDDQ=0.
      DO 306 J=1,6
      ALPHA=1.
      IF(J.GT.3)ALPHA=0.
      BETA=1.
      IF(J.GT.3)BETA=2.
      DOM=OMEGE(J)-OMEGB(J)
      DDCDDQ=Q4*(SIGB(J)-2.*OMEGB(J)/3.-ALPHA*PRESB)
     1-Q7*(2.*AMU*DET(J)-ALPHA*2.*AMU*DVOL/3.-2.*DOM/3.)
      DDCDDQ=DDCDDQ/(2.*AMU)
      DDRDDQ=DDRDDQ+2.*BETA*DDCDDQ*DC(J)/(3.*DR)
  306 CONTINUE
      DFDQDDQ=1.-3.*AMU*Q3*DDRDDQ*DT/(AK*(DR/DT)**ANIN)
C***** REFINE DQ WITH NEWTON-RAPHSON ITERATION
      IF(DFDQDDQ.EQ.0.)GO TO 7127
      RATIO=FDQ/DFDQDDQ
      IF(ABS(RATIO).GT.DQ)GO TO 7127
      DQ=DQ-RATIO
 7127 CONTINUE
      Q4=EXP(-DQ)
      IF(ABS(DQ).LE.1.E-4)Q5=1.-.5*DQ+DQ*DQ/6.-DQ*DQ*DQ/12.
      IF(ABS(DQ).GT.1.E-4)Q5=(1.-Q4)/DQ
      IF(KELTYP.EQ.2)
     1DET(3)=(2.*AMU*DC(3)-ALAM*(DET(1)+DET(2)))/(ALAM+2.*AMU)
      DVOL=DET(1)+DET(2)+DET(3)
      PRESE=PRESB+(ALAM+2.*AMU/3.)*DVOL
C***** RECOMPUTE STRESS AT END OF SUBINCREMENT
      DO 307 J=1,6
      ALPHA=1.
      IF(J.GT.3)ALPHA=0.
      DOM=OMEGE(J)-OMEGB(J)
      SIGE(J)=2.*OMEGB(J)/3.+ALPHA*PRESE+Q4*(SIGB(J)-2.*OMEGB(J)/3.
     1-ALPHA*PRESB)+Q5*(2.*AMU*DET(J)-ALPHA*2.*AMU*DVOL/3.-2.*DOM/3.)
  307 CONTINUE
C***** RECOMPUTE INELASTIC STRAIN SUBINCREMENT
      DO 308 J=1,6
      ALPHA=1.
      IF(J.GT.3)ALPHA=0.
      DC(J)=(ALPHA*ALAM*DVOL+2.*AMU*DET(J)-SIGE(J)+SIGB(J))/(2.*AMU)
  308 CONTINUE
      ERR=.01
C***** TEST FOR CONVERGENCE OF ITERATIONS
      DRG=SINV(DC(1),DC(2),DC(3),DC(4),DC(5),DC(6))
      DR=SQRT(DR)
C***** EXIT FROM ITERATION LOOP IF IN ELASTIC REGION
      DETEQ=SINV(DET(1),DET(2),DET(3),DET(4),DET(5),DET(6))
      D1=.01*SQRT(DETEQ)
      IF(DR.LE.D1.AND.NIT.EQ.2)GO TO 501
      IF(NIT.EQ.MAXIT)GO TO 501
      IF(NIT.LT.MINIT)GO TO 73
      TEST=(DR-DRG)/DRG
      TEST=ABS(TEST)
      IF(TEST.GT.ERR) GO TO 73
  501 CONTINUE
C***** COMPUTE INELASTIC STRESS SUBINCREMENT ACCORDING TO ELEMENT TYPE
```

Appendix 17. Fortran Listing of Functional Theory in Subroutine HYPELA (Continued)

```
809      GO TO(809,810,809),KELTYP
         CONTINUE
         DO 812 J=1,6
         DSIGIN(J)=-2.*AMU*DC(J)
312      CONTINUE
         GO TO 902
810      CONTINUE
         DO 813 J=1,6
         ALPHA=1.
         IF(J.GT.3) ALPHA=0.
         DSIGIN(J)=ALPHA*2.*AMU*ALAM*DC(3)/(ALAM+2.*AMU)-2.*AMU*DC(J)
813      CONTINUE
902      CONTINUE
C*****UPDATE SUBINCREMENT VARIABLES
         DEG=DEG+DDEG
         RB=RB+DR
         DO 113 J=1,6
         OMEGB(J)=OMEGE(J)
         SIGB(J)=SIGE(J)
         CB(J)=CE(J)
         SUMIN(J)=SUMIN(J)+DSIGIN(J)
113      CONTINUE
C*****END OF SUBINCREMENT LOOP
5        CONTINUE
C*****PUT ELASTICITY MATRIX IN D AND INELASTIC STRESS INCREMENT IN G
         GO TO(814,815,816),KELTYP
814      CONTINUE
         G(1)=SUMIN(1)
         G(2)=SUMIN(2)
         G(3)=SUMIN(3)
         G(4)=SUMIN(4)
         DO 817 J=1,4
         DO 817 K=1,4
         D(J,K)=0.
817      CONTINUE
         DO 818 J=1,3
         DO 818 K=1,3
         ALPHA=0.  ALPHA=1.
         IF(J.EQ.K) ALPHA=1.
         D(J,K)=C5+ALPHA*C3
818      CONTINUE
         D(4,4)=C4
         GO TO 903
815      CONTINUE
         G(1)=SUMIN(1)
         G(2)=SUMIN(2)
         G(3)=SUMIN(3)
         D(1,1)=C2
         D(1,2)=C1
         D(1,3)=0.
         D(2,1)=C1
         D(2,2)=C2
         D(2,3)=0.
         D(3,1)=0.
         D(3,2)=0.
         D(3,3)=C4
         GO TO 903
816      CONTINUE
         DO 821 J=1,6
         G(J)=SUMIN(J)
```

181

```
  821 CONTINUE
      DO 819 J=1,6
      DO 819 K=1,6
      D(J,K)=0.
  819 CONTINUE
      DO 820 J=1,3
      DO 820 K=1,3
      ALPHA=0.
      IF(J.EQ.K) ALPHA=1.
      D(J,K)=C5+ALPHA*C3
  820 CONTINUE
      D(4,4)=C4
      D(5,5)=C4
      D(6,6)=C4
  903 CONTINUE
C*****COMPUTE MARC STRESS INCREMENTS
      DO 822 J=1,NGENS
      SUM=0.
      DO 823 K=1,NGENS
      SUM=SUM+D(J,K)*DE(K)
  823 CONTINUE
      DS(J)=SUM+G(J)
  822 CONTINUE
C*****PUT STATE VARIABLE INCREMENTS INTO STORAGE ARRAYS FOR NEXT MARC INCREMENT
      DTEMP(3)=RB-TEMP(3)
      DTEMP(16)=0.
      TEMP(16)=AK1-AK2*EXP(-AN7*RB)
      DO 923 KA=1,6
      J=KA+3
      DTEMP(J)=OMEGE(KA)-TEMP(J)
      DTEMP(J+6)=CE(KA)-TEMP(J+6)
  923 CONTINUE
      IF(IPR.EQ.0) GO TO 12
      IF(NELPP.NE.N) GO TO 12
      IF(NN.NE.NPRIN) GO TO 12
      IF(NCYCLE.EQ.0) NWALK=0
      NWALK=NWALK+1
      NQ=NWALK-2*NCYCLE
      NQQ=NCYCLE-1
      WRITE(6,20) INC
   20 FORMAT(' INCREMENT' ,I5)
      WRITE(6,750) NIT
  750 FORMAT(' ITERATIONS',I5)
      WRITE(6,753)N,NN
  753 FORMAT(' ELEMENT',I5,' INTEGRATION POINT',I5)
      IF(NQ.EQ.0) WRITE(6,23) NQQ
      IF(NQ.GT.0) WRITE(6,39) NCYCLE
   23 FORMAT(' VALUES OF PARAMETERS DURING SOLUTION OF RECYCLE NUMBER'
     1,I5)
   39 FORMAT(' VALUES OF PARAMETERS DURING ASSEMBLY OF RECYCLE NUMBER'
     1,I5)
      WRITE(6,751) TEST
  751 FORMAT(' ITERATION TEST',F10.6)
      WRITE(6,29)
   29 FORMAT(' STRAIN INCREMENTS')
      WRITE(6,30) (DE(J),J=1,NGENS)
   30 FORMAT(1P6E15.6)
      WRITE(6,31)
   31 FORMAT(' STRESS INCREMENTS')
      WRITE(6,30) (DS(J),J=1,NGENS)
   12 RETURN
      END
```